Anja Wehling

The Dynamics of L$_3$ Phases

Cuvillier Verlag Göttingen

The Dynamics of L₃ Phases

Inaugural-Dissertation

zur

Erlangung des Doktorgrades

der Mathematisch-Naturwissenschaftlichen Fakultät

der Universität zu Köln

vorgelegt von

Anja Wehling

aus Goslar

Meinen Eltern

und Thimo

Abstract

As in ordinary fluids, the understanding of the dynamic processes is important to understand the equilibrium properties of complex fluids. As model system, the so-called L_3 phase was studied by using different relaxation techniques. Temperature jump relaxation and a newly developed isothermal shear apparatus with different detection methods were applied. The influence of structure parameters, i.e. the bilayer thickness and the interbilayer distance, on the dynamics of the L_3 phase were examined in detail. For that purpose, ternary mixtures of water (A), n-alkane (B) and a nonionic surfactant C_iE_j (n-alkylpolyoxyethylenoxide, C) were chosen allowing to change the surfactant / (surfactant + oil) volume ratio as well as the bilayer volume fraction. Minor changes in the sample's composition resulted in enormous changes of the relaxation time covering a range of many orders of magnitude from microseconds to minutes. A strong dependence of the relaxation time constants on the bilayer volume fraction was observed for a constant bilayer thickness. On the other hand, for a given bilayer volume fraction the relaxation time constant passes through a minimum in dependence of the surfactant / (surfactant + oil) volume ratio. A geometric model, which was tested and confirmed by SANS measurements, was defined to explain the influence of the structure parameters on the dynamics of the L_3 phase quantitatively. An interpretation of the experimental results was discussed towards a generalized description of the dynamics of the L_3 phase.

Kurzzusammenfassung

Genau wie bei normalen Flüssigkeiten ist für die Betrachtung von Gleichgewichtseigenschaften Komplexer Fluide ein Verständnis der dynamischen Prozesse unabdingbar. Als Modellsystem wurde die sogenannte L_3-Phase mit Hilfe verschiedener Relaxationsmethoden untersucht. Neben einer traditionellen Störungsmethode, dem Temperatursprung, wurde eine Neuentwickelung, die isotherme Scherung, wobei jeweils unterschiedliche Detektionsmethoden Anwendung finden. Um den Einfluß von Strukturparametern, wie die Dicke der geschwollenen Tensiddoppelschicht und der Abstand zwischen den Bilayern, auf die Dynamik der L_3-Phase detailliert untersuchen zu können, wurden ternäre Mischungen des Typs Wasser (A) — *n*-Alkan (B) — nichtionisches Tensid C_iE_j (*n*-Alkylpolyoxyethylenoxid, (C)) betrachtet. An diesen Systemen wurden der Tensid / (Öl + Tensid) Volumenbruch und der Membranvolumenbruch systematisch variiert. Geringe Änderungen in der Probenzusammensetzung führten zu Änderungen in den gefundenen Relaxationszeiten über mehrere Größenordnungen, von Mikrosekunden bis hin zum Minutenbereich. Es wurde eine starke Abhängigkeit der Relaxationszeitkonstanten vom Membranvolumenbruch bei konstanter Membrandicke gefunden. Gleichzeitig durchlaufen die experimentellen Relaxationszeitkonstanten als Funktion des Tensid / (Öl + Tensid) Volumenbruchs bei konstantem Membranvolumenbruch ein Minimum. Ein durch SANS Messungen verifiziertes geometrisches Model dient zur quantitativen Beschreibung des Einflusses der strukturellen Eigenschaften auf die beobachtete Dynamik der L_3-Phase. Die Diskussion der experimentellen Ergebnisse wird in Richtung einer universellen Beschreibung der Stabilität, Struktur und Dyamik der L_3-Phasen geführt.

Danksagung

Die vorliegende Arbeit wurde von Oktober 1998 bis Mai 2001 am Institut für Physikalische Chemie der Universität zu Köln unter Anleitung von Herrn Prof. Dr. Reinhard Strey angefertigt. Ihm danke ich herzlich, daß er mich so vertrauensvoll in seine Arbeitsgruppe aufgenommen hat und durch viele Anregungen und stete Freude am Diskutieren das Gelingen dieser Arbeit ermöglichte.

Herrn Prof. Dr. Georg Ilgenfritz danke ich für die Übernahme des Korreferats und seinem Interesse an „meinen" L_3-Phasen.

Herrn Peter Uhrmeister möchte ich für die Einarbeitung in die *T*-Sprung Apparatur, die Beantwortung unzähliger „Computer-Hilfeschreie", die ‚lustige' Zeit im Ecklabor zusammen mit Herrn Stefan Müller und für noch vieles mehr danken.

Während dieser Arbeit bestand eine Kollaboration mit Dr. Henrique Leitao von der Universität Lissabon, ermöglicht durch Mittel des Deutschen Akademischen Austauschdienstes (DAAD). Für zahlreiche Diskussionen und geduldige Erklärungen zur theoretisch-physikalischen Seite dieser Arbeit, möchte ich Dr. Leitao danken.

Für die sorgfältige Durchsicht der Dissertation, und stete wissenschaftliche, aber auch moralische Unterstützung, möchte ich vor allem Dr. Cosima Stubenrauch und Dr. Thomas Sottmann danken.

Herrn Wolfgang Röhl und der Feinmechanischen Werkstatt unter der Leitung von Herrn Herbert Metzner danke ich für Ihre Hilfe beim Bau und der Instandhaltung aller relaxationskinetischer Anlagen. Ohne sie hätte diese Arbeit gar nicht entstehen können.

Dr. Thomas Sottmann, Britta Jakobs und Peter Uhrmeister danke ich für die SANS Messungen meiner Proben in Grenoble, deren Ergebnisse einen wesentlichen Beitrag zum Gelingen dieser Arbeit geleistet haben.

Weiterhin möchte ich allen Kollegen für ihre Hilfsbereitschaft und das gute Arbeitsklima danken, wobei mein besonderer Dank jenen gilt, die auf vielfältige Art und Weise zum Gelingen dieser Arbeit beigetragen haben.

Table of Contents

Abbreviations and symbols

a	structure prefactor (depending on the model used)
a_C	surfactant headgroup area
a	water-rich phase
A/V	specific internal area
A	water component
A	prefactor of low ϕ_{B+C} relaxation regime
b	oil-rich phase
B	oil component
B	prefactor of high ϕ_{B+C} relaxation regime
c	surfactant-rich phase
C	surfactant component
C	capacity
c_0	spontaneous curvature
c_1, c_2	principle curvatures
C_iE_j	*n*-alkylpolyoxyethylenoxide
d	midplane distance of the L_α and L_3 phase
D	diffusion coefficient
DLS	dynamic light scattering
E_A	activation energy
d*E*	bending energy
g	genus of a randomly oriented structure, i.e. number of 'handles'
H	mean curvature
I_S	scattered light intensity (*T*-jump)
I_0	scattered light intensity before the *T*-jump
$\Delta I_S / I_0$	*T*-jump amplitude
I (*q*)	scattering intensity as a function of the scattering vector
k_B	BOLTZMANN constant
K	GAUSS'ian curvature
l_B	thickness of the oil layer in a surfactant bilayer
l_C	length of a surfactant molecule
L_α	lamellar phase
L_3	sponge phase
L_1, L_2	micellar phases

NMR	nuclear magnetic resonance
p	pressure
q	scattering vector
r_1, r_2	principle curvature radii
R_{cell}	resistance in the sample cell of the T-jump apparatus
SLS	static light scattering
SANS	small-angle neutron scattering
SAXS	small-angle X-ray scattering
t	time
t_0	starting time of T-jump
T	temperature
$\tilde{T}$	temperature of the fish tail point at $\alpha = 0.5$
$\bar{T}$	temperature of the fish tail point at any α
T_l	lower critical temperature of the three-phase body
T_u	upper critical temperature of the three-phase body
$T_l^{L_3}$	lower phase boundary temperature of the L_3 phase
$T_u^{L_3}$	upper phase boundary temperature of the L_3 phase
T_c	critical temperature
T_{spin}	spinodal temperature
TEM	transmission electron microscopy
U_{cap}	charging voltage of the capacitor
v_C	volume of the surfactant molecule
X	coordinates of the fish tail point ($\bar{\gamma}, \tilde{T}$)
α	mass fraction oil / (water + oil)
2ε	surfactant bilayer thickness
γ	mass fraction surfactant / (water + oil + surfactant)
η	viscosity
ϕ	volume fraction oil / (water + oil)
ϕ_{B+C}	membrane volume fraction oil + surfactant / (water + oil + surfactant)
ϕ_C	surfactant volume fraction surfactant / (water + oil + surfactant)
κ	bending elastic parameter, bending rigidity modulus
$\bar{\kappa}$	bending elastic parameter, saddle-splay modulus
κ_S	conductivity of the isothermal shear experiment

$\Delta\kappa_S$	amplitude of the isothermal shear experiment
λ	wavelength
ρ	scattering length density
ρ^{25}	densities at 25 °C
τ	relaxation time of L_3 phase dynamics
τ_C	cooling time of the T-jump
τ_H	heating time of the T-jump
ϑ	scattering angle
ω_b	surfactant / (oil + surfactant) volume fraction
ξ	characteristic length scale of microemulsions
ξ_κ	persistence length
$\xi_{\bar{\kappa}}$	topological persistence length
ζ	wandering exponent
1	one-phase microemulsion
$\bar{2}$	two-phase (microemulsion in lower phase)
$\underline{2}$	two-phase (microemulsion in upper phase)
3	three-phase (microemulsion in middle phase)

1   Introduction

1.1   The L$_3$ phase

Among the rich variety of structures and phases that are formed when surfactant molecules self-assemble in solution, a special phase, the L$_3$ [1] or sponge [2, 3, 4] phase, is found. This phase is described as being an anomalous isotropic phase, showing a couple of remarkable phenomena. It was first reported some 25 years ago by EKWALL et al. [5] for several ionic microemulsions. Some time later, similar observations were made by HARUSAWA et al. [6] and LANG and MORGAN [7], amongst others, for a number of amphiphilic systems ranging from binary nonionic surfactant solutions to more complex systems with three and more components. The prominent features of the L$_3$ phase are its optical isotropy, birefringence under shear, only moderate viscosity, the fact that it scatters light strongly and becomes increasingly more opalescent at high dilution. The L$_3$ phase is always found in vicinity of a dilute lamellar liquid crystalline phase L$_\alpha$ with smectic order. It is stable over a narrow range of temperature only, but can be diluted up to a very high water content [1]. Since the appearance of the L$_3$ phase is always correlated with the presence of the lamellar phase this indicates a similarity in their local structure. Both phases consist of fluid bilayers but each with a different large-scale arrangement [8]. However, since the crucial technologies, scattering techniques and electron microscopy, to distinguish such structures were not available in the required precision, it took some more effort and years until the structural geometries of this remarkable phase could be fully understood [9].

There are two ways of deducing the structure of the L$_3$ phase from geometric and energetic considerations. On the one hand it can be explained via a theory for multicomponent microemulsions, on the other hand by way of self-organization in simple binary systems of surfactant and water. Eventually both ways lead to the same answer.

Microemulsions are macroscopically homogeneous mixtures of water, oil, and surfactant. On a microscopic level, though, these solutions are characterized by domains of water and oil with surfactant monolayers at the interface [10, 11]. Depending on the relative amounts of water and oil in the mixture, there are manifold ways to divide space into domains of different polarity. If there is a lot more of one than the other in the mixture, droplet structures of water in oil or oil in water will be formed. However, if the amounts of water and oil in the microemulsion are similar, the amphiphilic monolayers energetically prefer a two-

dimensional arrangement in form of infinite films without edges and seams [12]. There are only three ways of arranging flexible interfaces like that with no edges in space. One is by packing flat sheets into stacks of infinite lamellae, the second is a phase of micelles, the main difference in these structures being the mean curvature <H> of the film, which is <H> = 0 for the flat lamellae, and <H> ≠ 0 for the globules. The third is that of a phase of multiply connected random films, which divide space into two bicontinuous subphases and although this film is locally curved, the mean curvature <H> of the latter structure is zero, as for the flat lamellae.

a)   b)   c)
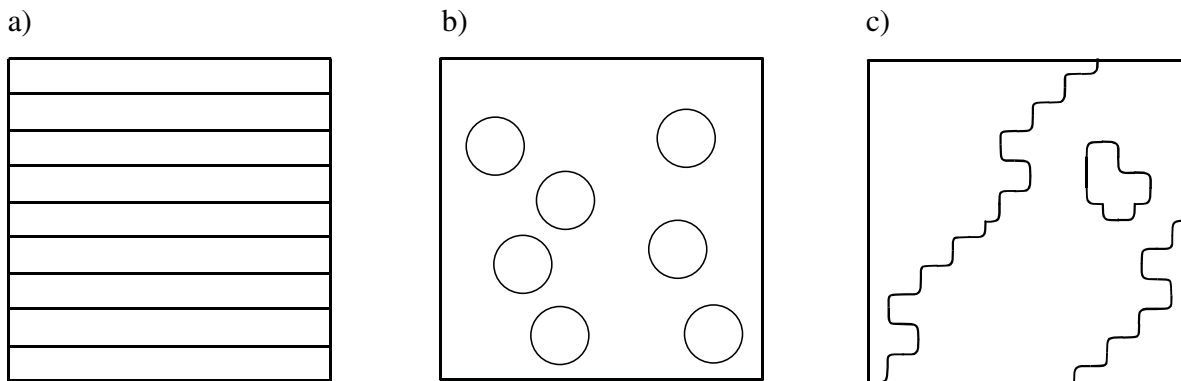
Fig. 1.1: Potential three-dimensional arrangement of infinite films a) stacks of lamellae b) globules c) random continuous configuration [2]

The third arrangement is realized in bicontinuous microemulsions, with equal volume fractions of water on one and oil on the other side of the multiply connected random interface. Freeze fracture electron microscopy (FFEM) images by JAHN and STREY [13] reveal a sponge-like structure with a zero mean curvature of the interfacial film. Returning now to the L_3 bilayer structure. It is straightforward to say that the same arguments that can be applied to a monolayer hold for a bilayer. The difference being the fact that the monolayer separates two different, whereas the bilayer separates two equivalent subphases. Therefore the L_3 phase should be a sponge-like structure of multiply connected bilayers without edges and seams, separating to equivalent subphases. This in fact has been shown by STREY et al. [14] by FFEM and supported by small angle neutron scattering (SANS) experiments [8].

The other way of explaining the L_3 structure is, to start from the L_α phase, with its quasi-long-range smectic order, and introduce the formation of connections between two adjoining bilayers by fusion as a result of fluctuations. This causes an elementary change in the local topology, which spreads spontaneously over the whole bilayer and leads to the destruction of the long-range order of the L_α phase. The result is the formation of a structure, which, like the

L_α phase, shows zero mean curvature, but this being a result of principle curvatures of opposite signs. Although the L_3 phase is an isotropic phase with no long-range positional order, scattering experiments show a well-defined peak, corresponding to the structural length of the passages in the L_3 phase [9, 15]. Fig. 2 shows a schematic representation of the L_3 phase structure as it was deduced from FFEM and SANS as analogous to a bicontinuous microemulsion [16], and from structural considerations as a transition from an L_α phase.

Fig. 1.2: Schematic representation of an L_3 sponge phase.

The wide interest in the microstructure of sponge phases certainly reflects that the disordered multiconnected bilayer of the L_3 phase is the most intriguing large-scale structure ever observed in surfactant solutions. However, the static picture of the microstructure does not reveal the highly dynamic nature of these phases. For a thorough understanding of the equilibrium properties of these self-aggregating structures the dynamic processes are of crucial importance, but there still is a lack of systematic investigations. While there are several studies concerning micelle kinetics [17, 18] and vesicle formation [19, 20], there is hardly any information about the dynamics of L_3 phases. Experiments on the dynamics of L_3 phases performed so far involved electric birefringence and temperature-jump measurements. MILLER at al. [21] performed electric birefringence experiments on the L_3 phase in a system composed of a zwitterionic surfactant, a long-chain alcohol as cosurfactant, and water. They provided a theoretical explanation of the resulting relaxation times based on the orientational relaxation of disc-like aggregates.

It is important to note that the sponge-like structure was still under investigation at that time. Based on general invariance arguments PORTE et al. [22] predicted that the relaxation time of the electric birefringence in the L_3 phase should depend on ϕ^3, with ϕ being the volume

fraction of bilayer in the sample. The respective measurements were performed on a betain system with pentanol and water, and the relaxation time of the KERR effect goes according to prediction. In contrast to MILLER, PORTE [23] interpreted his results as the relaxation of a distortion of a sponge-like structure. WATON and PORTE [24] claimed to be able to at least qualitatively explain experimental evidence for three different relaxation times in temperature jump experiments on the system cetylpyridiniumchloride-hexanol-brine. They tried to attribute them to a diffusion time of concentration fluctuations, a relaxation time for the breaking of the symmetry of the structure, and a relaxation time for the reestablishment of the connectivity of the bilayer. Altogether these studies seem to raise more questions then answers to the problem, which sums up to the fact that a general understanding of the kinetics of L_3 phases is still missing.

1.2   Motivation and Objectives

A group of researchers from Lund, Sweden, developed a free energy model for the thermodynamics of a non-ionic sponge phase based on light scattering data. This model tries to explain the mechanisms governing the narrow stability range of the L_3 phase [25]. To test the model the light scattering measurements were extended from the one-phase region into the two-phase region by employing our temperature jump apparatus. The experiments were conducted in cooperation with the Institute of Physical Chemistry of Cologne University and a first report can be viewed in T.D. LE, PhD thesis [26]. The main objective of that work was to determine the binodal and spinodal curves of the L_3 phase from combined phase equilibrium and temperature jump data and to further support the above-mentioned free energy model.

In the course of these experiments, so to say as an interesting 'by-product' it was found that the dynamics of this sponge structure extend over time scales of more than ten orders of magnitude depending on the bilayer concentration [27]. Since the L_3 phase dynamics investigations that were conducted to this day never yielded time scales that extended over more than three to four orders of magnitude, this was a highly remarkable result. Naturally this gives rise to a whole new approach for L_3 phase kinetic studies. The first question that comes to mind is concerned with the system used; here brine – *n*-decane – $C_{12}E_5$. Is the above-mentioned result a general property of sponge phase dynamics, or limited to the oil swollen bilayer system of a $C_{12}E_5$ surfactant? A first answer to this was found by SCHWARZ et al. [28], who examined the pseudo-binary system brine – $C_{10}E_4$ – decanol by applying

temperature jump and pressure jump relaxation measurements. Similarly high dependencies of the sponge phase relaxation times from the bilayer concentrations were found for the non-swollen bilayer, likewise for two different perturbation methods. Therefore, the extraordinary extensions of time scales over many orders of magnitude in dependence of the concentration seem to be a more general attribute of the L_3 phase dynamics, irrespective of the degree of swelling of the bilayer. If this is true, these findings could be of crucial importance for those sectors of industrial application of surfactant solutions that deal with wetting and spreading issues. Because then, a reduction in the surfactant concentration to reduce the costs for certain processes, could lead to a disproportionately high increase in the reaction time or process' duration. It should be noted that particularly rapid spreading is observed when the surfactant solution contains a bilayer structure [29, 30, 31, 32].

If L_3 phases of different systems behave similarly it should be possible to find a general description for the dynamics in sponge phases. It could help to clarify these kinds of issues if a model system is studied and thoroughly understood. The main objective of this work is to provide such experimental data on a model system and possibly initiate the search for a general description for the dynamics of L_3 phases.

In the examples given above the bilayer volume fraction was varied, however any information about the influence of the bilayer thickness is missing completely. As a basis for a more detailed investigation, a suitable model system had to be selected. The system water – *n*-octane – $C_{10}E_4$ is a good candidate for the following reasons. The binary system water – $C_{10}E_4$ is the first in the hydrophobic-hydrophilic series of alkyl polyglycol ethers, after C_8E_3, where an L_3 phase can be found at all, which turns it into the most basic system in this series as far as the sponge phase, is concerned. Another reason for choosing this ternary system is the fact that the structure of the L_3 phase can be varied by either swelling the bilayer with oil and/or changing the interbilayer distance by increasing its volume fraction. The last reason is a practical one. The phase inversion temperature (PIT) [33] for this system is very close to room temperature [34], thus creating an applicable temperature range for all measurements, even if the sample's oil content is very low [35]. This is an especially important argument when considering how narrow the L_3 phase stability range is.

For a systematic investigation of the dynamics, at first a detailed study of the phase behavior of the system was to be carried out. A thorough understanding of the phase characteristics of

the L_3 phase in dependence of the different parameters, like interbilayer distance and bilayer thickness is the basis for all following experiments and for a theoretical description. As to the latter a suitable geometric model for the microstructure as a function of the bilayer concentration and thickness was to be established. To this end SANS measurements were to be conducted. When both the phase behavior and the microstructure could be clarified, the interpretation of relaxation experiments on the dynamics in the sponge phase should be feasible.

2 Phase behavior

A basic requirement for experiments with L_3 phases is a detailed knowledge of their phase behavior. As the L_3 phases dealt with in the present study consist of water, oil and surfactant, the following chapter will supply the basic facts for a thorough understanding of the phase behavior of such ternary systems. This will be in form of schematic phase diagrams. Beginning with the well-known phase behavior of ternary microemulsions this chapter will lead to a detailed description of the L_3 phase, its behavior and position in the phase prism. The principal compounds for the following descriptions are water, an n-alkane as oil, and a non-ionic surfactant from the family of *n*-alkylpolyoxyethylenoxide $(H - (CH_2)_i - (OCH_2CH_2)_j - OH)$ denoted as C_iE_j.

2.1 Basics

The phase behavior of ternary mixtures of water (A), oil (B) and non-ionic surfactant (C) has been extensively studied by SHINODA and KUNIEDA et al. [36] and KAHLWEIT, STREY and coworkers [37, 38, 39, 40]. It is determined by the interactions of the three binary side systems: water – surfactant, oil – surfactant and water – oil. The phase behavior of such a ternary mixture is commonly presented in a phase prism with the temperature *T* as the ordinate and the Gibbs triangle A – B – C as the base. The compositions of the ternary mixtures are usually given in terms of the oil / (water + oil) mass fraction α and the total surfactant concentration, i.e. the surfactant mass fraction γ:

$$\alpha = \frac{m(B)}{m(A) + m(B)} \tag{2.1}$$

$$\gamma = \frac{m(C)}{m(A) + m(B) + m(C)} \tag{2.2}$$

The most important features of the phase behavior are observed by performing vertical sections through the phase prism at either constant oil / (water + oil) mass fraction α, usually at $\alpha = 0.5$, or at constant surfactant concentration γ, as can be seen in Fig. 2.1.
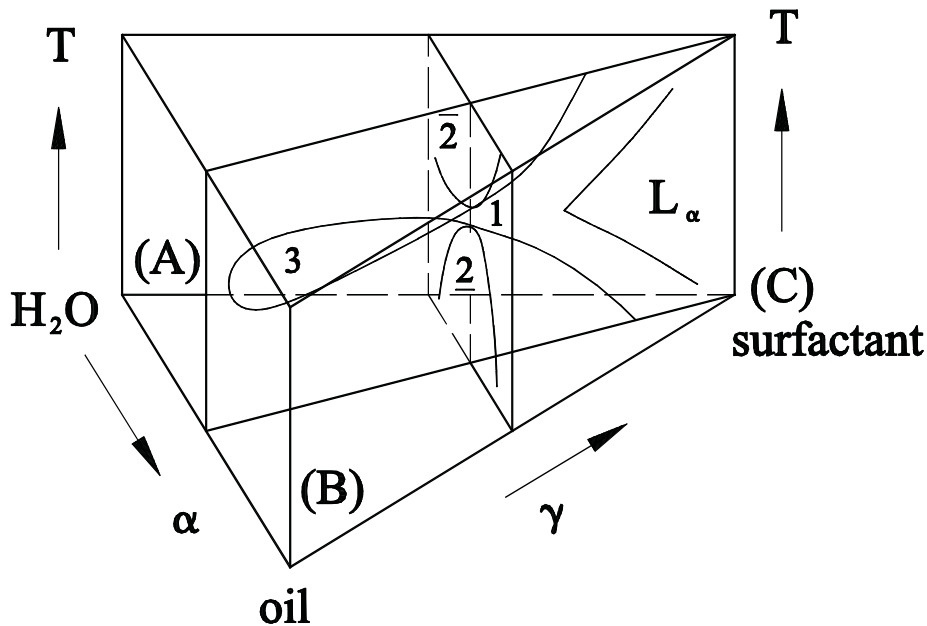
Fig. 2.1: Schematic phase prism showing the two vertical sections at either constant values of the oil / (water + oil) mass fraction α, or constant surfactant concentration γ.

For the characteristic section at constant α, the coexistence curves in the phase diagram form the shape of a "fish", shown in Fig. 2.2. For an explanation of this phase diagram it is important to mention that non-ionic surfactants are more soluble in water at low, and more soluble in oil at high temperatures. Therefore, at low temperatures a surfactant-rich water phase coexists with an oil phase, denoted by $\underline{2}$, whereas at high temperatures a surfactant-rich oil phase coexists with a water phase, denoted as $\overline{2}$. At low surfactant concentrations γ the phase sequence $\underline{2} \to 3 \to \overline{2}$ is formed as a function of temperature. The notation 3 indicates that both oil-rich and water-rich phases are in equilibrium with a surfactant-rich middle phase [41]. The microstructure of the surfactant-rich phases is such that oil-in-water microemulsions are formed at low, water-in-oil microemulsions at high, and so-called bicontinuous microemulsions are formed at intermediate temperatures. The corresponding temperature interval where the bicontinuous microemulsion coexists with both water and oil is defined as $\Delta T = T_u - T_l$, while the mean temperature is $\overline{T} = (T_u - T_l) / 2$. With increasing surfactant concentration more oil and water can be solubilized in the middle phase leading to the formation of a one-phase region, denoted as 1. The phase boundaries between the upper and lower two phase regions and the one-phase region form the so-called "fish tail". The point of contact between the one- and three-phase regions marks the characteristic "fish tail point" $\tilde{X}$, which is unambiguously defined by the surfactant concentration $\tilde{\gamma}$ at the temperature $\tilde{T}$. This point is a measure for the efficiency of the surfactant, since $\tilde{\gamma}(\tilde{X})$ is the minimum concentration of surfactant that is necessary to completely solubilize equal amounts of water

and oil. Towards the low γ region of the diagram the surfactant concentration γ_0 is marking the amount of surfactant that is monomerically dissolved in the excess water and oil phases. Not until $\gamma > \gamma_0$ microstructures can be formed. At very high surfactant concentrations γ, there might be a formation of a lamellar L_α phase, surrounded by a coexistence region of a bicontinuous microemulsion and an L_α phase.
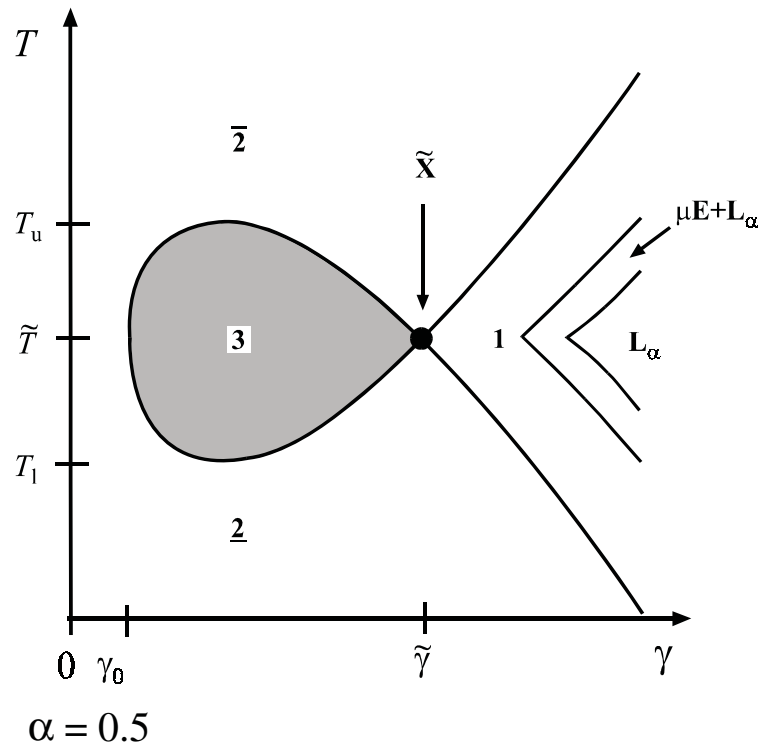
Fig. 2.2: Schematic representation of a vertical γ-T section through a phase prism at constant oil / (water + oil) mass fraction α = 0.5. γ_0 represents the surfactant volume fraction of monomerically dissolved surfactant, whereas $\tilde{\gamma}$ is the surfactant volume fraction that just completely solubilizes equal amounts of oil and water. At high surfactant concentrations a lamellar phase L_α appears in the one-phase region which is surrounded by a coexistence region of bicontinuous microemulsion + L_α.

For a more detailed insight into the phase behavior of ternary mixtures, especially at higher surfactant concentrations, another section through the phase prism, the so-called "SHINODA cut" [42], can be performed. This is done by cutting vertically through the phase prism parallel to the water-oil-T side at a constant surfactant concentration γ that is higher than $\tilde{\gamma}$ (see Fig. 2.1). The resulting schematic phase diagram cuts through the "fish tail" and lies on a plane perpendicular to the one of the "fish" diagram discussed before. The phase diagram in Fig. 2.3 shows a one-phase microemulsion channel extending from the water-rich to the oil-rich side of the phase diagram, i.e. over the full range of α. This channel is surrounded by the two-phase regions $\underline{2}$ and $\overline{2}$. In addition to microemulsion phases discussed so far it features

isotropic liquid L_3 and liquid crystalline L_α phases. Like the one-phase microemulsion channel these phases progress from the water-rich to the oil-rich side of the phase diagram, thereby showing a temperature dependence reverse to the one of the microemulsion channel.
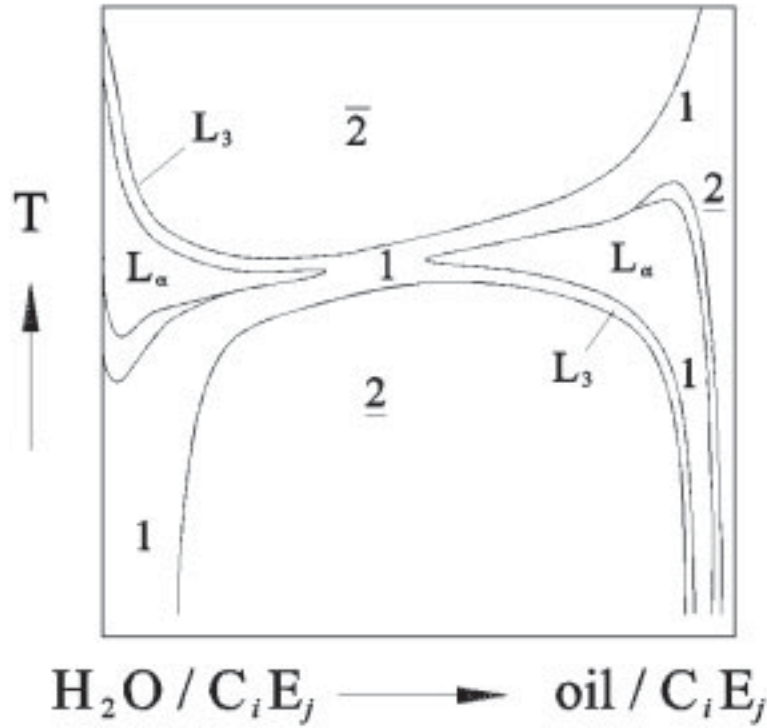
Fig. 2.3: Schematic diagram of a "SHINODA cut" at a constant surfactant concentration higher than $\tilde{\gamma}$. The one-phase microemulsion channel (1) extends from the water to the oil side. The two disconnected L_3 phases, one water-rich and the other oil-rich, are both adjacent to L_α phases [41].

The two very narrow channels of L_3 phases, one on the water-rich, the other on the oil-rich side of the diagram, both open out onto the broader microemulsion channel. The water-rich L_3 phase starts out at high temperatures on the binary water - surfactant side of the phase diagram. With a rising amount of oil in the mixture, the L_3 channel progresses towards lower temperatures and grows increasingly narrow, until it seems to disappear into the one-phase channel at a temperature close to $\overline{T}$. At a sufficiently high oil concentration another L_3 phase appears, apparently out of the microemulsion channel, to progress with increasing oil content towards lower temperatures and a broadened temperature range. Both L_3 phases are adjacent to lamellar phases. The water-rich L_α phase exists in a temperature range below that of the L_3, while the opposite is true on the oil side. For the temperature $\overline{T}$ both L_α phases extend far into the middle of the phase diagram [35, 41, 43].

In addition to the above mentioned sections through the phase prism, the evolution of the L_3 and the L_α phase as a function of the surfactant concentration γ and the temperature T are of

interest [44, 45]. From Fig. 2.3 it was deduced that the L_3 phase occurs only for very high water or oil contents respectively. Consequently the evolution of the L_3 phase as a function of the surfactant concentration γ and the temperature T can only be discussed at very high or very low values of the oil / (water + oil) mass fraction α. For simplicity, the water – surfactant – temperature side of the phase prism, which is tantamount to $\alpha = 0$, is chosen (Fig. 2.4).
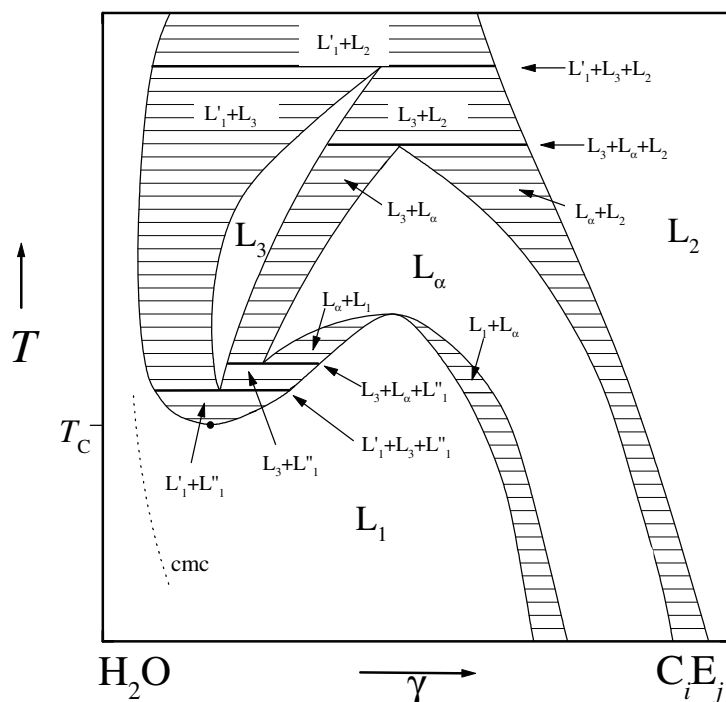
Fig. 2.4: Schematic phase diagram of the binary system water – non-ionic surfactant. The isotropic liquid L_3 phase is found in the low, whereas the dilute liquid crystalline L_α phase is found in the intermediate to high concentration range respectively. There is always a two-phase region separating two one-phase regions from each other, as well as two two-phase regions are always separated by a three-phase line [14, 46].

At temperatures below T_C the phase diagram shows the following features. For low surfactant concentrations the surfactant molecules are monomerically dissolved in the water phase. If the surfactant concentration γ is increased, a certain characteristic value will be reached, the critical micelle concentration or cmc. The surfactant molecules self-organize into micelles for concentrations $\gamma \geq \gamma_{cmc}$ which leads to the micellar phase L_1. At high surfactant concentrations a lamellar phase L_α is formed. Note that a wide variety of different liquid crystalline phases exist. For the sake of simplicity only the L_α phase is drawn schematically in Fig. 2.4. Finally a phase of reverse micelles, L_2, is found, close to the pure surfactant. A significantly different phase behavior can be observed for higher temperatures over the full range of γ. Returning to low surfactant concentrations and increasing the temperature above the lower critical

temperature T_C (cloud point) leads to a phase separation of L_1 into two liquid phases, one poor (L_1') and the other rich (L_1") in surfactant. At a certain higher temperature the surfactant-rich aqueous phase L_1" separates into two phases $L_3 + L_1$". Between these two-phase regions there is a triple line L_1' $+ L_3 + L_1$". The existence of the two-phase region $L_3 + L_1$" clearly rules out that the dilute lamellar phase is in direct contact with the dilute aqueous phase L_1' [45]. With another slight increase in temperature another triple line is encountered, $L_3 + L_\alpha + L_1$", which is followed by an $L_3 + L_\alpha$ coexistence with further increased temperature. A similar complexity is found where the L_3 and L_α terminate. The maximum temperatures of L_3 and L_α are close to each other. However, the L_3 phase extends to a slightly higher temperature than L_α. Consequently the L_α terminates at a triple line $L_3 + L_\alpha + L_2$, while the L_3 phase ends at the triple line $L_3 + L_\alpha + L_1$' at slightly higher temperatures. This is followed by the two-phase region L_1' $+ L_2$. In between these four three-phase lines the L_3 and the dilute L_α phase are found. The L_3 one-phase region is always shifted parallel towards lower concentrations in relation to the dilute L_α phase for a given temperature and has a narrow stability range of just a few Kelvin. This narrow stability range gives the L_3 phase the appearance of a channel. In contrast, the dilute L_α phase has a wide stability range, extending to high surfactant concentrations and very low temperatures.

As mentioned before, the just described binary phase diagram actually represents the water – C_iE_j – T side of the phase prism of a ternary system water – oil – non-ionic surfactant (see Fig. 2.1). One of the most important issues in regard to the aim of this work is the way the L_3 phase develops when oil is added to the binary system water – surfactant. With such a ternary system both the amount of the bilayer as well as its properties can be varied. Since this work deals mostly with ternary systems water – oil – surfactant, the expression "bilayer" in the context of ternary systems always denotes an oil-swollen bilayer. Whereas for binary systems water – surfactant the term "non-swollen bilayer" will be used from now on. Suitable parameters to describe the dependencies in ternary systems are found in Eq. (2.3) and Eq. (2.4). The surfactant / (oil + surfactant) volume ratio ω_b and the bilayer concentration ϕ_{B+C} can be expressed as:

$$\omega_b = \frac{V_{surf}}{V_{oil} + V_{surf}} \tag{2.3}$$

$$\phi_{B+C} = \frac{V_{oil} + V_{surf}}{\sum\limits_{i} V_i} \tag{2.4}$$

The corresponding parameters are schematically presented in the phase prism seen in Fig. 2.5:
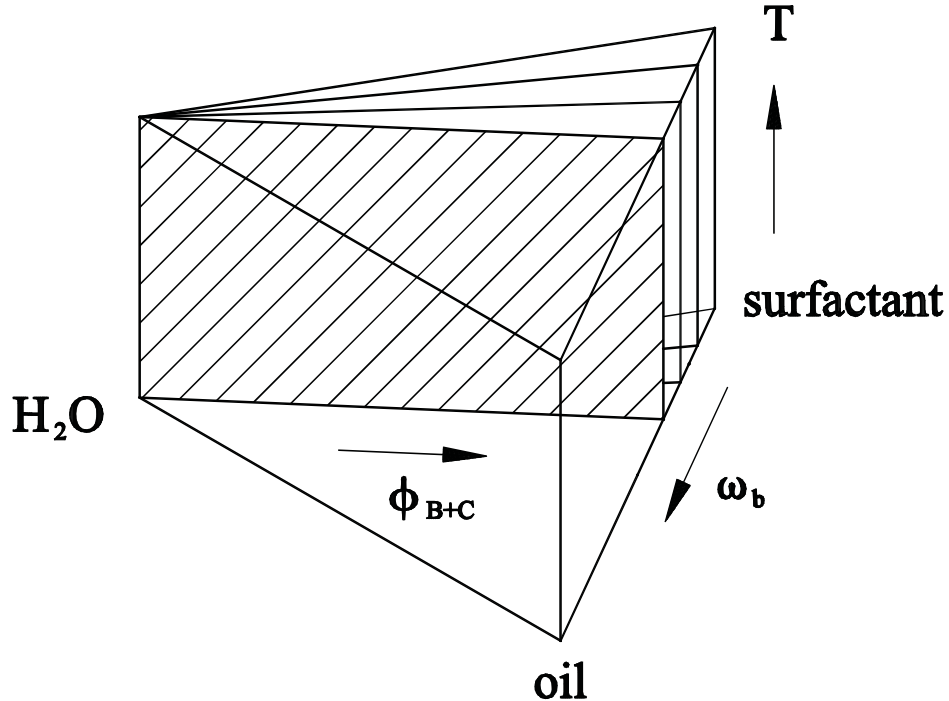
Fig. 2.5: Sections through the phase prism for constant ω_b's. After a suggestion by PORTE [47] this phase prism can be imagined as being a book, with the water corner as the spine, the water – oil – T side as the front and the water – surfactant – T side as the back of the book. Then every section at constant ω_b represents one page in this book.

For a better understanding the phase prism in Fig. 2.5 can be regarded as a book. The water corner is representing the spine, the water – oil – T side the front page, and the water – surfactant – T side the back of the book. In this scenario each section through the phase prism from the water corner towards the oil – surfactant side, i.e. each cut through the prism at constant surfactant / (oil + surfactant) volume fraction ω_b, represents a page in this book.

Taking into account the definition given in Eq. (2.3), the book cover stands for $\omega_b = 0$, and thus representing the binary water – oil – T side of the phase prism. Since water and oil are immiscible, the miscibility gap extends over the whole temperature range and therefore plays no role for the evolution of the water-rich L_3 phase. Unlike the front page, the back of the book, i.e. $\omega_b = 1$, is very important since it represents the binary water – surfactant phase diagram discussed in Fig. 2.4. When oil is added to this binary system, the book is leafed through from the back. Pages further towards the middle of the book will be opened. In a book with 100 pages, page 50 will look like the phase diagram depicted in Fig. 2.6.
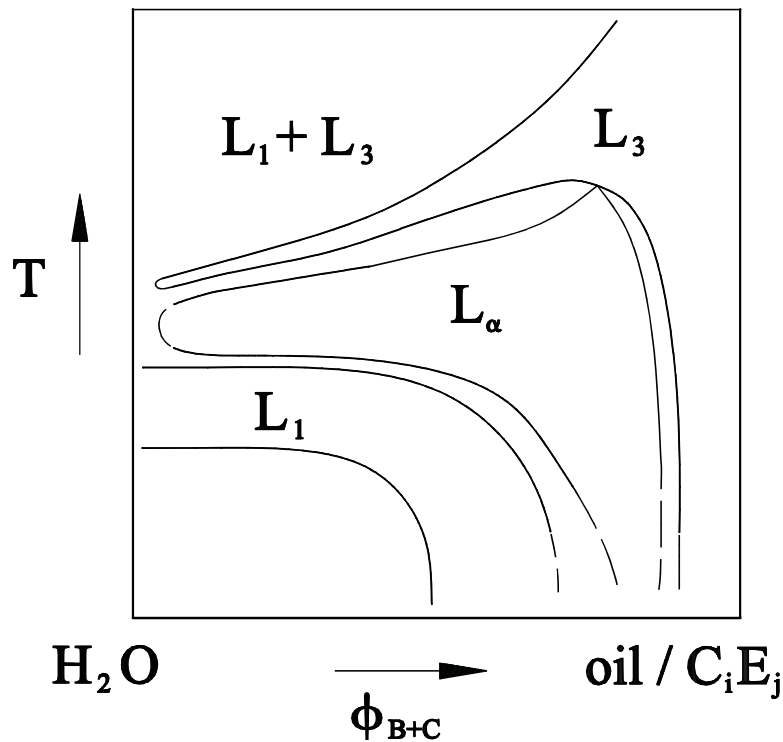
Fig. 2.6: Page 50 in the phase prism seen as a book. Schematic $\phi_{B+C} - T$ section through a phase prism for the system water – oil – C_iE_j for $\omega_b = 0.5$. Shown are the L_3, L_α and L_1 phases [11, 26].

Comparing Fig. 2.4 and Fig. 2.6 it becomes evident that the phase behavior of the ternary system is analogous to the one for the binary system water - C_iE_j if ω_b is kept constant. The general appearance of the L_3 phase region has not changed. It still forms a narrow band as a function of the temperature T, yet compared to the binary system this narrow channel extends to much higher bilayer concentrations ϕ_{B+C}, in fact it opens out to the L_2 phase region for very high ϕ_{B+C}. Furthermore, the L_3 phase channel has shifted towards lower temperatures and its width has decreased. This is in agreement with the L_3 phase channel observed in the phase diagram shown in Fig. 2.3, where the water-rich L_3 phase disappears with increasing ϕ. Also the L_α phase extends its stability range with decreasing ω_b, thus reaching further into the water corner. As a consequence the L_3 channel looses its tilted appearance and becomes increasingly flatter.

2.2   Phase diagrams

It was shown in chapter 2.1 that for descriptions of the phase behavior it has proven useful to perform different vertical sections through the phase prism of a ternary mixture. Different binary or pseudo binary phase diagrams are obtained. The general features of these simpler phase diagrams are analogous to those of the more complicated systems, thus providing the

elementary understandings to start from. This is the reason why studies involving the phase behavior of surfactants always start with the simplest system, usually the binary system water – surfactant.

For this project ternary mixtures of water / NaCl, *n*-octane and the nonionic surfactant $C_{10}E_4$ (*n*-decyltetraoxyethylenoxide) were chosen to study the properties of this systems L_3 phases. In all ternary phase diagrams shown here water was substituted by 0.1m NaCl to support the subsequent measurement and detection techniques (see chapter 8). Only for the binary phase diagram pure water was used. The choice of the system water – *n*-octane – $C_{10}E_4$ serves two purposes. One is the opportunity to vary the bilayer concentration ϕ_{B+C} of the L_3 phase as well as the surfactant / (oil + surfactant) volume fraction ω_b, and the other is to provide a convenient temperature range for experimentation. In addition, the binary system water – $C_{10}E_4$ is the first in the homologous series of water – *n*-alkylpolyoxyethylenoxides (C_iE_j) systems featuring an L_3 phase, thus providing the most basic system to start with.The phase behavior of the binary system water – $C_{10}E_4$ was examined in detail. The resulting phase diagram is depicted in Fig. 2.7.
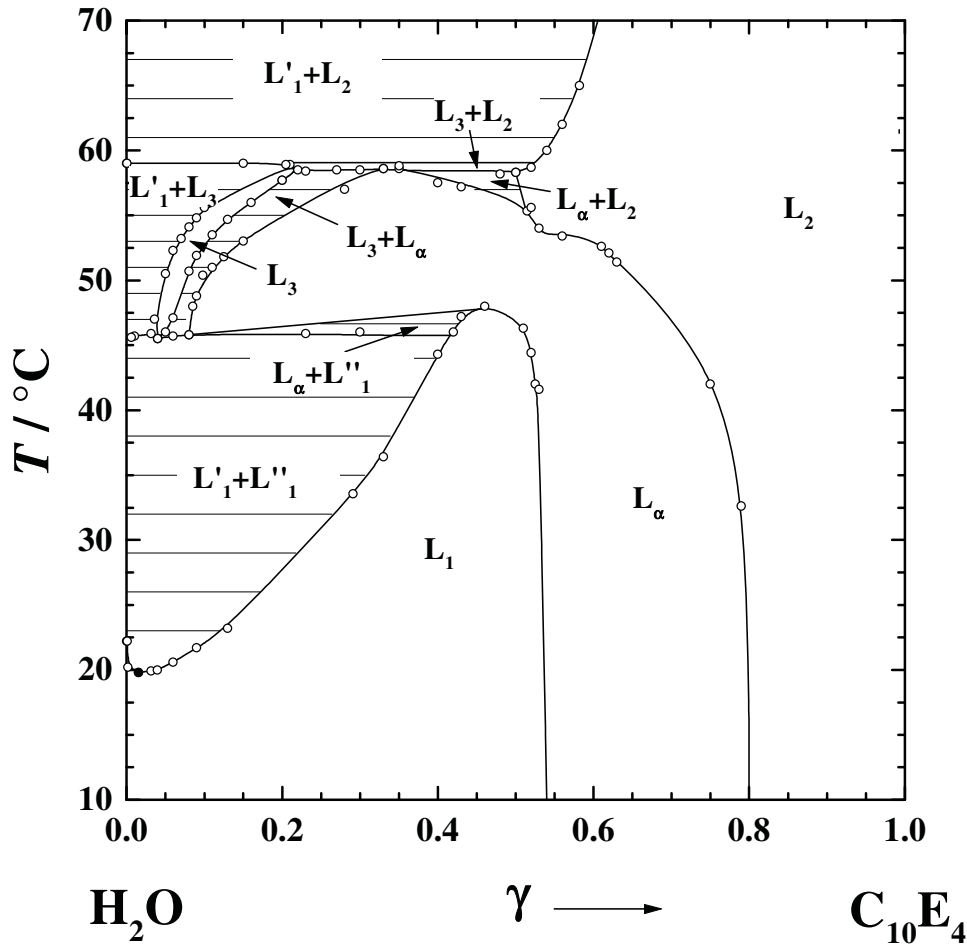
Fig. 2.7: $\gamma - T$ diagram for the binary system water – $C_{10}E_4$ [46].

This phase diagram shows the expected typical phase sequence as a function of surfactant concentration γ and temperature T (see Fig. 2.4). To depict the true proportions of the different phase regions in the phase diagram the concentration axis is drawn on a linear scale. As a result the critical micelle concentration cannot be pictured in this diagram but is found experimentally to be $\gamma_{cmc} \approx 0.0003$ at $T = 20°C$. The micellar L_1 phase extends up to the cloud point curve. The coordinates of the lower critical point (black dot), i.e. where the L_1 phase separates into two phases, L_1' and L_1'', are $T_c = 19.8°C$ and $\gamma_c = 0.026$. The $L_1' + L_1''$ coexistence region reaches up to about 45°C. For higher temperatures up to about 59°C the L_3 phase appears in the phase diagram as a narrow band, never wider than 4K. It extends over a large concentration range from $\gamma = 0.03$ to $\gamma = 0.2$. The L_3 phase is easily identified by being an optically isotropic fluid of low viscosity, which scatters light strongly and exhibits birefringence under shear. Shifted towards higher surfactant concentrations γ in the same temperature range, the dilute L_α phase can be observed. It extends far into the high concentration region of the phase diagram, reaching down to very low temperatures. In the

high concentration region ($\gamma > 0.5$) the L_α phase separates the micellar L_1 from its inverse counterpart, the L_2 phase. A point worth mentioning is the fact that at high concentrations the phase boundary between the L_2 and the L_α phase is indented at temperatures around 55°C. This is a first hint for the observation that the pseudo-binary system water – $C_{10}E_4$ / $C_{10}E_5$ forms two separated L_α phases [48]. In other words this 'dent' can be interpreted as a tendency to create two separated L_α phases, one in the low and the other in the high concentration range of the phase diagram. Two separated L_α phases were first observed by WAGNER and STREY [30] for the binary system water – trimethylsilane surfactant. Therefore this is not a special feature of C_iE_j surfactants but could be a general feature of surfactants, depending on the balance between their hydrophobic and hydrophilic parts.

Since it is the aim of this work to investigate the properties of the L_3 phase by varying the bilayer concentration ϕ_{B+C} and surfactant / (oil + surfactant) volume fraction ω_b, what follows will focus on the phase behavior of the L_3 phase only.

Adding oil to the binary system water – $C_{10}E_4$ leads to a continuous shift of the L_3 phase channels towards lower temperatures and to decreasing widths of the L_3 phase channels as discussed in chapter 2.1. It has to be kept in mind that the extension of the L_3 phase channel is itself a function of the bilayer concentration ϕ_{B+C}. This behavior was explained above for the "phase prism book" in Fig. 2.5 and Fig. 2.6. Note that an increasing amount of oil in the mixture shows in declining ω_b's, i.e. page numbers. Given that it is difficult to picture more than one ω_b section through the phase prism at one time, an illustration (see Fig. 2.8) is used where all the L_3 channels measured for the different surfactant / (oil + surfactant) volume fractions ω_b are projected onto the last page of the book, page 100 for $\omega_b = 1$. Since this last page represents the binary water – $C_{10}E_4$ phase diagram, the binary L_3 phase can be observed at the highest temperature, with the L_3 projections for the decreasing ω_b values "stacked" towards lower temperatures.
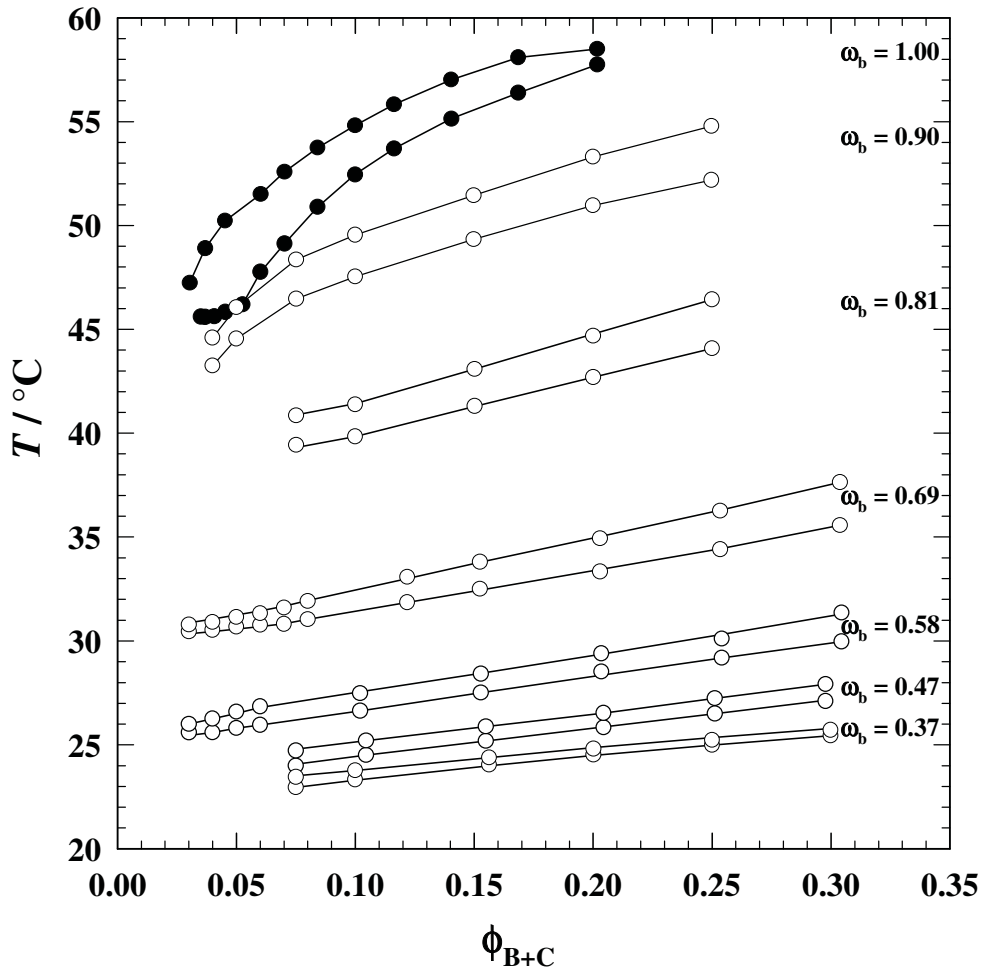
Fig. 2.8: Projection of L_3 phase channels measured as a function of bilayer concentration ϕ_{B+C} and temperature T onto the binary water – $C_{10}E_4$ phase diagram revealing the monotonic shift towards lower temperatures, the decreasing width and reduced slopes of the L_3 phase channels under addition of oil (decreasing ω_b).

Fig. 2.8 shows the shift of the L_3 bands towards lower temperatures with decreasing surfactant / (oil + surfactant) volume ratio ω_b. In addition to this, the width of the L_3 temperature range is reduced, from about 4K for the binary L_3 phase down to ~ 0.3K for $\omega_b = 0.37$. This value of ω_b corresponds closely to the oil / (water + oil) volume fraction ϕ where the L_3 phase disappears into the one phase microemulsion region for a given surfactant concentration (see Fig. 2.3). Also the shape of the L_3 stability region changes considerably with addition of oil. For $\omega_b = 1$ it shows a tilted appearance, leaning towards the lamellar L_α phase that comes about at higher surfactant concentrations. For the lowest ω_b values it lies almost flat perched on top the L_α phase. This can be seen as a consequence of the extension of the L_α phase further towards the water corner of the phase prism. Considering the influence of the bilayer concentration ϕ_{B+C} it can be seen that the L_3 channel width increases as a function of ϕ_{B+C}.

Each L_3 phase channel can be diluted down to very low bilayer concentrations ϕ_{B+C}, until the phase channels close at bilayer concentrations ϕ_{B+C} of about 0.03.

All subsequent measurements will take place at either constant ω_b with a varying bilayer concentration ϕ_{B+C} (see Fig. 2.8) or with varying surfactant / (oil + surfactant) volume ratios ω_b at a constant ϕ_{B+C}. To illustrate the latter ϕ_{B+C}–dependence the phase behavior of the L_3 phase at constant ϕ_{B+C} and varying ω_b is needed. This phase diagram can simply be extracted from the data presented in Fig. 2.8. Exemplarily the L_3 phase is shown as a function of ω_b and T, for a constant bilayer concentration $\phi_{B+C} = 0.15$.

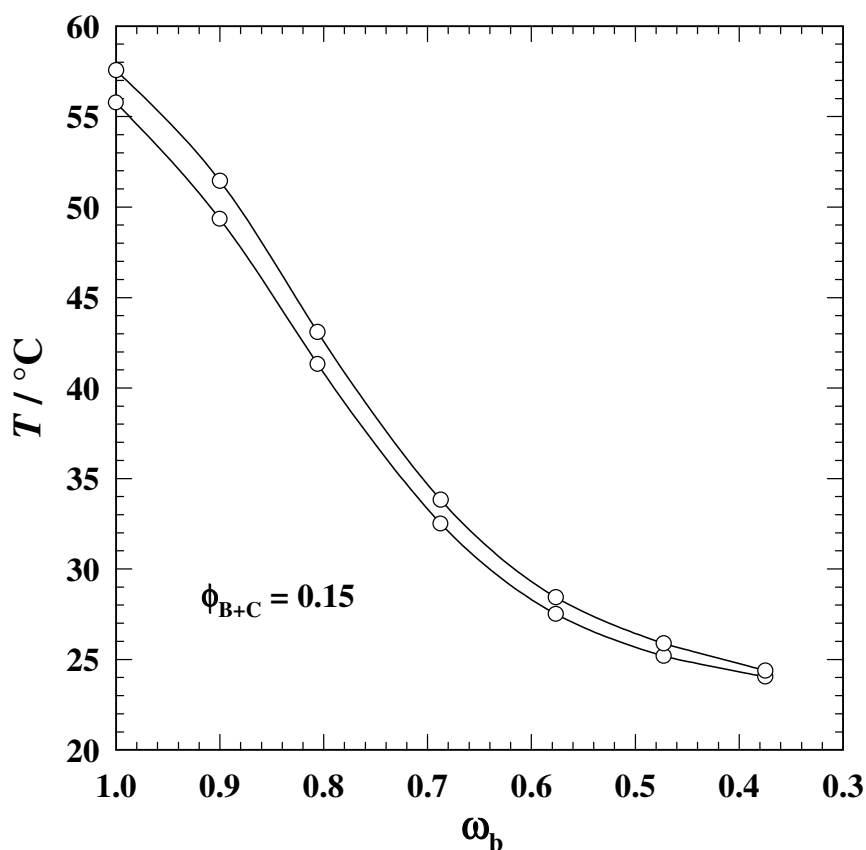Fig. 2.9: L_3 phase diagram as a function of the surfactant / (oil + surfactant) volume ratio ω_b and temperature T, for a constant bilayer concentration of $\phi_{B+C} = 0.15$.

3   Theoretical approach

For the formation and stability of the L_3 phase the properties of surfactant films are essential. This film could be (a) a mono- or bilayer, (b) located at the water-air or the water-oil interface, (c) curved or plane, to mention just a few possible appearances.

For the theoretical description of surfactant films a successful model was introduced by HELFRICH [49] with a mathematical expression for the bending energies of phospholipid membranes. This so-called *flexible surface model* has been applied for surfactant bilayers or monolayers alike. In the following the model will be explained by means of surfactant monolayers. Then the description will be extended to surfactant bilayers and consequently a model for the surface free energy of the L_3 phase will be obtained (for a more detailed treatment of these theoretical ideas see [50, 51, 52, 53]). In a second part an approach to the theoretical analysis of the L_3 phase dynamics will be given, which is different to the theories developed by PORTE [9]. This analysis is motivated by the dramatic dependence of the relaxation time constants on the bilayer volume fraction that was first observed by UHRMEISTER [27] in temperature jump experiments and studied in detail in this work. It was developed in collaboration with DR. HENRIQUE LEITAO from the University of Lisbon, who started theoretical calculations to clarify this phenomenon. The project leading to this collaboration was funded by the DAAD.

3.1   Flexible surface model

The great variety of structures formed in self-assembled systems like spherical and cylindrical micelles, cylinder-networks, lamellae and bicontinuous structures, is believed to be a consequence of the variation of the curvature of the amphiphilic interfacial films due to the minimization of the interfacial energy. Prior to discussing formation and stabilization of these structures, the properties of the underlying amphiphilic films have to be characterized. These structural properties are defined by the curvature of the surfactant monolayers. However, in the context of L_3 phases they also have to be discussed for surfactant bilayers.

3.1.1   Monolayers

The mean curvature at any position of a two-dimensional isotropic film can be described with two principle curvatures c_1 and c_2. These are expressed in form of their principle curvature radii

$$r_1 = \frac{1}{c_1} \quad \text{and} \quad r_2 = \frac{1}{c_2}, \tag{3.1, 3.2}$$

where the principle curvatures c_1 and c_2 can be of opposite sign. By convention the curvatures around the oil are defined as positive and curvatures around the water as negative. In Fig. 3.1 the radii r_1 and r_2 are illustrated for a saddle-like surface.
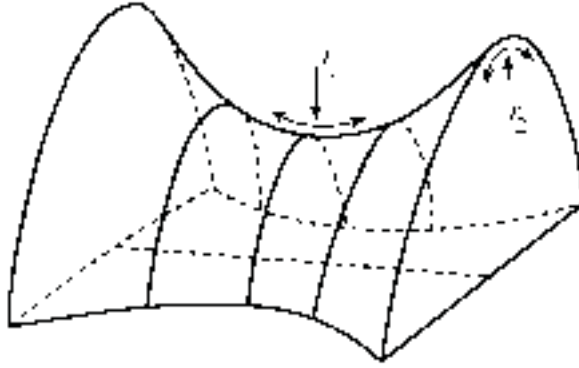
Fig. 3.1: Curvature radii for a surface with a saddle-point structure. Any point on this three-dimensional surface can be described by two radii with opposite signs. For clarity this illustration shows the radii r_1 and r_2 for two different points with curvatures of opposite sign.

The mean curvature H of any given point on a surface is defined by

$$H = \frac{1}{2}\left(\frac{1}{r_1} + \frac{1}{r_2}\right) = \frac{1}{2}(c_1 + c_2), \tag{3.3}$$

while for the GAUSSian curvature K the following applies:

$$K = \frac{1}{r_1} \cdot \frac{1}{r_2} = c_1 \cdot c_2. \tag{3.4}$$

The temperature dependence of many properties of self-assembled surfactant systems, like phase behavior [54], microstructure [10, 55] or interfacial tension [56, 57, 58], can be explained by a variation of the mean curvature H of the amphiphilic film. The temperature dependence of H is shown in Fig. 3.2 for a system water – *n*-alkane – non-ionic surfactant (C$_i$E$_j$).
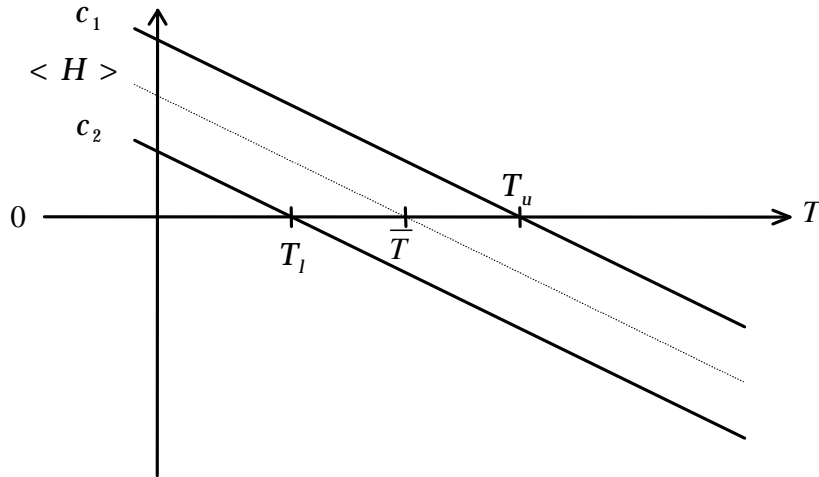
Fig. 3.2: Temperature dependence of the two principle curvatures c_1 and c_2, as well as the resulting mean curvature *<H>* for a non-ionic surfactant system [10, see also 27].

It was shown by STREY [10] that the mean curvature H is linearly dependent on the temperature, resulting in

$$H = c \cdot (\overline{T} - T),\tag{3.5}$$

where c is the temperature coefficient of the curvature and $\overline{T}$ the mean temperature of the three-phase body as shown in Fig. 2.2. Since H is the sum of c_1 and c_2 (Eq. (3.3)) it has been assumed by STREY that the principle curvatures c_1 and c_2 also show a linear dependence on the temperature, so that

$$c_1 = c \, (T_u - T) \quad \text{and} \quad c_2 = c \, (T_1 - T),\tag{3.6, 3.7}$$

where T_1 and T_u are the lower and upper boundary temperatures of the three-phase body (Fig. 2.2).

Considering the different structures found in self-assembled surfactant systems, it follows from Eq. (3.3) and Eq. (3.4) that for a spherical micelle *<H>* $= 1 / r$ and $K = 1 / r^2$ with $c_1 \approx c_2$. Cylindrical structures where one of the principal curvatures is unequal zero, whereas the other is zero, so that *<H>* $= 1 / 2 \, r$ and $K = 0$, can be found at T_1 and T_u. Special cases are the lamellar structure and the bicontinuous microemulsion with its saddle-point structure, which appear at temperatures close to $\overline{T}$. For both structures $H \approx 0$, but for the first $c_1 \approx c_2 \approx 0$ with $K = 0$, while for the latter $c_1 \approx - c_2$ and thus $K < 0$.

In order to "create" these different structures the surfactant film has to be bent. The most general expression for the elastic energy of a flexible surface was derived by HELFRICH [49] to be

$$dE = \left[\frac{\kappa}{2}(c_1 + c_2 - 2c_0)^2 + \bar{\kappa} c_1 c_2 \right] dA \tag{3.8}$$

or

$$dE = \left[2\kappa(H - c_0)^2 + \bar{\kappa} K \right] dA, \tag{3.9}$$

with dA being an area element. Therefore three quantities are required to describe the elasticity of the amphiphilic film: c_0, κ and $\bar{\kappa}$. c_0 is the spontaneous curvature of the surfactant film and represents the curvature the film would adopt without restrictions. Furthermore, κ and $\bar{\kappa}$ are the elastic bending moduli. The so-called rigidity modulus κ (≥ 0) is a measure for the bending rigidity of the amphiphilic film and $\bar{\kappa}$ is the so-called saddle splay modulus, whose magnitude represents the preferred topology of the curved surface.

In order to determine the structure and phase behavior of these systems various approximations have been used. All the arguments above ignore the thermal fluctuations of the membranes. In [59, 60] the role of membrane fluctuations was emphasized, using the scale-dependent reduction of the elastic moduli [61].

$$\kappa(\xi) = \kappa - \frac{\alpha_\kappa k_B T}{4\pi} \ln \frac{\xi}{a} \tag{3.10}$$

and

$$\bar{\kappa}(\xi) = \bar{\kappa} + \frac{\alpha_{\bar{\kappa}} k_B T}{4\pi} \ln \frac{\xi}{a} \tag{3.11}$$

with the microscopic length scale $a = v_C / a_C$ that can be related to the effective length of the surfactant molecule in the interface, and $\alpha_\kappa = 3$ and $\alpha_{\bar{\kappa}} = 10/3$. The characteristic structural length ξ is inversely proportional to the surfactant volume fraction ϕ_C by $\phi_C \sim a / \xi$ (see Eq.

(5.4)). Taking this into account, the two "topological persistence lengths" ξ_κ [62] and $\xi_{\bar{\kappa}}$ [63, 64], are defined as the length scales for which $\kappa(\xi_\kappa) = 0$ or $\bar{\kappa}(\xi_{\bar{\kappa}}) = 0$, i.e.,

$$\xi_\kappa = a \exp\left(\frac{4\pi\kappa}{\alpha_\kappa k_B T} \right) \tag{3.12}$$

and

$$\xi_{\bar{\kappa}} = a \exp\left(-\frac{4\pi\bar{\kappa}}{\alpha_{\bar{\kappa}} k_B T} \right). \tag{3.13}$$

Up to this point the properties of surfactant monolayers were considered. In view of the L_3 phase membrane structure studied in this work and the theoretical work by MORSE [63], GOLUBOVIC [64] and GOMPPER [65], who always refer to the lamellar-to-L_3 transition in binary systems water – surfactant, the structural properties of bilayers structures will be discussed below.

3.1.2   Bilayers

The static picture of a bilayer or membrane structure is that of two identical monolayers fixed opposite to each other. As these two monolayers have an identical solvent on either side the resulting bilayers are locally symmetrical with respect to their midsurface [66]. If both individual monolayers of such a bilayer have zero mean curvature ($H_{mono} = 0$), a planar bilayer is formed. At the level of the midsurface for the bilayers in these lamellar structures, both principal curvatures are zero $c_1 \approx c_2 \approx 0$ and therefore the mean curvature of the bilayer $H_{bil} = 0$ and the GAUSSian curvature of the bilayer $K_{bil} = 0$. However, the individual monolayers forming the L_3 phase bilayer have a mean curvature towards water with $H_{mono} < 0$. This is a consequence of the smaller area of the bilayer surface at the surfactant headgroup position compared to the bilayer midplane. When fixed to each other in a planar bilayer each monolayer will feel frustrated [67]. The frustration of the monolayers can be partially relieved by forming the distorted three-dimensional saddle-shaped structure that has been established for the L_3 phase [14]. For the bilayers in a dilute L_3 phase the principle curvatures at the midsurface are then small but non-zero and have opposite signs with $c_1 \approx -c_2$. Consequently they still add up to a mean curvature $H_{bil} = 0$, but in contrast to the L_α phase, have a negative GAUSSian curvature $K_{bil} < 0$.

Since L_3 as well as L_α bilayers are locally symmetrical in respect to their midsurface, the energy spend for bending must therefore be invariant upon changing the signs of both principle curvatures c_1 and c_2, i.e. the spontaneous curvature of the bilayer $c_{0,\text{bil}}$ ought to be zero. Eq. (3.8) reduces to

$$dE = \left[\frac{\kappa_{bil}}{2}(c_1 + c_2)^2 + \overline{\kappa}_{bil} c_1 \cdot c_2 \right] dA \qquad (3.14)$$

resulting in the elastic bending energy of symmetric bilayers. This expression can be written in an alternative form [58]

$$E = \int dA \left[\frac{\kappa_+}{2}(c_1 + c_2)^2 + \frac{\kappa_-}{2}(c_1 - c_2)^2 \right]. \qquad (3.15)$$

where $\kappa_+ = \kappa + \overline{\kappa}/2$, and $\kappa_- = -\overline{\kappa}/2$. The lamellar phase is energetically stable only for $\kappa_+ > 0$ and $\kappa_- > 0$. For $\kappa_- < 0$, the flat phase is unstable to the formation of infinite minimal surfaces, i.e. sponge phases [65], with $c_1 \approx -c_2$. While on the other hand for $\kappa_+ < 0$, there is instability towards creating a vesicle phase, with $c_1 \approx c_2$. Including the effects of thermal fluctuations results in the renormalization of the elastic constants expressed by [68].

$$\kappa_\pm(\xi)/k_B T = \kappa_\pm / k_B T - \frac{\alpha_\pm}{4\pi} \ln \frac{\xi}{a}. \qquad (3.16)$$

with $\alpha_\kappa = 3$ and $\alpha_{\overline{\kappa}} = 10/3$. This equation is equivalent to Eq. (3.10) and (3.11).

Before addressing the dynamics of the L_3 phase it is worth reviewing some theoretical results regarding the stability of the L_α phase.

3.1.3 Lamellar-to-sponge transition

In first studies about the lamellar phases, their membranes were characterized by a persistence length, ξ_p, defined as the length for which the normal orientations of the membrane become uncorrelated. It can be shown that this persistence length is identical to ξ_κ, that is, $\xi_p \equiv \xi_\kappa = a \exp(4\pi\kappa/\alpha_\kappa k_B T)$ (Eq. (3.12)). Essential for understanding the stability of the

lamellar phase are membrane fluctuations. This is provided by the entropic interaction, as explained in a well-known argument by HELFRICH [69].

To describe the lamellar-to-sponge transition, DEGENNES [62] argued that this transition occurs when the interbilayer distance d is of the order of the persistence length, $d \approx \xi_\kappa$. Recent studies, however, have shown that this transition is preempted by a transition governed by $\bar{\kappa}$ [64, 63]. Melting to a sponge-like phase happens when $d \approx \xi_{\bar{\kappa}} << \xi_\kappa$, and the number of passages between membranes increases dramatically. With Eq. (3.13) and $a / \xi_{\bar{\kappa}} \approx \phi_C / \phi_0$, the lamellar-to-sponge transition is predicted [63] to happen when

$$\ln\left(\frac{\phi_C}{\phi_0}\right) = \frac{6\pi}{5}\left(\frac{\bar{\kappa}}{k_B T}\right) \tag{3.17}$$

and $\bar{\kappa}_{bil} < 0$, where ϕ_0 is a constant of order unity (dashed line in Fig. 3.3 (left)). GOMPPER et al. [65] confirmed this picture. They found a similar dependence of the lamellar-to-sponge transition on $\bar{\kappa}$ for a systematic Monte Carlo simulation study of the phase behavior of fluid membranes of fluctuating topology in which the fluctuations are controlled by the curvature energy. In Fig. 3.3 (left) the simulated lamellar(L_α)-to-sponge(L_3) and L_3 to L_1' + L_3 transition data are shown as a function of ϕ_C and $\bar{\kappa}$ for $\kappa / k_B T = 1.7$ (filled symbols + solid line). Their data were compared to the lamellar-to-sponge phase boundary with the prediction (Eq. (3.17)) for the stability limit of the L_α phase. Rewriting Eq. (3.11) for constant $\bar{\kappa} = -1$ and varying T yields a phase diagram in the conventional form $T = f(\phi_C)$, Fig. 3.3 (right) [70]. The general features and relative positions of L_α and emulsification failure in Fig. 3.3 (left) is similar to those found in experimental phase diagrams.
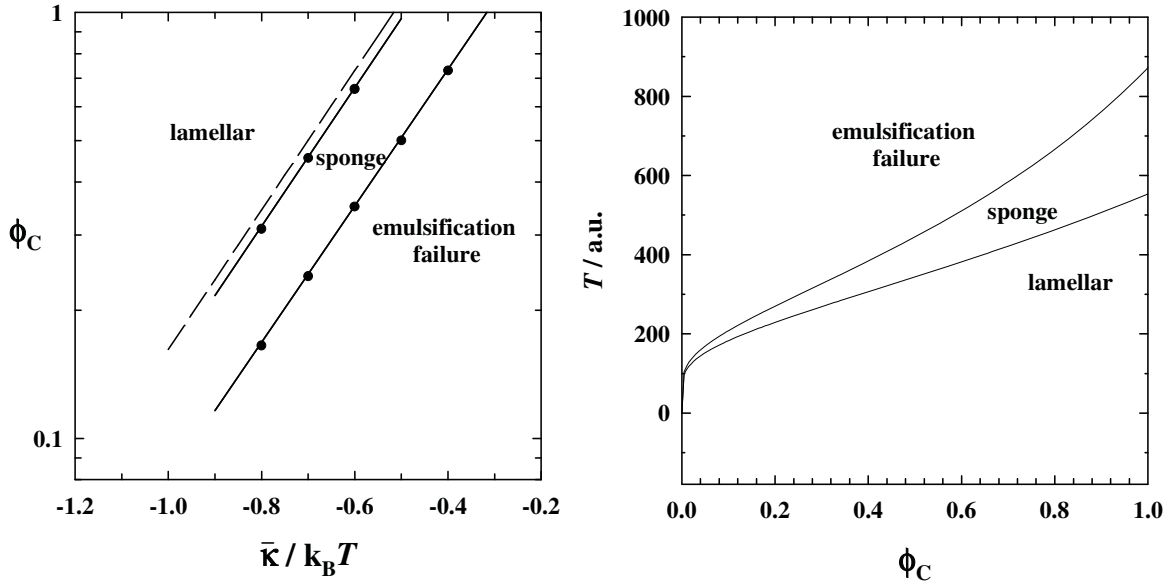
Fig. 3.3 (left): Phase diagram for $\kappa / k_B T = 1.7$. The upper data set shows the location of the sponge-to-lamellar transition from MC-simulation and the lower data set shows the location of the emulsification failure. The approximation for the sponge-to-lamellar transition from Eq. (3.17) with $\phi_0 = 7.0$ is shown as a dashed line [redrawn from [65]. Fig. 3.3 (right): Phase diagram $T = f(\phi_C)$ for $\bar{\kappa} = -1$ calculated from Eq. (3.11) [70].

An alternative view (but with a similar outcome) of the L_α-to-L_3 transition was proposed by PORTE [9] who emphasized the difference in topology between the L_α phase and L_3 phase while also regarding $\bar{\kappa}$ as the main control parameter. The GAUSS-BONNET theorem [51] states that the integral over the GAUSSian curvature distribution,

$$\int dA \cdot K = 4\pi (1 - g) \tag{3.18}$$

is directly related to the topological genus g, which is proportional to the number of 'handles' of the surface under analysis [71, 63]. The left part of Eq. (3.18) multiplied with a negative value of $\bar{\kappa}$ is the energy cost for the formation of handles. Consequently the parameter $\bar{\kappa}$ in Eq. (3.14) can be seen as the chemical potential for the formation of handles. PORTE argued that strongly negative values of $\bar{\kappa}$ favor the formation of many disconnected pieces with no seams, because the GAUSSian term in the HELFRICH equation is negative so that the formation of handles costs a lot of energy. For more positive values of $\bar{\kappa}$ the energy cost decreases and becomes zero for $\bar{\kappa} = 0$. Thus the formation of one large aggregate with a multiconnected structure is favored. Therefore $\bar{\kappa}$ plays a role every time a structural transformation involves a topological change of the membranes, whereas the bending rigidity κ determines the energies of topology-preserving deformations of the bilayers, like curvature fluctuations [9].

PORTE derived the bending elastic properties of the bilayer from those of the monolayers, as seen in Eq. (3.8). As long as the surfaces of the monolayers remain at a constant distance ε from the midplane (see Fig. 3.4), it follows that

$$c_{0,\text{bil}} = 0 \tag{3.19}$$

$$\kappa_{\text{bil}} = 2 \cdot \kappa_{\text{mono}} \tag{3.20}$$

$$\bar{\kappa}_{\text{bil}} = 2 \cdot \bar{\kappa}_{\text{mono}} - 4 \cdot \varepsilon \cdot c_{0,\text{mono}} \cdot \kappa_{\text{mono}} \tag{3.21}$$

where 2ε is the thickness of the bilayer. This means that for the dilute L_α phase with $c_{0,\text{mono}} = 0$, Eq. (3.21) will turn into $\bar{\kappa}_{\text{bil}} = 2 \cdot \bar{\kappa}_{\text{mono}}$, where $\bar{\kappa}_{\text{mono}} < 0$. In those parts of the phase diagram where c_0 is already negative, an increasingly negative $c_{0,\text{mono}}$ brings a positive contribution to $\bar{\kappa}_{\text{bil}}$ making the formation of a saddle easier. Eventually $\bar{\kappa}_{\text{bil}}$ approaches zero and the GAUSSian term in Eq. (3.14) drives the transition from L_α to L_3. An increase of $\bar{\kappa}_{\text{bil}}$ beyond zero results in a constant gain in the elastic bending energy due to a constant growth of the connectivity of the bilayer. This would result in an L_3 phase with smaller and smaller length scales and consequently to the collapse of the L_3 phase. Following PORTE, this collapse is prevented by entropic fluctuations [9]. When comparing this earlier model by PORTE [9] to the results from more recent Monte Carlo simulations by GOMPPER et al. [65] it can be argued that both studies reach equivalent results. In both models the lamellar-to-sponge transition is considered a result of increasingly positive values of $\bar{\kappa}$.
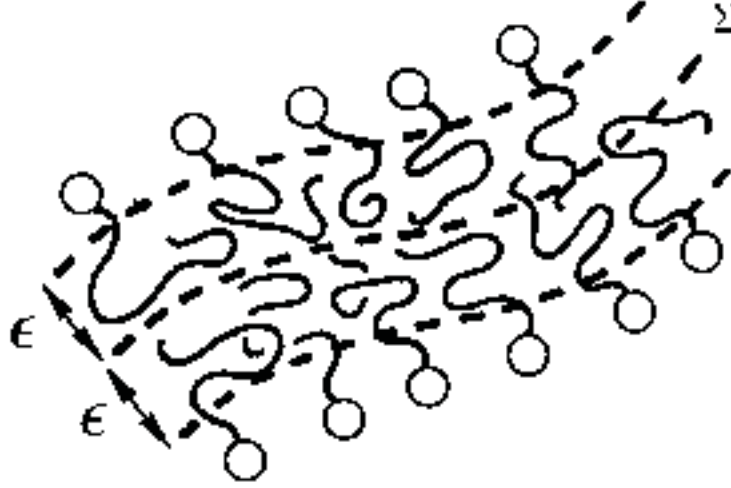
Fig. 3.4: Structural organization of the surfactant bilayer from two identical monolayers. The monolayers are at a distance ε from the midsurface Σ [66].

3.2   Theoretical analysis of the dynamics of L$_3$ phases

To understand the dependence of the relaxation times τ on the concentration variable ϕ_{B+C} in temperature jump experiments [27] it is necessary to understand what happens in the L$_3$ phase. The basic argument is as follows [72]: The sudden variation in temperature induced by the *T*-jump, abruptly changes the spontaneous curvature of the amphiphilic monolayers. The frustration induced in the bilayer will be released via the creation of passages between adjacent bilayers. Passage formation [73] is a two-step process: Adjacent membranes have to meet (or collide) and after this, a passage has to be formed. This means that the apparent experimental relaxation rate is a product of two terms:

$$\tau_{\exp}^{-1} = \tau^{-1} \cdot \exp\left(-\frac{E_A}{RT}\right) \tag{3.22}$$

The first term, τ^{-1}, is the probability for two membranes to meet. It is essentially controlled by the membrane rigidity, κ, and it will be strongly dependent on the interbilayer distance, *d*, as will be shown below. The second term, $\exp\left(-\frac{E_A}{RT}\right)$, is the probability to form a passage between two membranes that are touching each other. On general grounds, it is expected that this term depends on the properties of the bilayer, namely, on the bilayer thickness 2ε as well as on the monolayer parameters, κ_{mono}, $\overline{\kappa}_{mono}$ and $c_{0,mono}$. An estimation of the above-described terms will be given in the following.

3.2.1   Lamellar structure

In the case of the lamellar phase the calculation for the probability of collision between two membranes is straightforward. One uses a MONGE representation [52] for the amphiphilic membrane, which is the standard approach for membranes of the L_α phase, but which corresponds only to a rough approximation when used for an L_3 phase. In this representation it is assumed that the reference state is flat and only smooth deviations are allowed. The MONGE representation considers the x-y plane as the reference plane. Each point within the membrane is localized by an internal coordinate, $s \equiv (x, y)$, and its elevation from the x-y plane is $z = h(x, y)$. Then the HELFRICH bending energy is given by:

$$E = \frac{\kappa}{2} \int (\nabla^2 h)^2 \, d^2 s \tag{3.23}$$

where κ is the bending constant. It was also assumed that the topology of the membrane remains invariant, and thus the GAUSSian term [49, 51] can be neglected. This can be assumed since only the probability of collisions between membranes is considered, and not what happens afterwards. A FOURIER transform of Eq. (3.23) with $h_q = \int d^2 q e^{i q \cdot s} h(s)$ yields:

$$E = \frac{\kappa}{2} \sum_q q^4 |h_q|^2 \tag{3.24}$$

The equipartition theorem ascribes to the average of each mode an energy of $k_B T / 2$ and hence gives:

$$\left\langle |h_q|^2 \right\rangle = \frac{k_B T}{\kappa q^4} \tag{3.25}$$

The fluctuations of a membrane of finite size L (or area L^2) are to be inspected. Eq. (3.25) is integrated to get an estimate of the fluctuation amplitude. The contributions of all the modes consistent with the finite size of the membrane are summed.

$$\left\langle h^2 \right\rangle_L = \int_{\pi/L}^{\infty} d^2 q \left\langle |h_q|^2 \right\rangle = \frac{k_B T}{\kappa} \int_{\pi/L}^{\infty} \frac{d^2 q}{q^4} \tag{3.26}$$

In this expression, the finite size imposes a low-q cutoff at π / L. The integration yields the important result

$$\left\langle h^2 \right\rangle_L \sim L^2 , \tag{3.27}$$

which means that in a free membrane the squared amplitude of the fluctuations increases like L^2. That is, a membrane portion of linear size L will have transversal fluctuations, i.e. fluctuations normal to the surface, of the same order. With keeping this in mind the L$_\alpha$ phase can be considered as a stack of membranes separated from each other by an average distance d. Two of these membranes will touch when, on average, the size of their transversal fluctuations is identical to the inter-membrane spacing d. The size of the transversal fluctuations is, via Eq. (3.27), determined by the linear size L of the membrane. Therefore, the specific membrane size $\tilde{L}$, which has fluctuations equal to the membrane spacing d, can be calculated to be

$$\left\langle h^2 \right\rangle_{\tilde{L}} \sim d^2 , \tag{3.28}$$

which, according to Eq. (3.27) means that $\tilde{L} \sim d$. It follows that there will be one collision between the L$_\alpha$ membranes in each elementary volume of the dimension $\tilde{L} \times \tilde{L} \times d$, that is, in each elementary volume of size d^3. Since the relaxation time τ is proportional to this volume, it follows that $\tau \sim d^3$. This is a well-known result for interactions due to entropic fluctuations between membranes [69]. Using the fact that the average domain size obeys $d \sim \phi_C^{-1}$ with ϕ_C being the surfactant volume fraction, it becomes

$$\tau^{-1} \sim \phi_C^{3}. \tag{3.29}$$

Evidently, regarding the fluctuations of an L$_\alpha$ phase structure on a local scale is not sufficient to explain the high powers of the bilayer volume fraction ϕ_{B+C} that have been observed in *T*-jump experiments on the L$_3$ phase. Consequently, a careful analysis of how the L$_3$ phase structure influences the membrane fluctuations is required.

3.2.2   L$_3$ phase structure

It can be expected that Eq. (3.24) has to be modified for the L$_3$ phase, since the transversal membrane fluctuations are inhibited by the randomly oriented bilayers of the continuous three-dimensional structure. On a local scale the L$_3$ phase membrane resembles the one of the L$_\alpha$ phase, in that the local mean curvature *H* is zero in both cases. Probed on a local scale, it is to be expected that the L$_3$ phase exhibits a similar response to that of an L$_\alpha$ phase. However, when probing the L$_3$ phase membranes on larger scales the existence of passages will have the effect of inhibiting fluctuations that take place on scales of the order of *d*. Due to the structural nature of the L$_3$ phase the bending constants of such membranes will show a dependence on low-*q* values of the type

$$\kappa(q) \sim q^{-\alpha} \tag{3.30}$$

which will affect the FOURIER transformed bending energy *E* in Eq. (3.24). The calculation of the probability for two membranes to touch is done analogously including this *q*-dependence of κ and the bending energy in Eq. (3.24) takes on the form of

$$\tilde{E} \propto \sum_q q^{4-\alpha} \left| h_q \right|^2. \tag{3.31}$$

The exponent α is related to ζ, the so-called wandering exponent [52] by $\zeta = (2 - \alpha) / 2$. Whereby ζ can take on values between $\zeta = 0$, for a system purely controlled by interfacial tension, and $\zeta = 1$, for a system that shows free membrane behavior, i.e. is controlled by the bending energy only, as for the L$_\alpha$ in Eq. (3.24). Following along the same lines Eq. (3.27) changes into Eq. (3.32) for a membrane controlled by contribution from bending energy and interfacial tension:

$$\left\langle h^2 \right\rangle_L \sim L^{2\zeta}. \tag{3.32}$$

This means that in the L$_3$ phase a membrane portion of linear size L$\parallel$ will have transversal fluctuations of the size L$_\perp$ which follow the relation L$_\perp$ ~ L$^\zeta\parallel$. As before for the L$_\alpha$ phase, the probability for two membranes to meet is calculated. Therefore the specific membrane size

$\tilde{L}$, which has fluctuations equal to the average distance d between the L_3 phase membranes, can be calculated to be

$$\langle h^2 \rangle_{\tilde{L}} \sim d^2 \Rightarrow \tilde{L}^{2\zeta} \sim d^2, \tag{3.33}$$

which is, $\tilde{L} \sim d^{1/\zeta}$. On average there will be a collision between membranes on each elementary volume of dimension $\tilde{L} \times \tilde{L} \times d$ or with Eq. (3.32) in each elementary volume of size $d^{(2/\zeta)+1}$. Since the relaxation time τ is proportional to this volume it follows that $\tau \sim d^{\frac{2}{\zeta}+1}$. Using the approximation $d \sim \phi_{B+C}^{-1}$ leads to

$$\tau^{-1} \sim \phi_{B+C}^{\frac{2}{\zeta}+1} \tag{3.34}$$

It is now obvious that exponents higher than ϕ^3 can be obtained. Fig. 3.5 shows the exponents to be expected for the ϕ_{B+C} dependence of the relaxation times τ as a function of the wandering exponent ζ. In sum, it was shown that large exponents in the τ^{-1} versus ϕ_{B+C} dependence of the L_3 phase can be obtained due to the topological configuration of this phase.
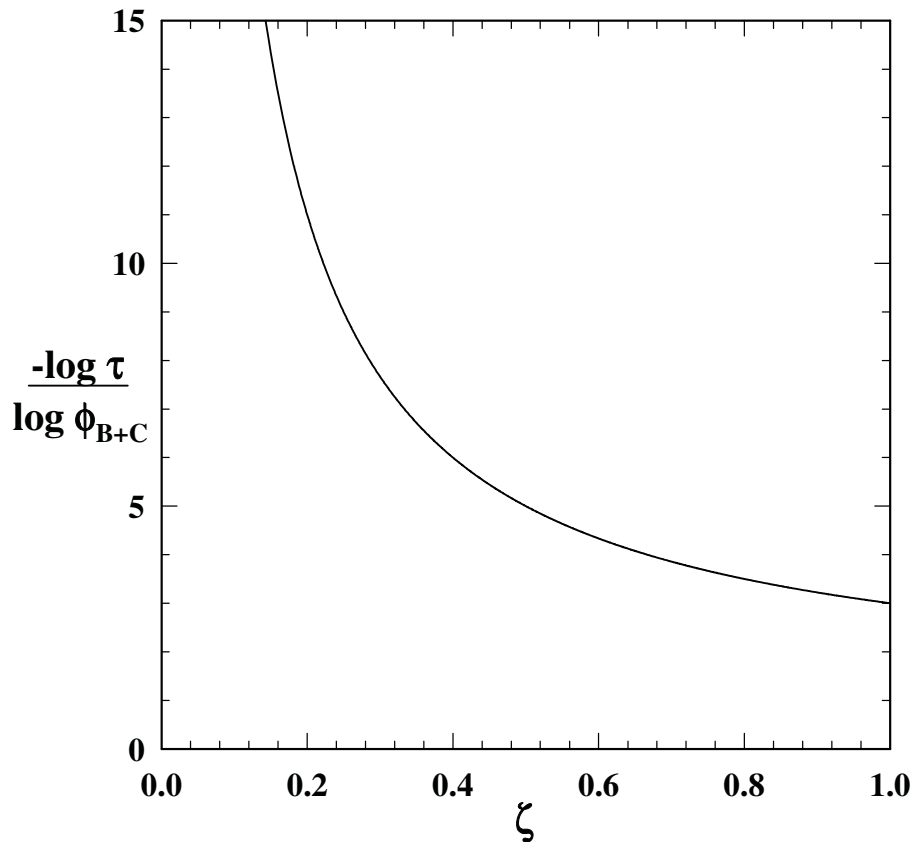
Fig. 3.5: Model calculation for the influence of the wandering exponent ζ on the ϕ_{B+C} dependence of the relaxation times τ.

It should be mentioned at this point that chapter 3.2 was derived by DR. HENRIQUE LEITAO from the University of Lisbon. This theoretical approach was triggered by the first observations of the striking phenomena regarding the dynamics of L_3 phases by LE and coworkers [25], SCHWARZ [28] and UHRMEISTER [27]. It was the basis for a collaboration between our group and DR. LEITAO, funded by the DAAD, and resulting in the detailed experimental data that provided further inspiration for the ongoing theoretical discussions about the structure, stability and dynamics of L_3 phases.

4 Investigations of the dynamics

The difference between a complex fluid and an ordinary fluid is the fact that the former is structured on a microscopic scale. Examples for these complex fluids [74] are microemulsions, micelles, liquid crystals and the L_3 phase amongst others. Their microstructure has been extensively studied with well-established scattering methods like dynamic light scattering (DLS) [75], static light scattering (SLS), small-angle neutron scattering (SANS) [16, 76, 77, 78], small-angle X-ray scattering (SAXS) [79, 80] and other techniques such as nuclear magnetic resonance (NMR) [81, 82, 83, 84] or transmission electron microscopy (TEM) [13, 85, 86], to name just a few.

Based on these experiments a relatively clear idea of the microstructure of complex fluids could be established. It is important to realize that the picture of the microstructure is a static one, ignoring the highly dynamic nature of such a fluid. However, it is above all the dynamics, i.e. the time-dependent properties that are of interest in a lot of applications. Typical examples include the fusion and fission of membranes, changes of the overall structural topology and vesicle formation.

4.1 Basics

In order to study the dynamics of self-organized surfactant systems in solution, relaxation techniques are used. The principle of relaxation techniques [87, 88, 89], such as temperature [90] and pressure jump methods [28, 91], Kerr effect measurements [28, 92], stopped flow techniques and ultrasonic absorption, can be briefly described. A system at equilibrium is perturbed by creating a rapid but very small change of one of the external parameters that determines the system's equilibrium state. This results in a shift of the system to a new equilibrium determined by the final value of the parameter that was changed. As the system relaxes from the old to the new equilibrium condition, its evolution can be characterized by one or more time constants, the so-called relaxation time constants. Consequently, the relaxation time reflects the ability of a system to follow the perturbation and hence, they are dependent on the dynamic processes being studied. This means that different perturbation techniques, depending if they induce thermodynamical, mechanical, electric or chemical perturbations result in different relaxation processes and therefore in different relaxation times. A small perturbation ensures that the system remains close to equilibrium and that the dynamics of the relaxation to the new equilibrium takes on a rather simple mathematical form [93].

Investigations of the dynamics of self-assembled systems started foremost with micellar solutions. There has been a lot of interest for many years in micelle kinetics. Many micellar systems have been examined by stopped flow, pressure jump, temperature jump and ultrasonic relaxation measurements [94, 95, 96, 97]. These measurements frequently identify two well-separated relaxation times, a rapid relaxation which occurs on a time scale of microseconds and a slower process, which requires milliseconds to seconds [17, 18]. ANIANSSON and WALL [17] assigned the fast process to an association-dissociation process involving the exchange of individual surfactant molecules between the micelles and the water phase and attributed the slower process to a more inherent rearrangement of the system involving the creation and destruction of micelles. While the kinetics of micelles are fairly well understood today, the dynamics of vesicles, i.e. globular structures with bilayer membranes, remained elusive in spite of their obvious importance in a wide range of applications [20, 98]. In a study by YATCILLA and coworkers [99] a surfactant of opposite charge is added to a micellar solution of an ionic surfactant and vesicles are formed from spherical micelles. The composition of the bilayer and the partitioning of surfactant molecules between the inner and outer monolayers of the vesicles play an important role in setting the equilibrium bilayer curvature. A likely mode of adjusting these monolayer compositions is via a so-called surfactant flip-flop through the bilayers, which occurs on time scales up to days. These time scales are much longer than typical exchange rates of surfactant monomers between the aqueous and aggregated states, which is the only mass transfer mode necessary for micelles to equilibrate. ZANA [100] studied the rate constants for the exchange of solubilized compounds between formed vesicles. They were found to be at least four magnitudes faster than the ones measured for micellar systems. For the first time FRIBERG et al. [19] observed the formation of vesicles directly from a molecular dispersion by diluting a solution of vesicle forming surfactants with water using a stopped flow technique. They found a relaxation time for the formation of vesicles varying from microseconds to several seconds depending on the concentration of the vesicle forming surfactant and being at least five orders of magnitude slower than that for micelles. Nevertheless, all these studies involve the kinetics of vesicle formation or the exchange rates of solubilized compounds between vesicles rather than the actual time dependent properties of stable vesicle phases. This is unlike studies concerned with the actual dynamics of stable micellar [18] or L_3 phases [28].

For matters concerning the dynamics of L_3 phases there are still many open questions. A brief "state of the art" review of L_3 phase dynamics was given in the chapter 1 for works by MILLER [21], PORTE [22] and WATON [24]. Some aspects will be presented in more detail.

From electric birefringence measurements it was found that the relaxation time constants τ^{-1} depend on the surfactant volume fraction ϕ like $\tau^{-1} \propto \phi^3$. This was attributed to an orientational relaxation of disk-like aggregates in the case of MILLER [21] for the zwitterionic system water – $C_{14}DMAO$ – *n*-hexanol. PORTE [22] also found this ϕ^3 dependence, using the system water – betain – *n*-pentanol. However, he attributed this dependence to a distortion of a sponge-like L_3 structure that relaxes. These structural discrepancies stem from a time before the L_3 structure had been unambiguously proven as a sponge-like structure by SANS and FFEM. This was accomplished in 1990 by FFEM [14] and supported by SANS in 1992 by STREY et al. [8]. Later PORTE and WATON [24] theoretically predicted the existence of three different relaxation processes, and therefore three different relaxation times. These three relaxation times are supposed to originate from a diffusion time of concentration fluctuations, a relaxation time for the breaking of the structure's symmetry, and a relaxation time for the reestablishment of the connectivity of the bilayer. In the same study a corresponding set of experiments was presented. They followed the temperature jump relaxation by detection of the scattered light for the pseudo-binary ionic system brine – cetylpyridiniumchloride – *n*-hexanol and claim to have found experimental evidence for three different time constants. These ϕ dependencies of the three different τ were checked on two samples respectively and found to scale as ϕ^{-3} and ϕ^{-4}. Although the experimentally obtained relaxation time constants might qualitatively explain, or at least be associated with, the predicted time constants one has to be aware that only a very limited number of data were presented.

Recently, some very promising studies were carried out by SCHWARZ et al. [28]. Here the dynamics of L_3 phases for the non-ionic system H_2O – $C_{10}E_4$ – *n*-decanol were studied. Temperature jump relaxation, pressure jump relaxation, time-resolved electric birefringence, and dynamic light scattering experiments were performed. Different experimental time constants and dependencies on the surfactant volume fraction ϕ_C were expected since the different techniques used, probe different processes. Instantaneous temperature or pressure changes alter the spontaneous curvature of the monolayers constituting the bilayer of the L_3 phase and may lead to the formation of new passages. Temperature jump and pressure jump experiments are therefore expected to yield information on the dynamics of passage formation, which is equal to a topology change in the L_3 phase structure. In time-resolved Kerr effect measurements the applied electric field may induce a distortion of the sponge

structure without a change in the actual topology of the L_3 phase. Differently to these perturbation methods dynamic light scattering experiments (DLS) show spontaneous fluctuations in the L_3 phase. The observed relaxations were all found to be single exponentials. The time constants τ^{-1} obtained by the different methods vary over several orders of magnitude and reveal strong dependencies on surfactant volume fraction ϕ_C resulting in scaling laws of $\tau^{-1} \propto \phi^n$, with $n = 9$ for temperature and pressure jump relaxation, $n = 3$ for the electric birefringence measurements and $n = 1$ for the dynamic light scattering experiments.

In this work an attempt for a better understanding of the actual processes following an instantaneous perturbation is made to eventually find a general description for the dynamics of L_3 phases. In the examples given above all experiments were performed as a function of the concentration of the non-swollen bilayer. Any information about the influence of the bilayer thickness, i.e. swelling the bilayer with oil, is missing. Since the bilayer thickness is as fundamental for the L_3 phase structure as the bilayer concentration, relaxation processes as a function of the bilayer thickness should yield some important information concerning the dynamics of L_3 phases. As a basis for a detailed investigation the system water – *n*-octane – $C_{10}E_4$ was chosen because the structure of the L_3 phase can be varied by either swelling the bilayer with oil, i.e. changing the surfactant / (oil + surfactant) volume fraction ω_b or by varying the bilayer volume fraction ϕ_{B+C}. First of all, temperature jump experiments were performed. However, in order to have excess to a much wider time range a second perturbation method, called isothermal shear, was developed. These two methods, which complement each other perfectly, will be presented in detail in the following. The results obtained by these two methods will then be presented and discussed.

These investigations, though unspoken, always refer to the water-rich L_3 phase as described in the phase diagram in Fig. 2.3. The existence of an oil-rich L_3 phase was also taken into account in this work. As the experimentally accessible L_3 phase on the oil-rich side is restricted to a small concentration range, extensive measurements as a function of the surfactant / (water + surfactant) volume fraction ω_a and the bilayer volume fraction ϕ_{A+C} could not be performed. Consequently, no additional information was gained from the *T*-jump experiments on the oil-rich L_3 phase. In order not to disturb the train of thoughts the corresponding experiments and results are discussed separately in chapter 9.

4.2 Temperature jump

The temperature jump apparatus consists of a high-voltage discharge unit containing the thermostatted cell and the optical unit for monitoring the change in the intensity of the scattered light [101]. The principle behind this setup is to rapidly heat the cell, i.e. disturb the equilibrium state of a given sample, located between platinum electrodes, by means of discharging the high-voltage capacitor through the sample. The height of the generated *T*-jump as a function of the voltage charge of the capacitor can be calculated using the relation $\Delta T = bU_{\text{cap}}^2$, with b being an empirical constant. A value of $b = 7.1 \ (\pm 0.5) \times 10^{-3} \ \text{K} \ (\text{kV})^{-2}$ was obtained from calibration measurements (see chapter 8 for details). Therefore charging voltages between 2.5 and 11 kV yield temperature jumps of 0.04 to 0.86 K. The heating time $\tau_{\text{H}} = R_{\text{cell}} \cdot C / 2$, where R_{cell} is the resistance of the sample in the cell and C the capacitance (10 nF) of the capacitor, is dependent on the electrolyte concentration and the sample's composition. The heating time was found to be $\tau_{\text{H}} = 2 \ (\pm 1) \ \mu\text{s}$ with typical sample resistances of $100 - 1000 \ \Omega$. Because of heat exchange with the surrounding cell the temperature inside the sample decreases again until it reaches the initial temperature T_0. The corresponding time to this process is called the cooling time τ_{C}. From fitting the long time based measurements (see chapter 8) τ_{C} was determined to be almost constant with $\tau_{\text{C}} = 18 \ (\pm 2) \ \text{s}$ while its exact value is of minor relevance for the determination of relaxation times of less than seconds. It follows that reliable relaxation times τ can only be observed for $\tau \ll \tau_{\text{C}}$ and $\tau \gg \tau_{\text{H}}$. The time window in which dynamic processes can be investigated by this method is therefore limited to $10^{-4} \ \text{s} < \tau < 1.5 \ \text{s}$.

4.2.1 Results

To resolve the dynamics of L_3 phases as a function of their structure, temperature jump experiments are performed for different bilayer volume fractions $\phi_{\text{B+C}}$ and varying surfactant / (oil + surfactant) volume fractions ω_{b}. A schematic representation of the samples' compositions is given in Fig. 4.1.
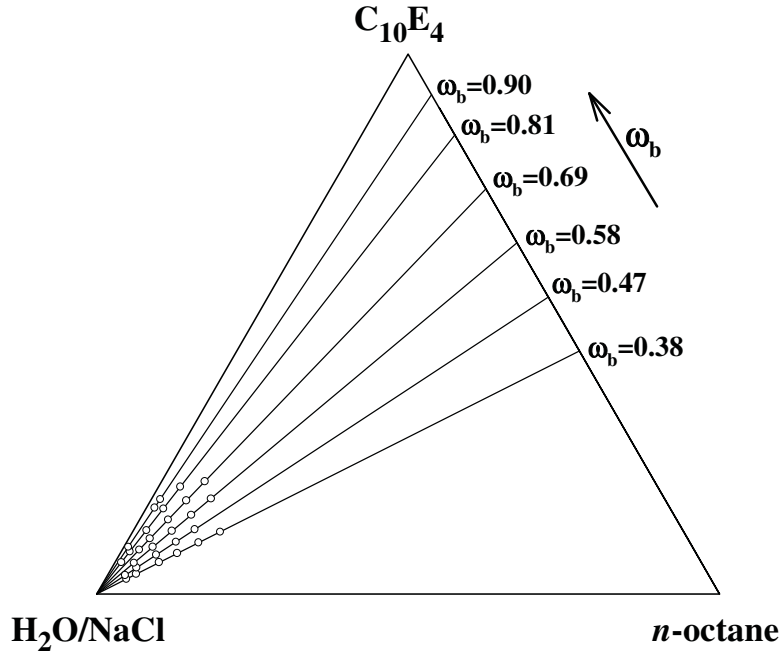
Fig. 4.1: Schematic representation of the composition of the samples for the different bilayer volume fractions ϕ_{B+C} and surfactant / (oil + surfactant) volume fractions ω_b.

All experiments are carried out inside the temperature range of the stable L_3 phase. Temperature jumps are always performed from a temperature within the stable L_3 phase region towards the upper L_3 phase boundary temperature $T_u^{L_3}$ (see Fig. 2.8), this choice of temperature will be explained in detail later. For each temperature jump the scattered light intensity is monitored simultaneously for five different angles ϑ. Fig. 4.2 shows a typical temperature jump experiment. In the upper diagram the instantaneous temperature jump from the initial temperature T_0 to the new equilibrium temperature $T_u^{L_3}$ can be seen. The corresponding relaxation curve of the scattered light intensity as a function of time is illustrated in the central picture. The relaxation of the scattered light intensity was found to be single exponential for all examined samples. Taking this into account and considering the fact that the cooling time τ_C is correlated to the return time back to T_0, the relaxation process as seen in the central diagram can be quantitatively described by

$$\frac{I_S(t)}{I_0} = 1 + \frac{\Delta I_S}{I_0} \cdot \frac{1}{1 - \frac{\tau}{\tau_C}} \cdot \left(\exp\left(-\frac{t}{\tau_C} \right) - \exp\left(\frac{t}{\tau} \right) \right) \tag{4.1}$$

with I_0 being the intensity of the scattered light before the jump, and I_S the time-dependent scattered light intensity. The amplitude $\Delta I_S / I_0 \cdot 1 / (1 - \tau / \tau_C)$ is determined by the intensity

increase associated with the temperature jump ΔT. For all presented experiments, however, $\tau_C \gg \tau$ consequently the second term of the amplitude, $1 / (1 - \tau / \tau_C)$, can be neglected. The values for I_0 can be determined from the experimental data. A fixed value of $\tau_C = 17.7$ s is used, which is known from calibration measurements (see chapter 8). The relaxation time τ is the time that passes until a new equilibrium situation corresponding to the increased temperature is reached. For the example in Fig. 4.2 the fit function (Eq. (4.1)) yields the amplitude $\Delta I_S / I_0 = 0.305$ and the relaxation time $\tau = 0.385$ s. The residual plot at the bottom of Fig. 4.2 documents the quality of the fit. It shows some background noise, but no systematic deviations between the measured data points and the fitted curve obtained by non-linear regression.
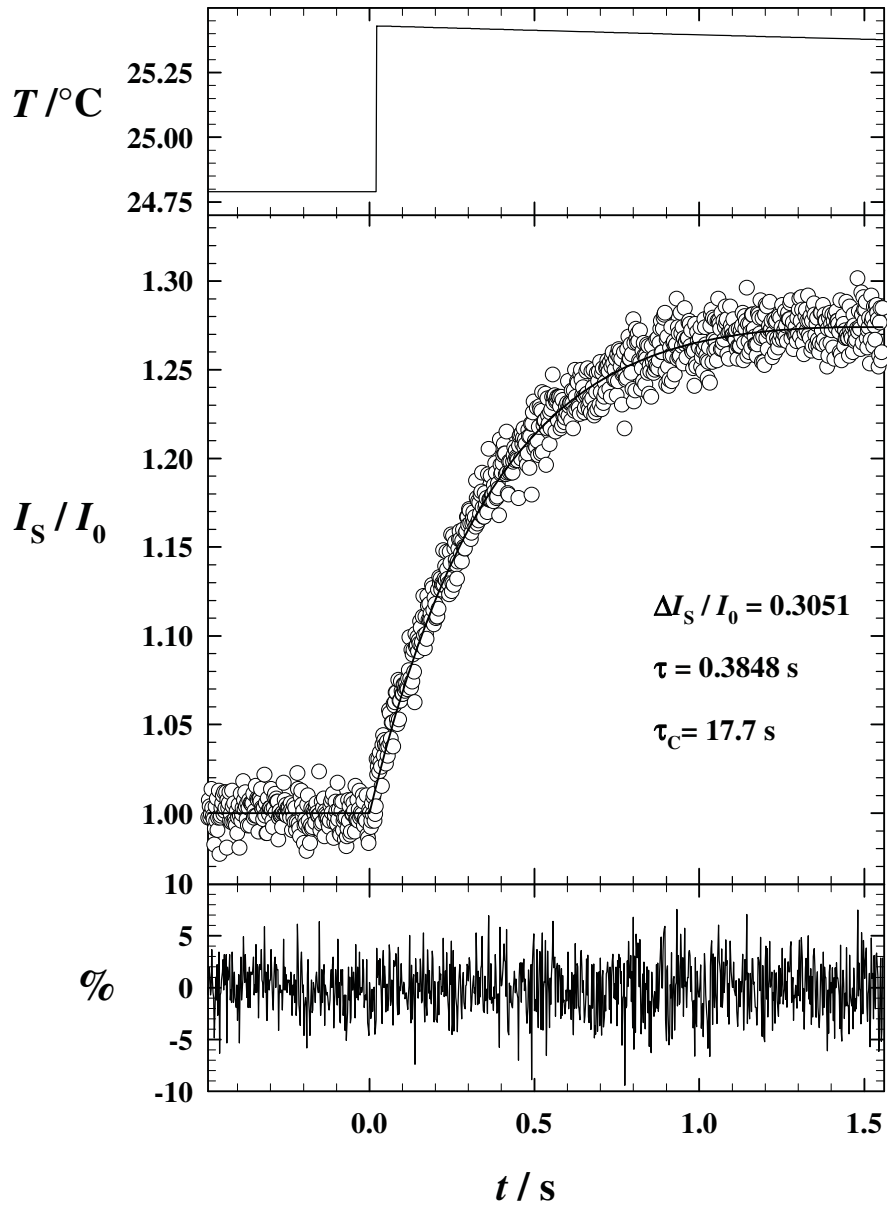
Fig. 4.2: A typical analysis of a *T*-jump from T_0 = 24.79 °C to T = 25.43 °C (top) for a sample with ϕ_{B+C} = 0.1045 and ω_b = 0.69 observed at ϑ = 90°. This experiment can be entirely described by Eq. (4.1). With given values for I_0, t and τ_c the amplitude $\Delta I_S / I_0$ and the relaxation time τ can be obtained from nonlinear regression (middle). The residual plot shows no systematic deviations between the measured data points and the fitted curve (bottom).

For using the intensity of the scattered light as detection method for the temperature jump experiment, a correlation between the scattered light intensity and the temperature has to be guaranteed. This correlation is illustrated in Fig. 4.3:
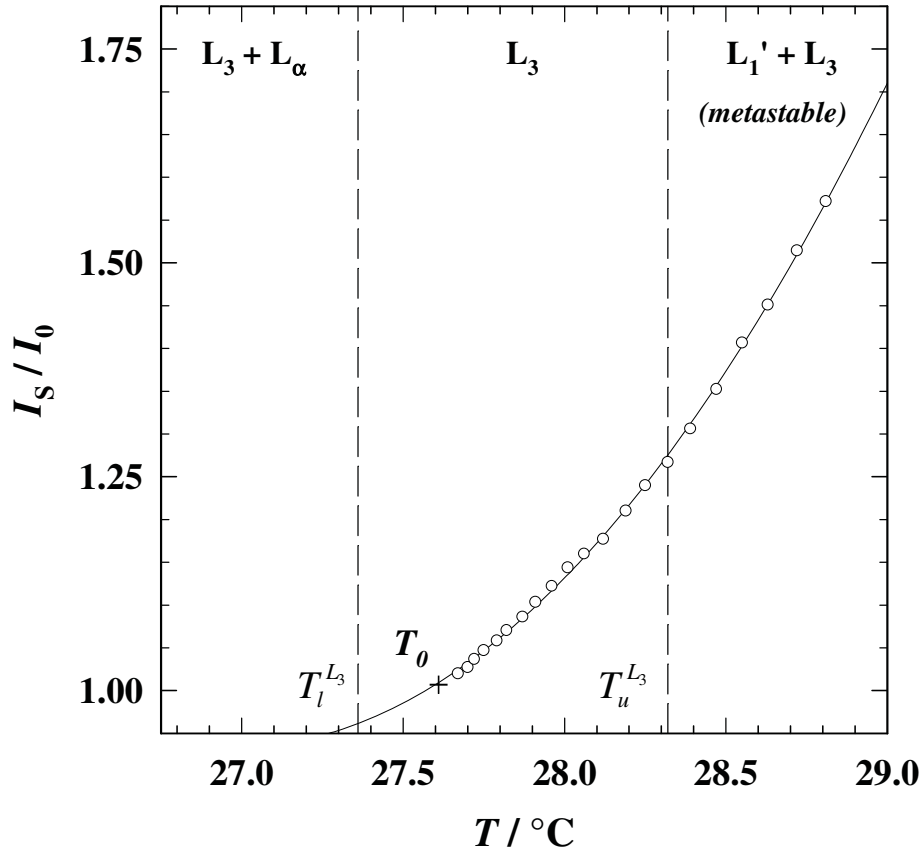
Fig. 4.3: Intensity of the scattered light I_S / I_0 as a function of temperature T for a sample with $\omega_b =$ 0.58 and $\phi_{B+C} = 0.1528$. The lower and upper L_3 phase boundary temperatures are determined to $T_l^{L_3} =$ 27.36°C and $T_u^{L_3} = 28.32$°C (dashed lines). For temperatures higher than $T_u^{L_3}$ the L_3 phase stays in a metastable state. Phase separation does not take place due to kinetic hindrance.

With increasing temperature the light scattering intensity I_S increases monotonically, i.e. every temperature jump is inevitably followed by an increase in the scattering intensity. Therefore a temperature jump perturbation causes an amplitude ΔI_S, a change in the intensity of the scattered light. Note that the amplitudes $\Delta I_S / I_0$ change with the temperature difference between the initial and the final state. In other words: Whereas every absolute value of I_S / I_0 is defined by a certain T, the amplitude $\Delta I_S / I_0$ is depending on the applied T-jump and is not a function of the L_3 phase dynamics.

The time that is needed to reach the final intensity determines the relaxation time τ of the process, which was induced by the instantaneous temperature rise. In contrast to the light scattering amplitudes, these relaxation times τ are equal for T-jumps performed up to a fixed temperature irrespective of the initial temperature. Therefore every T-jump with a defined final temperature T is characterized by a distinct relaxation time τ, which is illustrated in Fig. 4.4:
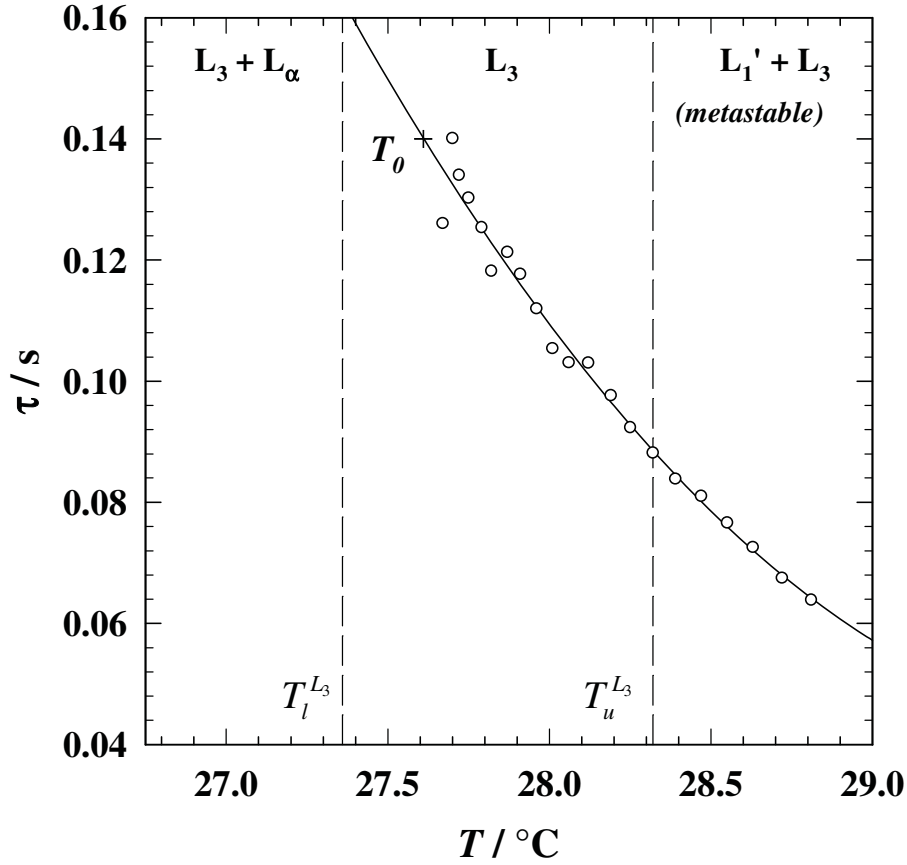
Fig. 4.4: Relaxation times τ as a function of temperature T for a sample with $\omega_b = 0.58$ and $\phi_{B+C} = 0.1528$. The lower and upper L_3 phase boundary temperatures are determined to $T_l^{L_3} = 27.36$°C and $T_u^{L_3} = 28.32$°C (dashed lines), T_0 is the initial temperature before the jump. For temperatures higher than $T_u^{L_3}$ the L_3 phase stays in a metastable state.

From experiments it becomes clear that the relaxation times do not depend on the initial temperature T_0 from were the T-jump is performed as long as the jumps are carried out onto the same final temperature. This final temperature should be characteristic for all samples to serve as a common reference. Since the binodal temperature or $T_u^{L_3}$ is such a feature, it is used as a reference temperature in T-jump experiments when comparing samples with varying compositions, i.e. different temperatures $T_u^{L_3}$.

Fig. 4.4 also shows the possibility to determine the temperature dependence of the relaxation times, since starting from the same initial temperature T_0 and jumping onto different final temperatures, yields different relaxation times. This will be explained in detail in the following.

Temperature dependence of the relaxation time

The temperature dependence of the relaxation time was examined for varying bilayer volume fractions ϕ_{B+C} as well as surfactant / (oil + surfactant) volume fractions ω_b. This was done by temperature jump experiments onto various temperatures T in the stable L_3 phase region. This means that several T-jumps from a fixed temperature T_0 with rising jump amplitudes ΔT onto different final temperatures were performed. In contrast the concentration dependencies of the relaxation times were establish by jumps onto one reference temperature, the binodal or upper phase boundary temperature $T_u^{L_3}$ (see Fig. 4.4). Fig. 4.5 shows three exemplary jumps for rising ΔT starting from $T_0 = 28.54$ °C. The relaxation process becomes faster with increasing height of the temperature jump, i.e. when the binodal line is approached.
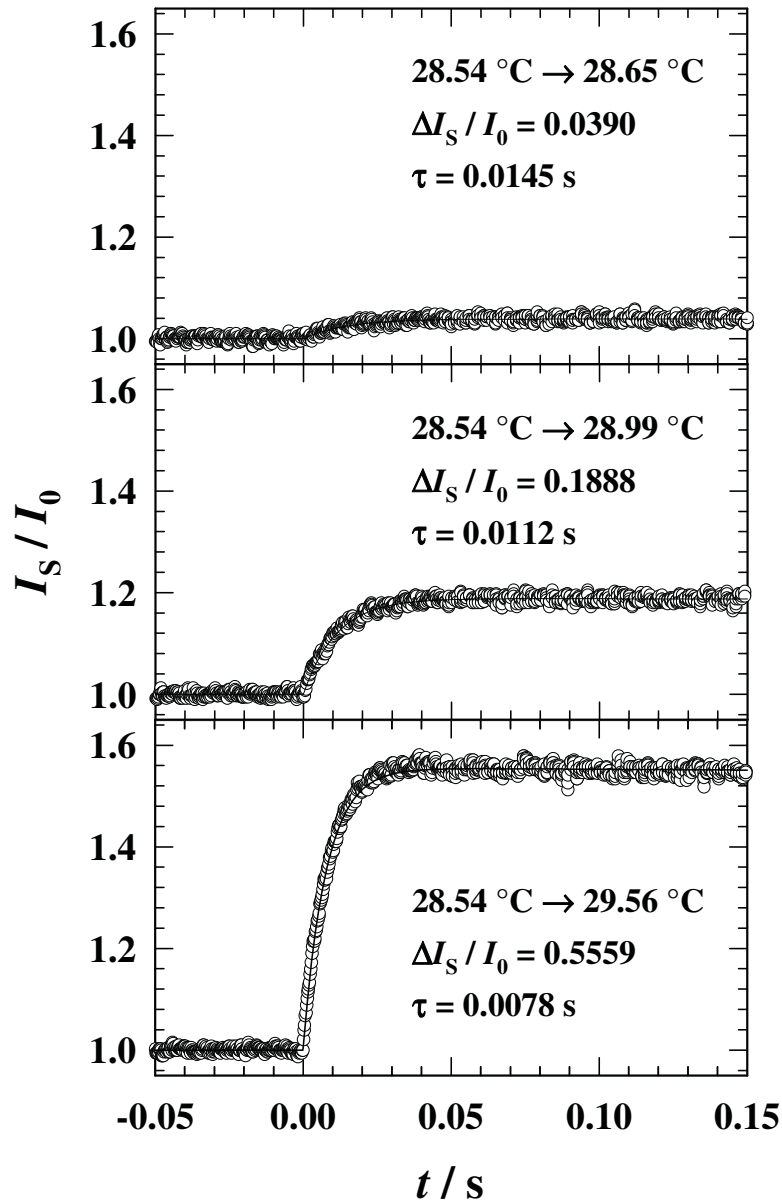
Fig. 4.5: Relaxation curves for three different *T*-jumps of a sample with the bilayer volume fraction $\phi_{B+C} = 0.2035$ and a surfactant / (oil + surfactant) volume fraction $\omega_b = 0.58$. *T*-jumps are performed for rising ΔT starting from a constant temperature $T_0 = 28.54$ °C for $\vartheta = 90°$. The resulting relaxation times τ become shorter with increasing ΔT.

Scattering angle dependence of the relaxation time

Temperature jump experiments for each sample were carried out for detection angles of $\vartheta = 40°$, $60°$, $90°$, $120°$ and $140°$. The resulting relaxation times τ are, apart from the experimental error, independent of the angle of detection of the scattered light, as can be seen in Fig. 4.6.
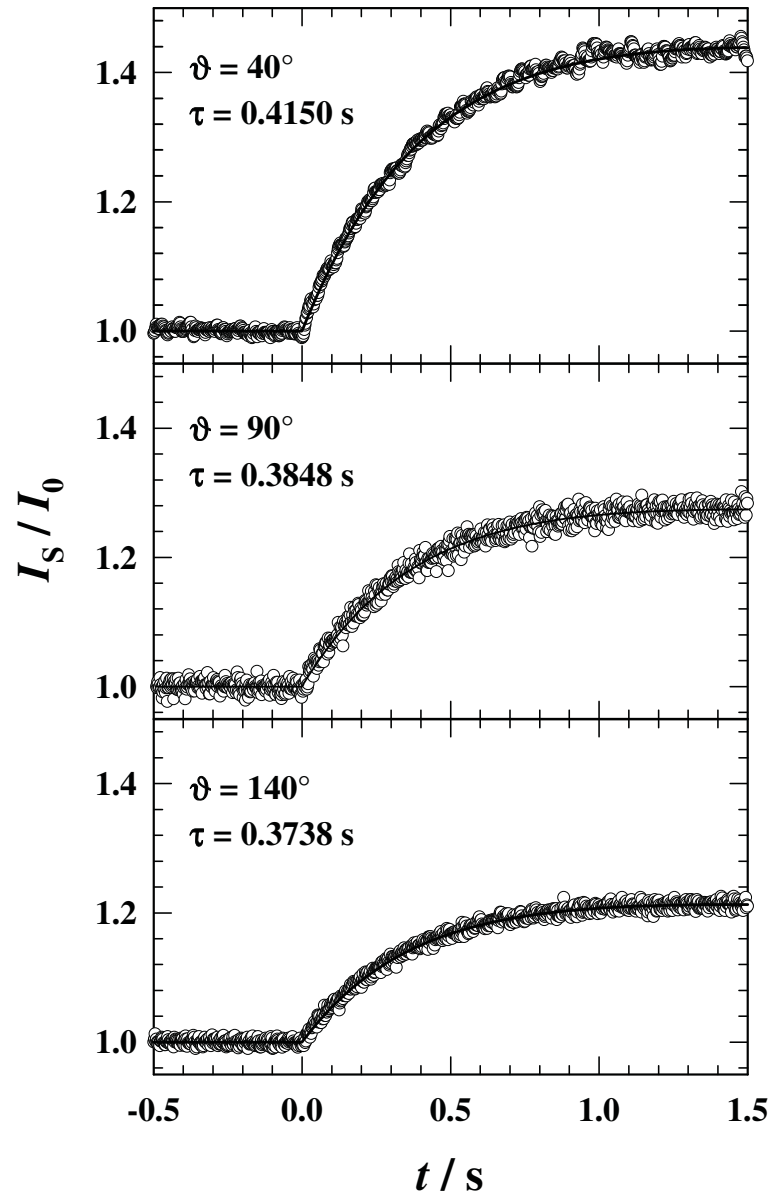
Fig. 4.6: Relaxation curves with a single relaxation time τ (taking into account the experimental error) for T-jumps 24.79°C $\rightarrow$ 25.43°C for a sample $\phi_{B+C} = 0.1045$ and $\omega_b = 0.47$ at detection angles of $\vartheta = 40°$, $90°$ and $140°$.

Fig. 4.6 emphasizes the independence of the relaxation times of the scattering angle. All following relaxation curves will be presented for scattering angles $\vartheta = 90°$ only, if not stated otherwise. Furthermore Fig. 4.6 shows that even when the relaxation times are the same for one single jump under different scattering angles, the amplitudes $\Delta I_S / I_0$ are not, i.e. the relaxation times are not dependent on the amplitudes. Since the relaxation times and the amplitudes $\Delta I_S / I_0$ are not directly related to each other the amplitudes will not be discussed further.

Dependence of the relaxation time on the bilayer volume fraction ϕ_{B+C}

For samples at constant values of ω_b the bilayer volume fractions ϕ_{B+C} were varied between 0.1 and 0.3 in steps of 0.05, if applicable. In Fig. 4.7 an exemplary comparison of temperature jumps onto the binodal temperature for three samples with different compositions ($\phi_{B+C} \approx$ 0.15, 0.20, 0.25) for a constant $\omega_b = 0.69$ is shown. For the lowest concentration the relaxation time is about two tenth of a second, for the medium concentration it is two hundredth of a second, while for the highest it is around two thousandth of a second. The resulting picture is one where the relaxation curve spans the whole time range of 1 s for low, is greatly reduced in its expanse for medium, and hardly recognizable as a curve for the high bilayer volume fraction ϕ_{B+C}. To emphasize that the curves of medium and high ϕ_{B+C} are of the same shape as the one for low ϕ_{B+C} the curves are shown again in inlets, just on different time scales. This comparison demonstrates evidently that the relaxation time τ of the L_3 phase shows very strong concentration dependence. Increases of 0.05 in the bilayer volume fraction ϕ_{B+C} result in decreases of the relaxation time τ by one order of magnitude.
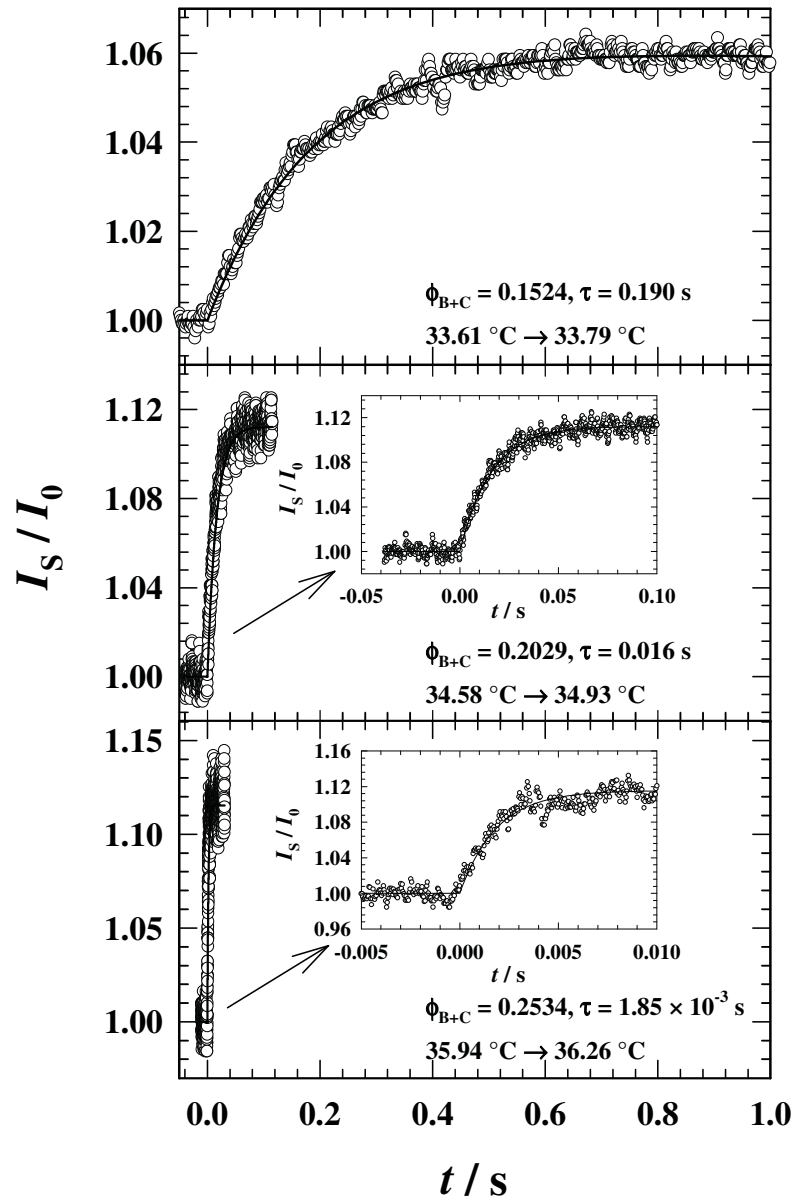
Fig. 4.7: Comparison of the relaxation curves for three samples of different composition at constant ω_b for *T*-jumps onto the binodal temperature for $\vartheta = 90°$. The relaxation process becomes increasingly faster with rising bilayer volume fractions ϕ_{B+C}. For an increase in bilayer concentration of 10% the relaxation time shortens by two orders of magnitude. The inlets show the relaxation curves on time scales of one tenth or one hundredth respectively.

Variations of the bilayer volume fraction ϕ_{B+C} were performed for six different surfactant / (oil + surfactant) volume fractions ω_b in the range of 0.9 to 0.37. All ϕ_{B+C} variations for these different ω_b's exhibit qualitatively the same relaxation behavior, i.e. they all show a pronounced dependence of the relaxation time on the bilayer volume fraction ϕ_{B+C}.

Dependence of the relaxation time on the surfactant / (oil + surfactant) volume fraction ω_b

Since the variations of the bilayer volume fraction ϕ_{B+C} were performed for six different surfactant / (oil + surfactant) volume fractions ω_b, the relaxation behavior of the L_3 structure can also be looked upon as a function of ω_b. Comparing the relaxation curves for three different surfactant / (oil + surfactant) volume fractions ω_b at constant $\phi_{B+C} = 0.2$ leads to the diagram shown in Fig. 4.8. Starting from high ω_b, shown in the upper plot, the relaxation time increases at first when oil is added to the system (middle plot), i.e. the relaxation process for these samples becomes slower. If even more oil is added, i.e. ω_b is further reduced, the relaxation process becomes faster again, as pictured in the lower diagram. This shows that the relaxation time of L_3 phases is not only dependent on the bilayer volume fraction ϕ_{B+C} at constant ω_b but is also a function of the surfactant / (oil + surfactant) volume fractions ω_b at constant ϕ_{B+C}. The difference is that with increasing ϕ_{B+C} the relaxation process becomes monotonically faster, while for varying ω_b the relaxation time τ runs through a maximum for intermediary values of ω_b.
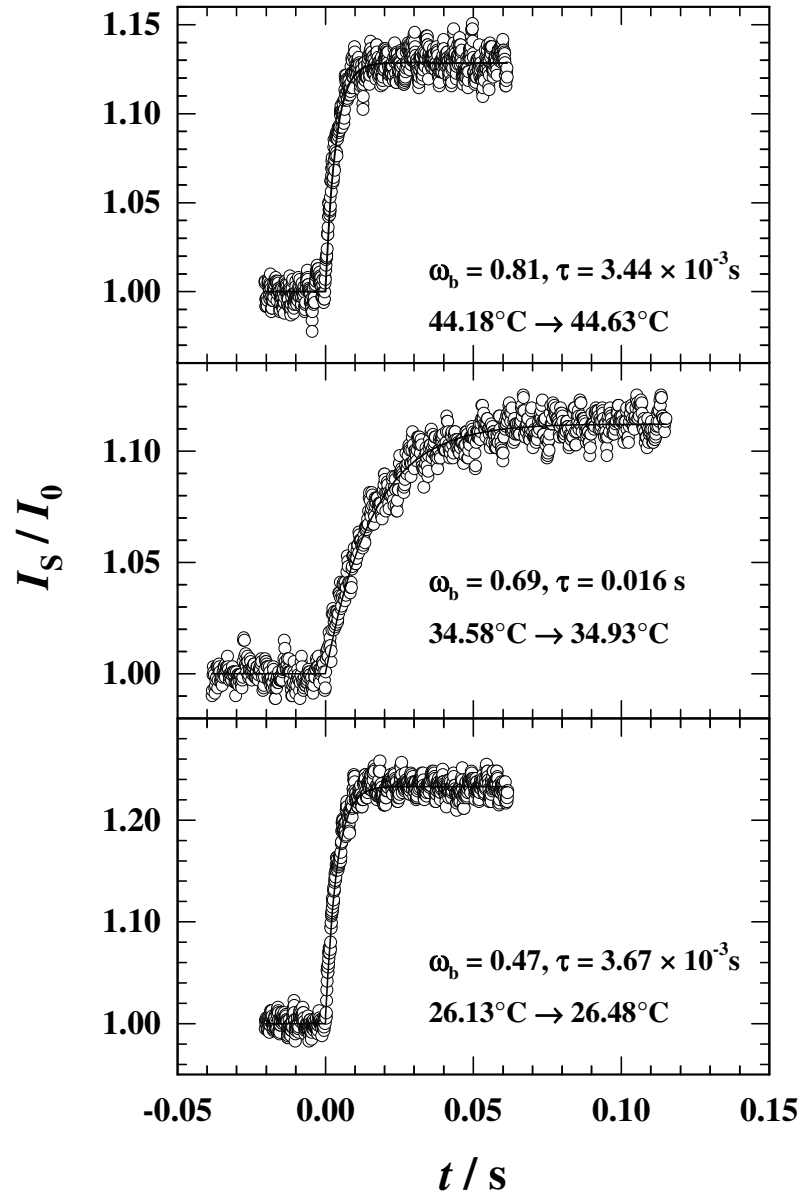
Fig. 4.8: Comparison of the relaxation curves for three samples of different surfactant / (oil + surfactant) volume fractions ω_b of constant ϕ_{B+C} for *T*-jumps onto the binodal temperature for $\vartheta = 90°$. The resulting relaxation times run through a maximum for intermediary values of ω_b.

4.2.2 Discussion

In this discussion first of all the temperature dependencies of the relaxation time constants for different samples will be presented in an ARRHENIUS-like plot, associating these dependencies to effective activation energies. Then the consequences resulting from the q^2-independence of the relaxation times for a single sample will be discussed. At last the resulting relaxation time constants of the above mentioned variations for the bilayer volume fraction ϕ_{B+C} and the surfactant / (oil + surfactant) volume fraction ω_b will be presented in such a way that the fundamental relationships between these dependencies will be revealed. It is common practice

for all studies concerned with the examination of dynamical processes to consider reciprocal relaxation times τ corresponding to rates or time constants τ^{-1}. This principle therefore will be taken up in the following discussions.

Temperature dependence of the relaxation time constants

The temperature dependence of the relaxation time constants τ^{-1} can be presented as an ARRHENIUS-like plot. For this the relaxation time constants are plotted logarithmically against the inverse final temperature T. At one constant ω_b this plot yields a set of parallel straight lines each for a different bilayer volume fraction ϕ_{B+C}, as can be seen in Fig. 4.9.
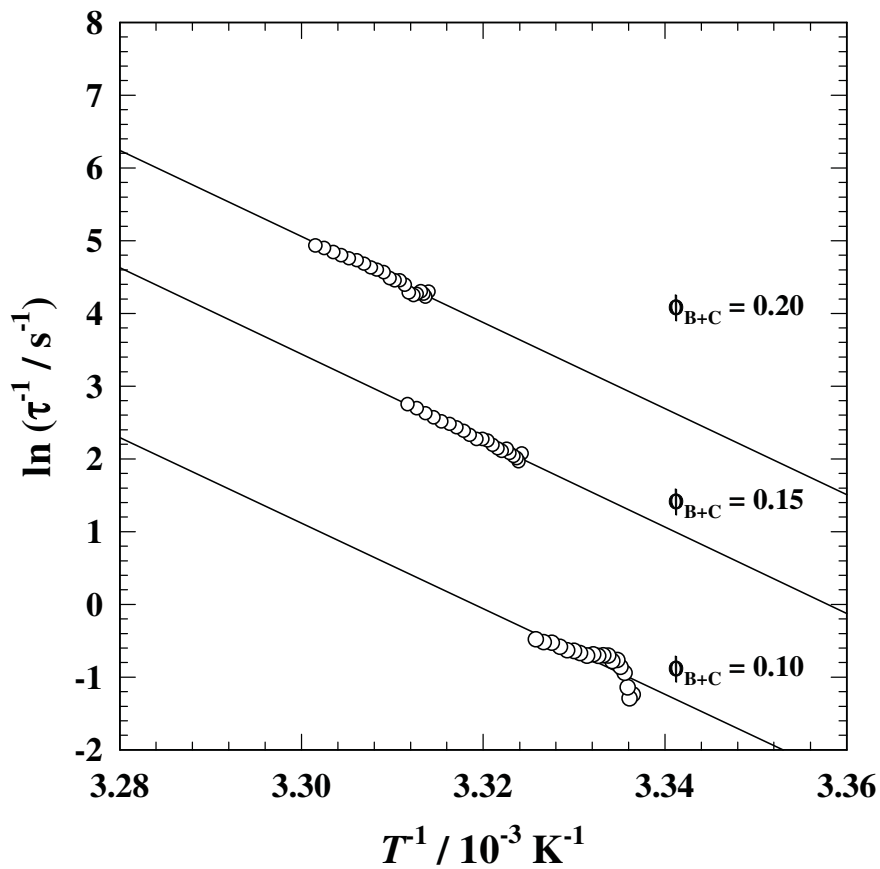
Fig. 4.9: Temperature dependence of the relaxation time constants in an ARRHENIUS-like plot for three different bilayer volume fractions ϕ_{B+C} = 0.20, 0.15 and 0.10 for a constant value ω_b = 0.58.

According to

$$\tau^{-1} = A \cdot \exp\left(-\frac{E_a}{RT}\right) \qquad (4.2)$$

the slope of these plots can be associated with an effective "activation energy" E_a. For the representative example given in Fig. 4.9 a numerical value of $E_a = 492 \pm 3$ kJ / mol is found. The parallel lines for the different bilayer volume fractions ϕ_{B+C} indicate that the temperature dependence of the relaxation times is independent of ϕ_{B+C}. This might indicate that the mechanism of relaxation is the same irrespective of the bilayer volume fraction.

On the other hand a clear dependence on ω_b was observed. ARRHENIUS-like plots for different constant values of ω_b have been evaluated. The values for the activation energies E_a taken from these plots are presented in Fig. 4.10 as a function of the surfactant / (oil + surfactant) volume fraction ω_b.
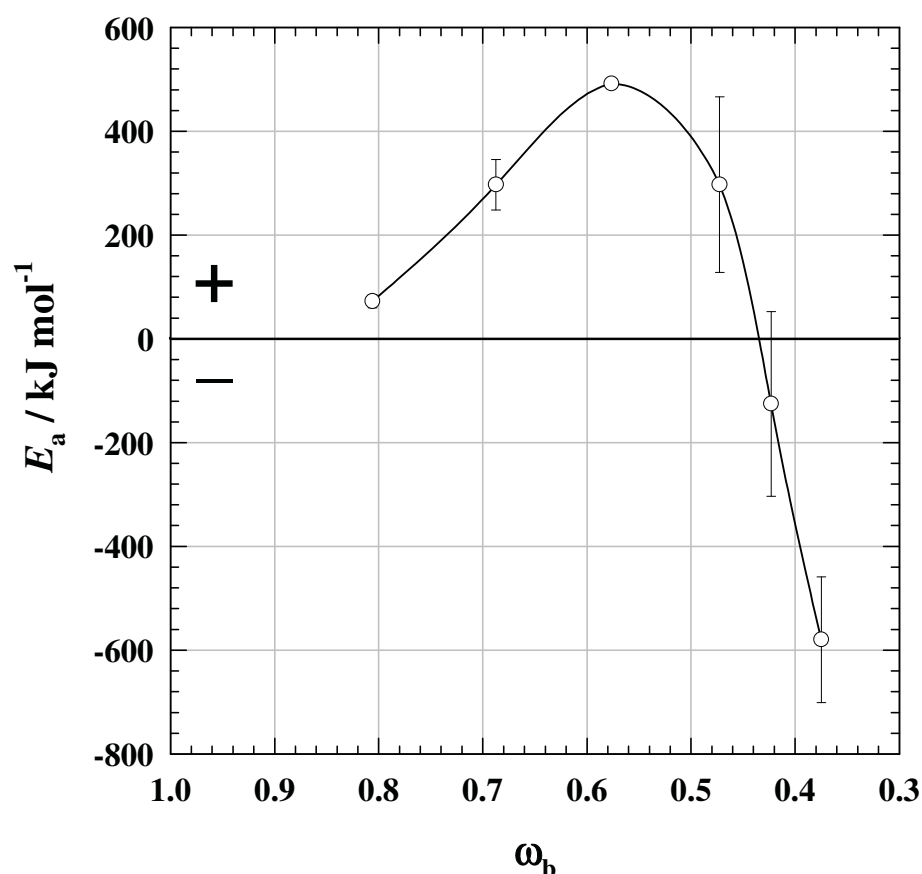
Fig. 4.10: Dependence of the "activation energy" E_a on the surfactant / (oil + surfactant) volume fraction ω_b. The error bars indicate the variations in the slopes for changing bilayer volume fractions ϕ_{B+C} in the individual ARRHENIUS-like plots.

While the same relaxation process can be assumed for a variation in the bilayer volume fractions ϕ_{B+C} at constant ω_b, this is not the case for a variation of the surfactant / (oil + surfactant) volume fraction ω_b. A strong variation in the "activation energy" can be observed,

running through a maximum at $\omega_b = 0.58$. Furthermore, a change in the sign of E_a from positive to negative with an increasing amount of oil indicates a dramatic change in the mechanism of relaxation of the L_3 phase when the surfactant / (oil + surfactant) volume fraction ω_b is decreased.

q^2-independence of the relaxation time constants

The observation of a single relaxation time τ for different detection angles, as shown for three relaxation curves in Fig. 4.6, can be best elucidated in comparison with time constants τ_{DLS}^{-1} determined by dynamic light scattering. The dynamic light scattering experiments were performed using a commercial ALV goniometer which is described in detail elsewhere [46, 28]. An angular range of 30° to 150° is routinely covered to explore the q-dependence of the time constants of the samples bilayer fluctuations. The wave vector q is defined as

$$q = 4\pi \frac{n_D}{\lambda} \sin \frac{\vartheta}{2} \tag{4.3}$$

with λ the wavelength of the laser, n_D the refractive index of the medium at λ and the scattering angle ϑ. The result of each dynamic light scattering experiment is an intensity – intensity autocorrelation function. The data points of this function are fitted with CONTIN [102] and yield the q^2-dependent time constants Γ:

$$\Gamma = \frac{1}{2\tau_{DLS}} = Dq^2 \tag{4.4}$$

with D being the mutual diffusion coefficient.

Fig. 4.11 shows linear plots of the time constants τ^{-1} from a temperature jump experiment and τ_{DLS}^{-1} from dynamic light scattering as a function of q^2 for a sample with $\omega_b = 0.47$ and $\phi_{B+C} = 0.204$.
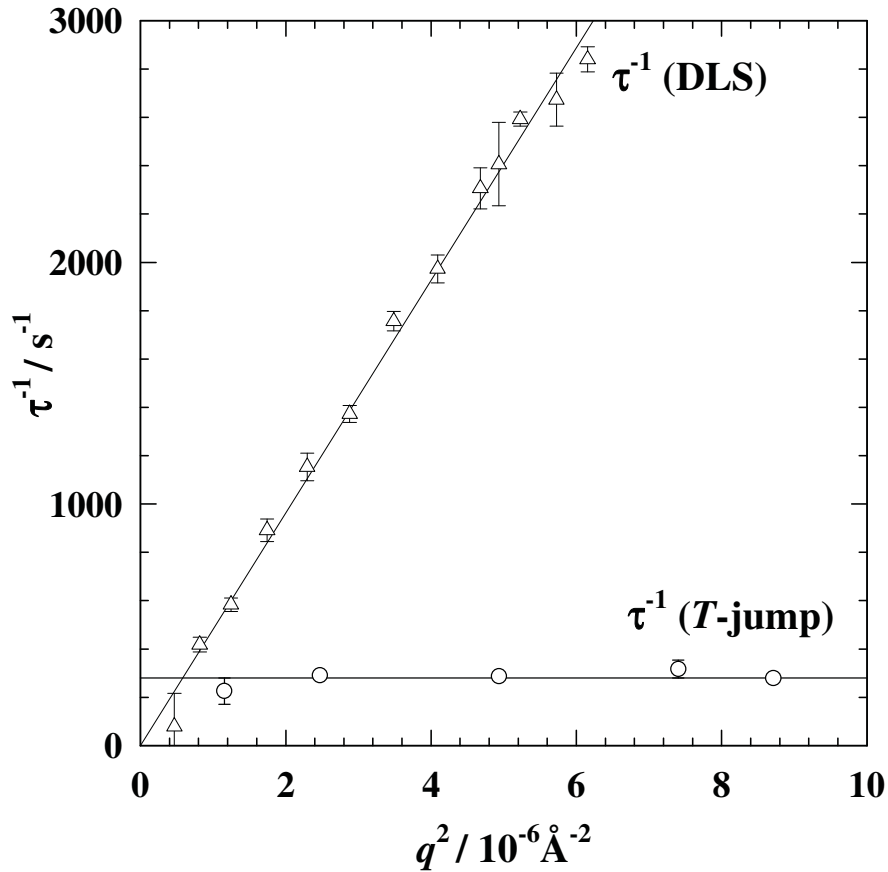
Fig. 4.11: q^2-dependence of the time constants from dynamic light scattering τ^{-1} (DLS) (triangles) at $T = 26.2$ °C and from T-jump (26.13°C → 26.53°C) τ^{-1} (T-jump) (circles) for a sample with $\omega_b = 0.47$ and $\phi_{B+C} = 0.204$.

While the time constants from dynamic light scattering τ_{DLS}^{-1} change with the scattering vector q, i.e. show q^2-dependence, the relaxation time constants from the T-jump experiment remain constant with changing q. This q-independent relaxation time constant τ^{-1} comes as no surprising result in these kinds of experiments. SCHWARZ et al. [28] made the observation of a single time constant describing both pressure and temperature jump relaxation of the same sample. As the relaxation process after the pressure jump is detected via the conductivity of the sample, equal relaxation time constants for the p- and the T-jump can only be obtained if τ^{-1} does not depend on the detection angle ϑ in the T-jump experiment. To understand the relevance of the q^2-independence of the relaxation time constants it is important to understand the meaning of the q^2-dependence of τ^{-1} (DLS). Following the LANDAU-PLACZEK argument, see Eq. (4.4), a q^2-dependence is characteristic for diffusive fluctuation processes. Consequently the q^2-independence clearly defines a relaxation process, which is not based on diffusive fluctuations. It rather is an indication for the detection of structural changes inside a

phase as it was described by PAKUSCH and STREY [103, 104] for the related subject of micelle kinetics.

Since no q^2-dependencies can be detected in the *T*-jump experiments it can be deduced that the relaxation processes observed in this work can be discussed in terms of structure variations only.

Dependence of the relaxation time constants on the bilayer volume fraction ϕ_{B+C}

According to Fig. 4.12 a double logarithmic plot of the relaxation time constants τ^{-1} as a function of ϕ_{B+C} for different ω_b reveals a strikingly strong ϕ_{B+C}-dependence of τ^{-1}.
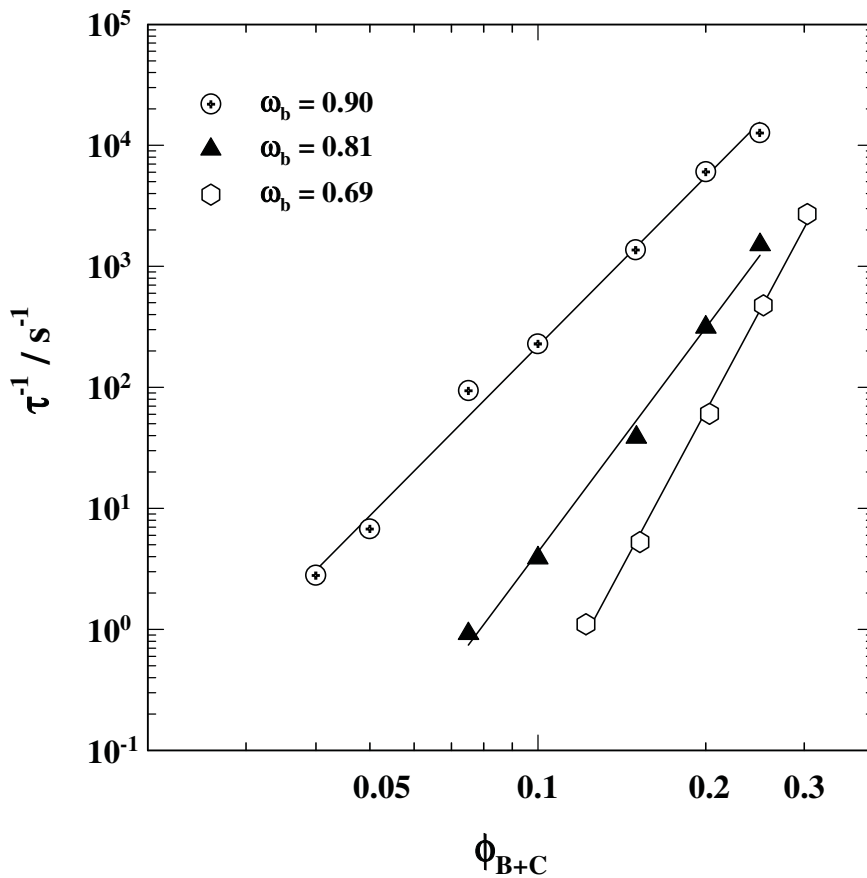
Fig. 4.12: Double logarithmic plot of the relaxation time constants τ^{-1} as a function of the bilayer volume fraction ϕ_{B+C} for different surfactant / (oil + surfactant) volume fractions ω_b = 0.90, 0.81 and 0.69.

Plotting the data for each constant value of ω_b results in a set of straight lines. The chosen representation illustrates the strong ϕ_{B+C}-dependence of τ^{-1}, which can be expressed in terms of an effective power law:

$$\tau^{-1} \propto \phi_{B+C}^{n} \tag{4.5}$$

with n = 4.7, 6.2 and 8.6 for ω_b = 0.90, 0.81 and 0.69 respectively. The most pronounced dependence is observed for ω_b = 0.69 where a change in the bilayer volume fraction ϕ_{B+C} by a factor of 3, from ϕ_{B+C} = 0.1 to 0.3, causes an enormous reduction of the relaxation time τ from 1 s to less than 400 µs, i.e. a change of four orders of magnitude. For the higher values of ω_b this effect is less prominent, but still results in very high reductions of the relaxation times as a function of ϕ_{B+C}. These results seem to indicate that for a further decrease of ω_b, which equals more oil in the mixture, the power law factor n for the strong ϕ_{B+C}-dependence of τ^{-1} is increasing. However, the opposite is observed with decreasing ω_b, the following diagram, Fig. 4.13 can be deduced from experimental data.
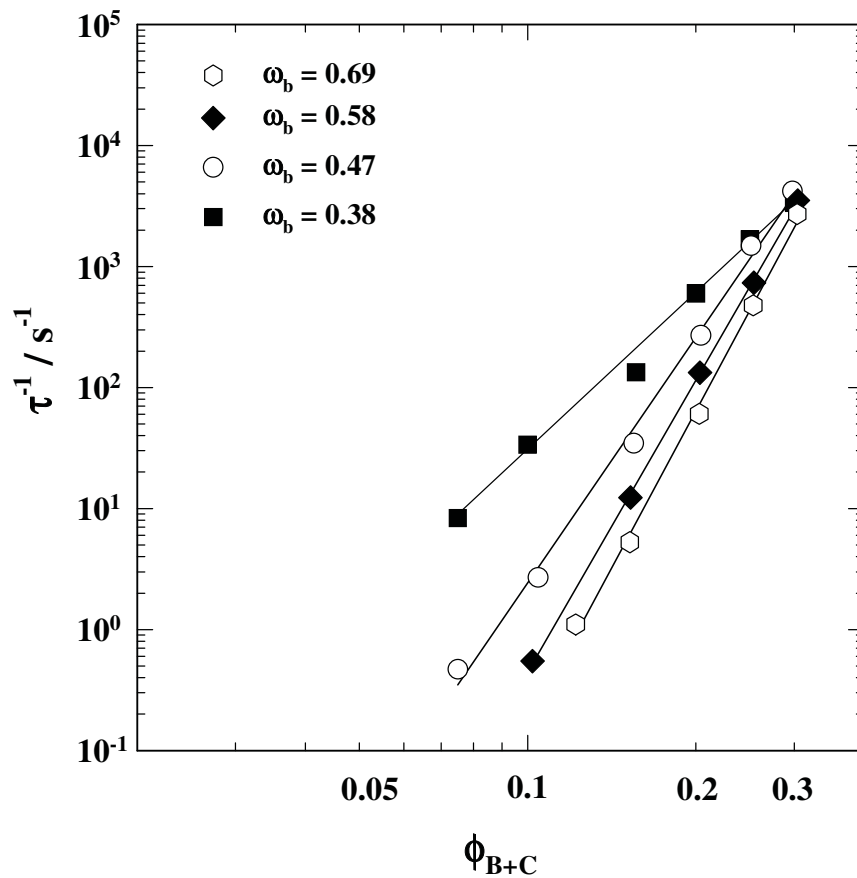
Fig. 4.13: Double logarithmic plot of the relaxation time constants τ^{-1} as a function of the bilayer volume fraction ϕ_{B+C} for different surfactant / (oil + surfactant) volume fractions ω_b = 0.69, 0.58, 0.47 and 0.37.

Again, all of the plots in Fig. 4.13 show strong dependencies of τ^{-1} on ϕ_{B+C}, with n = 8.6, 8.0, 6.7 and 4.3 (see Eq. (4.4)) for ω_b = 0.69, 0.58, 0.47 and 0.37 respectively. However, it is noteworthy that still the plot for constant ω_b = 0.69 shows the strongest ϕ_{B+C}-dependence of τ^{-1}. This means that the ϕ_{B+C}-dependence of τ^{-1} runs through a minimum for varying values of ω_b.

These enormously strong dependencies did not come as a complete surprise since they were seen before by SCHWARZ et al. [28] for the pseudo-binary system water – $C_{10}E_4$ – $C_{10}E_0$ and by UHRMEISTER [27] for the system water – n-decane – $C_{12}E_5$. What certainly came as a surprise was the fact that the ϕ^n-dependencies of τ^{-1} changed so considerably with ω_b. However, even for the highest and lowest experimentally accessible values of ω_b, where the ϕ^n-dependencies of τ^{-1} are less pronounced, the literature predictions for non-swollen bilayers with $n = 3 - 4$ [22, 24] were not reached. On the other hand, in view of the presented results, for $\omega_b = 1$, i.e. the non-swollen bilayer system, it might be reasonable to estimate a ϕ^3-dependence of the relaxation time constants.

Dependence of the relaxation time constants on the surfactant / (oil + surfactant) volume fraction ω_b

According to the information gathered from the ϕ_{B+C}-dependence of τ^{-1}, a plot of the relaxation time constants τ^{-1} as a function of ω_b at constant bilayer volume fraction ϕ_{B+C} seems useful to elucidate the above mentioned relationships between the relaxation times and the surfactant / (oil + surfactant) volume fractions. The ω_b-dependence of τ^{-1} is represented in Fig. 4.14.
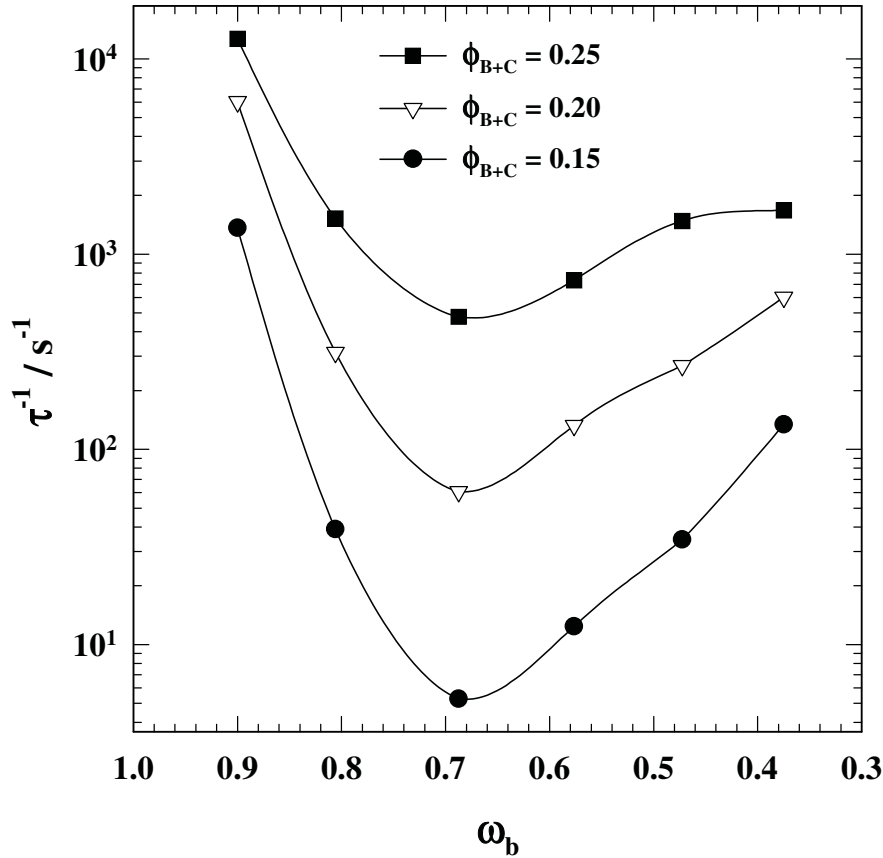
Fig. 4.14: Double logarithmic plot of the relaxation time constants τ^{-1} as a function of the surfactant / (oil + surfactant) volume fraction ω_b for different bilayer volume fractions $\phi_{B+C} = 0.25$, 0.20, and 0.15.

The curves of the relaxation time constants τ^{-1} as a function of the surfactant / (oil + surfactant) volume fraction ω_b show a minimum for all values of constant ϕ_{B+C}. This minimum is to be found around the value of $\omega_b = 0.69$ for each curve. In relation to each other, the curve for the lowest constant value of ϕ_{B+C} shows the most distinct minimum in the relaxation time constants τ^{-1}, i.e. here the slowest relaxation processes can be observed. So, obviously the variation of the surfactant / (oil + surfactant) volume fraction ω_b has a more dramatic influence on the relaxation times in the L_3 phase for lower values of ϕ_{B+C}. For the higher values of ϕ_{B+C} the curves still show a minimum in $\omega_b = 0.69$, however this becomes less pronounced with increased values of the bilayer volume fraction.

4.3 Isothermal shear

When describing the temperature jump method above the so-called cooling time τ_C was defined as the time it takes for the sample to reach the initial temperature T_0 again after a temperature jump. This process is due to heat exchange with the surrounding cell. The corresponding time to this process was mentioned to be almost constant with $\tau_C = 18$ (± 2) s.

For the determination of relaxation times of less than seconds the exact value of the cooling time τ_C is of minor importance. However, for processes governed by relaxation times of more than seconds, this cooling time τ_C reaches major importance. Since now a cooling process reducing the intensity of the scattered light is superimposing the slowly rising signal induced by the temperature jump. An exact definition of the desired τ becomes unachievable for relaxation times of $\tau > 1 - 2s$. Given that the cooling time τ_C is constant due to the setup of the temperature jump apparatus, it sets the upper limit of relaxation times τ to obtain with this particular perturbation method to $1 - 2$ seconds. However, considering the strong ϕ_{B+C}-dependence of the relaxation time constants τ^{-1} (see Fig. 4.12 and Fig. 4.13), relaxation times of more then seconds are expected for bilayer volume fractions ϕ_{B+C} of less then 0.1. Consequently to be able to measure relaxation times of more then seconds, another perturbation method has to be applied.

There was no method available taking into account the unique experimental limits dictated by the phase behavior of the L_3 phase on the one hand, and on the other hand providing a chance to measure relaxation times τ longer than 2 seconds.

In the end a new, yet simple, setup was employed, which was inspired by the L_3 phase's unique feature of showing birefringence under shear. The L_3 phase shows very distinctive shear birefringence when viewed in a thermostatted test tube under crossed polarizers for any bilayer volume fraction. For higher ϕ_{B+C} this birefringence disappears immediately when the stirrer is stopped. However, at very low ϕ_{B+C} a slow vanishing of the birefringence can be observed, given rise to the assumption that the process observed here is actually a structure relaxation after a perturbation by shear. To measure the time of this process the obvious would be to employ an optical detection method. Unfortunately no optical methods like dynamic light scattering or UV-VIS spectrometry were available to apply shear to the sample in question. Therefore another detection method that has proven successful, e.g. for pressure jump perturbation techniques [28], has been applied. The conductivity in a thermostatted sample cell (see chapter 8) is measured as a function of time after shear was applied to the sample. Thus the reestablishment of the disrupted microstructure is monitored, yielding the structural relaxation time τ of the sample.

Unlike the temperature jump technique, which is a perturbation method changing an intensive thermodynamical parameter of the sample rapidly, this technique works at a certain well controlled temperature and achieves the change of the sample's equilibrium by mechanical perturbation. Accordingly this new technique was named 'isothermal shear'.

4.3.1   Results

To extend the knowledge already gathered about the dynamics of L_3 phases by temperature jump measurements, isothermal shear experiments are performed for very low bilayer volume fractions ϕ_{B+C} at different constant surfactant / (oil + surfactant) volume fractions ω_b. Again all experiments are carried out inside the temperature range of the stable L_3 phase, but in contrast to the *T*-jump where $T_u^{L_3}$ serves as the reference temperature for all samples the common reference now is the mean L_3 temperature, which is defined by $(T_u^{L_3} - T_l^{L_3}) / 2$ for the given ϕ_{B+C}. The perturbation is induced through shear applied by stirring at constant frequency. The reequilibration of the microstructure after shear can be observed by monitoring the conductivity κ_S in the sample cell. A single exponential decay function is sufficient to characterize the change in conductivity by

$$\kappa_S(t) = \kappa_S(t_0) + \Delta\kappa_S \cdot \exp\left(-\frac{t-t_0}{\tau}\right) \qquad (4.6)$$

with $\kappa_S(t_0)$ being the conductivity at t_0, i.e. the moment the stirring stops and the measurement begins, and τ the relaxation time of the L_3 phase. The value of $\kappa_S(t_0)$ is the very first value of conductivity measured immediately after the shear was stopped (t_0) and therefore does not carry any information concerning the relaxation process but simply serves as a fit parameter marking the start of the measurement. This is in contrast to the value of I_0 in the *T*-jump experiments, which is indeed the light scattering intensity of the sample before any perturbation occurred, and the value the system returns to after the cooling time period. Fig. 4.15 shows a typical relaxation curve obtained in an isothermal shear experiment.
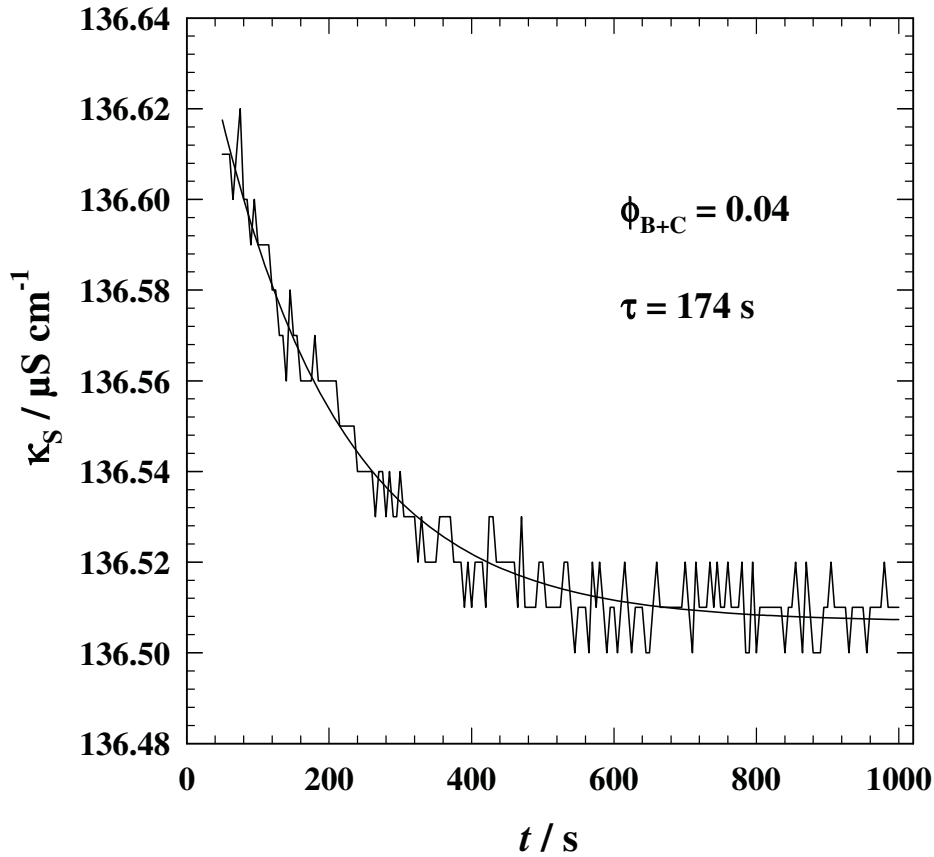
Fig. 4.15: A typical analysis of an isothermal shear experiment for a sample with $\phi_{B+C} = 0.04$ and $\omega_b = 0.69$. With given values for $\kappa_S(t_0)$ and t_0 the amplitude $\Delta\kappa_S$ and the relaxation time τ can be obtained from nonlinear regression (Eq. (4.6)).

The relaxation process for the isothermal shear method is characterized by the relaxation time τ and the amplitude $\Delta\kappa_S$. This is in agreement with *T*-jump experiments where the relaxation process also shows two characterizing variables, the relaxation time τ and the amplitude $\Delta I_S / I_0$. For this method $\Delta\kappa_S$ is rather a function of the shear rate (see below) than of the L_3 phase dynamics. This is in close analogy to the *T*-jump method where $\Delta I_S / I_0$ is a function of ΔT and not of the kinetics of the L_3 phase. $\Delta\kappa_S$ will therefore not be discussed further in matters concerning the dynamics. However, the amplitudes are a limitation to this method because they decrease considerably with increasing dilution, i.e. at very low bilayer volume fractions ϕ_{B+C}. One possible reason for this may be the shear-induced sponge-to-lamellar transition of highly diluted lyotropic systems [105]. Shearing of the L_3 phase results in a reversible phase separation to $L_3 + L_\alpha$. According to CATES and MILNER [106] the critical shear rate for this transition is $\langle\dot{\gamma}\rangle_c \propto 1 / d^3$ where d equals the interbilayer distance. Therefore a very high dilution (see chapter 5) or a prolonged shear period will promote the sponge-to-lamellar transition. In order to prevent phase separation in the case of very low

ϕ_{B+C}, i.e. high dilution, the shear period has to be reduced, which accordingly results in a very small amplitude $\Delta\kappa_S$ (see bottom Fig. 4.17).

For experiments with higher values of ϕ_{B+C}, i.e. at bilayer concentrations less susceptible to shear transition, a shear period of two times the relaxation time proved to be most successful. To illustrate the influence of the shear period on the relaxation curves an example for an experiment in the higher bilayer concentration range but for a too prolonged shear period can be seen in Fig. 4.16. Since shear is applied before the measurement actually starts a probable sponge-to-lamellar transition cannot be measured actively. The assumption is that what actually is observed is the reverse transition from the $L_3 + L_\alpha$, which shows much lower conductivities κ_S, back to the L_3 phase.
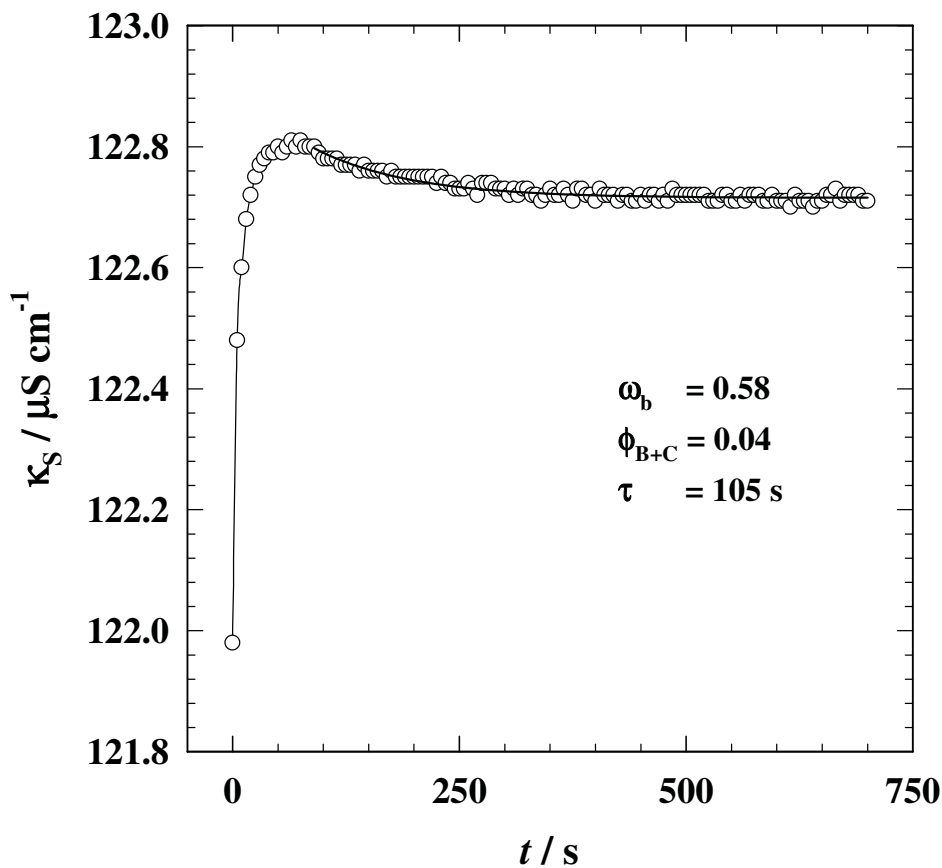
Fig. 4.16: A typical curve for an isothermal shear experiment for a sample exposed to shear for more then two times its relaxation time τ. The very steep increase in the conductivity κ_S at the start of the measurement indicates the reverse phase transition from the L_α phase to the L_3 phase.

Practically, there is no time limit towards long relaxation times τ for this method. Here, the limiting factor is given by the samples. They show a too narrow temperature stability range for this technique at very low concentrations. However, towards higher bilayer volume

fractions ϕ_{B+C} and therefore shorter relaxation times τ there is a time limit caused by the motion of the sample solution in the sample cell even after the stirrer was stopped. As long as the solution surrounding the conductivity electrode is not completely stationary, no defined relaxation times can be determined. The period of motion after the stirrer was stopped was found to be about 25 s, thus defining the lower relaxation time limit of this isothermal shear method.

Dependence of the relaxation time obtained from isothermal shear on the bilayer volume fraction ϕ_{B+C}

For samples at constant values of ω_b the bilayer volume fractions ϕ_{B+C} were varied between 0.07 and 0.03 in steps of 0.01. In Fig. 4.17 an exemplary comparison of isothermal shear experiments at constant temperature of three different compositions ($\phi_{B+C} = 0.06, 0.04, 0.03$) for a constant $\omega_b = 0.69$ is shown.
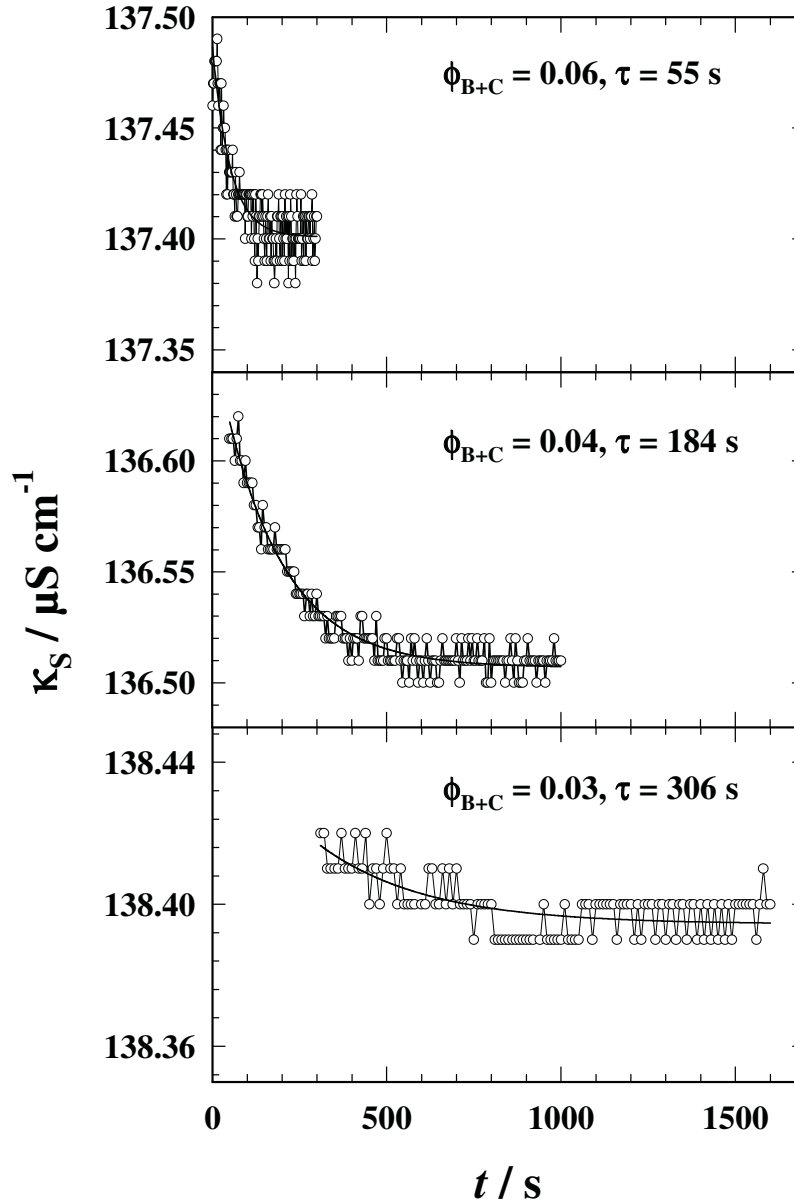
Fig. 4.17: Comparison of the relaxation curves of three different compositions (ϕ_{B+C} = 0.06, 0.04, 0.03) at constant ω_b = 0.69. Isothermal shear experiments were performed at constant L_3 phase mean temperatures ($T_u^{L_3}$ - $T_l^{L_3}$) / 2. The relaxation process becomes slower with decreasing bilayer volume fractions ϕ_{B+C}, but not to the same extent as observed for the high ϕ_{B+C} in Fig. 4.7.

For the highest volume fraction the relaxation time is about 55s, for the medium 183s and almost twice that (306s) for the lowest value of the bilayer volume fraction ϕ_{B+C}. Comparing these results to the ones shown in Fig. 4.7 for much higher ϕ_{B+C} but the same constant ω_b = 0.69, it becomes clear that the ϕ_{B+C}-dependence of the relaxation time τ seems to be less strong for these low values of the bilayer volume fraction ϕ_{B+C}. In the bottom diagram it can be seen that the amplitude $\Delta\kappa_S$ of this shear experiment is greatly reduced in comparison to the curves in the upper two plots. It was explained above (see also Fig. 4.16) that the

amplitudes present a limiting factor to this method when the temperature stability range of the L_3 phase becomes increasingly narrow at very low ϕ_{B+C}.

4.3.2   Discussion

In Fig. 4.18 the resulting relaxation times for very low bilayer volume fractions ϕ_{B+C} at two different surfactant / (oil + surfactant) volume fractions ω_b are shown. The results from isothermal shear experiments are presented as an addition to the ones shown in the diagram in Fig. 4.13 for the temperature jump relaxation measurements.
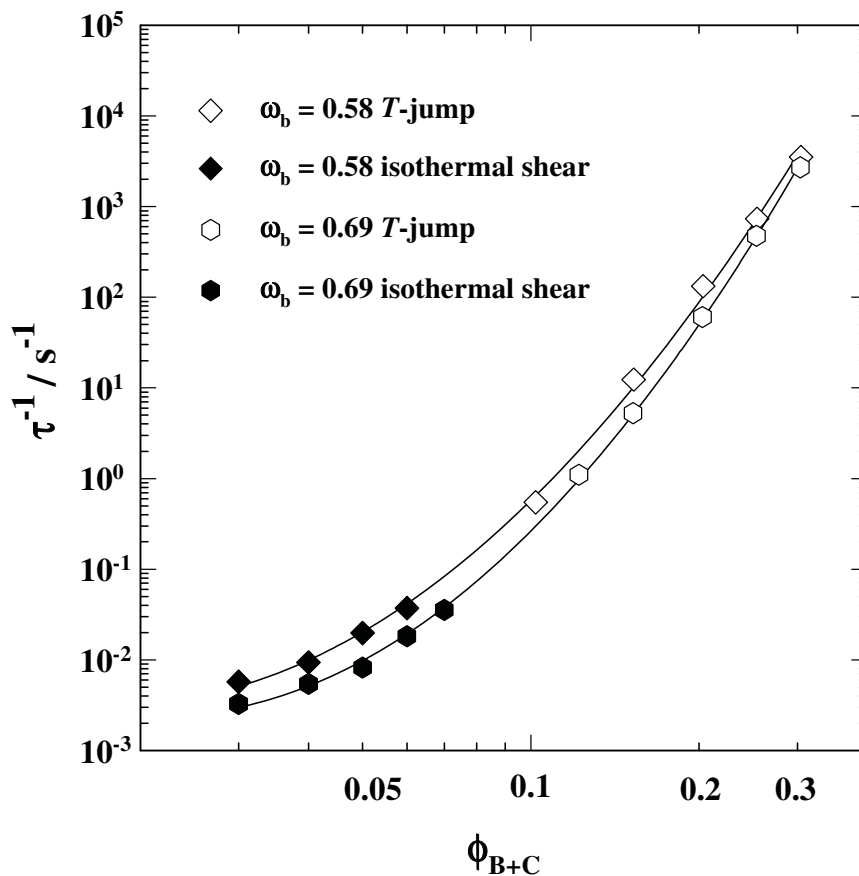
Fig. 4.18: Double logarithmic plot of the relaxation time constants τ^{-1} as a function of the bilayer volume fraction ϕ_{B+C} for surfactant / (oil + surfactant) volume fractions $\omega_b = 0.69$ and 0.58.

The assumption that τ^{-1} depends on ϕ_{B+C} according to the power law $\tau^{-1} \propto \phi_{B+C}^{n}$ with n = const. does not hold for low bilayer volume fractions of ϕ_{B+C}. Instead of straight lines in a double logarithmic plot, curves with non-linear dependencies emerge. In addition, experiments were performed for surfactant / (oil + surfactant) volume fractions $\omega_b = 0.81$ and 0.47 with very low ϕ_{B+C}, but no relaxation times τ could be determined.

Similar results were obtained by WILKE [107], using a temperature jump setup suitable for slow relaxation times. For the system investigated in this study a deviation from the straight lines observed in the "fast" *T*-jump was found at very low ϕ_{B+C}. This is further confirmation to the fact that relaxation times do not depend on the perturbation method used.

As described in chapter 4.3.1 there is no effective upper time limit restricting this isothermal shear method towards very long relaxation times. However, the lower time limit was determined to be 25 s with the consequence that relaxation times of less than 25 s cannot be measured. Thus it is reasonable to assume that the associated relaxation times are less then 25 s. Relaxation times of less than 25 s are also in agreement with the observation that τ^{-1} does not simply depend on ϕ_{B+C} according to the power law $\tau^{-1} \propto \phi^n_{B+C}$. If that were the case the relaxation times would have been accessible by isothermal shear. This leads to the conclusion that the relaxation times of those ω_b at very low ϕ_{B+C} that are not experimentally accessible by isothermal shear should also diverge from linear dependencies. A suitable method to fill this gap of about 25 s has still to be found.

4.4   Summary

Measurements of relaxation times τ with the *T*-jump method, which has an experimental time window of 10^{-4} s to 1.5 s, at higher membrane concentrations ϕ_{B+C} yielded apparently linear dependencies in a double logarithmic plot, i.e. $\tau^{-1} \propto \phi^n_{B+C}$, where *n* is a function of ω_b and takes on values of 4<*n*<9. However extending the experiment's time frame to slower relaxation times at high dilution with the isothermal shear method revealed a behavior where the power law factor *n* is not a constant anymore for constant ω_b (Fig. 4.18). This behavior could be measured for two of the seven different surfactant / (oil + surfactant) volume fractions ω_b (ω_b = 0.58, 0.69). For ω_b > 0.69 and ω_b < 0.58 relaxation times larger than those accessible with the *T*-jump could not be measured. However, this result does not exclude an equally non-linear dependence of τ^{-1} on ϕ^n_{B+C}, i.e. a variable *n*. On the contrary the same general behavior is expected (indicated by the black dotted line in Fig. 4.19 for ω_b = 0.81) with relaxation times between 1.5 s and 25 s, a time window, which is not accessible so far.
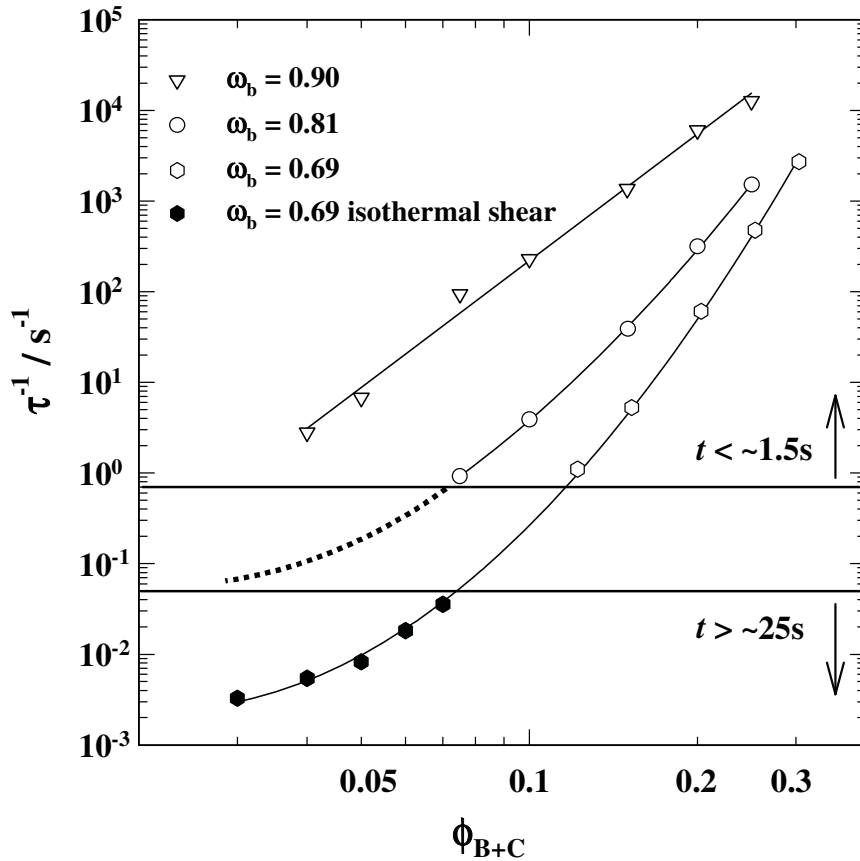
Fig. 4.19: Double logarithmic plot of the relaxation time constants τ^{-1} as a function of the bilayer volume fraction ϕ_{B+C} for surfactant / (oil + surfactant) volume fractions $\omega_b = 0.90$, 0.81 and 0.69.

The dynamics of the L_3 phase have been investigated as a function of the temperature T, as well as the bilayer volume fraction ϕ_{B+C} and the surfactant / (oil + surfactant) volume fraction ω_b. The question is in what way these parameters determine the mechanism of relaxation. It was mentioned above that the relaxation times of the T-jump experiments must refer to structure relaxations on the basis of their q^2-independence. Furthermore the relaxation times of the isothermal shear experiments are certainly structure related, corresponding to the reestablishment of the microstructure after disruption by shear. In order to find a way to explain the dynamics of the L_3 phase generally, the parameters determining the dynamics of the L_3 phase have to be related to its structure. In the next chapter it will be shown how the bilayer volume fraction ϕ_{B+C} and the surfactant / (oil + surfactant) volume fraction ω_b influence the microstructure of the L_3 phase and what conclusions can be drawn from this towards a description of the L_3 phase dynamics.

5 Investigations of the microstructure by SANS

In the previous chapter the dynamics of L_3 phases could be determined quantitatively. It was found that the relaxation times of the L_3 phase structures are crucially dependent on the their composition. The relaxation time constants τ^{-1} vary over four orders of magnitude for only minor increases in the bilayer volume fraction ϕ_{B+C} at constant surfactant / (oil + surfactant) volume fraction ω_b. In addition, with varying ω_b the relaxation time constants run through a minimum if the bilayer volume fraction ϕ_{B+C} is kept constant.

If indeed the relaxation process is conducted mainly by passage formation, as proposed in chapter 3, the underlying microstructure is of critical importance for the L_3 phase dynamics. It is known that the composition of the L_3 phase determines its microstructure. Thus it should be possible to deduce a quantitative correlation between the bilayer volume fraction ϕ_{B+C} and the surfactant / (oil + surfactant) volume fraction ω_b on the one hand and the characteristic lengths of the microstructure on the other hand. Experimentally, the characteristic length scales of the L_3 phase microstructure can be measured by small-angle neutron scattering (SANS). In the following a short review of SANS studies on L_3 phases will be given. Along with this the basic understandings of neutron scattering experiments will be explained before the actual scattering function and results for the L_3 phase structures will be focused on in detail. The relationship between the measured characteristic lengths and the composition will be discussed.

5.1 Basics

The microstructure of the L_3 phase was found to be that of a multiply connected randomly oriented bilayer that divides space into two equivalent water-continuous subvolumes. STREY, WINKLER and MAGID investigated the non-swollen L_3 phase of the binary system water – $C_{12}E_5$ by small-angle neutron scattering [16]. They found that the scattering is characteristic of a locally flat structure with a diffuse interface, which arises from the penetration of solvent molecules. From the scattering curves they obtained the thickness of the bilayers and the effective areas occupied by the surfactant molecules. In a different study, STREY and co-workers [8] investigated the non-swollen L_3 phase bilayers of the system water / NaCl – AOT. It was found that the most frequently occurring film – film distance $\bar{d}$ is approximately the tubular diameter of a passage in the L_3 phase structure and scales as $\bar{d} \propto \phi_C^{-1}$ with ϕ_C being the surfactant volume fraction. The results were confirmed by SKOURI et al. [108, 9]. In

addition, they found that the scattering patterns of one given phase at different surfactant concentrations along a dilution line will remain identical when plotted as a function of the reduced wave vector $Q = q \cdot \bar{d}$. This basically means that the dilution acts as a simple dilation on the structure of a given L_3 phase. Hence any characteristic length scales are simply proportional to the inverse surfactant volume fraction, i.e. $\bar{d} \propto \phi_C^{-1}$.

The SANS studies mentioned above dealt with the microstructure of L_3 phases of either non-ionic or ionic surfactant systems. They all had in common that the investigated L_3 phases were those of binary systems, i.e. L_3 phases with a non-swollen bilayer structure. There is only one characteristic length scale varying with the composition, i.e. the surfactant volume fraction, namely the averaged film – film distance or the tubular diameter $\bar{d}$ of the L_3 phase passages. For the ternary system water – *n*-octane – $C_{10}E_4$ studied in this work the oil penetrates into the surfactant bilayer, causing it to swell. Consequently, there is a new characteristic length scale to be considered, the thickness of the oil-swollen L_3 phase bilayer.
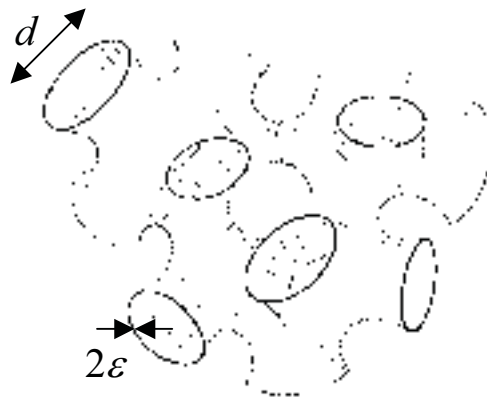
Fig. 5.1: Schematic illustration of the characteristic length scales of the L_3 phase structure with the midplane distance *d* and the bilayer thickness 2ε.

The two characteristic length scales determining the L_3 phase microstructure of ternary systems are shown schematically in Fig. 5.1. The first is the distance between the respective midplanes of two bilayers, the so-called midplane distance *d*. Qualitatively the midplane distance *d* ought to be proportional to the inverse surfactant volume fraction ϕ_C, i.e. $d \propto \phi_C^{-1}$ [9, 108, 8] as long as the surfactant / (oil + surfactant) volume fraction ω_b is kept constant. The second is the bilayer thickness 2ε, comprising the surfactant hydrocarbon-tails and the apolar solvent swelling the bilayer. Under the assumption that all the oil penetrates into the bilayer, the bilayer thickness 2ε ought to be directly proportional to the oil content, i.e. being inversely proportional to the surfactant / (oil + surfactant) volume fraction ω_b, or $2\varepsilon \propto \omega_b^{-1}$.

5.2 Small-angle neutron scattering (SANS)

Light and neutron scattering are well-established methods to investigate the structure of complex fluids [76, 10, 16]. The required contrast is given by the differences in the refractive index or the scattering length densities ρ, respectively. Scattering occurs when the length scales of the studied structures are similar to the applied wavelength λ. As the structures of self-assembled surfactant systems like micelles, bicontinuous microemulsions or L_α and L_3 phases are noticeably smaller then the wavelength of light, they scatter visible light weakly. In contrast to this, with neutrons very small structures can be investigated as the wavelength of neutrons is $\lambda = 6$ Å. In order to extend the range of measurable length scales, neutron scattering experiments are performed at small scattering angles θ, such that the range of the scattering vector q is usually $0.001 < q < 1$ Å^{-1}, where

$$q = \frac{4\pi}{\lambda} \sin \frac{\theta}{2} \qquad (5.1)$$

and θ is the scattering angle. The BRAGG relation $\lambda = 2d \sin (\theta / 2)$ and Eq. (5.1) combine to $q = 2 \pi / d$. Consequently particles or structures with a length scale of $6 < d < 6000$ Å can be determined by SANS.

The scattering intensity I in SANS experiments is measured as a function of the scattering vector q, where $I \propto < \Delta\rho >^2$. The scattering length density ρ of a component can be calculated by means of the characteristic scattering lengths b of the atoms to be:

$$\rho = \sum_i b_i \frac{\rho^m \cdot N_A}{M_w} \qquad (5.2)$$

with AVOGADRO's number N_A, and M_w the molecular weight and ρ^m the macroscopic density of the component. One of the most useful features of the small-angle neutron scattering lies in the diverse scattering behavior of various isotopes, which have different scattering length densities ρ. This effect is especially pronounced in the case of protons (H) and deuterons (D). It forms the basis for a range of experiments where different protonated and deuterated substances can be used to generate different contrasts, so-called contrast variation experiments. The appropriate contrast variations to investigate the structure of the L_3 phase

are bulk contrast for the determination of the midplane distance *d*, and the film contrast to measure the thickness of the bilayer 2ε of the L_3 phase microstructure.

Fig. 5.2 shows the scattering length density profiles for the bulk contrast, above, and the film contrast, below. For the bulk contrast just one of the solvent components is deuterated. The difference between the scattering length densities of the two solvents provides for the scattering intensity, i.e. the periodicity of the surfactant bilayers is measured, which is called the midplane distance *d*. For the film contrast deuterated water as well as deuterated oil is used. Similar scattering length densities for the solvent subphases are therefore measured. Hence the periodicity of the surfactant monolayers, which have different scattering length densities ρ from those of the solvents, is detected. As a result the bilayer thickness 2ε and the midplane distance *d* can be determined by film contrast.
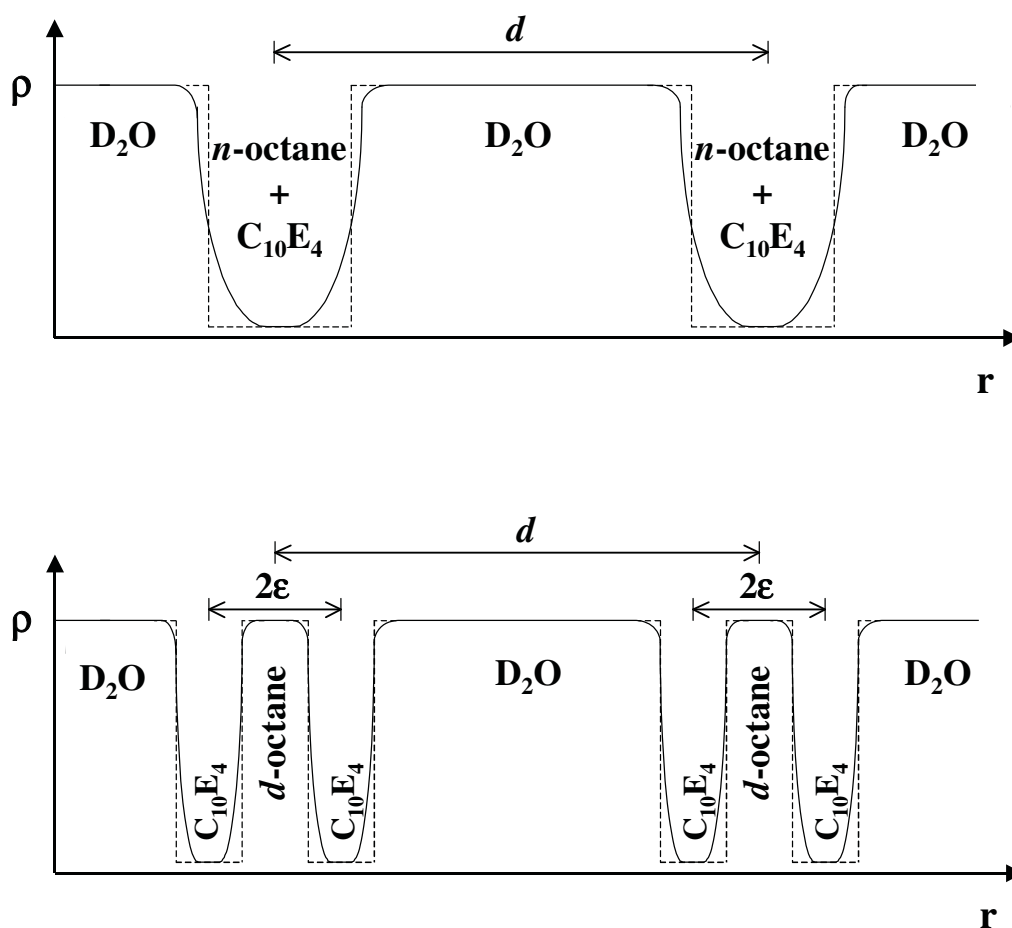
Fig. 5.2: Scattering length density profiles of the bulk (top) and the film contrast (bottom). In the bulk contrast just one (D_2O), in the film contrast both solvents (D_2O and *d*-alkane) are deuterated.

5.2.1 Scattering function for swollen bilayers in film contrast

In order to describe the scattering curves measured for the swollen bilayers, a scattering function based on that for diffuse interfaces for non-swollen bilayers is used. The model is extended to include the distance ε of one of the bilayer forming monolayers from the bilayer midplane. The effect of the polydispersity σ in ε is described by a GAUSSIAN distribution, while the diffuseness of each monolayer, described by the variance *t* of the GAUSSIAN density profile, is kept constant. This scattering density profile ρ (z) varies quite smoothly as indicated in Fig. 5.2. As pointed out by POROD [109], due to the planar symmetry of a locally flat structure, the three-dimensional FOURIER transform of the scattering length density profile is reduced to a one-dimensional cosine transform which gives

$$I(q) = f \cdot \frac{8\pi\phi_{C_i}}{2q^2} \cdot \frac{v_C}{a_C}(\Delta\rho)^2 \cdot e^{-q^2 t^2} \cdot 0.5 \cdot (1 + \cos(2q\varepsilon) \cdot e^{-2\sigma^2 q^2}) + I_{Incoh.} \tag{5.3}$$

where Δρ is the scattering length density difference, I_{incoh} is the incoherent background, *f* is a factor accounting for errors in the absolute calibration and σ / ε is the polydispersity [110].

5.2.2 Results

All in the following described results from SANS experiments were obtained with the D22 spectrometer at the Institute Laue Langevin (ILL) in Grenoble, France and kindly measured by Dr. T. Sottmann, B. Jakobs and P. Uhrmeister. To examine the influence of the L_3 phase composition on the microstructure sets of samples were measured with either bulk contrast or film contrast. For the bulk contrast H_2O in the samples is substituted for D_2O, while the oil component, here *n*-octane, remains protonated. Therefore the scattering length densities ρ of the continuous water subphases and the oil-swollen bilayer are different and the small-angle neutron scattering detects the periodicity *d* of the bilayers. For the film contrast deuterated water as well as oil, i.e. *d*-octane, is used. Thus the scattering length densities for the continuous water subphases and the continuous oil subvolume inside the bilayer are similar so that the periodicity 2ε of the surfactant monolayers is detected in addition to *d*. Note that Δρ between the oil-swollen bilayer and water is higher in bulk than in film contrast experiments, so that *d* is usually measured in bulk contrast. In the spectra *q* (*d*) can be taken from the position of the maximum, while *q* (2ε) has to be fitted with the scattering function introduced in chapter 5.2.1.

On the one hand, samples were prepared with varying surfactant volume fractions ϕ_C at constant ω_b to investigate the periodicity of the bilayers in the L_3 structure, i.e. the midplane distances d. While on the other hand, samples with an ω_b variation at constant ϕ_C were prepared to examine the bilayer thickness 2ε. All samples were characterized in respect to their phase behavior prior to the experiments to establish the stable L_3 phase temperature range. SANS measurements took place at the mean temperature of the stable L_3 phase temperature range for each sample, i.e. at about $(T_u^{L_3} - T_l^{L_3}) / 2$. Additionally the temperature dependence of the microstructure was investigated. A sample with an adequate L_3 phase channel width was chosen to perform SANS measurements at different temperatures inside the stable L_3 phase region.

Dependence of the characteristic length scales on the L_3 phase composition

(a) Variation of ϕ_C at constant ω_b

Scattering experiments in bulk contrast were performed for the system $D_2O - n\text{-}C_8H_{18} - C_{10}E_4$ with four different surfactant volume fractions varying between $\phi_C = 0.080$ and 0.306 at constant $\omega_b = 0.69$. Fig. 5.3 shows the neutron scattering curves obtained from these experiments. The individual curves are multiplied by factors of ten to shift them in respect to each other for transparency. What can be observed is that the position of the maximum, the so-called BRAGG peak, in the low q region of these curves shifts towards higher q values with increasing surfactant volume fractions ϕ_C. As this q value is a measure for the average distance d between the midplanes of two neighboring bilayers the latter can be calculated according to $d = 2\pi / q$ when the q value of the BRAGG peak's maximum is known. The fact that the position of the maximum shifts to higher q values, i.e. to smaller length scales, with increasing ϕ_C, is in agreement with the observations of $d \propto \phi_C^{-1}$ made by STREY and PORTE [8, 9] amongst others. With q values changing between 0.0125 Å^{-1} and 0.0549 Å^{-1} for the variation in the surfactant volume fraction ϕ_C, midplane distances d between 502 Å and 114 Å were obtained from the neutron scattering curves (see chapter 5.2.3 for details).

Fig. 5.3: Neutron scattering curves in bulk contrast of the system $D_2O - n\text{-}C_8H_{18} - C_{10}E_4$ at varying surfactant volume fraction ϕ_C and a constant surfactant / (oil + surfactant) volume fraction $\omega_b = 0.69$.

In Fig. 5.4 neutron scattering curves in film contrast can be seen of the system $D_2O - d\text{-}C_8D_{18} - C_{10}E_4$ for seven different surfactant volume fractions ϕ_C varying between $\phi_C = 0.080$ and 0.306 at a constant $\omega_b = 0.69$. Again the curves are multiplied by factors of ten for clarity. The compositional variations in the L_3 phase are the same as the ones seen in Fig. 5.3 in the bulk contrast. Therefore the positions of BRAGG peaks in the scattering curves in the low q region show the same trend and provide the same quantitative values of d in both contrasts. However for the film contrast there is an additional peak in the high q region, representing the periodicity of the surfactant monolayers and with this the bilayer thickness 2ε of the oil-swollen bilayer. As this peak neither changes its appearance nor its position it represents a constant bilayer thickness 2ε, which could be fitted with the scattering function derived in chapter 5.2.1 to be at a q value of 0.2685 Å^{-1} corresponding to a bilayer thickness 2ε of 23.4 Å.

Fig. 5.4: Neutron scattering curves in film contrast of the system $D_2O – d\text{-}C_8D_{18} – C_{10}E_4$ at varying surfactant volume fraction ϕ_C and a constant surfactant / (oil + surfactant) volume fraction $\omega_b = 0.69$. The solid lines in the high q region illustrate the fit according to the scattering function derived in chapter 5.2.1.

(b) Variation of ω_b at constant ϕ_C

Fig. 5.5 shows the neutron scattering curves for the film contrast of the system $D_2O – n\text{-}C_8D_{18}$ $– C_{10}E_4$ for six surfactant / (oil + surfactant) volume fractions ω_b varying between $\omega_b = 1.00$ and 0.47 and a constant surfactant volume fraction $\phi_C = 0.1$. In accordance with the two previous figures, the curves are shifted by factors of ten to pronounce the variations in the single curves in respect to each other. In contrast to Fig. 5.3 and Fig. 5.4 the BRAGG peak in the low q region of these scattering curves does not change its position, i.e. the midplane distance d is constant. The peaks maximum is positioned at a q value of 0.0167 Å^{-1} relating to a midplane distance d of 376 Å. In the high q region of these curves the scattering peak denoting the bilayer thickness 2ε shifts towards higher q values with increasing surfactant / (oil + surfactant) volume fractions ω_b. By applying the scattering function introduced in

chapter 5.2.1 the peaks in the high q regions of the scattering curves are fitted which is illustrated by the solid lines. Hence, the peak maximum moves from a *q* value of 0.1518 Å^{-1} for ω_b = 0.47 to q = 0.5712 Å^{-1} for ω_b = 1.00. Thus the bilayer thickness is reduced from 2ε = 41.4 Å for ω_b = 0.47 to 2ε = 11.0 Å for ω_b = 1.00. It has to be kept in mind that ω_b = 1.00 represents the binary system D_2O – $C_{10}E_4$, and therefore a non-swollen L_3 phase bilayer. Therefore, 2ε for ω_b = 1.00 represents the length of two surfactant tails of the surfactant $C_{10}E_4$.
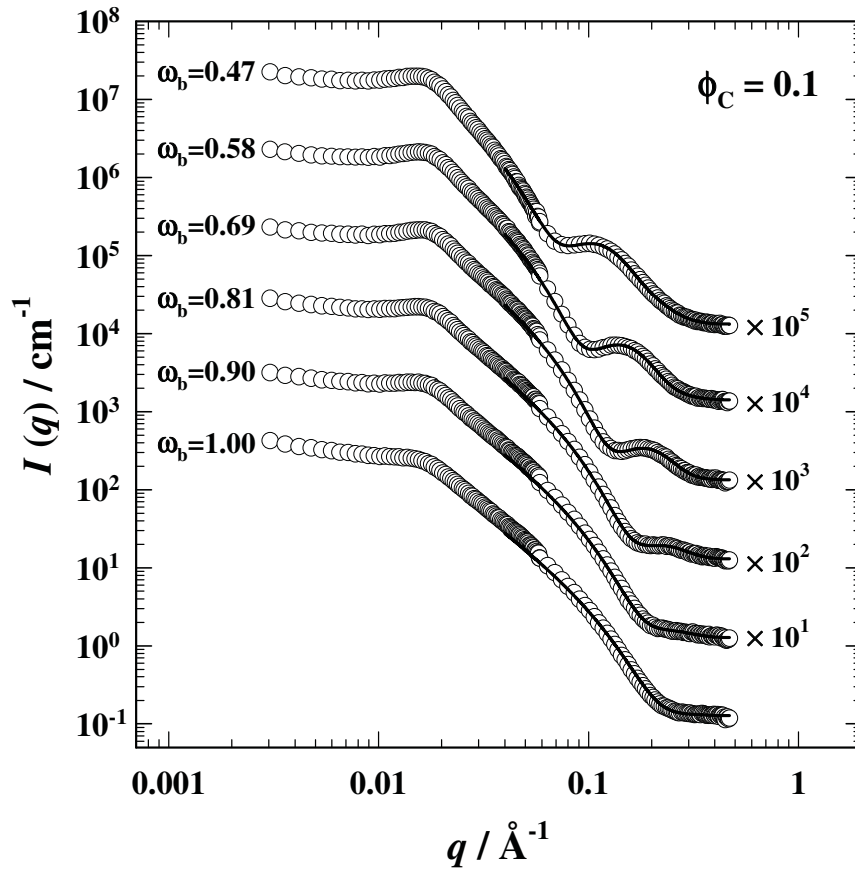
Fig. 5.5: Neutron scattering curves in film contrast of the system D_2O – n-C_8D_{18} – $C_{10}E_4$ at varying surfactant / (oil + surfactant) volume fractions ω_b and constant surfactant volume fraction ϕ_C = 0.1. The solid lines in the high q region illustrate the fit according to the scattering function derived in chapter 5.2.1.

Temperature dependence of the microstructure

To investigate the influence the temperature has on the microstructure, i.e. on the characteristic length scales of the L_3 phase, a film contrast sample of the system D_2O – d-C_8D_{18} – $C_{10}E_4$ with surfactant volume fraction ϕ_C = 0.306 and a surfactant / (oil + surfactant) volume fraction ω_b = 0.69 was chosen. The stable L_3 phase region for this sample extends

from $T_l^{L_3}$ = 38.68 °C to $T_u^{L_3}$ = 41.25 °C. Neutron scattering curves where recorded for five different temperatures inside this temperature interval. The resulting curves are presented in Fig. 5.6. For better comparison the curves are multiplied by factors of three, while the inlet shows the curves in their original form. In the high q region of the curves the peak depicting the periodicity of the surfactant monolayers, i.e. the bilayer thickness can be observed. It does not change its appearance or position with increasing temperature, i.e. the thickness of the bilayer 2ε is not dependent on the temperature of the system. The same holds for the position of the maximum of the curves in the low q region, i.e. the midplane distance d on average does not change with the temperature. In contrast to this, however, the scattering intensity increases with temperature for very low q values (see inlet of Fig. 5.6), indicating the appearance of structures with greater length scales as a function of temperature. Since the integral over the area beneath the scattering curves is constant for samples of the same composition, the increase in the scattering intensity for very low q values is associated with a decrease of $I(q)$ in the area of the BRAGG peak. In addition the peaks increase in width with increasing temperature. This broadening of the scattering peak for low to medium q values is equal to an increase in the polydispersity of the L_3 microstructure with temperature.
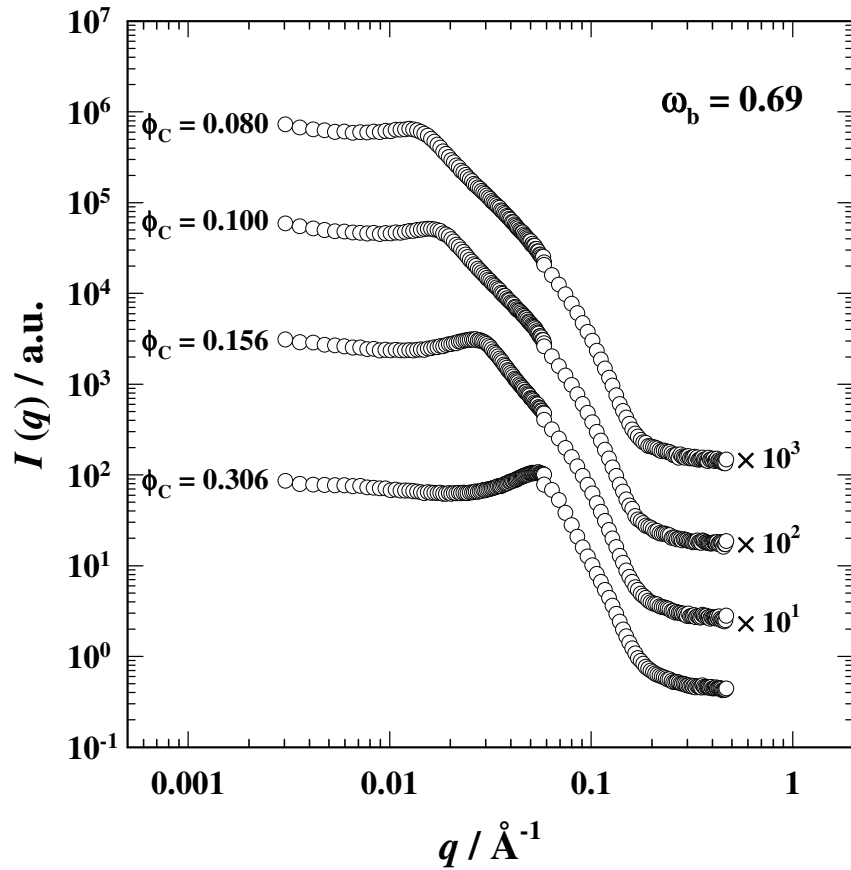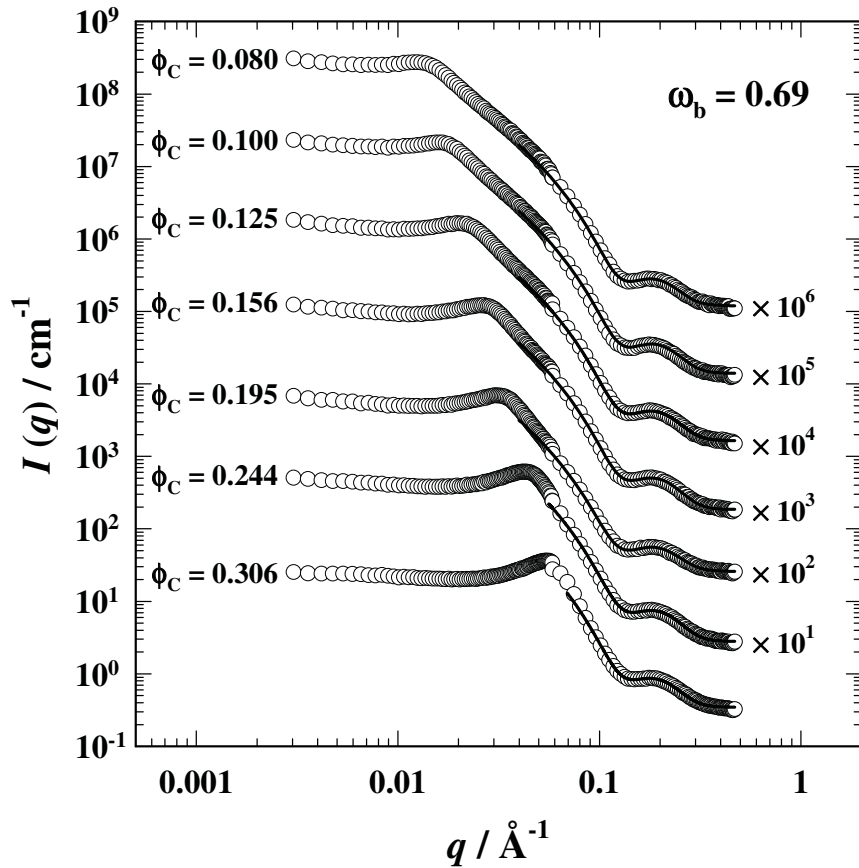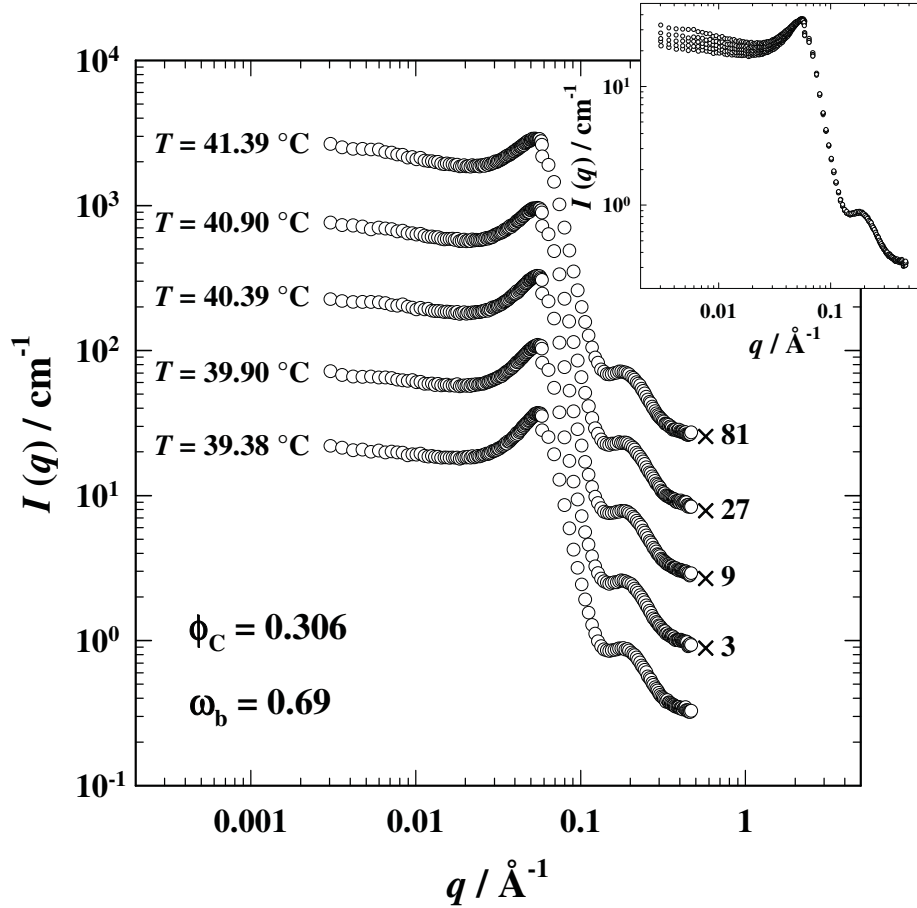
Fig. 5.6: Neutron scattering curves in film contrast of the system $D_2O - n\text{-}C_8D_{18} - C_{10}E_4$ at constant surfactant volume fraction $\phi_C = 0.306$ and constant surfactant / (oil + surfactant) volume fraction $\omega_b = 0.69$. The curves were measured for five different temperatures inside the stable L_3 phase region from $T_l^{L_3} = 38.68$ °C to $T_u^{L_3} = 41.25$ °C. The inlet shows the original scattering curves, while in the main diagram the scattering intensity is shifted by factors of three for transparency.

5.2.3 Discussion

In the following discussion the characteristic L_3 phase length scales determined by SANS experiments in bulk and film contrast will be presented in dependence of the composition of these L_3 phases. The midplane distance d was measured as a function of the surfactant volume fraction ϕ_C in both bulk and film contrast (Fig. 5.7) for a constant ω_b. The bilayer thickness 2ε, however, was examined with varying surfactant / (oil + surfactant) volume fraction ω_b in film contrast (Fig. 5.8) at constant ϕ_C. To establish the quantitative relationship between the characteristic L_3 length scales and its composition geometrical models were developed to fit the measured data. At the end the temperature dependence of the microstructure will be discussed.
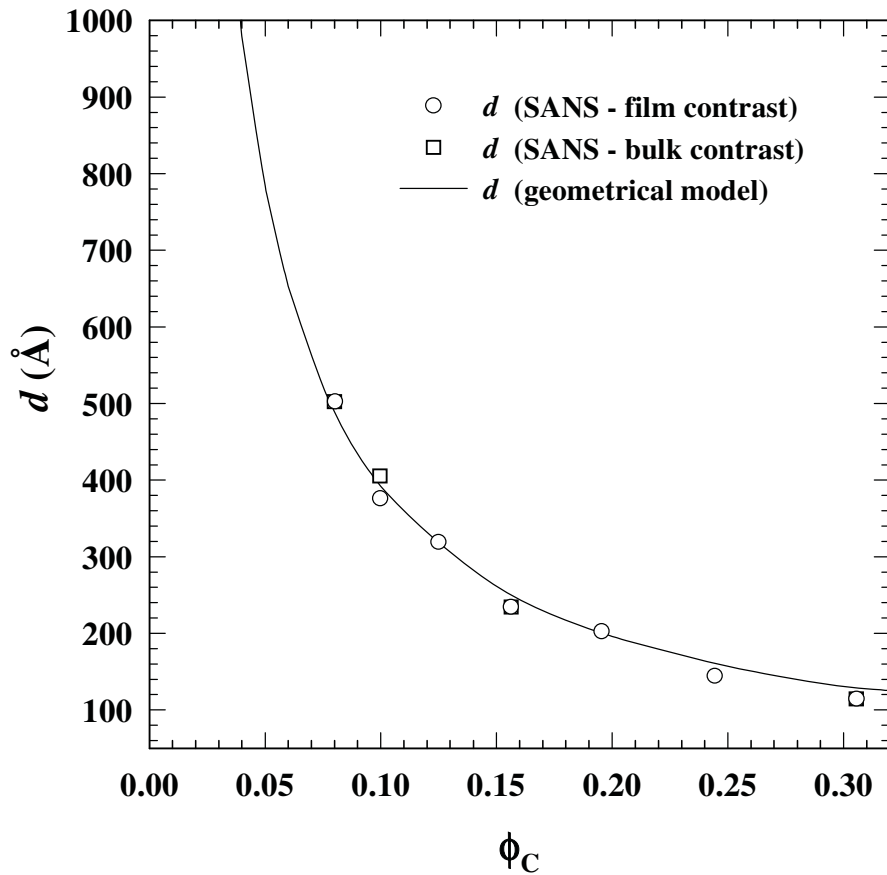
Fig. 5.7: Midplane distance *d* as a function of the surfactant volume fraction ϕ_C measured by SANS in film (circles) and bulk (squares) contrast. The solid line represents data calculated according to the geometric model.

Fig. 5.7 shows that upon addition of surfactant the midplane distance *d* is indeed declining, i.e. it follows the simple law $d \propto \phi_C^{-1}$ on geometrical grounds. The exact dependence of *d* on the surfactant bilayer volume fraction ϕ_C goes back to a model proposed by TALMON and PRAGER [111]. This was later simplified by DE GENNES and TAUPIN [62] who predicted the characteristic length scale ξ of bicontinuous microemulsions

$$\xi = a \frac{\phi(1-\phi)}{(A/V)} \tag{5.4}$$

to be set by the specific internal area $(A / V) = \phi_C \cdot a_C / v_C$, with a_C being the area and v_C being the volume per surfactant molecule, respectively. ϕ is the oil / (water + oil) volume fraction, or more generalized the fraction of the solvents on both sides of the surfactant film, and *a* is a prefactor depending on the model used.

Going from a bicontinuous microemulsion with interfacial monolayers to the L_3 phase bilayer structure, the specific internal area (A / V) turns into

$$\frac{A}{V} = \frac{1}{2} \frac{a_C}{v_C} \cdot \phi_C .$$

(5.5)

Furthermore, since the fraction of water is equal on both sides of the surfactant film, $\phi = 0.5$. With Eq. (5.4) and $\phi = 0.5$ the characteristic length scale ξ of the periodicity of the bilayers in the L_3 phase, i.e. the midplane distance d, can be calculated to be

$$d = 0.5a \frac{v_c}{a_c} \cdot \frac{1}{\phi_C} .$$

(5.6)

With values of $a_C = 52.9$ Å^2 and $v_C = 57.9$ Å^3 for the surfactant $C_{10}E_4$ and a prefactor $a = 7.16$ determined by SANS measurements [55], the data presented as a solid line in Fig. 5.7 were calculated. The data derived from the geometrical model and the experimentally measured data are in very good agreement.
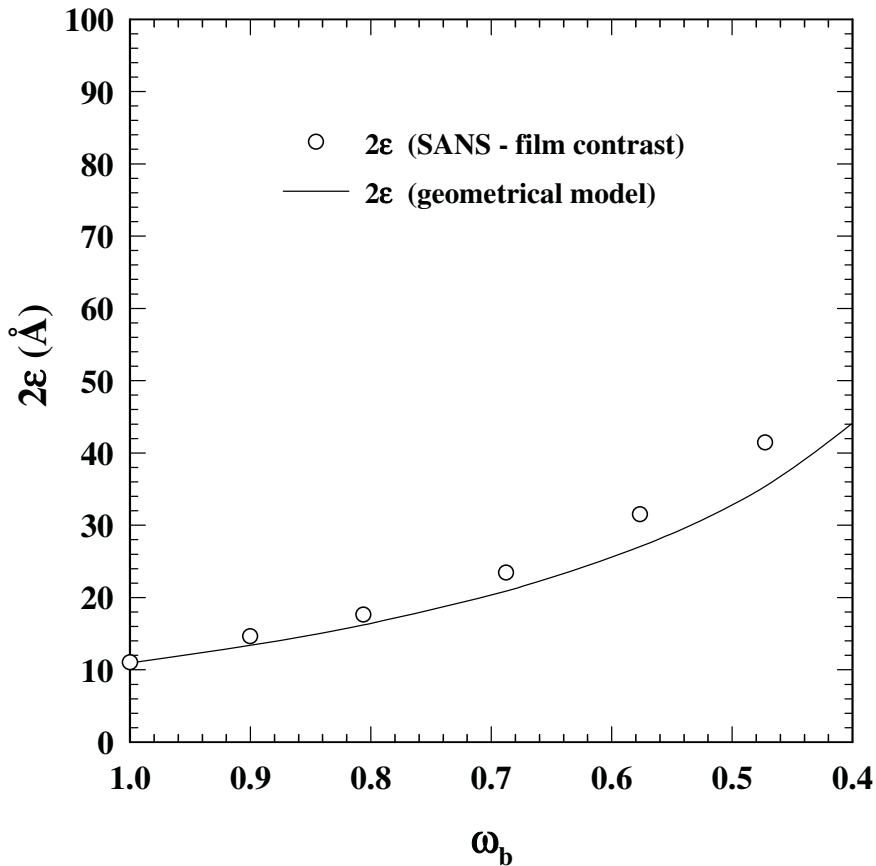
Fig. 5.8: Bilayer thickness 2ε as a function of the surfactant / (oil + surfactant) volume fraction ϕ_{B+C} for SANS experiments in bulk contrast. The solid line represents data calculated according to the geometric model.

Fig. 5.8 presents the values for the bilayer thickness 2ε, i.e. the periodicity of the monolayers assembling the L_3 bilayers, as a function of the surfactant / (oil + surfactant) volume fraction ω_b as measured by SANS in film contrast. The bilayer thickness 2ε is inversely proportional to ω_b, i.e. the bilayer becomes thicker with a higher oil fraction in the system. The quantitative dependence of 2ε on the surfactant / (oil + surfactant) volume fraction ω_b can be explained by purely geometrical considerations. A schematic illustration of the geometrical proportions of an L_3 bilayer is shown in Fig. 5.9.
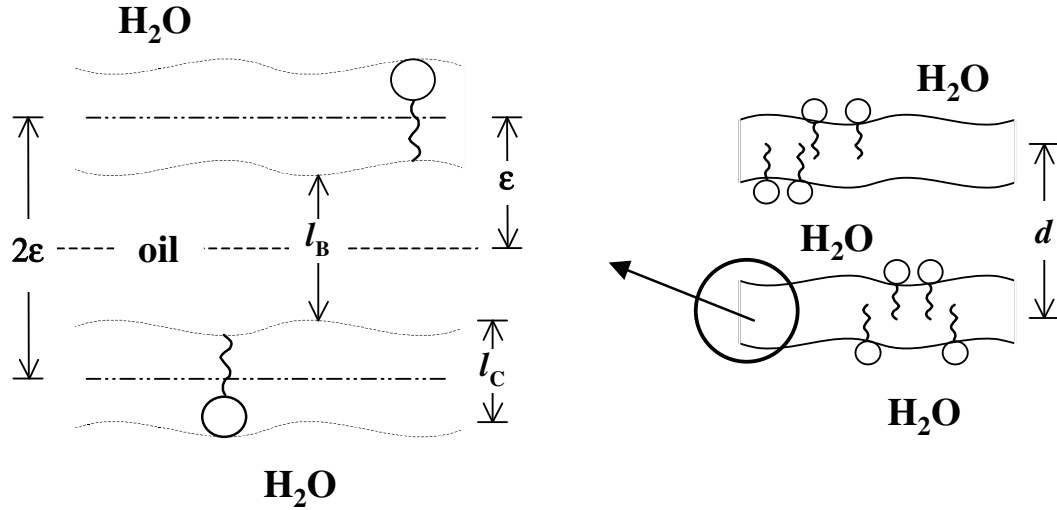
Fig. 5.9: Schematic illustration of the geometrical proportions of an L$_3$ phase bilayer, with l_B being the oil layer thickness and l_C the total length of a surfactant molecule.

The thickness of the oil layer l_B between the two surfactant monolayers can be calculated to be

$$l_B = \frac{V_B}{A} = \frac{\phi_B \cdot V}{A} = \frac{\phi_B}{\dfrac{A}{V}} \tag{5.7}$$

with V_B the volume of oil and (A / V) the specific internal area of the bilayer as defined in Eq. (5.4). Substituting (A / V) by Eq. (5.5) yields

$$l_B = \frac{2\phi_B \cdot v_C}{a_C \cdot \phi_C} \tag{5.8}$$

which for $\phi_B = \phi_{B+C} \cdot (1 - \omega_b)$ and $\phi_C = \phi_{B+C} \cdot \omega_b$ turns into

$$l_B = \frac{2v_C}{a_C} \cdot \frac{1 - \omega_b}{\omega_b} \, . \tag{5.9}$$

Taking into account that $2\epsilon = l_B + l_C$ with the assumption that $l_{C,\text{head}} = l_{C,\text{tail}}$ in $l_C = l_{C,\text{head}} + l_{C,\text{tail}}$ then the bilayer thickness is defined by

$$2\varepsilon = \frac{2v_C}{a_C} \cdot \frac{1 - \omega_b}{\omega_b} + l_C \ . \qquad\qquad (5.10)$$

With values of $a_C = 52.9$ Å^2, $v_C = 57.9$ Å^3 and $l_C = v_C / a_C$ for the surfactant $C_{10}E_4$ the data presented as a solid line in Fig. 5.8 were calculated. The data derived from the geometrical model and the experimentally measured data are in good agreement at low ω_b. The measured data show slightly higher bilayer thickness compared to the calculated ones. An explanation for this small deviation could not be found, yet.

To sum up this chapter it can be said that the dependence of the characteristic length scales d and 2ε on the composition of the model L_3 phase system H_2O – n-octane – $C_{10}E_4$ could be quantified by SANS measurements. Additionally, a geometrical model could be established for the quantitative description of the characteristic length scales in dependence of the surfactant volume fraction ϕ_C and the surfactant / (oil + surfactant) volume fraction ω_b. The nearly quantitative match with the SANS data makes the geometrical model valuable as time-consuming and cost-intensive SANS measurements can be reduced.

The last point that should be discussed is the temperature dependence of the microstructure at fixed composition. It was found that while the composition and hence the midplane distance d remains constant on average, the polydispersity of d increases with temperature. Consequently, the number and scale diversity of the passages of the L_3 structure varies with temperature. This is a very important result for the understanding of the relaxation times τ from T-jump experiments, since it is the first experimental evidence to support the assumption that passage formation takes place during a T-jump experiment. Therefore this result will be the basis for the final discussion following in chapter 6.

6   Discussion

Extensive data material on many properties of L_3 phases, like phase behavior, microstructure and dynamics, has been collected during this work. What is left to do for this chapter is to combine these experimental results to a complete picture of the L_3 phase and compare them to theoretical ideas about the existence and stability of the L_3 phase as known in the literature. The applicability of the theoretical approach introduced in chapter 3 will be discussed taking into account the static as well as the dynamic behavior of the L_3 phase.

6.1   Structure and stability of the L_3 phase

As mentioned in chapter 3.1 it was suggested previously that the lamellar-to-sponge transition occurs when the persistence length ξ_κ becomes of the order of the interbilayer distance d [62]. GOLUBOVIC and MORSE [64, 63] have recently argued that not ξ_κ but the topological persistence length $\xi_{\bar\kappa}$ has to be in the order of d. Thus, melting to a sponge-like phase happens when $d \approx \xi_{\bar\kappa} << \xi_\kappa$, and the number of passages between membranes increases dramatically. It was stated by MORSE [63] that "experiments to examine the effects of various control parameters upon both $\bar\kappa$ and the structural length ξ of either the L_3 or bicontinuous microemulsion phase would provide the best way of further testing these ideas". The experimental results of this work allow a critical test of the theoretical description, and, as will be seen, a confirmation.

First it has to be established that $\xi_{\bar\kappa} << \xi_\kappa$. As shown in chapter 3.1

$$\xi_\kappa = a\exp\left(\frac{4\pi\kappa_{bil}}{3k_BT}\right) \quad \text{and} \quad \xi_{\bar\kappa} = a\exp\left(-\frac{6\pi\bar\kappa_{bil}}{5k_BT}\right) \qquad (6.1, 6.2)$$

where a is a molecular length which is set to the bilayer thickness 2ε. For this system the value of $\kappa_{bil} = 2\kappa_{mono} = 1.96$ k$_B T$ [112, 55]. $\bar\kappa_{bil}$ is calculated following the relation between the saddle-splay modulus of a monolayer and bilayer which has been derived by Porte [9] to be

$$\bar\kappa_{bil} = 2\bar\kappa_{mono} - 4\varepsilon \cdot c_{0,mono}\kappa_{mono}, \qquad (6.3)$$

where the subscript *bil* refers to the bilayer, and *mono* to the monolayer quantities, respectively and c_0 is the spontaneous curvature of the monolayer.

All quantities to calculate $\overline{\kappa}_{bil}$ are known from experiments. The bilayer thickness 2ε is determined by SANS measurements on the L_3 phase in film contrast (see chapter 5). The value of $\overline{\kappa}_{mono} = -0.37$ $k_B T$ was also taken from [55]. The spontaneous curvature of the L_3 phase monolayers varies linearly with temperature so that $c_{0,mono} = <H> = c\,(\overline{T} - T)$ (see chapter 3), with the temperature coefficient $c = 0.0014$ (1/ Å K) [55], and the mean temperature of the three-phase body $\overline{T} = 24.74$ °C for the system water – *n*-octane – $C_{10}E_4$; $T = T_l^{L_3}$, the lower L_3 phase boundary temperature. In Fig. 6.1 the values for $\overline{\kappa}_{bil}$ calculated from Eq. (6.3) are illustrated as a function of ω_b for a constant $\phi_C = 0.10$.
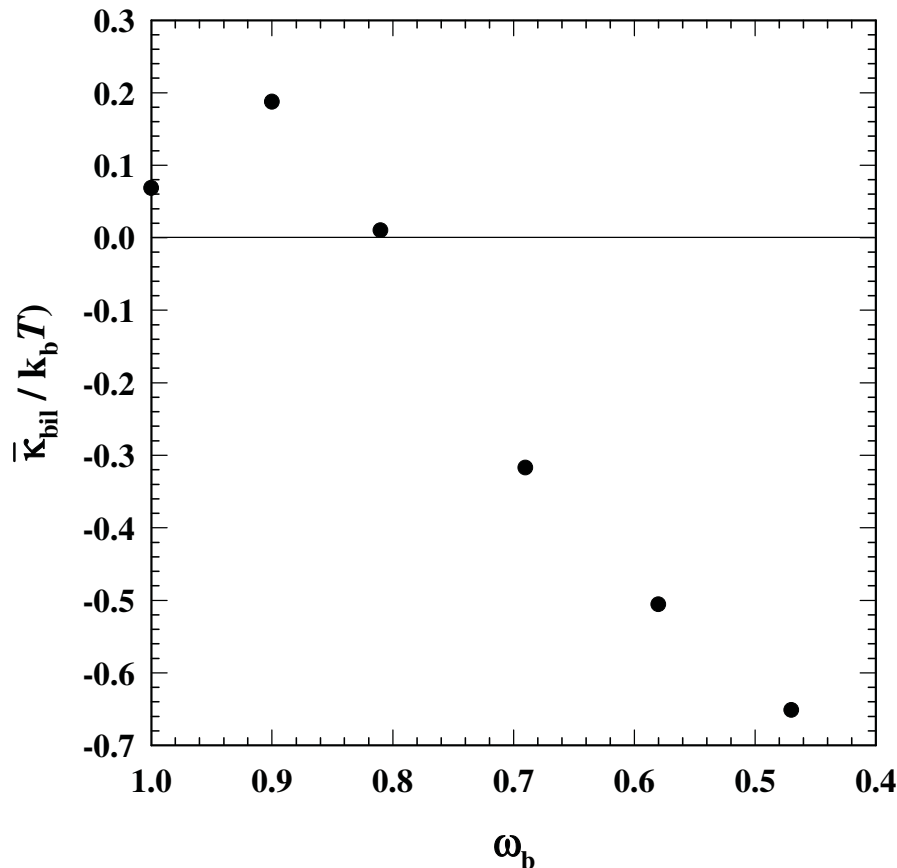
Fig. 6.1: $\overline{\kappa}_{bil}$ as a function of the surfactant / (oil + surfactant) volume fraction ω_b. The values of $\overline{\kappa}_{bil}$ are decreasing with decreasing ω_b and become negative for values of $\omega_b < 0.8$.

As one can see the saddle-splay modulus of the bilayer, $\overline{\kappa}_{bil}$ calculated from Eq. (6.3), is decreasing with decreasing ω_b and becomes negative for values of $\omega_b < 0.8$. Having

determined $\bar{\kappa}_{bil}$, now the values for ξ_κ and $\xi_{\bar{\kappa}}$ can be calculated, see Table 6.1. To check the stability condition of the L$_3$ phase $\xi_{\bar{\kappa}} \ll \xi_\kappa$ and $d \approx \xi_{\bar{\kappa}}$, in Fig. 6.2 the ratios of $\xi_\kappa / \xi_{\bar{\kappa}}$ and $d/\xi_{\bar{\kappa}}$ are plotted versus the surfactant / (oil + surfactant) volume fraction ω_b, with d determined experimentally by SANS (chapter 5). The two ratios decrease with decreasing ω_b but show a pronounced difference in their average values with $\xi_\kappa / \xi_{\bar{\kappa}}$ being more than two orders of magnitude larger than $d/\xi_{\bar{\kappa}}$.
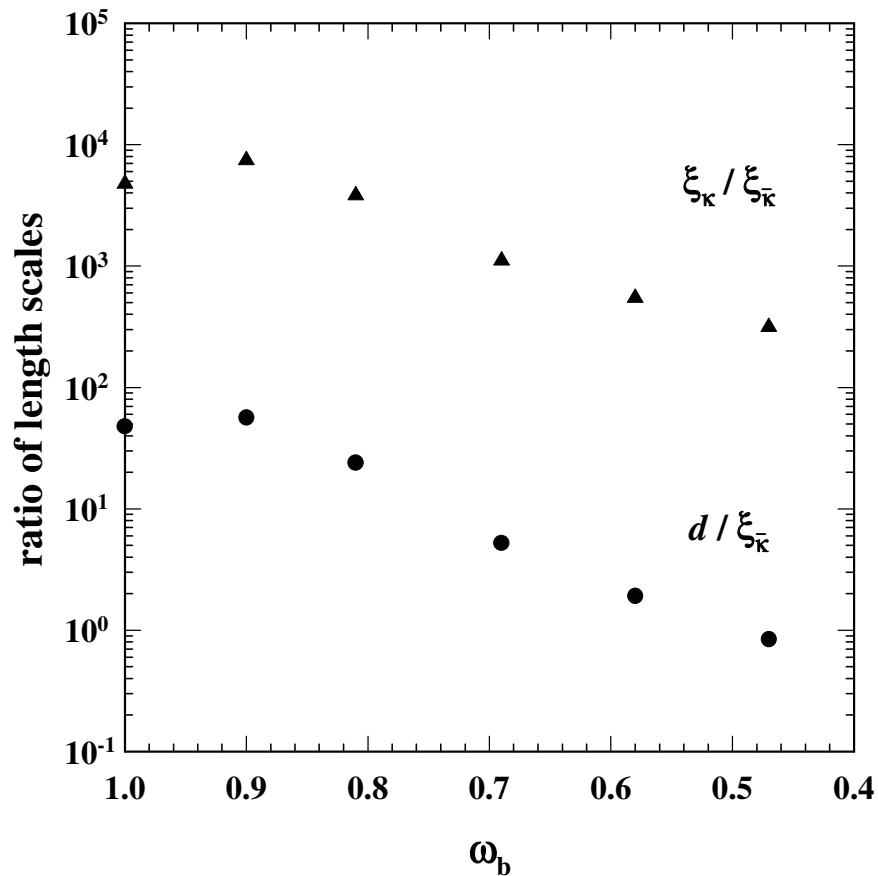
Fig. 6.2: Ratio of the length scales $\xi_\kappa / \xi_{\bar{\kappa}}$ and $d / \xi_{\bar{\kappa}}$ as a function of the surfactant / (oil + surfactant) volume fraction ω_b. $\xi_\kappa / \xi_{\bar{\kappa}}$ is considerably larger than $d / \xi_{\bar{\kappa}}$.

Table 6.1: Surfactant / (oil + surfactant) volume fraction ω_b, lower L_3 phase boundary temperature $T_l^{L_3}$ [°C], the spontaneous curvature of the monolayers c_0 [Å^{-1}], bilayer thickness 2ε [Å], saddle-splay modulus $\overline{\kappa}_{bil}$ [k$_B$T], the persistence length ξ_κ [Å] and the topological persistence length $\xi_{\overline{\kappa}}$ [Å]. Values are calculated with $\kappa_{bil} = 1.96$ k$_B$T, $\overline{\kappa}_{mono} = -0.37$ k$_B$T and $a = 2\varepsilon$, at $\phi_C = 0.1 \Rightarrow d = 405$ Å.

ω_b	$T_l^{L_3}$ / °C	c_0 / Å^{-1}	2ε / Å	$\overline{\kappa}_{bil}$ / k$_B$T	ξ_κ / Å	$\xi_{\overline{\kappa}}$ / Å
1.0000	51.5300	-0.375	11.00	0.0686	40451.6317	8.4924
0.9000	47.8900	-0.324	14.60	0.1874	53690.3475	7.2021
0.8100	40.2700	-0.217	17.60	0.0100	64722.6107	16.9481
0.6900	31.3200	-0.091	23.40	-0.3175	86051.6528	77.4534
0.5800	27.4500	-0.038	31.50	-0.5058	115838.7634	212.0109
0.4700	25.5200	-0.011	41.40	-0.6514	152245.2319	482.4840

This is the first experimental test of the theoretical ideas by MORSE and GOLUBOVIC. It is indeed true that $d \approx \xi_{\overline{\kappa}} << \xi_\kappa$ for the sponge-to-lamellar transition.

Furthermore by calculating the values of $\overline{\kappa}_{bil}$ as a function of the volume fraction of surfactant ϕ_C, the predicted lamellar-to-sponge transition [63]

$$\ln\left(\frac{\phi_C}{\phi_0}\right) = \frac{6\pi}{5}\left(\frac{\overline{\kappa}}{k_B T}\right) \tag{6.4}$$

can be checked, where ϕ_0 is a constant of order unity. Fig. 6.3 is obtained by plotting the natural logarithm of the surfactant volume fraction ϕ_C as a function of the saddle-splay modulus $\overline{\kappa}_{bil}$ for different surfactant / (oil + surfactant) volume fractions ω_b. Fig. 6.3 is the experimentally determined counterpart to Fig. 3.3 (left), which shows the theoretical lamellar-to-sponge transition obtained by Monte Carlo simulations and the MORSE expression [65, 63]. The diagrams are in good qualitative and quantitative agreement. The slopes of the transition lines all show values close to the theoretically predicted value of $6\pi/5$, as is illustrated by the solid line in Fig. 6.3. This is the first time the lamellar-to-sponge transition line was calculated from experimental data and compared to data obtained from theoretical descriptions or Monte Carlo simulations. With increasing ω_b the lamellar-to-sponge transition lines shift to less negative values of $\overline{\kappa}_{bil}$.
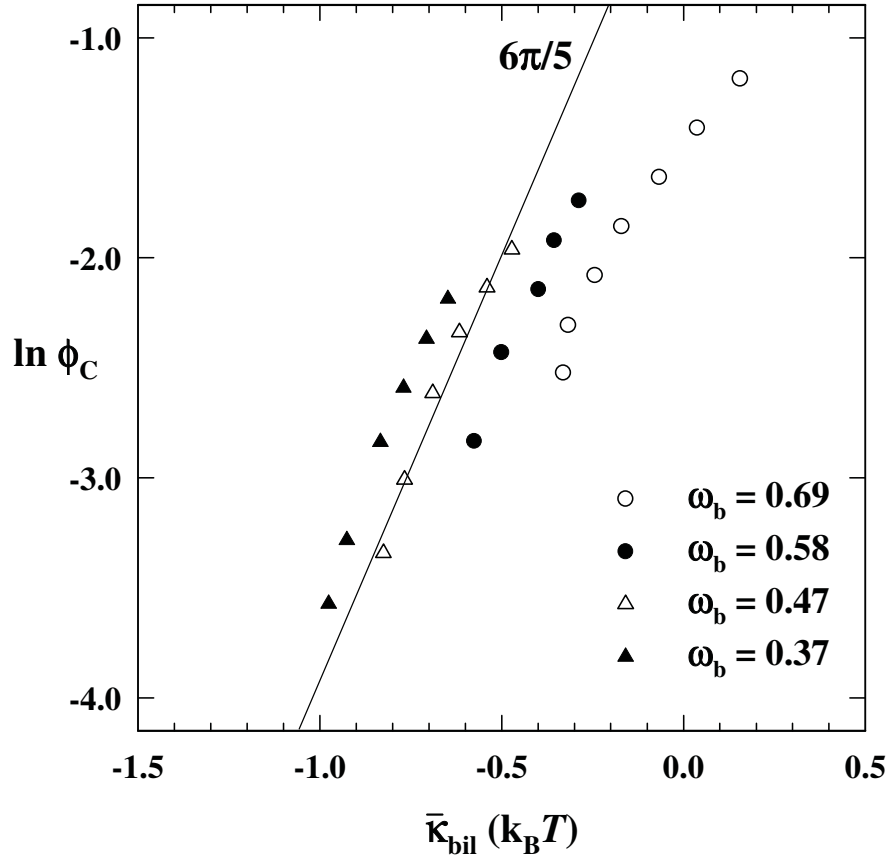
Fig. 6.3: $\overline{\kappa}_{bil}$ as a function of the surfactant volume fraction ϕ_C predicting the lamellar-to-sponge transition at different surfactant / (oil + surfactant) volume fractions ω_b. An illustration of the predicted slope of $6\pi/5$ is given by the solid line.

Above, $\overline{\kappa}_{bil}$ was determined as a function of the surfactant volume fraction ϕ_C. To find, now, $\xi_{\overline{\kappa}}$ as a function of ϕ_C for constant values of ω_b, Eq. (6.3) is employed again. The results are plotted together with the midplane distance d (as measured by SANS) in dependence of the surfactant volume fraction ϕ_C. Fig. 6.4 shows diagrams for four different values of ω_b to illustrate the relative magnitudes of $\xi_{\overline{\kappa}}$ and d. All diagrams have in common that they show two almost parallel straight lines for d and $\xi_{\overline{\kappa}}$ as a function of ϕ_C. However for the highest values of $\omega_b = 0.69$ these parallel lines are far apart with the midplane distance d larger than the topological persistence length $\xi_{\overline{\kappa}}$. For decreasing values of ω_b these lines approach each other until at $\omega_b = 0.47$ they meet and for $\omega_b = 0.37$ the line of the topological persistence length $\xi_{\overline{\kappa}}$ is even at higher values than the midplane distance d. Crudely speaking, the structure and stability is more fluctuation-dominated for $\omega_b > 0.58$ and dominated by strong curvatures for $\omega_b < 0.58$.
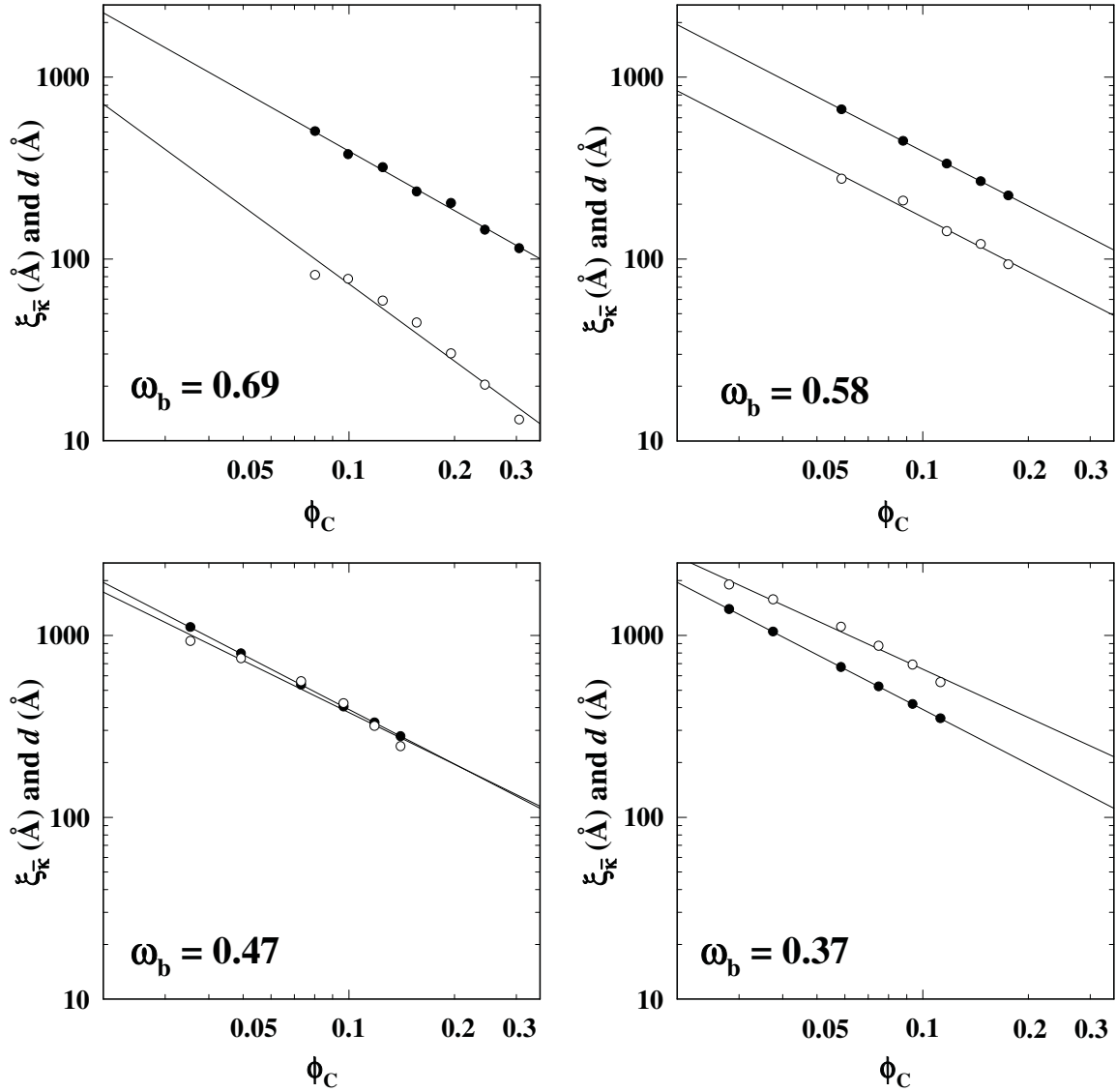
Fig. 6.4: Topological persistence length $\xi_{\bar{\kappa}}$ (hollow circles) and midplane distance d (filled circles) as a function of ϕ_C for constant value of ω_b.

6.2   Dynamics of the L₃ phase

After discussing the structure and stability of the L₃ phase, now the dynamic behavior will be elucidated. As mentioned before, only a couple of papers about the dynamic behavior exist. The first theoretical analysis of the dynamical behavior of the L₃ phase was provided by MILNER, CATES and ROUX [113]. They suggested the existence of two relevant time scales: τ_ψ, the leakage time of the solvent across the bilayer, if pores exist in the membrane (with $\tau_\psi = \infty$ for microemulsions); and τ_h the relaxation time for the topology, associated with the creation and destruction of passages between the membranes. Furthermore, they pointed out that τ_h should obey an ARRHENIUS-type law $\tau_h \approx \tau_0 \exp(E/k_BT)$, where E denotes the

energy necessary to activate the process. MILLER at al. [21] performed electric birefringence measurements in the L_3 phase of a system composed of water, a zwitterionic surfactant and a long-chain alcohol as cosurfactant. They measured relaxation times to go as $\tau^{-1} \approx \phi^3$, where ϕ is the volume fraction of the bilayer. They also provided a rough theoretical explanation of these results, based on the orientational relaxation of disk-like aggregates that led to $\tau^{-1} \approx \phi^3$. It is, however, difficult to accept that this theoretical description, based on the rotation of undeformable bodies in a viscous medium can be the correct explanation of the observed phenomena. Based on the dilatation invariance argument PORTE et al. [22] predicted that in an L_3 phase the relaxation time of the electric birefringence should go as $\tau_R^{-1} \approx \phi^3$. They performed electric birefringence measurements in a betain system, and measured the relaxation times of the Kerr effect to go according to their prediction. Again following MILNER, CATES and ROUX [113], it was observed that while τ_R should correspond to structural changes keeping the topology constant, for longer times it is plausible to assume that topological changes occur. WATON and PORTE [24] claimed to have found experimental evidence for three distinct relaxation times in temperature-jump experiments performed in the system brine – cetylpyridiniumchloride – *n*-hexanol. On theoretical grounds, and following a line of reasoning similar to MILNER et al. they predicted the existence of different relaxation processes and therefore different relaxation times: The ϕ dependencies of the three different τ were checked on two samples respectively and found to scale as ϕ^{-3} and ϕ^{-4}. Although the experimentally obtained relaxation time constants might qualitatively explain, or at least be associated with the predicted time constants one has to be aware that only a very limited number of data were presented.

Recently, SCHWARZ et al. [28] studied the dynamics of L_3 phases for the non-ionic system H_2O – $C_{10}E_4$ – *n*-decanol. Temperature jump relaxation, pressure jump relaxation, time-resolved electric birefringence, and dynamic light scattering experiments were performed. The observed relaxations were all found to be single exponentials. The time constants τ^{-1} obtained by the different methods vary over several orders of magnitude and reveal strong dependencies on surfactant volume fraction ϕ_C resulting in scaling laws of $\tau^{-1} \propto \phi^n$, with $n = 9$ for temperature and pressure jump relaxation, $n = 3$ for the electric birefringence measurements and $n = 1$ for the dynamic light scattering experiments. They associate the three observed relaxation time dependencies with processes of passage formation, elastic deformation and concentration fluctuations.

In the present work the dynamics of L_3 phases have been established experimentally by *T*-jump and isothermal shear relaxation (see chapter 4). Relaxation times were measured as a function of the membrane volume fraction ϕ_{B+C}, corresponding to a varying midplane distance *d*, and as a function of the surfactant / (oil + surfactant) volume fraction ω_b, determining the bilayer thickness 2ε. Following these experiments two different tendencies can be observed. On the one hand, an enormous increase of the relaxation time constants τ^{-1} with the bilayer volume fraction ϕ_{B+C} at a given surfactant / (oil + surfactant) volume fraction ω_b. On the other hand, swelling the bilayer at constant bilayer volume fraction ϕ_{B+C} results in relaxation time constants that run through a minimum with varying ω_b (see Fig. 4.14).

6.2.1 Phenomenological description

ω_b-dependence

Phenomenologically, a correlation of the minimum in the τ^{-1} vs. ω_b curves and the extension of the stability of the L_α phase is obvious. The consideration of the L_α phase in search for explanations for the minimum in the τ^{-1} versus ω_b curves is motivated by the similarities between the L_α and the L_3 phase. They both consist of bilayers and can be diluted with water or brine up to 95%, while the change in the repeat distance is qualitatively the same [8]. In Fig. 6.5 the extension of the L_α phase in a ternary phase diagram of the system water – *n*-octane – $C_{10}E_5$ is shown. This system behaves qualitatively very similar to the system used in this study. The illustrated L_α phase is stable down to high dilutions with both water and oil. The widest extension of the L_α into the water corner of the phase diagram at a surfactant / (oil + surfactant) volume fraction of $\omega_b = 0.69$ corresponds to the minimum in the τ^{-1} versus ω_b curves for a given ϕ_{B+C}. Consequently the slowest relaxation processes in the L_3 phase are observed where the L_α is most stable.

This almost quantitative correlation between the extension of the L_α phase and the minimum in the τ^{-1} versus ω_b plots is striking. A possible theoretical link of the two behaviors will be discussed below.
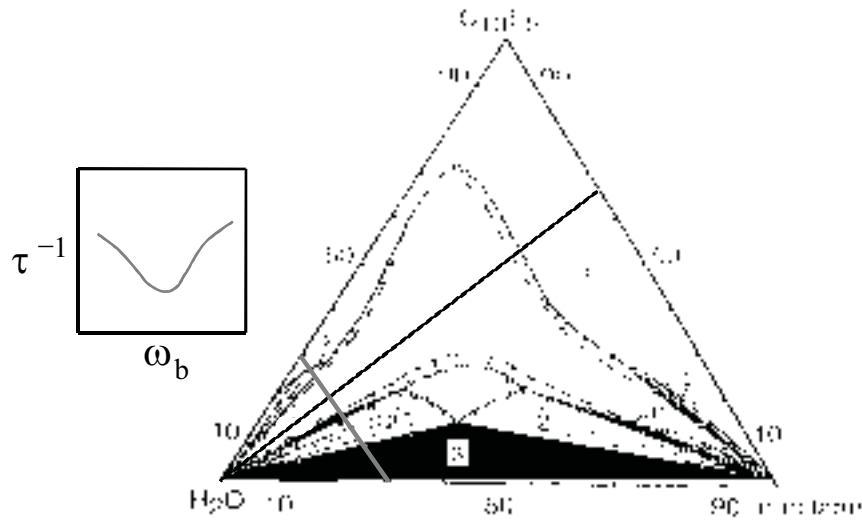
Fig. 6.5: Extension of the L_α phase in a ternary phase diagram of the system H_2O – *n*-octane – $C_{10}E_5$ [114]. The extension of the L_α is maximal around $\omega_b = 0.7$. For this value the highest ϕ_{B+C}-dependence of the relaxation time constants was found, i.e. this value relates to the slowest process for a given ϕ_{B+C} (see inlet).

ϕ_{B+C}-dependence

Enormously high dependencies of the relaxation time constants τ^{-1} on the bilayer volume fraction ϕ_{B+C} were found from *T*-jump experiments (Fig. 4.12 and Fig. 4.13). In a double logarithmic plot this results in linear dependencies, which are expressed by effective power laws $\tau^{-1} \propto \phi_{B+C}^n$ with $3 < n < 9$. However, matters were further complicated by the observation of deviations from the linear behavior with the setup of the isothermal shear perturbation allowing to measure slower relaxation times than those accessible with *T*-jump. With dilution, increasingly non-linear behavior is revealed, for which presently no theoretical model exists.

A way to explain this non-linearity is by assuming two different relaxation regimes with different dependencies on the composition, one for lower and the other for higher bilayer volume fractions ϕ_{B+C}. In Fig. 6.6 the relaxation time constants in dependence of the membrane volume fraction ϕ_{B+C} are shown for surfactant / (oil + surfactant) bilayer fractions between $\omega_b = 0.81$ and $\omega_b = 0.37$. The data are fitted for both regimes, the low ϕ_{B+C} with $\tau^{-1} \propto \phi_{B+C}^3$ weighted with a prefactor *A* and the high ϕ_{B+C} with $\tau^{-1} \propto \phi_{B+C}^{8.8}$ with a prefactor *B*, i.e.

$$\tau^{-1} = A \cdot \phi_{B+C}^3 + B \cdot \phi_{B+C}^{8.8}. \tag{6.5}$$

As one can see in Fig. 6.6, all data can be fitted with this function. The prefactor *A* for the low ϕ_{B+C} regime changes considerably with the surfactant / (oil + surfactant) volume fractions ω_b while the absolute value of the prefactor *B* for the high ϕ_{B+C} regime can be considered as being almost constant.
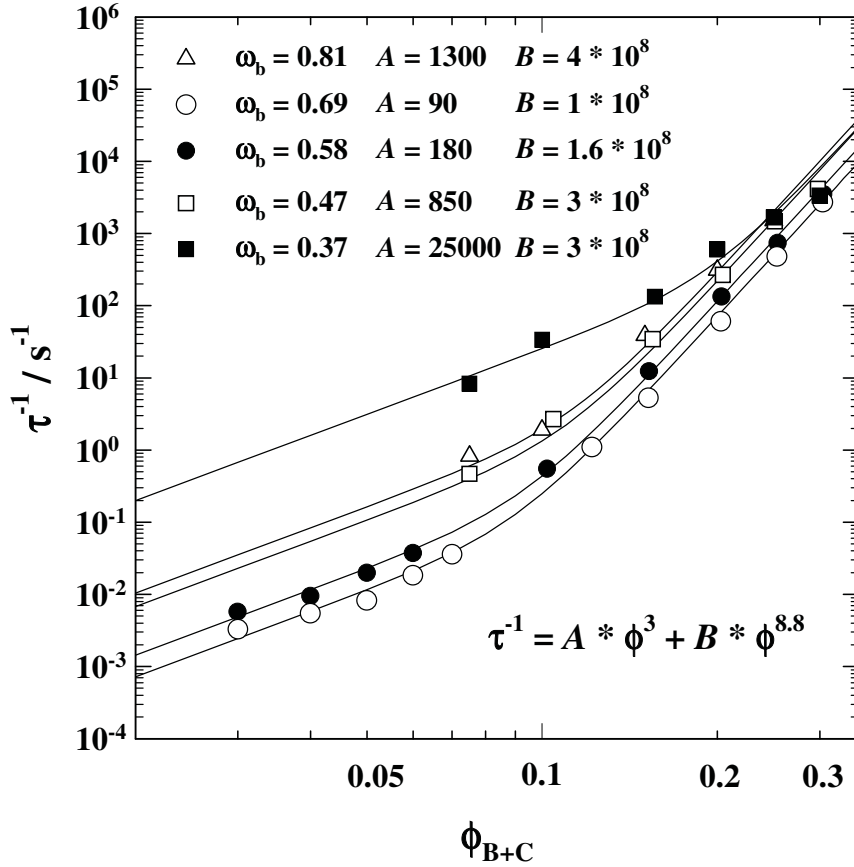
Fig. 6.6: Fits of the data for the dependence of the relaxation time constants τ^{-1} on the bilayer volume fraction ϕ_{B+C} for different surfactant / (oil + surfactant) volume fractions ω_b. Two linear regimes are added to each other and weighted with different prefactors *A* and *B* for each ω_b.

The observation of two different regimes in the dynamic behavior of L_3 phases as a function of the membrane volume fraction ϕ_{B+C} suggests different relaxation mechanisms for very high and very low dilution. A hint towards these two different regimes was already given above, regarding the stability of the L_3 phase. There, the values for the topological persistence length $\xi_{\bar{\kappa}}$ and the interbilayer distance *d* vary in their relative positions as a function of ω_b. It applies that the structure and stability is more fluctuation-dominated for $\omega_b > 0.58$ and more topology-controlled for $\omega_b < 0.58$.

Furthermore, these two regimes also explain why previous workers measured a dependence of $\phi_C{}^3$ on the relaxation time constants τ^{-1} for highly diluted L_3 phases [24]: They measured in the regime of the small ϕ_C–dependence only.

6.2.2 Theoretical description

ω_b-dependence

The minimum in the experimental results of the τ^{-1} vs. ω_b curves, which was discussed phenomenologically in 6.2.1, can be understood in the following way. Upon swelling the bilayer (at constant ϕ_C, that is at constant mid-plane distance d) there are two competing tendencies. The decrease in τ^{-1} (relaxation slowing down) can be explained [72] by

$$\tau^{-1} \sim \frac{1}{\kappa_{bil}} \phi_{B+C}^{\frac{2}{\zeta}+1} . \qquad (6.6)$$

and the fact that $\kappa_{bil} \approx 2\varepsilon^p$, where $2 \le p \le 3$ [115, 116]. This means, that swelling the bilayer will increase the bilayer rigidity κ_{bil}. This will lead to fewer collisions between membranes, and consequently, to slower relaxation times. At the same time a tendency to faster processes is present, which will eventually dominate the regime controlled by the rigidity at low ω_b, i.e. large swelling of the bilayer. This can be understood in the following way. KABALNOV and WENNERSTRÖM [117, 118] have shown that the spontaneous curvature strongly affects the energy E_p necessary to create a passage, with a very pronounced decrease in E_p when $c_0 \to 0$. Since the L_3 phase is the manifestation of the spontaneous curvature of the monolayers [1] the phase diagram, more precisely the $L_\alpha + L_3 \to L_3$ transition temperature, allows determining the spontaneous curvature. In Fig. 6.7 the values (by convention a spontaneous curvature around the water is calculated as negative) of the spontaneous curvature of the L_3 phase monolayers are plotted against the surfactant / (oil + surfactant) volume fraction ω_b.
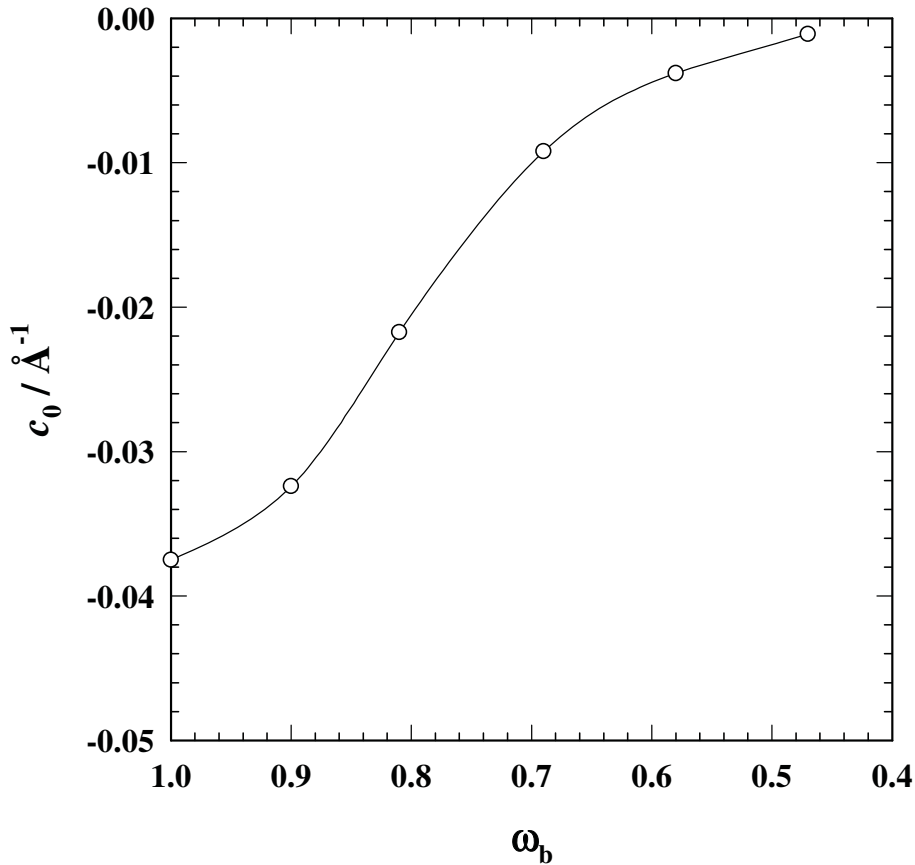
Fig. 6.7: Spontaneous curvature c_0 of the monolayers as a function of the surfactant / (oil + surfactant) ω_b for a constant surfactant volume fraction $\phi_C = 0.1$.

It can be seen from Fig. 6.7, that the spontaneous curvature increases (i.e. becomes less negative) with decreasing ω_b, as the L_3 phase approaches $\overline{T}$, where c_0 becomes zero. Hence, the energy to form a passage E_p decreases [117, 118] so that passages are easier formed and the relaxation times as a function of ω_b will become faster again with decreasing ω_b. The increase of κ_{bil} and the decrease in the energy to form a passage with decreasing ω_b presumably are responsible for the pronounced variation in the "activation energies" which run through a maximum (see Fig. 4.10).

ϕ_{B+C}-dependence

In the phenomenological discussion of the ϕ_{B+C}-dependence of τ^{-1} two different relaxation regimes were found. To correlate these to the plots of the topological persistence length $\xi_{\overline{\kappa}}$ and the midplane distance d against ϕ_C, the relaxation time constants also have to be pictured as a function of ϕ_C.

For plotting τ^{-1} versus ϕ_C in Fig. 6.8, two different relaxation regimes appear to be discernible. At high dilution the dependence of the relaxation time constants on the surfactant volume

fraction is small, whereas at high ϕ_C the dependence is large. The points of intersection of the two regimes shift towards lower ϕ_C and higher τ^{-1} with decreasing ω_b. In accordance with Fig. 6.4 this shift can be explained by the existence of two different regimes. For small values of ω_b the system is more topology-controlled, while for higher values of ω_b it is rather fluctuation-dominated.
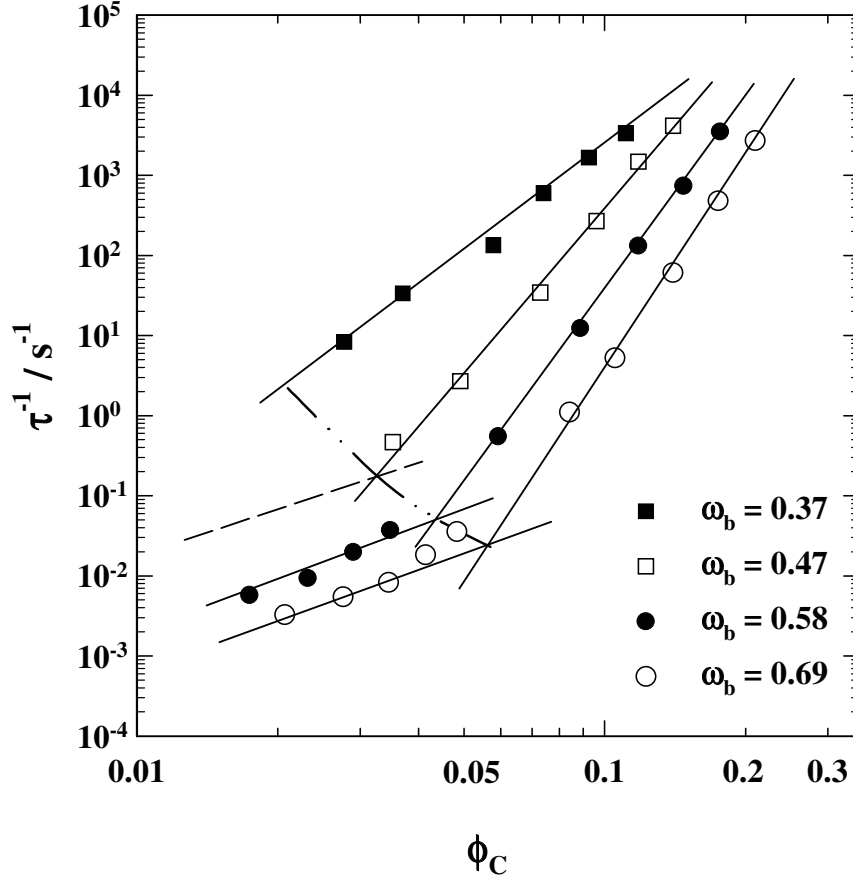
Fig. 6.8: Relaxation time constants τ^{-1} as a function of the surfactant volume fraction ϕ_C for different surfactant / (oil + surfactant) volume fractions ω_b.

A possible explanation for these two regimes is the following: At low ϕ_C the system is so dilute that the influence of d is larger than that of $\xi_{\overline{K}}$ and the dynamics are controlled by d^3. Thus the fluctuations can be pictured, in a first approximation, as insensitive to the topology, and $\tau^{-1} \sim \phi_C^3$. Such behavior is similar to that of the lamellar phase [69, 22], and indeed is observed. For higher values of ϕ_C, however, the topological configuration of the L_3 phase greatly affects the fluctuations. As mentioned in chapter 3.2, the peculiar topological structure of the L_3 phase will hinder the fluctuations and high powers in the τ^{-1} versus ϕ_C relation are to be expected. The experimental results show a clear crossover between the two situations.

The results of this discussion provide useful information on the stability and structure of L_3 phases, which presents the chance to theoretically describe the experimental findings of the

dynamics of these phases. A complete theoretical description would require, however, a quantitative description of the topology of the L_3 phase and the calculation of the energy to form a passage in the L_3 phase.

7   Summary

This work was triggered by the striking observation of L_3 phase dynamics ranging over as much as ten orders of magnitude in time constants when only moderately changing the composition, while at the same time a theoretical description for the dynamics of L_3 phases was lacking. In order to find a remedy for this unsatisfactory situation, the actual parameters influencing the L_3 phase dynamics were to be found and quantitatively described.

The L_3 phase comprises a multiply connected randomly oriented bilayer that divides space into two equivalent water subvolumes. A schematic illustration of this structure can be seen in Fig. 1.2. An L_3 phase is always to be found in the vicinity of an L_α phase. It is stable over a wide range of bilayer volume fraction while it exhibits only small temperature stability, giving it the appearance of a narrow phase channel that shifts to higher temperatures for increasing bilayer volume fractions. The L_3 phase is existent in binary systems water – surfactant, but the bilayers can also be swelled with oil resulting in a ternary system with a variable bilayer thickness 2ε, expressed by a varying surfactant / (oil + surfactant) volume fraction ω_b. A change in the bilayer volume fraction ϕ_{B+C} will change the distance d between two adjacent bilayers at constant thickness.

To accomplish the aim of this work ternary mixtures of H_2O / NaCl, *n*-octane, and $C_{10}E_4$ were chosen as an L_3 phase model system. The advantage of this pseudo-ternary system is the possibility to change the structural parameters of the L_3 phase by varying the interbilayer distance d and the bilayer thickness 2ε of the L_3 phase. Furthermore, the binary system H_2O - $C_{10}E_4$ is the first in the series of *n*-alkylpolyethylenoxide surfactants that, with increasing hydrocarbon chain length, exhibits an L_3 phase, making this the most basic L_3 phase system in this series. Additionally, this system provides suitable experimental conditions, i.e. the position of the L_3 phase on the temperature scale for the binary as well as the ternary system are closer to room temperature than for higher homologues of this series.

As a basis for the investigation of the dynamics the phase behavior of this model L_3 phase system needed to be thoroughly understood. For the binary system H_2O - $C_{10}E_4$ the stable L_3 phase region appears as a narrow band of 3 – 4 K width at temperatures around 50°C. With the addition of *n*-octane, i.e. decreasing surfactant / (oil + surfactant) volume fractions ω_b, the L_3 phase channels shift towards lower temperatures, become increasingly narrower and

appear to become less dependent on the bilayer volume fraction ϕ_{B+C}, which is illustrated in Fig. 2.8.

The dynamics of this model L_3 phase were quantified by using different relaxation techniques. Temperature jump experiments were performed from temperatures inside the stable L_3 region onto the binodal temperature, yielding relaxation times τ, which covered a time window from 10^{-4}s to 1s. The relaxation time constants τ^{-1} vary over many orders of magnitude in dependence of the bilayer volume fraction ϕ_{B+C} for constant surfactant / (oil + surfactant) volume fractions ω_b. Presented in a double logarithmic plot steep effective power law dependencies τ^{-1} on ϕ_{B+C}^n (3<n<9) can be observed for higher bilayer volume fractions ϕ_{B+C}, where *n* is a function of the surfactant / (oil + surfactant) volume fraction ω_b, as illustrated in Fig. 4.12 and Fig. 4.13. To extend the experimental window to longer relaxation times τ than those experimentally accessible by *T*-jump, and thus for higher dilution of the L_3 phase, a newly developed technique, the isothermal shear, was applied. This method comprises shear perturbation and conductivity detection, covering a relaxation time frame of 25 s to 10^3 s. Relaxation times at low bilayer volume fractions ϕ_{B+C} could be measured for two of the eight different surfactant / (oil + surfactant) volume fractions ω_b (ω_b = 0.58, 0.69), see Fig. 4.18. In contrast to the higher bilayer volume fractions (Fig. 4.12 and 4.13) this double logarithmic plot reveals non-linear behavior. For ω_b > 0.69 and ω_b < 0.58 relaxation times larger than those accessible with the *T*-jump could not be measured. However, this result does not exclude an equally non-linear dependence of τ^{-1} on ϕ_{B+C} for ω_b > 0.69 and ω_b < 0.58. On the contrary, the same general behavior is expected (see Fig. 4.19) with relaxation times between 1.5 s and 25 s, a time window, which was not accessible so far. In dependence of the surfactant / (oil + surfactant) volume fraction ω_b the relaxation time constants for *T*-jump experiments run through a minimum for constant bilayer volume fractions ϕ_{B+C}, where the position of the minimum can always be observed for ω_b = 0.69, as can be seen in Fig. 4.14.

To support a theoretical description for the dynamics of L_3 phases, a suitable geometrical model had to be found to relate the characteristic length scales of the L_3 phase to its composition. SANS measurements were conducted to establish a quantitative description of the L_3 phase microstructure as a function of bilayer volume fraction and thickness. The interbilayer distance *d* and the bilayer thickness 2ε could be extracted from the neutron scattering curves, see Fig. 5.7 and 5.8, revealing the exact numerical dependencies of the

bilayer volume fraction ϕ_{B+C} on d and of the surfactant / (oil + surfactant) volume fraction ω_b on 2ε.

The theoretical interpretation of the dynamics of L_3 phases was based on the assumption that the relaxation process in L_3 phases is one of passage formation. This assumption could be confirmed by SANS measurements, illustrated in Fig. 5.5 and 5.6. A first theoretical approach took into account thermal fluctuations of the bilayers and calculated the probability of a collision between two adjacent undulating membranes as being proportional to the relaxation time τ. This could qualitatively explain the high exponents of the ϕ_{B+C} dependence on τ^{-1}, but was not feasible for the minimum in the ω_b dependence on τ^{-1} and especially could not clarify the non-linear behavior of the relaxation time constants for low bilayer volume fractions. This first approach is certainly a part of the puzzle but is has to be combined with considerations of the free energy situation that actually leads to the formation of a passage after two membranes have collided.

The highlights of this work are the exact SANS results elucidating the bilayer structures of the L_3 phase, correlating the characteristic length scales d and 2ε of the L_3 phase to its composition by way of a geometrical model. Including the measured phase behavior to determine the spontaneous curvature c_0 of the monolayers, the model for the lamellar-to-sponge transition by MORSE [63] and GOMPPER [65] could be confirmed (Fig. 6.3). Furthermore, could the experimentally determined length scale d be associated with the persistence lengths ξ_κ and $\xi_{\bar{\kappa}}$, while it was shown for the first time that $d \approx \xi_{\bar{\kappa}} << \xi_\kappa$ (Fig. 6.2) for the melting of lamellae into sponges. Qualitative explanations could be found for the high powers of the L_3 phase relaxation times on the bilayer volume fraction. Two relaxation regimes could be determined in dependence of the bilayer volume fraction, one for low ϕ_{B+C} controlled by fluctuations only, the other, at high ϕ_{B+C} controlled by the bending energy (Fig. 6.6). The two regimes can be correlated with an L_3 phase structure where the influence of the midplane distance d is larger then that of the topological persistence length $\xi_{\bar{\kappa}}$ and one where the opposite is true (Fig 6.4). The minimum in the τ^{-1} vs. ω_b curves can be explained by two competing tendencies. With increasing bilayer thickness 2ε the bilayer rigidity κ_{bil} will increase, leading to fewer collisions and consequently slower relaxation times. On the other hand, c_0 approaches zero with decreasing ω_b (Fig. 6.7), thereby reducing the energy to form a passage [117, 118] and presenting a tendency to faster processes.

7.1   Zusammenfassung

Die Haupttriebkraft dieser Arbeit ist der bemerkenswerte Befund, daß bei der Untersuchung der Dynamik der L_3-Schwammphase eine Variation der gefundenen Relaxationszeitkonstante über fast 10 zeitliche Größenordnungen bei geringfügiger Änderung der Probenzusammensetzung gefunden wurde. Mit den bisher vorhanden Ansätzen ist eine theoretische Beschreibung dieser Dynamik nicht möglich. Im Rahmen dieser Arbeit wird versucht, ein phänomenologisches Model zu entwickeln, das eine quantitative Beschreibung ermöglicht.

Die L_3-Phase besteht aus vielfach miteinander verbunden, zufällig orientierten Tensiddoppelschichten, die den Raum in zwei gleichwertige Subvolumina unterteilen. Fig. 1.2 zeigt eine schematische Darstellung dieser Struktur. Die L_3-Phase wird immer in der Nähe einer lamellaren L_α-Phase gefunden. Sie zeigt Stabilität über einen großen Konzentrationsbereich bis zu sehr hohen Verdünnungen, breitet sich allerdings nur über einen geringen Temperaturbereich aus. Dies führt zu einem schmalen Phasenkanal, der sich mit zunehmendem Membranvolumenbruch zu höheren Temperaturen verschiebt. Man findet die L_3-Phase bereits im binären System Wasser – Tensid beim Einsatz hinreichend effizienter Tenside. Die Tensiddoppelschichten können durch Öleinlagerung angeschwollen werden. Beim ternären System wird die Membrandicke 2ε durch den Tensid / (Öl + Tensid) Volumenbruch ω_b bestimmt. Eine Änderung des Membranvolumenbruchs ϕ_{B+C}, führt zu einer Änderung des Abstandes *d* zwischen zwei benachbarten Membranen.

Die genannten strukturellen Parameter lassen sich beim Modellsystem H_2O / NaCl – *n*-Oktan – $C_{10}E_4$ in einem experimentell gut handhabaren Temperaturbereich variieren. Beim binären System H_2O – $C_{10}E_4$ handelt es sich um das erste einer homologen Reihe von *n*-Alkylpolyethylenoxid Tensiden mit ausreichender Effizienz zur Bildung der L_3-Phase, welches somit das elementarste System dieser Reihe darstellt.

Als Grundlage für die Untersuchung der Dynamik mußte das Phasenverhalten der L_3-Phase eingehend bestimmt werden. Für das binäre System H_2O – $C_{10}E_4$ befindet sich der stabile Bereich der L_3-Phase in einem schmalen Band von 3 – 4 K Breite in einem Temperaturbereich von ca. 50 °C. Mit der Zugabe von *n*-Oktan, d.h. mit abnehmendem Tensid / (Öl + Tensid) Volumenbruch ω_b, verschiebt sich der L_3-Phasenkanal zu niedrigeren Temperaturen und wird zunehmend schmaler. Gleichzeitig wird die Temperaturabhängigkeit

der Phasengrenzen weniger abhängig vom Membranvolumenbruch ϕ_{B+C} (Fig. 2.8), d.h. die L$_3$-Phasenkanäle werden zunehmend flacher.

Für die Ermittlung experimenteller Daten zur quantitativen Beschreibung der Dynamik der L$_3$-Phase wurden verschiedene Relaxationsmethoden angewendet. Aus Temperatursprung-experimenten, ausgehend von Temperaturen innerhalb des stabilen L$_3$ Phasengebietes in Richtung der oberen Phasengrenze, d.h. der Binodaltemperatur, wurden Relaxationszeiten in einem zeitlichen Rahmen von 10^{-4} s bis 1 s gefunden. Die Relaxationszeitkonstanten τ^{-1} variieren über einen Bereich mehrerer Größenordnungen in Abhängigkeit des Membranvolumenbruchs ϕ_{B+C} bei konstantem Tensid / (Öl + Tensid) Volumenbruch ω_b. In doppeltlogarithmischer Auftragung kann die starke Abhängigkeit des Geschwindig-keitsgesetzes für τ^{-1} von ϕ_{B+C}^n (3 < n < 9) für hohe Membranvolumenbrüche gezeigt werden, wobei *n* eine Funktion des Tensid / (Öl + Tensid) Volumenbruches ω_b ist (Fig. 4.12 und Fig. 4.13). Zur erforderlichen Erweiterung des experimentellen Zeitfensters zu langsameren Zeiten ($\tau \geq 25$ s) bei niedrigeren Membranvolumenbrüchen ϕ_{B+C} wurde eine neuentwickelte Methode, die isotherme Scherung, angewendet. Diese Methode erfaßt die Änderung der Leitfähigkeit nach einer Störung, die durch Scherung hervorgerufen wird, wobei sie die Beobachtung der Relaxationszeit über einen Bereich von 25 s bis 10^3 s ermöglicht. Für zwei der sieben untersuchten Tensid / (Öl + Tensid) Volumenbrüche, $\omega_b = 0.58$ und $\omega_b = 0.69$ wurde bei niedrigen Membranvolumenbrüchen ϕ_{B+C} die Relaxationszeit bestimmt (Fig. 4.18). Im Gegensatz zu den hohen Membranvolumenbrüchen ϕ_{B+C} (Fig. 4.12 und Fig. 4.13) zeigt diese in doppeltlogarithmischer Darstellung keinen linearen Zusammenhang. Für $\omega_b > 0.69$ und $\omega_b < 0.58$ konnten keine längeren Relaxationszeiten, als mit dem Temperatursprung zugänglich sind, gemessen werden. Trotzdem schließt dieses Ergebnis ein gleichsam nichtlineares Verhalten für τ^{-1} in Abhängigkeit von ϕ_{B+C} für $\omega_b > 0.69$ und $\omega_b < 0.58$ nicht aus. Eher im Gegenteil kann gleiches Verhalten für Relaxationszeiten zwischen 1.5 s und 25 s erwartet werden (Fig. 4.19), wobei dieses ein Zeitfenster ist, das mit den bisher beschriebenen Methoden nicht zugänglich war. In Abhängigkeit vom Tensid / (Öl + Tensid) Volumenbruch ω_b bei konstantem Membranvolumenbruch ϕ_{B+C} laufen die Relaxationszeitkonstanten für Temperatursprungexperimente durch ein Minimum, wobei das Minimum immer bei $\omega_b = 0.69$ gefunden wird (Fig. 4.14).

Zur phänomenologischen Beschreibung der Dynamik von L_3-Phasen ist ein sinnvolles geometrisches Modell erforderlich, das eine Übertragung der eingewogenen Probenkomponenten in charakteristische Längenskalen ermöglicht. SANS Messungen wurden zur Aufklärung der Mikrostruktur und Verifikation dieses Modells durchgeführt. Aus den Neutronenstreukurven (Fig. 5.7 und 5.8) konnten der Abstand zwischen den Tensiddoppelschichten d und die Bilayerdicke 2ε ermittelt werden, wodurch die exakten Abhängigkeiten vom Membranvolumenbruch ϕ_{B+C} auf d und des Tensid / (Öl + Tensid) Volumenbruch ω_b auf 2ε bestimmt wurden.

Der bisherige theoretische Ansatz für die Erklärung der Dynamik von L_3-Phasen beruhte auf der Annahme, daß der Relaxationsprozess bei Temperatursprungexperimenten durch Passagenbildung vonstatten geht. Diese Annahme konnte durch temperaturabhängige SANS Messungen bestätigt werden (Fig. 5.5 und 5.6). Ein erster theoretischer Ansatz diskutiert die thermischen Fluktuationen der Membranen sowie die Wahrscheinlichkeit einer Doppelschicht-Doppelschicht-Berührung als proportionale Einflussgröße auf die Relaxationszeit τ. Damit wurde zwar qualitativ die hohe Abhängigkeit der Relaxationszeit-konstante τ^{-1} von ϕ_{B+C} erklärbar, aber weder die Existenz des Minimums in der Abhängigkeit von τ^{-1} von ω_b, noch das nichtlineare Verhalten der Relaxationszeitkonstanten für niedrige Membranvolumenbrüche konnte damit erklärt werden. Dieser erste theoretische Ansatz ist sicherlich ein Baustein des Ganzen, muß allerdings kombiniert werden mit Überlegungen bezüglich der freien Energie, die zur Passagebildung führt, nachdem zwei benachbarte Membranen miteinander kollidiert sind.

Die Highlights dieser Arbeit sind die Ergebnisse aus SANS Messungen, die zur genauen Aufklärung der Bilayerstruktur der L_3-Phase beigetragen haben und dazu führten, daß die charakteristischen Längen d und 2ε unter Entwicklung eines geometrischen Modells mit der Zusammensetzung der L_3-Phase korreliert werden konnten. Das von MORSE [63] und GOMPPER [65] entwickelte Modell für den Übergang von L_α-nach-L_3 konnte mit Hilfe des experimentell bestimmten Phasenverhaltens, welches zur Berechnung der spontanen Krümmung c_0 des Monolayers diente, bestätigt werden (Fig. 6.3). Des weiteren konnte die experimentell ermittelte Längenskala d mit den Persistenzlängen ξ_κ und $\xi_{\bar{\kappa}}$ in Verbindung gebracht werden und es konnte erstmals gezeigt werden, daß für das ‚Melting' von lamellaren zu Schwammphasen $d \approx \xi_{\bar{\kappa}} \ll \xi_\kappa$ (Fig. 6.2) gilt. Außerdem wurden qualitative Erklärungen

für die starke Abhängigkeit der Relaxationszeit der L_3-Phasen vom Bilayervolumenbruch gefunden. Dabei wurden zwei Relaxationszeitregime in Abhängigkeit des Bilayervolumenbruchs bestimmt. Ein Regime für niedrige ϕ_{B+C}, welches durch Fluktuationen bestimmt ist, und ein anderes nur durch Biegeenergien bestimmtes Regime für hohe ϕ_{B+C} (Fig. 6.6). Dieser Übergang zwischen zwei Regimes kann mit der L_3-Phasenstruktur korreliert werden. Hierbei ist in Abhängigkeit des Tensidvolumenbruchs bei der einen Struktur der Einfluß des Intermembranabstand d größer als der der topologischen Persistenzlänge $\xi_{\bar{\kappa}}$, bei der anderen Struktur trifft der umgekehrte Fall zu (Fig. 6.4). Weiterhin konnte das Minimum in den τ^{-1}-gegen-ω_b Kurven durch zwei gegenläufige Tendenzen beschrieben werden. Mit zunehmender Bilayerdicke 2ε erhöht sich die Biegesteifigkeit des Bilayers, und damit κ_{bil}. Dies führt zu einer Abnahme der Zusammenstösse zwischen den Membranen und folglich zu langsameren Relaxationszeiten. Andererseits nähert sich der Wert der spontanen Krümmung mit abnehmendem ω_b gegen null (Fig. 6.7). Hierdurch reduziert sich die Energie, die zur Bildung von Passagen benötigt wird [117, 118] und führt damit zu schnelleren Relaxationszeiten.

8   Experimentals

This chapter deals with the experimental methods and the equipment used to determine the phase behavior, the dynamics and the structure of the L_3 phase. It divides into materials, sample preparation and characterization, descriptions of the T-jump apparatus and its calibration, the isothermal shear method, and SANS experiments.

8.1   Materials

The nonionic surfactant *n*-decyltetraoxyethylenoxide ($C_{10}E_4$) was purchased from Bachem Biochemica GmbH, Heidelberg, Germany with a purity > 98 %. The purity of $C_{10}E_4$ can be judged from the critical point of the binary system water - $C_{10}E_4$. The value known from literature [119, 120] for the purified surfactant is T_c = 20.5 °C at a mass fraction of γ = 0.026. The critical point for the purchased surfactant without further purification was determined to T_c = 20.3 °C at γ = 0.026. Since this is sufficiently close to the literature value it can be deduced that the surfactant contains only minor impurities and can be used as purchased. N-octane was obtained from Sigma, Germany with a purity > 99%. H_2O was ultra pure Millipore water, type Milli-Q RG with a resistance of several $M\Omega \cdot cm$. The 0.1 M NaCl solution is prepared from a TITRISOL $^\circledR$ standard solution purchased from Merck, Darmstadt, Germany. The 1 mM NaCl solution required for the isothermal shear experiments was prepared by dilution from the 0.1 M NaCl stock solution.

The D_2O and *d*-octane needed for the SANS experiments were obtained from Cambridge Isotope Laboratories, Cambridge, MA, USA and used as purchased with a purity > 99%.

Table 8.1: Densities ρ^{25} at T = 25 °C and molecular weights M_w of the used chemicals

chemicals	$\dfrac{\rho^{25}}{g \cdot cm^{-3}}$	$\dfrac{M_w}{g \cdot mol^{-1}}$
H_2O / NaCl	0.998	18.02
D_2O	1.105	20.03
n-Octane	0.703	114.23
d-Octane	0.815	132.38
$C_{10}E_4$ (*n*-Decyltetraoxyethylenoxide)	0.959	334.49

8.2   Sample preparation and characterization

For *T*-jump experiments the samples were prepared by diluting stock solutions of *n*-octane – $C_{10}E_4$ at different surfactant / (oil + surfactant) volume fractions ω_b with 0.1 M H_2O / NaCl solution to reach the desired bilayer concentration ϕ_{B+C}. All compounds were weighted in for accuracy. The same procedure was applied to prepare samples for isothermal shear measurements with the exception that 1 mM H_2O / NaCl solution was used instead.

All samples were filled into capped test tubes (volume 20 mL) equipped with Teflon coated stirring bars. The sample tubes were thoroughly mixed and transferred into a thermostatic water bath, which is mounted on a magnetic stirrer [112]. The tubes are supposed to be completely submerged to allow sufficient heat transport. The $L_\alpha + L_3 \rightarrow L_3$ ($T_l^{L_3}$) and $L_3 \rightarrow L_1' + L_3$ ($T_u^{L_3}$) phase boundaries were determined by changing the water bath temperature in increments of ± 0.02 K, thus reaching a precision of the phase transition temperatures of ± 0.05 K. The transition from a one-phase region to a two-phase region is kinetically hindered thus causing incorrect boundary temperatures when measured in that direction. Therefore phase boundaries were always determined by going from a two-phase to a one-phase region. Additionally crossed polarizers were used to detect the birefringence in the $L_\alpha + L_3 \rightarrow L_3$ phase transition, since the L_α phase shows birefringence permanently, the L_3 phase just under shear.

8.3   Temperature jump

The temperature jump apparatus consists of three main elements: A high voltage discharge unit to introduce the temperature jump, a thermostatted sample cell, and an optical unit to detect the intensity of the scattered light [101].

High voltage discharge unit

Fig. 8.1 shows the schematic setup of the high voltage discharge unit of the temperature jump apparatus. The accumulation of the electric energy generated by the high voltage source (HV) is conducted by the capacitor C, which has a capacity $C = 10$ nF. The temperature jump ΔT and hence the amplitude $\Delta I_S / I_0$ can be varied by changing the capacitor's charging voltage U. With voltages U between 2.5 kV and 11 kV temperature jumps between approx. 0.05 K and 0.85 K can be achieved. However, the exact dependence between U and ΔT has to be specified by calibration, since sample properties like heat capacity, concentration and

conductivity have to be taken into account (see Calibration of the amplitudes ΔT of the *T*-jump).
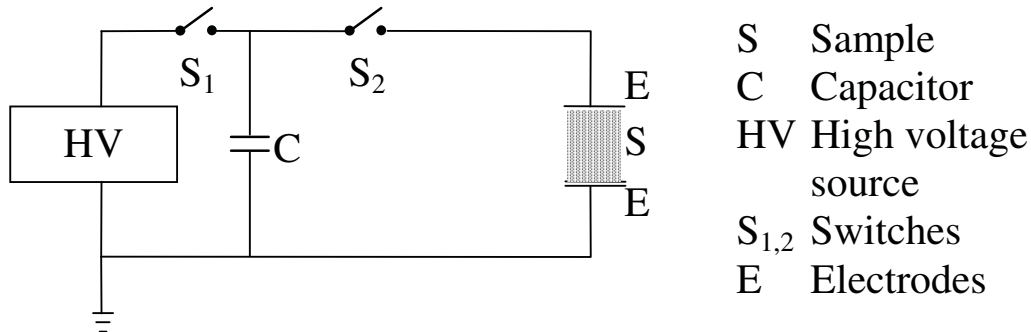
Fig. 8.1: Schematic setup of the temperature jump apparatus, explaining the high voltage discharge unit. By reducing the distance between the electrodes, the capacitor C discharges the energy stored through the sample (S) in the cell [27].

When the capacitor is fully charged, the connection between the high voltage source and the capacitor is intercepted by switch 1 (S_1). Switch 2 (S_2) is operated by an external pneumatic trigger impulse. By indirectly operating S_2 the distance between the electrodes is reduced and thus the energy stored in the capacitor is released into the sample (S) in the cell.

The temperature inside the sample cell can be determined via a thermistor, which is integrated into the upper electrode. Temperature measurements are conducted by matching the resistance of the thermistor with a WHEATSTONE bridge. By means of a known calibration function the temperature in the cell can be determined to a precision of ± 0.01 K.

Fig. 8.2 shows a section through one of the electrodes used in the setup. To prevent heat transfer between the electrodes and the sample in the cell the electrode wiring is supplied with a special jacketing. This is especially important since the measured L_3 phase samples with their narrow temperature range can phase separate for even small temperature deviations.
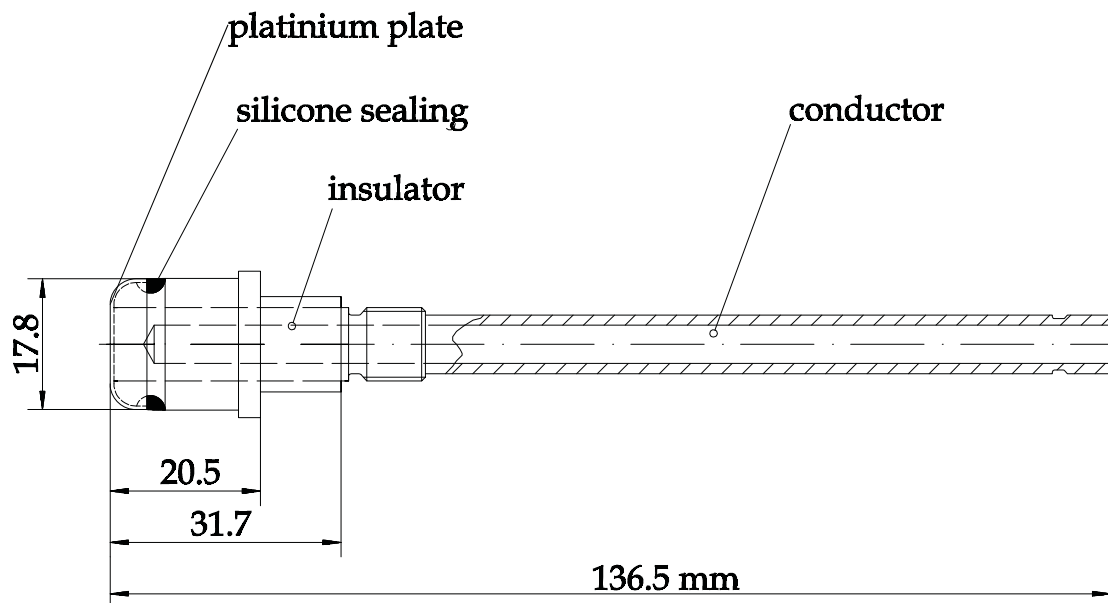
Fig. 8.2: Setup of the electrodes of the *T*-jump apparatus. Distances are in mm [27].

Since the trigger pulse generated by the capacitor is too short (< 10 μs) to be registered by the 12bit-AD-card in use, a pulse generator has to be introduced. This pulse generator releases a 1 ms signal with a positive edge, which then can be registered as a trigger signal by the AD card. This pulse defines the exact starting time t_0 of the *T*-jump.

Sample cell

Fig. 8.3 shows a vertical section through the measuring block. The sample solution is introduced into the cell by the sample inlet. The volume around the electrodes is considered completely filled once some of the solution has passed the sample outlet. The lower electrode is connected to the capacitor, the upper electrode to the grounding. The hollow spaces arranged around the electrodes are taken up by the thermostat fluid.
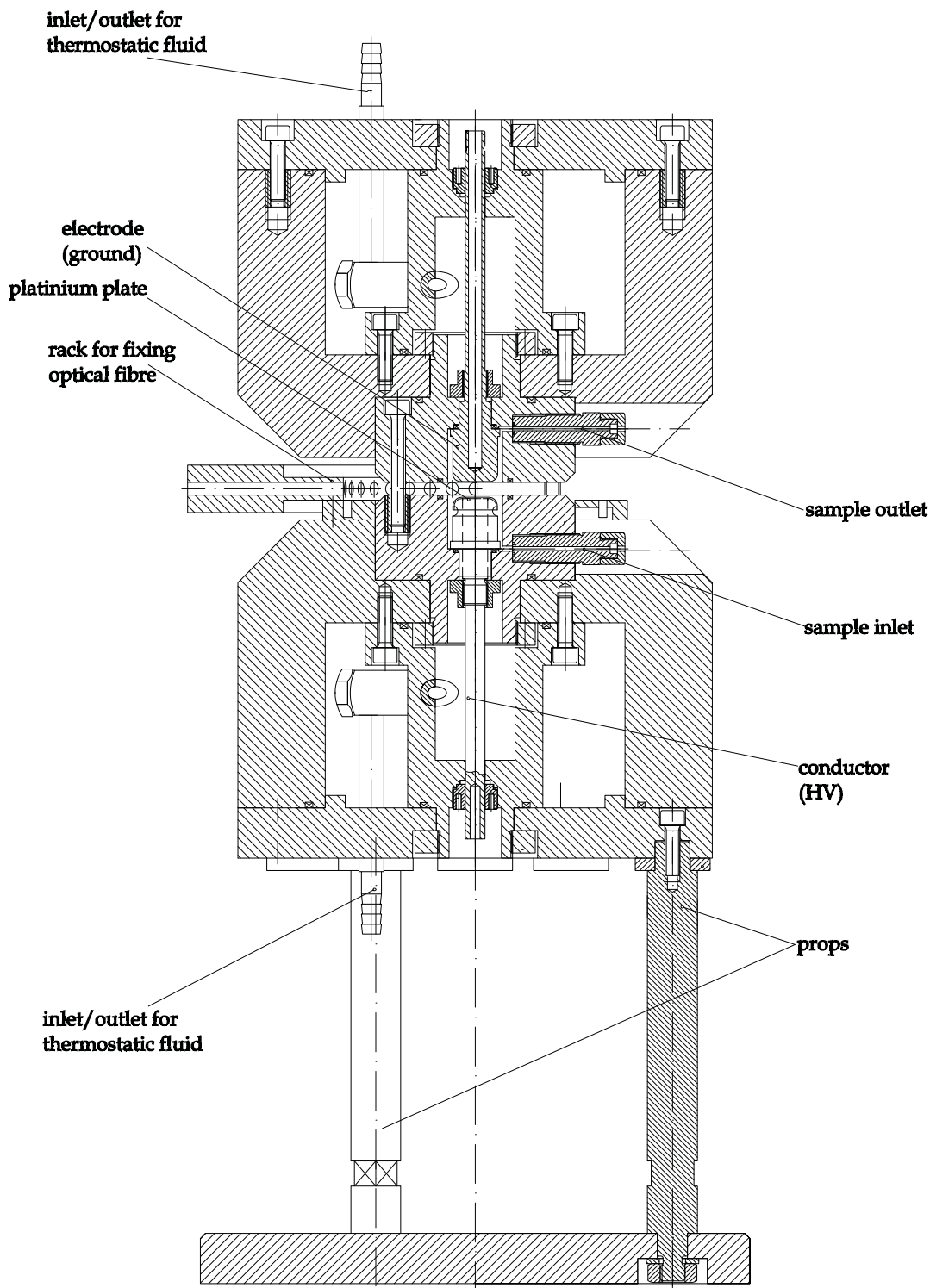
Fig. 8.3: Setup profile of the _T_-jump apparatus' measuring block [27].

The temperature control is subject to an elaborate combination of heating and cooling cycles. Fig. 8.4 shows a schematic illustration of this thermostatting system. It allows to keep the temperature inside the sample cell constant to a precision of ± 0.01 K.
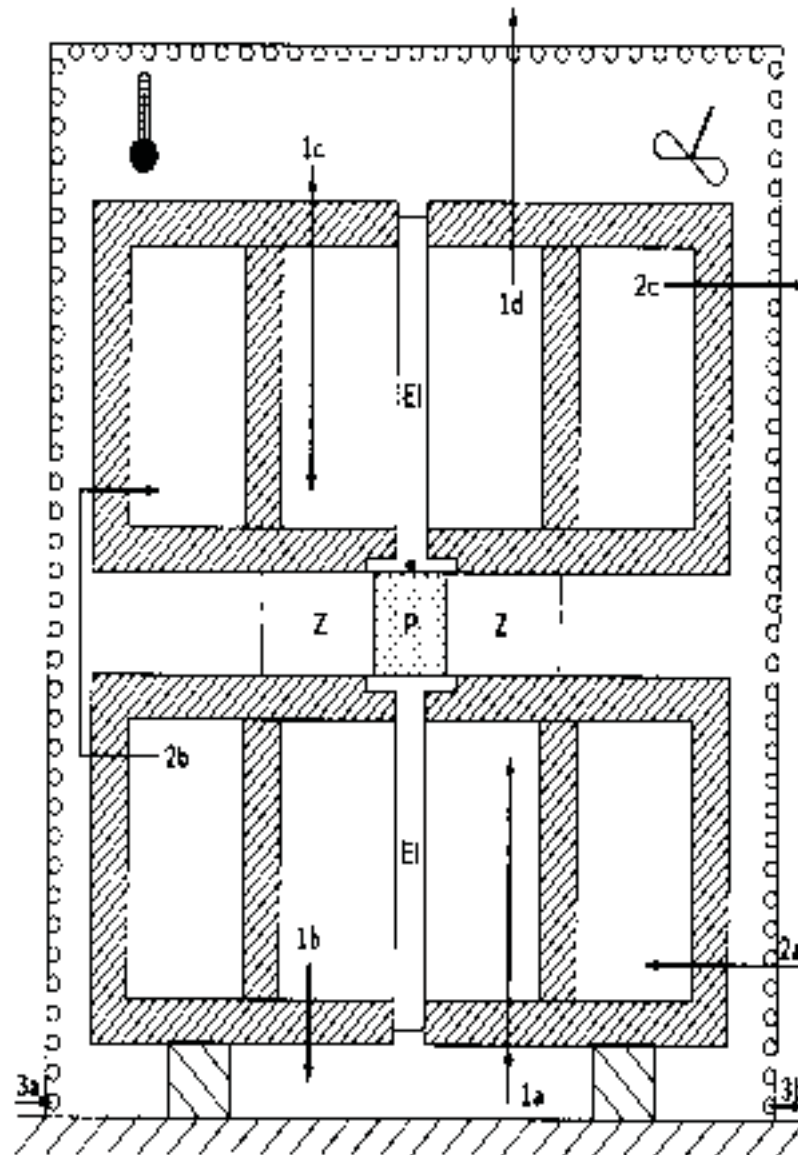
Fig. 8.4: Thermostat circuits of the measuring block (schematic) [121]. The inner and outer circuits run with transformer oil, for the hood a water / diethylenglycol mixture is used.

The temperature in the *T*-jump apparatus is controlled by two separate thermostat circuits. The measuring block itself is temperature controlled by transformer oil circulating through an inner (1a→1b→1c→1d) and outer (2a→2b→2c) circuit. An insulation hood surrounds the measuring block. The space underneath the hood is temperature controlled by the second thermostat (3a→3b), which circulates a water / diethylenglycol mixture. Due to these measures the temperature in the *T*-jump apparatus can be adjusted to the above-mentioned precision. This precision is noteworthy for the following reason. The capacitor is connected to the lower electrode by a copper cable of 10 mm diameter (see Fig. 8.3), which conducts the heat readily and seeks to equilibrate its temperature with that of the surroundings. Since the cable is at room temperature and the measuring cell tends to be mostly at higher temperatures

for the investigated L_3 phase systems, this poses a problem. Without an adequate temperature control and insulation for the electrode (see Fig. 8.2), the temperature in the cell could deviate towards lower temperatures and cause an irreversible phase separation of the sample from L_3 $\rightarrow L_3 + L_\alpha$.

The sample has to be introduced into the sample cell at a temperature in its stable L_3 phase region. To ensure that no phase separation takes place, not only the measuring block has to be of the exact temperature but a temperature-controlled syringe has to be used for transferring the sample in its one-phase state.

Another important issue that needs to be taken into account is the characteristic heating time of the sample inside the cell τ_H which is defined by

$$\tau_H = \frac{R_{cell} \cdot C}{2}. \tag{8.1}$$

The relaxation times τ of the investigated systems can be in the range between some hundred microseconds and seconds. The heating time τ_H should always be one order of magnitude lower then the relaxation time τ, i.e. $\tau_H \cdot 10 \leq \tau$. Otherwise the relaxation time can not be determined unambiguously. According to Eq. (8.1), at a fixed capacity $C = 10$ nF, the resistance measured in the sample cell, should not exceed a value of $R_{cell} = 2$ kΩ to keep the heating time at its required low value. This implies that the conductivity of the sample solution always has to be sufficiently high, why water is substituted for a 0.1 M NaCl solution in all samples.

The cooling time τ_C of the cell can be determined easily by using Eq. (4.1), if the relaxation times of the fast structural relaxation are smaller by orders of magnitude than the cooling time τ_C, i.e. $\tau_C \gg \tau$. In that case the second term of Eq. (4.1) is negligible and the cooling time can be fitted with an exponential decay function

$$I_S(t) = I_0 + \Delta I_S \cdot \exp\left(\frac{t - t_0}{\tau_C}\right) \tag{8.2}$$

Fig. 8.5 shows an exemplary cooling curve of the examined system H_2O / NaCl – *n*-octane – $C_{10}E_4$ in the stable temperature range of the L_3 phase. This curve shows a complete temperature jump perturbation and relaxation. The intensity of the scattered light I_S increases after the *T*-jump from I_0 by an amplitude ΔI_S and returns to its initial intensity after a few seconds.
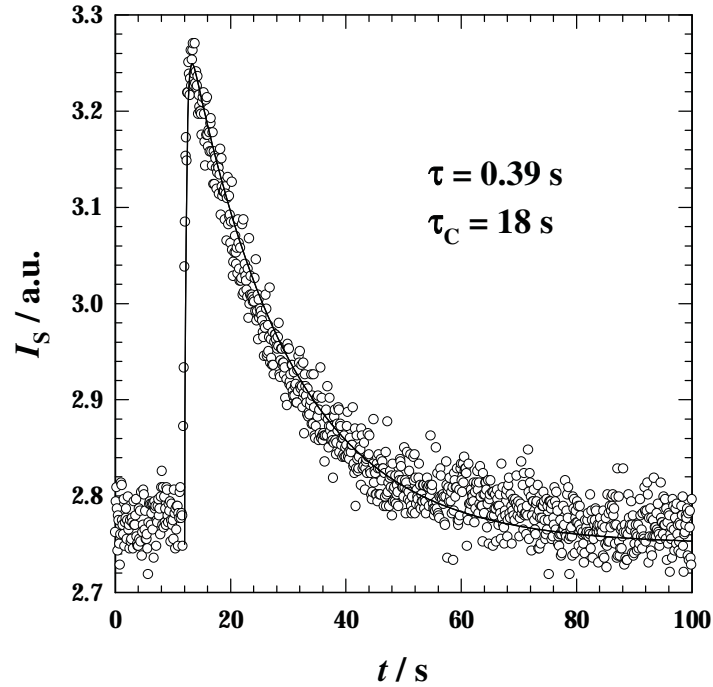
Fig. 8.5: Experimental determination of the cooling time τ_C of the temperature jump apparatus. The intensity of the scattered light I_S returns after the *T*-jump to the initial intensity I_0. The solid line shows the fit calculated from a single exponential decay function for a sample with $\phi_{B+C} = 0.1$ and $\omega_b = 0.47$ and a *T*-jump from 24.79°C → 25.19°C.

Using Eq. (8.2), the cooling time τ_C is always found to be about 20 ± 2 s independently of the sample's composition or jump amplitudes ΔT. In comparison to the enormous dependence of the structural relaxation times τ on the bilayer concentration ϕ_{B+C} this means that the cooling time τ_C is almost a constant and its exact value is of subordinate importance for determining relaxation times of less then seconds.

Optical unit

The optical unit of the temperature jump apparatus is illustrated in Fig. 8.6.
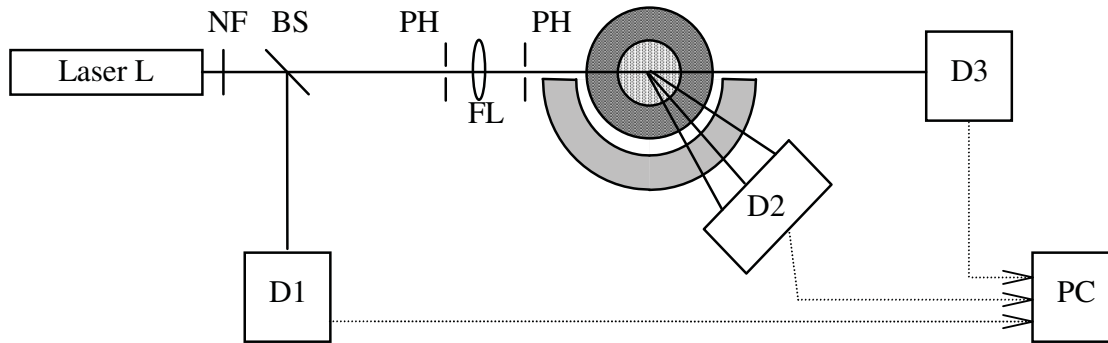
Fig. 8.6: Setup of the *T*-jump apparatus, illustrating the optical layout [27].

The operating light source for this setup is a "Millennia II" laser, produced by Spectra-Physics GmbH, Darmstadt, Germany. It is a continuous wave diode laser, emitting visible green light of the wavelength $\lambda = 532$ nm with a power output of 0.2 – 2 W, variable in steps of 0.01 W. For the experiments the power output is kept constant at 0.2 W.

The emitted laser beam can be attenuated by a neutral filter (NF) with an optical density OD = 3 for situations requiring a reduced laser intensity like sample introduction. By means of the attenuated transmitted light it can be observed whether phase separation has taken place during the introduction of the sample or if any bubbles remained in the cell. After that the emitted laser beam meets a beam splitter (BS). Part of the light is diffracted and monitored by a photodiode (D1), determining the intensity I_{ref} of the incident beam to detect potential deviations in the laser intensity. The other part has to pass a focusing unit, consisting of two pinholes (PH) and a focusing lens (FL) before entering the sample cell. Five photomultipliers (D2) are placed at different angles with respect to the incident laser, and another photodiode (D3) measures the turbidity of the sample, i.e. the transmitted light.

The change of the intensity of the scattered light can be measured as a function of time under five different detection angles. Simultaneously, the intensity of the transmitted light is measured. A rack is arranged halfway around the measuring block to keep the optical fibers in place at the different measuring angles, as can be seen in Fig. 8.7.
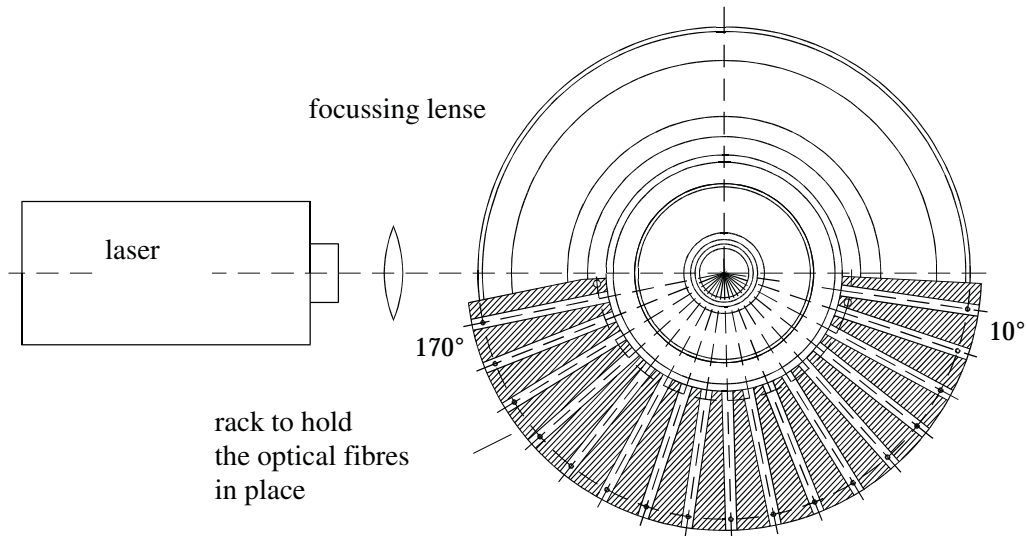
Fig. 8.7: Arrangement of optical fibers at different angles around the sample cell.

The scattered light is transferred to D2 (see Fig. 8.6) by optical fibers. D2 consists of two photomultipliers and three photodiodes (2 DIA-PMF, serial no. 0042 and 0049 from Dialog, Düsseldorf, 3 H5784-01, from Hamamatsu, Herrsching). The different photomultipliers are assigned to the different angles as follows:

Table 8.2: Assignment of the detection angles to the different photomultipliers

detector	angle ϑ
Dialog 42	40
Dialog 49	90
Hamamatsu PM1	120
Hamamatsu PM2	140
Hamamatsu PM3	60

The pneumatically actuated high voltage discharge indirectly generates a trigger impulse, which starts the monitoring of the intensity of the incident beam (I_{ref}) with the photodiode in D1, the transmitted light (I_{trans}) with the photodiode in D3 and the scattered light under the different detection angles (I_S) with the five photomultipliers in D2, shortly before and after the *T*-jump. The change of the light intensity with time is recorded with a customary 12bit-AD-card (BMC PC-20 from Conrad, Hirschau, Germany), which converts the analog voltage signal into digital information and assigns a time scale to the measured data, which are saved

as ASCI-files. The voltage range of the card is +10 V to – 10 V with a maximum resolution of 20 µs.

For the determination of I_0, the intensity of the scattered light before the T-jump perturbation, a pre-trigger period of usually 25 % is defined in which I_0 is monitored prior to the jump.

Calibration of the amplitudes ΔT of the T-jump

The amplitude of a T-jump, ΔT, is proportional to the voltage charge U applied to the capacitor. To find the exact dependence between ΔT and U a calibration curve has to be recorded.

A calibration for this T-jump apparatus was performed by UHRMEISTER [27] for the system water / NaCl – 2,6-Dimethylpyridin. This system contains a closed miscibility gap with a known critical point at $T_c = 30.62°C$ and $\gamma_c = 0.064$. Close to the critical point, i.e. near the temperature of phase separation T_c, the system shows a very strong, temperature-related increase in the intensity of the scattered light, which is governed by

$$I_S = I_0 \cdot \left(\frac{T_c - T}{T_c} \right)^{-\gamma} \tag{8.3}$$

with the critical exponent $\gamma = 1.23$. Since the temperature can be measured exactly by means of the thermistor in the upper electrode it is possible to assign single light scattering intensities of the system to certain temperatures. Measuring the scattering intensity for any number of temperatures yields an I_S-over-T-curve (see Fig. 4.3) that serves as a basis for the calibration. T-jumps are then performed from a fixed know temperature T with a constant laser power and amplifying rate of the photomultipliers (dynodes) but with different charging voltages U. Each applied charging voltage U_{cap} results in a jump with a different value of the maximally reached light scattering intensity. These maximum intensities can then be assigned to a certain end temperature by means of the I_S-over-T-plot. From the difference between the fixed starting temperature and the end temperature the amplitude ΔT can be unambiguously assigned to a certain charging voltage U.

It was found that the amplitude of the *T*-jump ΔT [K] is quadratically dependent on the capacitor's charging voltage U_{cap} [kV] [121]. Thus the following applies:

$$\Delta T = \frac{C \cdot U_{cap}^2}{2 \cdot \rho \cdot C_{p,i} \cdot V_{eff}} \equiv a \cdot U_{cap}^2 \tag{8.4}$$

with *C*   capacity

   U_{cap} voltage charge of the capacitor

   ρ   density of the sample

   $C_{p,i}$ intrinsic, isobar heat capacity

   V_{eff} effective cell volume

   a   specific constant of the *T*-jump apparatus

In Fig. 8.8 the determined jump amplitudes are plotted against the charging voltage U_{cap} of the capacitor:
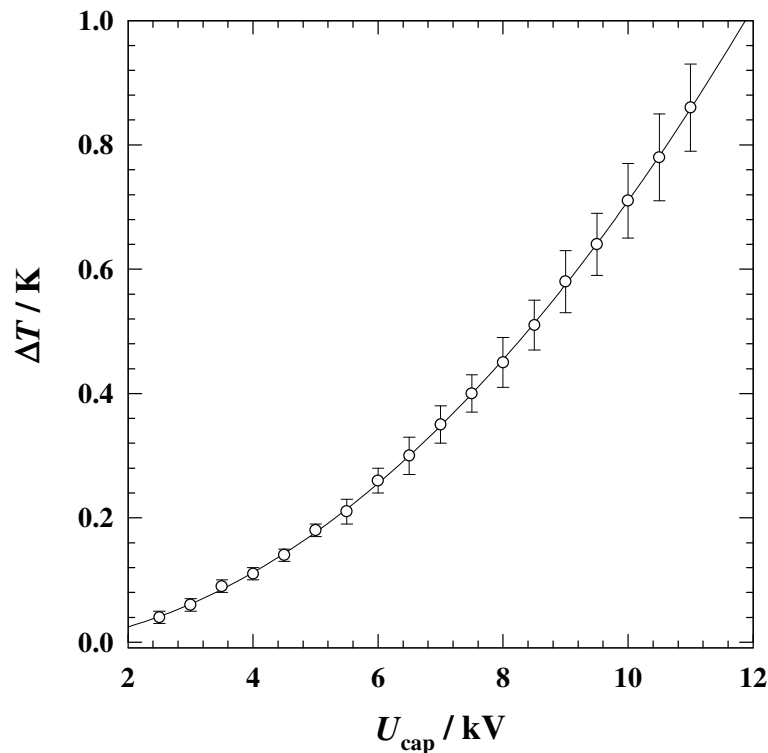
Fig. 8.8: Dependence of the determined ΔT on the charging voltage U_{cap} of the capacitor. The jump amplitude increases quadratically with the capacitor's voltage [27].

The error bars take into account that the brine – dimethylpyridin samples used for the calibration have not the same heat capacities $C_{p,i}$ and densities ρ as the samples investigated.

From a second order regression one obtains for the specific constant of the apparatus a value of $a = 7.1 \pm 10^{-3}$ [K / kV^2], i.e.

$$\Delta T = a \cdot U_{\text{cap}}{}^2 = (7.1 \pm 10^{-3}) \frac{K}{kV^2} \cdot U_{\text{cap}}{}^2 \tag{8.5}$$

In order to use Eq. (8.5) as a calibration curve for the present work the heat capacities and densities of the L$_3$ phase samples have to be comparable to those of the calibration system. To check this an L$_3$ phase sample was examined with the same calibration procedure. The difference is that the L$_3$ phase samples have a non-critical composition. As in this case the increase of the scattered light intensity is governed by the approach of the spinodal temperature T_{spin} Eq. (8.3) changes into:

$$I_S = I_0 \cdot \left(\frac{T_{spin} - T}{T_{spin}} \right)^{-\gamma} \tag{8.6}$$

The calibration was performed for an L$_3$ phase sample with $\phi_{\text{B+C}} = 0.2959$ at $\omega_b = 0.47$. The resulting dependence of ΔT on U_{cap} and the comparison with the critical system water – dimethylpyridin is illustrated in Fig. 8.9.
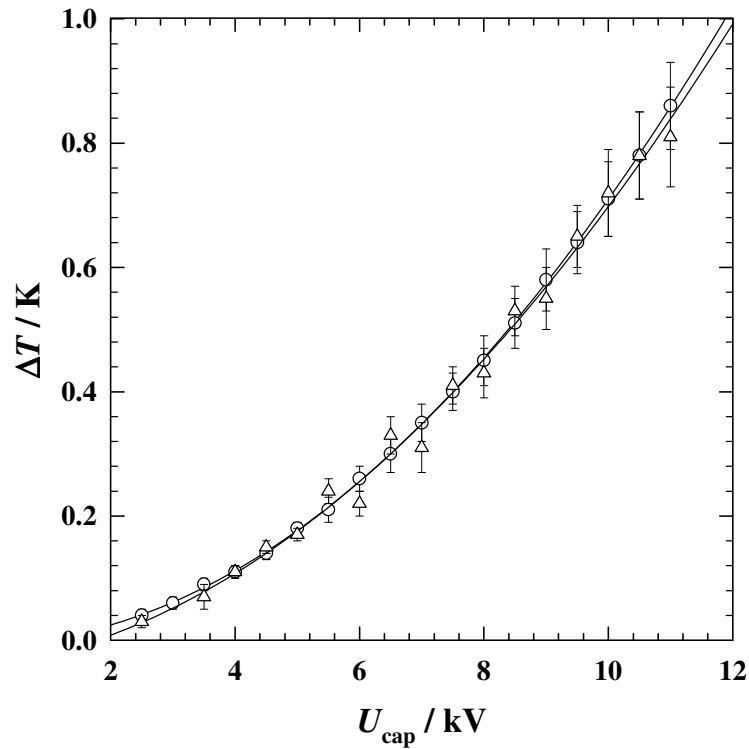
Fig. 8.9: Dependence of the determined ΔT on the charging voltage U_{cap} of the capacitor for an L_3 phase sample (triangles) and the sample with critical composition (circles). The jump amplitude increases quadratically with the capacitor's voltage.

The diagram in Fig. 8.9 proves that the heat capacities and the densities for the system brine / dimethylpyridin and the investigated systems are comparable. Thus it can be assumed that for slightly different compositions of the L_3 phase, i.e. different ϕ_{B+C} and ω_b, the heat capacities and densities of the samples will not change noteworthy. Any differences are accounted for in the margins of error. Table 8.3 shows the results of the calibration with the L_3 phase sample at $\phi_{B+C} = 0.2959$ and $\omega_b = 0.47$.

Table 8.3: Results of the calibration with the L$_3$ phase sample at $\phi_{B+C} = 0.2959$ and $\omega_b = 0.47$. With U_{cap} being the charging voltage of the capacitor, ΔT the resulting jump amplitude and $\delta\Delta T$ the error taking into account differences in the heat capacity and density due to changes in the composition

U_{cap} / kV	ΔT / K	$\delta\Delta T$ / K
2.50	0.03	0.01
3.50	0.07	0.01
4.00	0.11	0.01
4.50	0.15	0.01
5.00	0.17	0.01
5.50	0.24	0.02
6.00	0.22	0.02
6.50	0.33	0.03
7.00	0.31	0.03
7.50	0.41	0.03
8.00	0.43	0.04
8.50	0.53	0.04
9.00	0.55	0.05
9.50	0.65	0.05
10.00	0.72	0.06
10.50	0.78	0.07
11.00	0.81	0.07

8.4   Isothermal shear

In comparison to the *T*-jump experiment, the isothermal shear experiment also consists of three main elements. A magnetic stirrer providing the perturbation unit. A conductivity cell as the sample unit, and a conductivity electrode in combination with a conductivity bridge as the detection unit. The conductivity cell is mounted on a magnetic stirrer, thus providing perturbation by shear. The setup of these elements is illustrated schematically in Fig. 8.10.
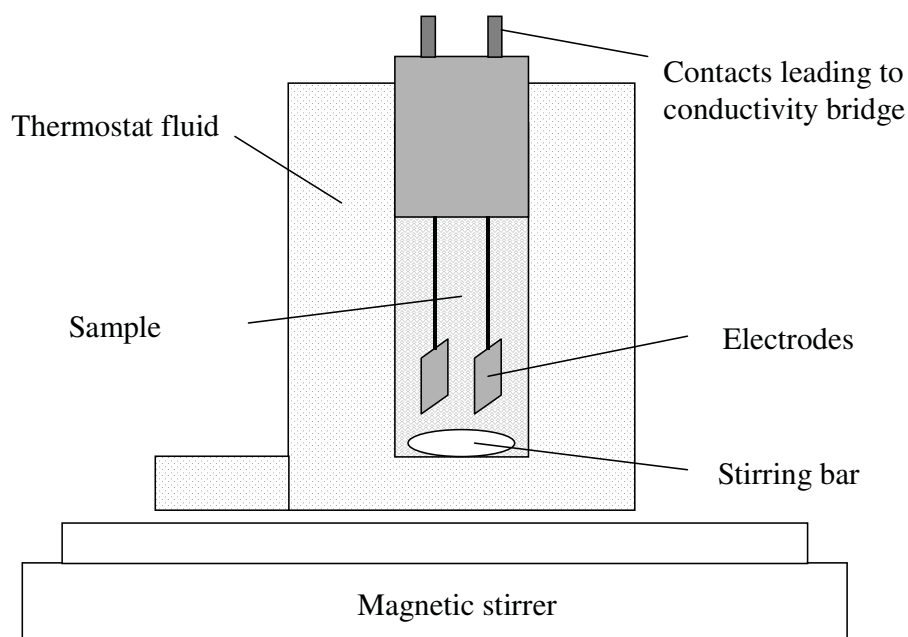
Fig. 8.10: Schematic illustration of the conductivity cell of the isothermal shear experiment.

The conductivity cell of the isothermal shear experiment consists of a custom-made jacketed test tube with a flat bottom of 15 mm diameter and a volume of about 12 mL. The jacket of the tube is connected to a customary thermostat circulating a water / diethylenglycol mixture to provide means of temperature control. The temperature is measured to a precision of ± 0.02 K by a thermocouple reaching directly into the thermostat fluid in the jacketing. For conductivity measurements a custom-made electrode is used which reaches into the test tube almost to the bottom. The electrode consists of two parallel metal plates perpendicular to the direction of flow as induced by shear. These metal plates are partially glass-coated to prevent corrosion.

The jacketed test tube is mounted on a customary magnetic stirrer MR 2000 from Heidolph, Kelheim. A 10 mm long Teflon$^{\circledR}$ coated stirring bar is located at the bottom of the conductivity cell to apply shear by setting the stirring bar in motion using the magnetic stirrer. The magnetic stirrer is infinitely variable between 0 – 1250 rpm however for all measurements a fixed frequency of 1000 rpm was applied.

Measurements of the conductivity and data acquisition are performed by an automatic precision bridge B 905 from Wayne Kerr Inc., West Sussex, England in connection with a PC equipped with a 12bit-AD-card of the type BMC PC-20 from Conrad, Hirschau, Germany. A measuring program was developed to set the stirrer in motion for the given time period, as well as starting the conductivity measurement after the shear period was completed. The change in the conductivity is monitored after shear and the resulting relaxation curves of κ_S as

a function of the time t are plotted. Fig. 8.11 shows an illustration of the complete setup of the isothermal shear method.
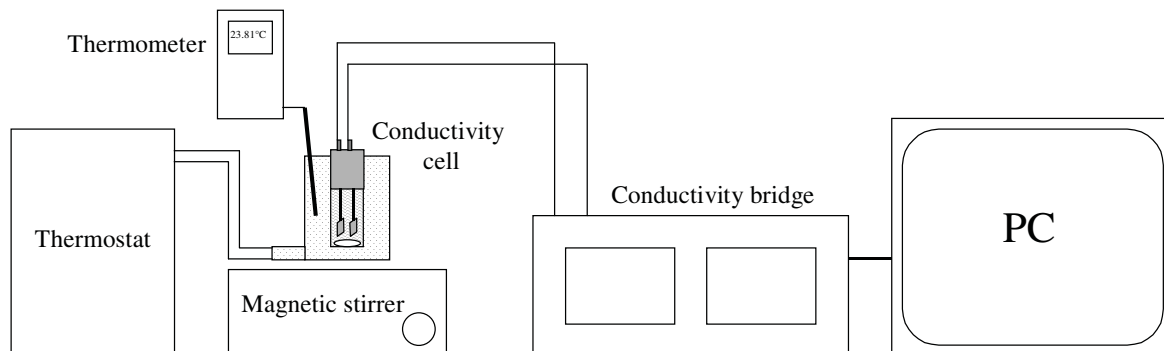
Fig. 8.11: Setup of the isothermal shear experiment.

8.5 Small-angle neutron scattering (SANS)

Small-angle neutron scattering experiments were performed at the Institute Laue Langevin (ILL) in Grenoble, France. The D22 spectrometer was used for these measurements. A schematic picture of a representative SANS setup is illustrated in Fig. 8.12.
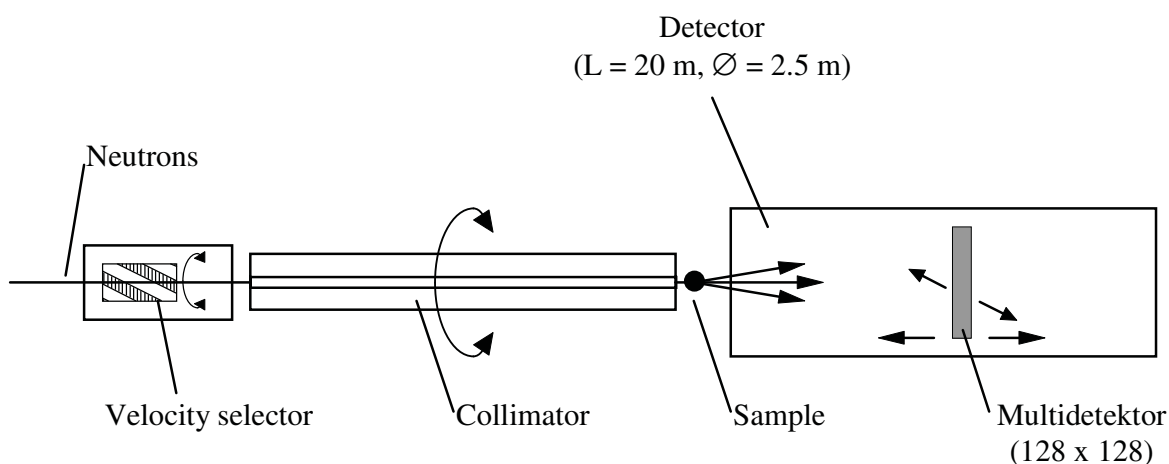
Fig. 8.12: Schematic setup of a typical SANS instrument [122].

The neutron source is produced in a nuclear reactor by fission of ^{235}U. By way of heavy water D_2O and liquid D_2 the wavelength of the neutrons is moderated to a range of $3 < \lambda < 40$ Å. Subsequently a mechanical velocity selector provides a monochromatic radiation source of $0.08 < \Delta\lambda / \lambda < 0.20$ for the experiments. The neutron beam runs through a collimator to be adjusted in diameter and divergence to directly meet the sample. In general the scattered neutron intensity is recorded by a two-dimensional sensitive area (128×128 pixel) detector.

The measurements for the L_3 phase samples were performed with a mean neutron wavelength of λ_{mean} = 6.0 Å with $\Delta\lambda / \lambda$ = 0.10. The q ranged from 0.0584 Å $^{-1}$ to 0.4698 Å $^{-1}$. The collimation was adjusted in order not to limit the resolution. Two sample-to-detector distances (17.56 m and 1.96 m) were measured with the detector 0.4 m of axis to provide data over a large q range.

Samples were equilibrated at temperatures inside the stable L_3 phase region in a separate water bath, and were then rapidly transferred to the cell holder. A custom-made cell holder was used, which could be thermally equilibrated to a precision of ±0.02 K. In this, the samples could be mixed and homogenized at the desired temperature after mounting [112]. The samples were measured in Hellma quartz cells of 0.2mm path length to minimize multiple scattering.

The raw data from the two-dimensional detectors were masked, normalized and radially averaged according to the standard procedures provided by the neutron facility. Each data set was put on absolute scale by measuring the incoherent scattering of H_2O. Data sets from the different distances overlapped without scale adjustment.

9   Appendix

9.1   *T*-jump experiments on the oil-rich L₃ phase

From the phase diagram in Fig. 2.3 it could be deduced that the L₃ phase occurs only for very high water or oil contents respectively. Consequently the evolution of the L₃ phase as a function of the surfactant concentration γ and the temperature *T* can be discussed at very high or very low values of the oil / (water + oil) mass fraction α only, i.e. either on the water-rich or oil-rich side of the phase diagram. Any mentioning of the L₃ phase in this work always refers to the water-rich L₃ phase as illustrated on the water-side of the phase diagram in Fig. 2.3. To complete the picture of the dynamics of the L₃ phases, the dynamics of oil-rich L₃ phases was also studied by *T*-jump relaxation. Unfortunately the experimental conditions, concerning the phase behavior as well as the *T*-jump experiments, were not as suitable as for the water-rich L₃ phases. These experimental circumstances will be described below along with the observed results.

9.1.1   Phase behavior

The oil-rich L₃ phase structure is inverse to that of the water-rich one. The expression "bilayer" now denotes a water-swollen bilayer dividing two equivalent oil subvolumes. Suitable parameters to describe the dependencies in these water-rich systems are found in Eq. (9.1) and Eq. (9.2). The surfactant / (water + surfactant) volume ratio ω_a and the bilayer volume fraction ϕ_{A+C} can be expressed by:

$$\omega_a = \frac{V_{surf}}{V_{water} + V_{surf}} \tag{9.1}$$

$$\phi_{A+C} = \frac{V_{water} + V_{surf}}{\sum_i V_i} \tag{9.2}$$

In Eq. (9.1) and Eq. (9.2) ω_a is equivalent to the surfactant / (oil + surfactant) volume ratio ω_b for the water-rich L₃ phase, while the bilayer concentration ϕ_{A+C} is related to the bilayer concentration ϕ_{B+C}, the difference is that oil is substituted by water. The phase behavior of the oil-rich L₃ phases was investigated and illustrated following Fig. 2.8. For the water-rich L₃

phase different ω_b represent pages in a phase prism book with the water corner of the phase prism being the spine of the book (see Fig. 2.5). Correspondingly, for the oil-rich L_3 phase the oil corner is the spine of the book, with ω_a representing different pages. In Fig. 9.1 the projection of the oil-rich L_3 channels onto one page of the inverse phase prism book are shown for three different surfactant / (water + surfactant) volume ratio ω_a with varying bilayer volume fractions ϕ_{A+C}.
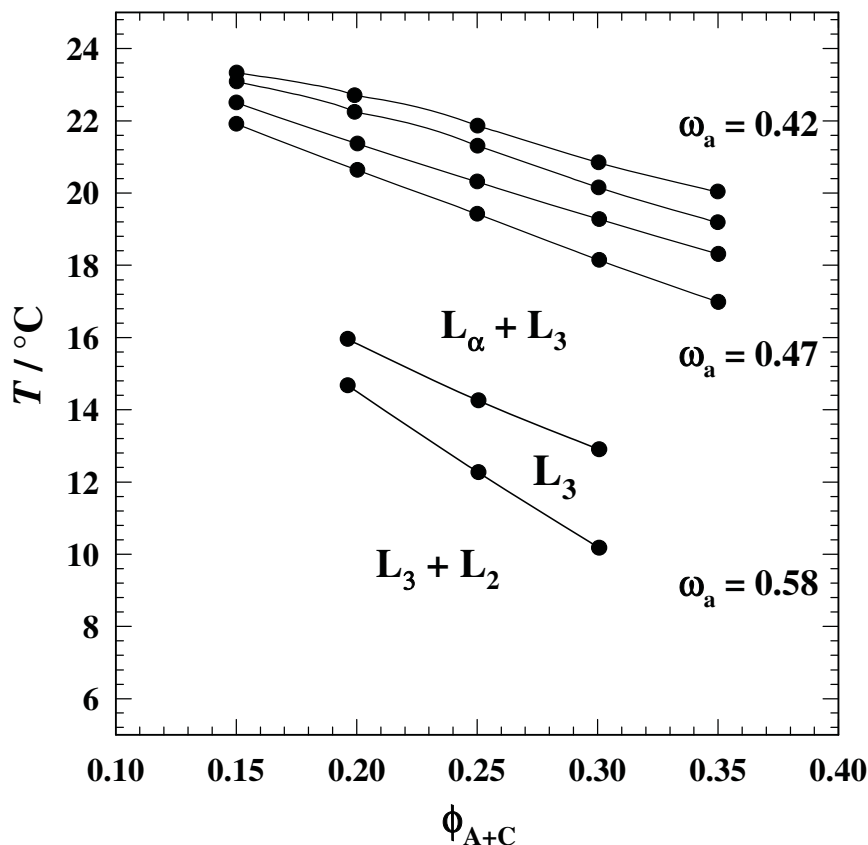
Fig. 9.1: Projection of the oil-rich L_3 phase channels measured as a function of bilayer concentration ϕ_{A+C} and temperature T onto one page of the phase prism at constant ω_a, revealing the monotonic shift towards higher temperatures, the decreasing width and reduced slopes of the L_3 phase channels under addition of water (decreasing ω_a).

Fig. 9.1 shows the shift of the L_3 bands towards higher temperatures with decreasing surfactant / (water + surfactant) volume ratio ω_a. In addition to this, the width of the oil-rich L_3 temperature range is reduced, from about 1.5 K for the L_3 phase at $\omega_a = 0.58$ down to ~ 0.3 K for $\omega_a = 0.42$. This projection of the oil-rich phase channels is already an indication for experimental difficulties. In contrast to the water-rich L_3 phases the width of the L_3 band decreases considerably with only small decreases in the surfactant / (water + surfactant) volume ratio ω_a. For any ω_a smaller than $\omega_a = 0.42$ the L_3 channel is so narrow that T-jump

experiments become impossible due to the experimental setup (see chapter 8 for details). Additionally, the one-phase L_3 channel at $\omega_a = 0.58$ is stable only at very low temperatures. Since the *T*-jump apparatus can only be operated at temperatures higher than 15 °C, no measurements are possible for $\omega_a = 0.58$. This leaves only a very restricted variation of surfactant / (water + surfactant) volume ratios ω_a for investigations of the dynamics of oil-rich L_3 phases.

9.1.2   *T*-jump relaxation

T-jump experiments were performed for $\omega_a = 0.47$ and $\omega_a = 0.42$ at varying bilayer volume fractions ϕ_{A+C}. A typical example of these *T*-jumps for a sample with $\phi_{A+C} = 0.25$ at $\omega_a = 0.47$ is illustrated in Fig. 9.2. The corresponding relaxation curve of the scattered light intensity as a function of time is illustrated in the central picture. In contrast to the scattering curves from *T*-jumps on the water-rich L_3 phase, shown in chapter 4, the scattering intensity for the oil-rich L_3 phase is decreasing with increasing temperature. This observation is in agreement with the fact that the binodal line of the oil-rich L_3 phase corresponds to the $L_3 + L_2$ phase boundary (see Fig. 2.3) whereas for the water-rich L_3 phase the binodal line is the $L_1' + L_3$ phase boundary (see chapter 5). While for the water-rich L_3 phase a *T*-jump is going towards the binodal line, the opposite is true for the oil-rich L_3 phase, hence the light scattering intensity is decreasing with temperature (for details see chapter 8, Eq. 8.6). A jump towards the binodal line is not possible with the *T*-jump apparatus, therefore the upper phase boundary of $T_{L_3 \rightarrow L_\alpha + L_3}$ is used as a reference temperature for the experiments. Taking into account the fact that the cooling time τ_C is correlated to the return time back to T_0, the initial temperature, the relaxation process as seen in the central diagram can be quantitatively described by

$$\frac{I_S(t)}{I_0} = 1 - \frac{\Delta I_S}{I_0} \cdot \left(\exp\left(-\frac{t}{\tau_C} \right) - \exp\left(\frac{t}{\tau} \right) \right) \tag{9.3}$$

with I_0 being the intensity of the scattered light before the jump, and I_S the time-dependent scattered light intensity. The amplitude $\Delta I_S / I_0$ is determined by the intensity decrease associated with the temperature jump ΔT. The values for I_0 can be determined from the experimental data. A fixed value of $\tau_C = 17.7$ s is used, which is known from calibration measurements (see chapter 8). For the example in Fig. 9.2 the fit function (Eq. (9.3)) yields

the amplitude $\Delta I_S / I_0 = 0.102$ and the relaxation time $\tau = 0.041$ s. The residual plot at the bottom of Fig. 9.2 shows some background noise, but no systematic deviations between the measured data points and the fitted curve obtained by non-linear regression, therefore this method is applicable likewise to the water-rich and the oil-rich L_3 phase.
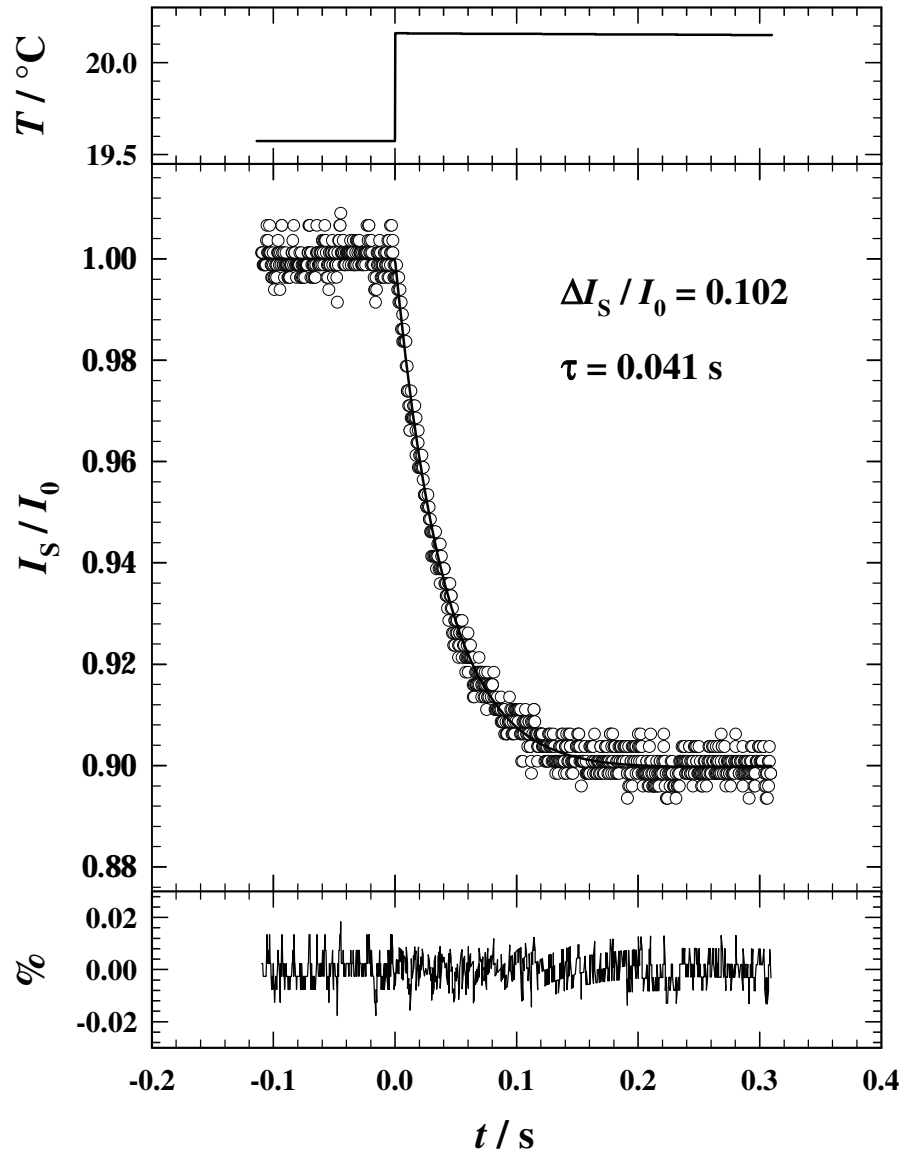
Fig. 9.2: A typical analysis of a *T*-jump from $T_0 = 19.58$ °C to $T = 20.16$ °C (top) for a sample with $\phi_{A+C} = 0.25$ and $\omega_a = 0.47$ observed at $\vartheta = 90°$. This experiment can be entirely described by Eq. (9.3). With given values for I_0, t and τ_c the amplitude $\Delta I_S / I_0$ and the relaxation time τ can be obtained from non-linear regression (middle). The residual plot shows no systematic deviations between the measured data points and the fitted curve (bottom).

One of the experimental problems encountered with this method on the oil-rich side is the fact that due to the smaller brine content, the conductivity of the sample in the cell is greatly

reduced. The heating time $\tau_H = R_{cell} \cdot C / 2$, with R_{cell} being the resistance of the sample in the cell and C the capacitance (10 nF) of the capacitor, is dependent on the sample's composition. With a greatly increased resistances of 3000 – 7000 Ω, in comparison to 100 – 1000 Ω in the water-rich L_3 sample, heating times between $\tau_H = 15$ μs and $\tau_H = 35$ μs were found. This means on the one hand, that the *T*-jump is not quasi-instantaneous anymore and on the other hand, more importantly, that non-uniform heat transfer through the sample can cause field-effects. An example of this is illustrated in Fig. 9.3.
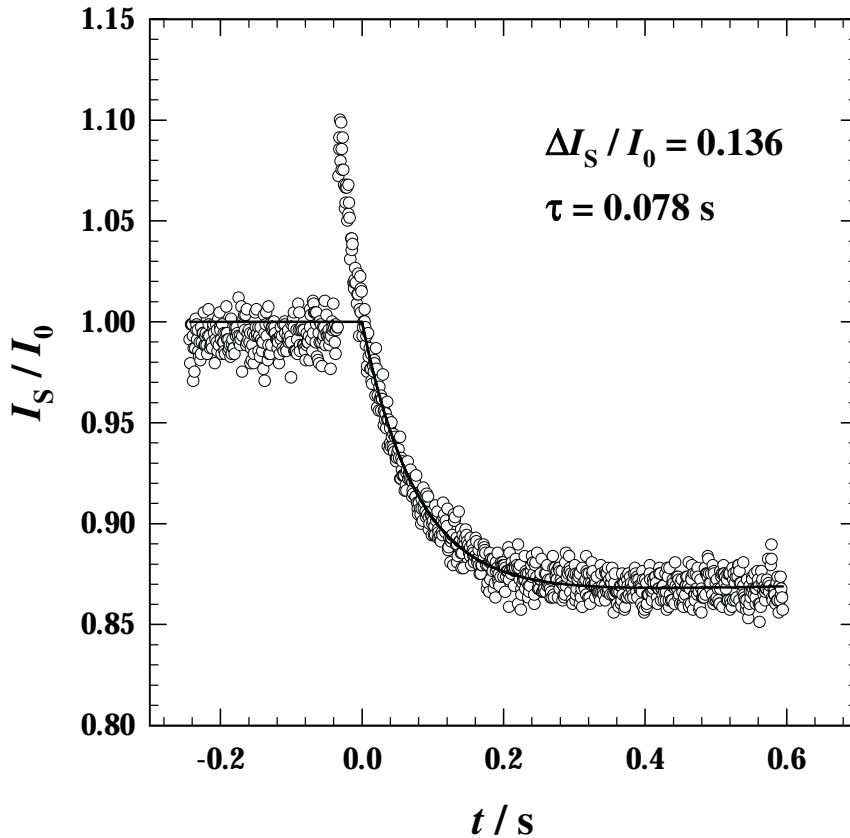
Fig. 9.3: Demonstration of a field-effect for a *T*-jump from $T_0 = 21.02$ °C to $T = 21.23$ °C (top) for a sample with $\phi_{A+C} = 0.15$ and $\omega_a = 0.47$ observed at $\vartheta = 90°$.

This field effect can either be expressed by an overshoot towards higher scattering intensities, as illustrated in Fig. 9.3, or more problematic, in a time-dependent overshoot towards lower light scattering intensities, resulting in a scattering curve that can not be described by a single exponential anymore.

Another problem is the height of the generated *T*-jump as a function of the voltage charge of the capacitor. For the water-rich L_3 phase this can be calculated using the relation $\Delta T = b \cdot U_{cap}^2$, with the empirical constant b having a value of $b = 7.1 \ (\pm 0.5) \times 10^{-3}$ K·(kV)$^{-2}$, which

was obtained from calibration measurements (see chapter 8 for details). Unfortunately calibration measurements on the oil-rich L_3 phase produced no conclusive results as to the value of *b*. However, the heights of the *T*-jumps are not crucial for the determination of the relaxation time constants, as long as the jumps are performed onto a fixed reference temperature. The actual height of the *T*-jumps can be roughly evaluated by means of the calibration used for the water-rich L_3 phase.

Those relaxation time constants that can be measured under these restricted conditions are plotted in Fig. 9.4 as a function of the bilayer volume fraction ϕ_{A+C} for two surfactant / (water + surfactant) volume fractions ω_a.
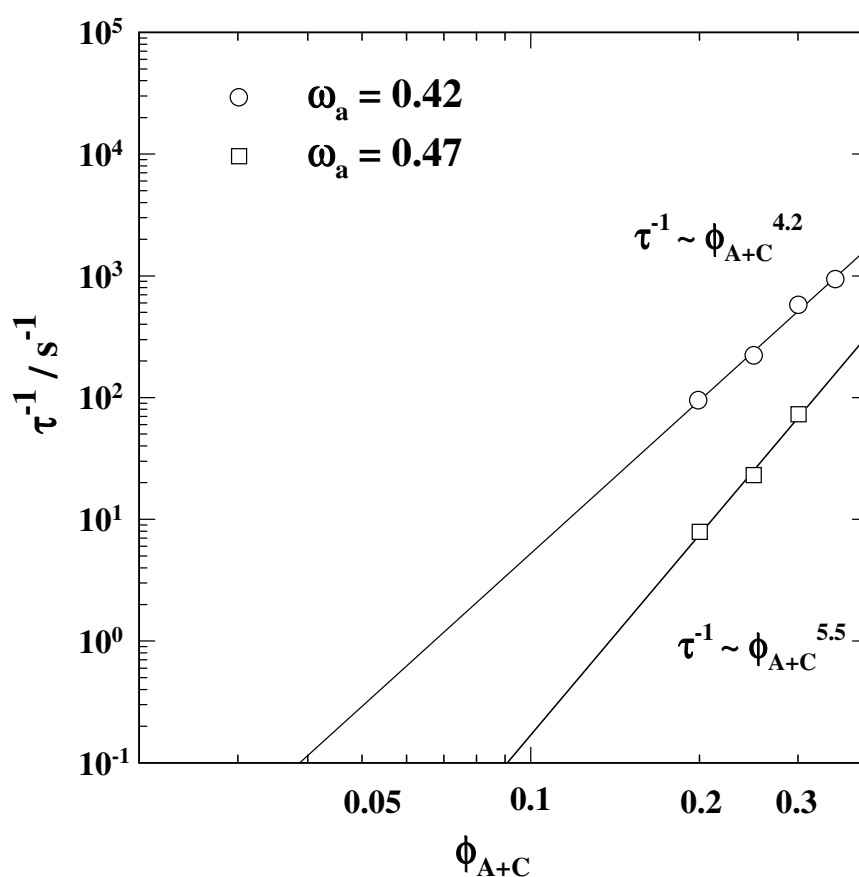
Fig. 9.4: Relaxation time constants τ^{-1} in dependence of the oil-rich L_3 phase bilayer volume fraction ϕ_{A+C} for the system H_2O / NaCl – *n*-octane – $C_{10}E_4$ for two different surfactant / (water + surfactant) volume fractions ω_a.

In the double-logarithmic plot (Fig. 9.4) the relaxation time constants can be fitted linearly, resulting in effective power law dependencies of $\tau^{-1} \sim \phi_{A+C}^{n}$ with *n* being 4.2 and 5.5 respectively. These results are similar to those in Fig. 4.12 and Fig. 4.13 for high bilayer

volume fractions ϕ_{B+C}. It has to be taken into account though that including very low ϕ_{B+C} into the curves resulted in non-linear dependencies (Fig. 4.19). The same could potentially be true for the oil-rich L_3 phase systems. However, due to the phase behavior of these systems (see Fig. 9.1) only a very limited number of data could be produced for bilayer volume fractions ϕ_{A+C} higher than $\phi_{A+C} \geq 0.2$; lower ϕ_{A+C} were not accessible by T-jump. As a result of this, as well as due to the problems arising from field effects and T-jump height calibration, these results were not generally included into the discussion of this work.

9.2   Tables

9.2.1   *T*-jump experiments

Tables 9.1: Bilayer volume fractions ϕ_{B+C}, compositions $m_{H_2O/NaCl}$, $m_{n-octane}$, and $m_{C_{10}E_4}$ of the L_3 phase samples for T-jump experiments in [g] and the phase boundary temperatures $T_{L_3+L_\alpha \to L_3}$ and $T_{L_3 \to L_1'+L_3}$ of the respective L_3 phase coexistence regions in [°C] for different surfactant / (oil + surfactant) volume fractions ω_b.

(a) $\omega_b = 1.00$

ϕ_{B+C}	$\dfrac{m_{H_2O/NaCl}}{g}$	$\dfrac{m_{n-octane}}{g}$	$\dfrac{m_{C_{10}E_4}}{g}$	$\dfrac{T_{L_3+L_\alpha \to L_3}}{°C}$	$\dfrac{T_{L_3 \to L_1'+L_3}}{°C}$
0.0346	13.5526	-	0.4661	43.2600	46.1500
0.0500	13.2740	-	0.6713	43.2100	49.5200
0.0700	12.9970	-	0.9401	48.1000	51.7700

(b) $\omega_b = 0.90$

ϕ_{B+C}	$\dfrac{m_{H_2O/NaCl}}{g}$	$\dfrac{m_{n-octane}}{g}$	$\dfrac{m_{C_{10}E_4}}{g}$	$\dfrac{T_{L_3+L_\alpha \to L_3}}{°C}$	$\dfrac{T_{L_3 \to L_1'+L_3}}{°C}$
0.0400	13.4161	0.0394	0.4834	43.2500	44.6000
0.0501	12.3254	0.0461	0.5618	44.5500	46.0600
0.0751	11.8730	0.0676	0.8335	46.7000	48.5900
0.1000	12.5155	0.0975	1.2023	47.5400	49.5500
0.1497	10.9218	0.1349	1.6643	49.3300	51.4400
0.1999	10.6979	0.1876	2.3134	50.9600	53.3000
0.2498	9.6384	0.2252	2.7769	52.1900	54.7800

(c) $\omega_b = 0.81$

ϕ_{B+C}	$\dfrac{m_{H_2O/NaCl}}{g}$	$\dfrac{m_{n-octane}}{g}$	$\dfrac{m_{C_{10}E_4}}{g}$	$\dfrac{T_{L_3+L_\alpha \to L_3}}{°C}$	$\dfrac{T_{L_3 \to L_1'+L_3}}{°C}$
0.0751	12.1819	0.1351	0.7653	39.4300	40.8500
0.1000	12.3487	0.1876	1.0629	39.8400	41.3700
0.1501	11.8160	0.2852	1.6159	41.3100	43.0800
0.2000	10.9757	0.3752	2.1259	42.7000	44.6800
0.2500	9.8775	0.4501	2.5507	44.0800	46.4400

(d) $\omega_b = 0.69$

ϕ_{B+C}	$\dfrac{m_{H_2O/NaCl}}{g}$	$\dfrac{m_{n-octane}}{g}$	$\dfrac{m_{C_{10}E_4}}{g}$	$\dfrac{T_{L_3+L_\alpha \to L_3}}{°C}$	$\dfrac{T_{L_3 \to L_1'+L_3}}{°C}$
0.1219	12.2910	0.3758	1.1273	31.8600	33.0800
0.1524	11.8768	0.4703	1.4109	32.5000	33.8100
0.2029	11.1829	0.6268	1.8804	33.3400	34.9300
0.2534	10.4858	0.7834	2.3502	34.4100	36.2600
0.3038	9.7798	0.9396	2.8187	35.5600	37.6400

(e) $\omega_b = 0.58$

ϕ_{B+C}	$\dfrac{m_{H_2O/NaCl}}{g}$	$\dfrac{m_{n-octane}}{g}$	$\dfrac{m_{C_{10}E_4}}{g}$	$\dfrac{T_{L_3+L_\alpha \to L_3}}{°C}$	$\dfrac{T_{L_3 \to L_1'+L_3}}{°C}$
0.1020	12.5757	0.4261	0.7914	26.6400	27.4800
0.1528	11.8762	0.6390	1.1867	27.5000	28.4200
0.2035	11.1776	0.8522	1.5825	28.6800	29.4000
0.2541	10.4820	1.0651	1.9780	29.1800	30.1000
0.3045	9.7835	1.2787	2.3731	29.9700	31.3500

(f) $\omega_b = 0.47$

ϕ_{B+C}	$\dfrac{m_{H_2O/NaCl}}{g}$	$\dfrac{m_{n-octane}}{g}$	$\dfrac{m_{C_{10}E_4}}{g}$	$\dfrac{T_{L_3+L_\alpha \to L_3}}{°C}$	$\dfrac{T_{L_3 \to L_1'+L_3}}{°C}$
0.0750	12.9246	0.3898	0.4756	23.9900	24.7200
0.1045	12.5134	0.5428	0.6634	24.5000	25.1900
0.1549	11.8090	0.8036	0.9822	25.1800	25.8800
0.2044	11.1180	1.0609	1.2967	25.8300	26.5300
0.2512	10.4682	1.3037	1.5905	26.5000	27.2300
0.2978	9.8133	1.5240	1.8898	27.1000	27.9100

(g) $\omega_b = 0.37$

ϕ_{B+C}	$\dfrac{m_{H_2O/NaCl}}{g}$	$\dfrac{m_{n-octane}}{g}$	$\dfrac{m_{C_{10}E_4}}{g}$	$\dfrac{T_{L_3+L_\alpha \to L_3}}{°C}$	$\dfrac{T_{L_3 \to L_1'+L_3}}{°C}$
0.0750	13.0938	0.4679	0.3828	22.9500	23.4500
0.1000	13.4973	0.6598	0.5399	23.3300	23.7600
0.1563	13.4927	1.1002	0.9002	24.0300	24.3800
0.2001	11.4941	1.2658	1.0356	24.5100	24.8100
0.2500	10.4926	1.5401	1.2600	24.9900	25.2300
0.2999	9.6219	1.8149	1.4849	25.4400	25.7200

Tables 9.2: Bilayer volume fraction ϕ_{B+C}-dependence of the relaxation times τ in [s] and the relaxation time constants τ^{-1} [s^{-1}] for T-jump experiments for different surfactant / (oil + surfactant) volume fractions ω_b

(a) $\omega_b = 0.90$

ϕ_{B+C}	$\dfrac{\tau}{s}$	$\dfrac{\tau^{-1}}{s^{-1}}$
0.0400	0.3588	2.7868
0.0500	0.1480	6.7552
0.0751	0.0107	93.7500
0.1000	4.3687e-3	228.8990
0.1497	734.10e-6	1362.2122
0.1999	166.01e-6	6023.5521
0.2498	79.004e-6	12657.5336

(b) $\omega_b = 0.81$

ϕ_{B+C}	$\dfrac{\tau}{s}$	$\dfrac{\tau^{-1}}{s^{-1}}$
0.0751	1.0870	0.9200
0.1000	0.2577	3.8800
0.1501	0.0258	38.7600
0.2000	3.1863e-3	313.8400
0.2500	664.28e-6	1505.4000

(c) $\omega_b = 0.69$

ϕ_{B+C}	$\dfrac{\tau}{s}$	$\dfrac{\tau^{-1}}{s^{-1}}$
0.1219	0.9077	1.1017
0.1524	0.1897	5.2709
0.2029	0.0165	60.6061
0.2534	2.0966e-3	476.9551
0.3038	369.48e-6	2706.4820

(d) $\omega_b = 0.58$

ϕ_{B+C}	$\dfrac{\tau}{s}$	$\dfrac{\tau^{-1}}{s^{-1}}$
0.1020	1.8252	0.5479
0.1528	0.0810	12.3406
0.2035	7.5367e-3	132.6837
0.2541	1.3616e-3	734.4166
0.3045	284.24e-6	3518.1330

(e) $\omega_b = 0.47$

ϕ_{B+C}	$\dfrac{\tau}{s}$	$\dfrac{\tau^{-1}}{s^{-1}}$
0.0750	2.1368	0.4680
0.1045	0.3713	2.6932
0.1549	0.0290	34.4828
0.2044	3.7243e-3	268.5068
0.2512	676.08e-6	1479.1061
0.2978	240.10e-6	4165.0000

(f) $\omega_b = 0.37$

ϕ_{B+C}	$\dfrac{\tau}{s}$	$\dfrac{\tau^{-1}}{s^{-1}}$
0.0750	0.1200	8.3333
0.1000	0.0297	33.6927
0.1563	7.4769e-3	133.7447
0.2001	1.6646e-3	600.7295
0.2500	597.98e-6	1672.3107
0.2999	297.62e-6	3359.9758

Table 9.3: Surfactant / (oil + surfactant) volume fractions ω_b, bilayer volume fractions ϕ_{B+C}, and compositions ($m_{H_2O/NaCl}$, $m_{n-octane}$, and $m_{C_{10}E_4}$) in [g] of the L_3 phase samples for the ARRHENIUS-like plots.

ω_b	ϕ_{B+C}	$\dfrac{m_{H_2O/NaCl}}{g}$	$\dfrac{m_{n-octane}}{g}$	$\dfrac{m_{C_{10}E_4}}{g}$
0.8059	0.1000	11.1326	0.1692	0.9582
0.8045	0.1504	10.6376	0.2594	1.4561
0.8060	0.2000	9.8783	0.3374	1.9125
0.6885	0.1226	13.1946	0.4044	1.2192
0.6870	0.1525	12.6888	0.5034	1.5072
0.6878	0.2027	11.9361	0.6675	2.0058
0.5756	0.1023	11.3254	0.3858	0.7138
0.5763	0.1528	10.6941	0.5761	1.0690
0.5769	0.2032	10.0607	0.7647	1.4221
0.4731	0.1046	11.2722	0.4885	0.5983
0.4699	0.1531	10.8442	0.7320	0.8853
0.4722	0.2046	10.0088	0.9572	1.1682
0.4217	0.1002	11.0837	0.5027	0.5000
0.4230	0.1500	10.4637	0.7504	0.7505
0.4231	0.1999	9.8449	0.9996	1.0000
0.4230	0.2501	9.2270	1.2508	1.2507
0.3749	0.0998	12.1772	0.5941	0.4861
0.3750	0.1560	12.1799	0.9914	0.8116
0.3742	0.2004	10.3447	1.1428	0.9322

Tables 9.4: The initial temperatures T_0 in [°C] and final jump temperatures T in [°C] of T-jumps determined for the ARRHENIUS-like plots, the resulting relaxation times τ in [s], the inverse final temperatures T^{-1} in [$10^{-3} \cdot \mathrm{K}^{-1}$] and the logarithm of the relaxation time constants $\ln \tau^{-1}$ for different surfactant / (oil + surfactant) volume fractions ω_b with three (0.10, 0.15 and 0.20) bilayer volume fractions ϕ_{B+C} each.

(a1) $\omega_b = 0.81$ and $\phi_{B+C} = 0.1000$

$\dfrac{T_0}{°C}$	$\dfrac{T}{°C}$	$\dfrac{\tau}{\mathrm{s}}$	$\dfrac{T^{-1}}{10^{-3} \cdot \mathrm{K}^{-1}}$	$\ln \tau^{-1}$
40.2800	40.3900	0.2630	3.1894	1.3356
40.2800	40.4200	0.3231	3.1891	1.1299
40.2800	40.4600	0.3319	3.1887	1.1029
40.2800	40.4900	0.3266	3.1884	1.1191
40.2800	40.5400	0.3280	3.1879	1.1147
40.3100	40.6100	0.3123	3.1871	1.1637
40.3100	40.6600	0.3085	3.1866	1.1759
40.3100	40.7100	0.3247	3.1861	1.1249
40.3100	40.7600	0.3250	3.1856	1.1239
40.3100	40.8200	0.3133	3.1850	1.1605
40.3100	40.8900	0.3183	3.1843	1.1448
40.3100	40.9500	0.3188	3.1837	1.1431
40.3100	41.0200	0.3030	3.1830	1.1941
40.3100	41.0900	0.3047	3.1823	1.1884
40.3100	41.1700	0.3134	3.1815	1.1602
40.3100	41.2500	0.2856	3.1807	1.2533
40.3100	41.3300	0.3116	3.1799	1.1659
40.3100	41.4200	0.3158	3.1789	1.1525
40.3100	41.5100	0.3018	3.1780	1.1979

(a2) $\omega_b = 0.81$ and $\phi_{B+C} = 0.1504$

$\dfrac{T_0}{°C}$	$\dfrac{T}{°C}$	$\dfrac{\tau}{s}$	$\dfrac{T^{-1}}{10^{-3} \cdot K^{-1}}$	$\ln \tau^{-1}$
41.6200	41.6800	0.0331	3.1763	3.4072
41.6200	41.7100	0.0417	3.1760	3.1773
41.6200	41.7300	0.0331	3.1758	3.4082
41.6200	41.7600	0.0305	3.1755	3.4900
41.6200	41.8000	0.0308	3.1751	3.4802
41.6200	41.8300	0.0311	3.1748	3.4695
41.6200	41.8800	0.0332	3.1743	3.4042
41.6200	41.9200	0.0310	3.1739	3.4748
41.6200	41.9700	0.0322	3.1734	3.4358
41.6200	42.0200	0.0325	3.1729	3.4265
41.6200	42.0700	0.0323	3.1724	3.4327
41.6200	42.1300	0.0313	3.1718	3.4641
41.6200	42.2000	0.0310	3.1711	3.4738
41.6200	42.2600	0.0308	3.1705	3.4792
41.6200	42.3300	0.0309	3.1698	3.4781
41.6200	42.4000	0.0300	3.1691	3.5077
41.6200	42.4800	0.0307	3.1683	3.4846
41.6200	42.5600	0.0297	3.1675	3.5166
41.6200	42.6400	0.0300	3.1667	3.5077
41.6200	42.7300	0.0289	3.1658	3.5451
41.6200	42.8200	0.0291	3.1649	3.5382
41.6200	42.9100	0.0287	3.1640	3.5520
41.6200	43.0100	0.0283	3.1630	3.5661

(a3) $\omega_b = 0.81$ and $\phi_{B+C} = 0.2000$

$\dfrac{T_0}{°C}$	$\dfrac{T}{°C}$	$\dfrac{\tau}{10^{-3} \cdot s}$	$\dfrac{T^{-1}}{10^{-3} \cdot K^{-1}}$	$\ln \tau^{-1}$
43.2900	43.3500	6.4052	3.1596	5.0506
43.2900	43.3800	6.9986	3.1593	4.9620
43.2900	43.4000	4.2706	3.1591	5.4560
43.2900	43.4300	6.1322	3.1588	5.0942
43.2900	43.4700	5.6578	3.1584	5.1747
43.2900	43.5000	5.7909	3.1581	5.1515
43.2900	43.5500	4.7180	3.1576	5.3564
43.2900	43.5900	5.2787	3.1572	5.2441
43.2900	43.6400	4.8605	3.1567	5.3266
43.2900	43.6900	5.3283	3.1562	5.2347
43.2900	43.7400	5.1965	3.1557	5.2598
43.2900	43.8000	5.1588	3.1551	5.2670
43.2900	43.8700	4.8959	3.1544	5.3194
43.2900	43.9300	4.9955	3.1538	5.2992
43.2900	44.0000	4.8431	3.1531	5.3302
43.2900	44.0700	4.9388	3.1524	5.3106
43.2900	44.1500	4.8934	3.1516	5.3199
43.2900	44.2300	4.7515	3.1508	5.3493
43.2900	44.3100	4.7436	3.1500	5.3510
43.2900	44.4000	4.7159	3.1491	5.3568
43.2900	44.4900	4.6366	3.1482	5.3738
43.2900	44.5800	4.5869	3.1473	5.3846
43.2900	44.6800	4.6469	3.1463	5.3716

(b1) $\omega_b = 0.69$ and $\phi_{B+C} = 0.1226$

$\dfrac{T_0}{^\circ C}$	$\dfrac{T}{^\circ C}$	$\dfrac{\tau}{s}$	$\dfrac{T^{-1}}{10^{-3} \cdot K^{-1}}$	$\ln \tau^{-1}$
32.5200	32.8200	0.2473	3.2683	1.3970
32.5200	32.8700	0.2372	3.2678	1.4389
32.5200	32.9200	0.2313	3.2672	1.4639
32.5200	32.9700	0.2290	3.2667	1.4742
32.5200	33.0300	0.2236	3.2661	1.4979
32.5200	33.1000	0.2158	3.2653	1.5332
32.5200	33.1600	0.2114	3.2647	1.5538
32.5300	33.2400	0.2051	3.2638	1.5841
32.5300	33.3100	0.1937	3.2631	1.6414
32.5300	33.3900	0.1930	3.2622	1.6449
32.5300	33.4700	0.1881	3.2614	1.6710
32.5300	33.5500	0.1822	3.2605	1.7025
32.5300	33.6400	0.1728	3.2596	1.7554

(b2) $\omega_b = 0.69$ and $\phi_{B+C} = 0.1525$

$\dfrac{T_0}{^\circ C}$	$\dfrac{T}{^\circ C}$	$\dfrac{\tau}{s}$	$\dfrac{T^{-1}}{10^{-3} \cdot K^{-1}}$	$\ln \tau^{-1}$
33.5200	33.8700	0.0319	3.2571	3.4462
33.5200	33.9200	0.0316	3.2566	3.4557
33.5200	33.9700	0.0303	3.2561	3.4977
33.5200	34.0300	0.0291	3.2554	3.5359
33.5200	34.1000	0.0281	3.2547	3.5732
33.5200	34.1600	0.0261	3.2540	3.6458
33.5200	34.2300	0.0264	3.2533	3.6331
33.5200	34.3000	0.0264	3.2526	3.6331
33.5200	34.3800	0.0255	3.2517	3.6691
33.5200	34.4600	0.0245	3.2509	3.7077
33.5200	34.5400	0.0235	3.2500	3.7522
33.5200	34.6300	0.0231	3.2491	3.7665
33.5200	34.7200	0.0221	3.2481	3.8107

(b3) $\omega_b = 0.69$ and $\phi_{B+C} = 0.2027$

$\dfrac{T_0}{°C}$	$\dfrac{T}{°C}$	$\dfrac{\tau}{10^{-3} \cdot s}$	$\dfrac{T^{-1}}{10^{-3} \cdot K^{-1}}$	$\ln \tau^{-1}$
35.1200	35.6300	3.2986	3.2386	5.7143
35.1200	35.7000	3.1911	3.2378	5.7474
35.1200	35.7600	3.1778	3.2372	5.7516
35.1200	35.8300	2.9127	3.2365	5.8387
35.1200	35.9000	2.8707	3.2357	5.8532
35.1200	35.9800	2.9582	3.2349	5.8232
35.1200	36.0600	2.8982	3.2340	5.8437
35.1200	36.1400	2.7712	3.2332	5.8885
35.1200	36.2300	2.6793	3.2323	5.9222
35.1200	36.3200	2.5929	3.2313	5.9550
35.1200	36.4100	2.5554	3.2304	5.9696
35.1200	36.5100	2.5152	3.2293	5.9854

(c1) $\omega_b = 0.58$ and $\phi_{B+C} = 0.1023$

$\dfrac{T_0}{°C}$	$\dfrac{T}{°C}$	$\dfrac{\tau}{s}$	$\dfrac{T^{-1}}{10^{-3} \cdot K^{-1}}$	$\ln \tau^{-1}$
26.5100	26.5700	3.4553	3.3364	-1.2399
26.5100	26.6000	3.6518	3.3361	-1.2952
26.5100	26.6200	3.1379	3.3359	-1.1436
26.5100	26.6500	2.5740	3.3356	-0.9455
26.5100	26.6900	2.3708	3.3351	-0.8632
26.5100	26.7200	2.1511	3.3348	-0.7660
26.5100	26.7700	2.1836	3.3342	-0.7810
26.5100	26.8100	2.0240	3.3338	-0.7051
26.5100	26.8600	2.0204	3.3332	-0.7033
26.5100	26.9100	2.0347	3.3327	-0.7104
26.5100	26.9600	1.9930	3.3321	-0.6896
26.5100	27.0200	2.0315	3.3314	-0.7088
26.5100	27.0900	1.9554	3.3307	-0.6706
26.5100	27.1500	1.9024	3.3300	-0.6431
26.5100	27.2200	1.8832	3.3292	-0.6330
26.5100	27.2900	1.7969	3.3285	-0.5861
26.5100	27.3700	1.6977	3.3276	-0.5293
26.5100	27.4500	1.6809	3.3267	-0.5193
26.5100	27.5300	1.6181	3.3258	-0.4813

(c2) $\omega_b = 0.58$ and $\phi_{B+C} = 0.1528$

$\dfrac{T_0}{°C}$	$\dfrac{T}{°C}$	$\dfrac{\tau}{s}$	$\dfrac{T^{-1}}{10^{-3} \cdot K^{-1}}$	$\ln \tau^{-1}$
27.6100	27.6700	0.1261	3.3242	2.0707
27.6100	27.7000	0.1401	3.3239	1.9654
27.6100	27.7200	0.1341	3.3237	2.0094
27.6100	27.7500	0.1303	3.3234	2.0382
27.6100	27.7900	0.1254	3.3229	2.0762
27.6100	27.8200	0.1182	3.3226	2.1354
27.6100	27.8700	0.1213	3.3220	2.1095
27.6100	27.9100	0.1177	3.3216	2.1399
27.6100	27.9600	0.1120	3.3210	2.1893
27.6100	28.0100	0.1054	3.3205	2.2497
27.6100	28.0600	0.1031	3.3199	2.2721
27.6100	28.1200	0.1030	3.3193	2.2727
27.6100	28.1900	0.0977	3.3185	2.3262
27.6100	28.2500	0.0924	3.3179	2.3820
27.6100	28.3200	0.0882	3.3171	2.4285
27.6100	28.3900	0.0839	3.3163	2.4781
27.6100	28.4700	0.0810	3.3154	2.5129
27.6100	28.5500	0.0766	3.3146	2.5692
27.6100	28.6300	0.0726	3.3137	2.6228
27.6100	28.7200	0.0675	3.3127	2.6951
27.6100	28.8100	0.0639	3.3117	2.7510

(c3) $\omega_b = 0.58$ and $\phi_{B+C} = 0.2032$

$\dfrac{T_0}{°C}$	$\dfrac{T}{°C}$	$\dfrac{\tau}{s}$	$\dfrac{T^{-1}}{10^{-3} \cdot K^{-1}}$	$\ln \tau^{-1}$
28.5400	28.6000	0.0136	3.3140	4.2952
28.5400	28.6300	0.0146	3.3137	4.2290
28.5400	28.6500	0.0141	3.3135	4.2639
28.5400	28.6800	0.0135	3.3131	4.3026
28.5400	28.7200	0.0141	3.3127	4.2639
28.5400	28.7500	0.0143	3.3124	4.2498
28.5400	28.8000	0.0138	3.3118	4.2831
28.5400	28.8400	0.0124	3.3114	4.3928
28.5400	28.8900	0.0117	3.3108	4.4510
28.5400	28.9400	0.0116	3.3103	4.4539
28.5400	28.9900	0.0113	3.3097	4.4830
28.5400	29.0500	0.0104	3.3091	4.5659
28.5400	29.1200	0.0101	3.3083	4.5966
28.5400	29.1800	9.7803e-3	3.3076	4.6274
28.5400	29.2500	9.2868e-3	3.3069	4.6792
28.5400	29.3200	8.8481e-3	3.3061	4.7276
28.5400	29.4000	8.6235e-3	3.3052	4.7533
28.5400	29.4800	8.2441e-3	3.3044	4.7983
28.5400	29.5600	7.8990e-3	3.3035	4.8410
28.5400	29.6500	7.4682e-3	3.3025	4.8971
28.5400	29.7400	7.2253e-3	3.3015	4.9302

(d1) $\omega_b = 0.47$ and $\phi_{B+C} = 0.1046$

$\dfrac{T_0}{°C}$	$\dfrac{T}{°C}$	$\dfrac{\tau}{s}$	$\dfrac{T^{-1}}{10^{-3} \cdot K^{-1}}$	$\ln \tau^{-1}$
24.5800	24.6400	0.3230	3.3581	1.1302
24.5800	24.6700	0.2871	3.3577	1.2480
24.5800	24.6900	0.3091	3.3575	1.1740
24.5800	24.7200	0.3057	3.3572	1.1850
24.5800	24.7600	0.2995	3.3567	1.2058
24.5800	24.7900	0.2900	3.3564	1.2378
24.5800	24.8400	0.3011	3.3558	1.2003
24.5800	24.8800	0.2964	3.3554	1.2160
24.5800	24.9300	0.2960	3.3548	1.2173
24.5800	24.9800	0.2932	3.3542	1.2270
24.5800	25.0300	0.2940	3.3537	1.2241
24.5800	25.0900	0.2956	3.3530	1.2189
24.5800	25.1600	0.2903	3.3522	1.2367
24.5800	25.2200	0.2874	3.3515	1.2470
24.5800	25.2900	0.2877	3.3508	1.2457
24.5800	25.3600	0.2833	3.3500	1.2612
24.5800	25.4400	0.2799	3.3491	1.2734
24.5800	25.5200	0.2751	3.3482	1.2906
24.5800	25.6000	0.2523	3.3473	1.3770
24.5800	24.6400	0.3230	3.3581	1.1302
24.5800	24.6700	0.2871	3.3577	1.2480

(d2) $\omega_b = 0.47$ and $\phi_{B+C} = 0.1531$

$\dfrac{T_0}{°C}$	$\dfrac{T}{°C}$	$\dfrac{\tau}{s}$	$\dfrac{T^{-1}}{10^{-3} \cdot K^{-1}}$	$\ln \tau^{-1}$
25.3600	25.4200	0.0562	3.3493	2.8794
25.3600	25.4500	0.0563	3.3490	2.8765
25.3600	25.4700	0.0583	3.3487	2.8422
25.3600	25.5000	0.0498	3.3484	2.9991
25.3600	25.5400	0.0538	3.3480	2.9231
25.3600	25.5700	0.0523	3.3476	2.9514
25.3600	25.6200	0.0495	3.3471	3.0051
25.3600	25.6600	0.0501	3.3466	2.9944
25.3600	25.7100	0.0497	3.3460	3.0018
25.3600	25.7600	0.0467	3.3455	3.0633
25.3600	25.8100	0.0459	3.3449	3.0820
25.3600	25.8700	0.0447	3.3443	3.1085
25.3600	25.9400	0.0429	3.3435	3.1497
25.3600	26.0000	0.0423	3.3428	3.1630
25.3600	26.0700	0.0403	3.3420	3.2106
25.3600	26.1400	0.0383	3.3412	3.2623
25.3600	25.4200	0.0562	3.3493	2.8794
25.3600	25.4500	0.0563	3.3490	2.8765
25.3600	25.4700	0.0583	3.3487	2.8422
25.3600	25.5000	0.0498	3.3484	2.9991
25.3600	25.5400	0.0538	3.3480	2.9231

(d3) $\omega_b = 0.47$ and $\phi_{B+C} = 0.2046$

$\dfrac{T_0}{°C}$	$\dfrac{T}{°C}$	$\dfrac{\tau}{10^{-3} \cdot s}$	$\dfrac{T^{-1}}{10^{-3} \cdot K^{-1}}$	$\ln \tau^{-1}$
25.8400	25.9000	3.8582	3.3439	5.5576
25.8400	25.9300	5.4114	3.3436	5.2192
25.8400	25.9500	4.8668	3.3434	5.3253
25.8400	25.9800	5.2290	3.3430	5.2535
25.8400	26.0200	4.8692	3.3426	5.3248
25.8400	26.0500	4.1497	3.3422	5.4847
25.8400	26.1000	4.5565	3.3417	5.3912
25.8400	26.1400	4.1733	3.3412	5.4791
25.8400	26.1900	4.3168	3.3407	5.4452
25.8400	26.2400	4.0257	3.3401	5.5151
25.8400	26.2900	4.1313	3.3396	5.4892
25.8400	26.3500	3.8886	3.3389	5.5497
25.8400	26.4200	3.8047	3.3381	5.5715
25.8400	26.4800	3.5856	3.3374	5.6308
25.8400	26.5500	3.5003	3.3367	5.6549
25.8400	26.6200	3.3481	3.3359	5.6994
25.8400	26.7000	3.3750	3.3350	5.6914
25.8400	26.7800	3.1221	3.3341	5.7692
25.8400	26.8600	3.2010	3.3332	5.7443
25.8400	25.9000	3.8582	3.3439	5.5576
25.8400	25.9300	5.4114	3.3436	5.2192

(e1) $\omega_b = 0.37$ and $\phi_{B+C} = 0.0998$

$\dfrac{T_0}{°C}$	$\dfrac{T}{°C}$	$\dfrac{\tau}{s}$	$\dfrac{T^{-1}}{10^{-3} \cdot K^{-1}}$	$\ln \tau^{-1}$
23.3300	23.4400	0.0257	3.3717	3.6613
23.3300	23.4700	0.0310	3.3713	3.4738
23.3300	23.5100	0.0268	3.3709	3.6181
23.3300	23.5400	0.0310	3.3705	3.4748
23.3300	23.5900	0.0293	3.3700	3.5302
23.3300	23.6300	0.0335	3.3695	3.3972
23.3300	23.6800	0.0338	3.3689	3.3863
23.3300	23.7300	0.0358	3.3684	3.3298
23.3300	23.7800	0.0360	3.3678	3.3252
23.3300	23.8400	0.0392	3.3671	3.2382
23.3300	23.9100	0.0405	3.3663	3.2073
23.3300	23.9700	0.0447	3.3656	3.1078
23.3300	24.0500	0.0460	3.3647	3.0791

(e2) $\omega_b = 0.37$ and $\phi_{B+C} = 0.1560$

$\dfrac{T_0}{°C}$	$\dfrac{T}{°C}$	$\dfrac{\tau}{10^{-3} \cdot s}$	$\dfrac{T^{-1}}{10^{-3} \cdot K^{-1}}$	$\ln \tau^{-1}$
24.0900	24.1500	4.5911	3.3636	5.3836
24.0900	24.1800	5.8541	3.3633	5.1406
24.0900	24.2000	6.4325	3.3630	5.0464
24.0900	24.2300	6.4175	3.3627	5.0487
24.0900	24.2700	5.4884	3.3622	5.2051
24.0900	24.3000	5.5711	3.3619	5.1902
24.0900	24.3500	6.0021	3.3613	5.1157
24.0900	24.3900	6.5640	3.3609	5.0262
24.0900	24.4400	6.5636	3.3603	5.0262
24.0900	24.4900	6.6709	3.3598	5.0100
24.0900	24.5400	6.9535	3.3592	4.9685
24.0900	24.6000	6.8434	3.3585	4.9845
24.0900	24.6700	7.1780	3.3577	4.9367
24.0900	24.7300	7.4072	3.3571	4.9053
24.0900	24.8000	7.5808	3.3563	4.8821
24.0900	24.8700	7.7863	3.3555	4.8554

(e3) $\omega_b = 0.37$ and $\phi_{B+C} = 0.2004$

$\dfrac{T_0}{°C}$	$\dfrac{T}{°C}$	$\dfrac{\tau}{10^{-3} \cdot s}$	$\dfrac{T^{-1}}{10^{-3} \cdot K^{-1}}$	$\ln \tau^{-1}$
24.5400	24.6500	1.1020	3.3580	6.8106
24.5400	24.6800	1.1198	3.3576	6.7946
24.5400	24.7200	1.1030	3.3572	6.8097
24.5400	24.7500	1.2937	3.3568	6.6503
24.5400	24.8000	1.3245	3.3563	6.6267
24.5400	24.8400	1.3006	3.3558	6.6449
24.5400	24.8900	1.3655	3.3553	6.5962
24.5400	24.9400	1.3612	3.3547	6.5994
24.5400	24.9900	1.5234	3.3541	6.4868
24.5400	25.0500	1.5327	3.3535	6.4807
24.5400	25.1200	1.6506	3.3527	6.4066
24.5400	25.1800	1.8001	3.3520	6.3199

(f1) $\omega_b = 0.42$ and $\phi_{B+C} = 0.1002$

$\dfrac{T_0}{°C}$	$\dfrac{T}{°C}$	$\dfrac{\tau}{s}$	$\dfrac{T^{-1}}{10^{-3} \cdot K^{-1}}$	$\ln \tau^{-1}$
23.8700	23.9300	0.0863	3.3661	2.4499
23.8700	23.9600	0.0818	3.3658	2.5035
23.8700	23.9800	0.0852	3.3655	2.4631
23.8700	24.0100	0.0944	3.3652	2.3606
23.8700	24.0500	0.0892	3.3647	2.4172
23.8700	24.0800	0.0907	3.3644	2.4002
23.8700	24.1300	0.0946	3.3638	2.3585
23.8700	24.1700	0.0934	3.3634	2.3712
23.8700	24.2200	0.0976	3.3628	2.3272
23.8700	24.2700	0.0984	3.3622	2.3187
23.8700	24.3200	0.1031	3.3617	2.2724
23.8700	24.3800	0.1061	3.3610	2.2431
23.8700	24.4500	0.1076	3.3602	2.2296
23.8700	24.5100	0.1108	3.3595	2.2003
23.8700	24.5800	0.1122	3.3587	2.1872
23.8700	24.6500	0.1139	3.3580	2.1721
23.8700	24.7300	0.1176	3.3571	2.1402

(f2) $\omega_b = 0.42$ and $\phi_{B+C} = 0.1500$

$\dfrac{T_0}{°C}$	$\dfrac{T}{°C}$	$\dfrac{\tau}{s}$	$\dfrac{T^{-1}}{10^{-3} \cdot K^{-1}}$	$\ln \tau^{-1}$
24.5700	24.6300	0.0158	3.3582	4.1499
24.5700	24.6600	0.0146	3.3578	4.2245
24.5700	24.6800	0.0149	3.3576	4.2064
24.5700	24.7100	0.0142	3.3573	4.2522
24.5700	24.7500	0.0140	3.3568	4.2663
24.5700	24.7800	0.0162	3.3565	4.1207
24.5700	24.8300	0.0153	3.3559	4.1777
24.5700	24.8700	0.0150	3.3555	4.1997
24.5700	24.9200	0.0143	3.3549	4.2475
24.5700	24.9700	0.0146	3.3544	4.2245
24.5700	25.0200	0.0145	3.3538	4.2359
24.5700	25.0800	0.0145	3.3531	4.2313
24.5700	25.1500	0.0148	3.3523	4.2131
24.5700	25.2100	0.0147	3.3517	4.2199
24.5700	25.2800	0.0144	3.3509	4.2382

(f3) $\omega_b = 0.42$ and $\phi_{B+C} = 0.1999$

$\dfrac{T_0}{°C}$	$\dfrac{T}{°C}$	$\dfrac{\tau}{10^{-3} \cdot s}$	$\dfrac{T^{-1}}{10^{-3} \cdot K^{-1}}$	$\ln \tau^{-1}$
25.2000	25.2600	3.6011	3.3511	5.6265
25.2000	25.2900	2.6195	3.3508	5.9448
25.2000	25.3100	3.1096	3.3505	5.7733
25.2000	25.3400	2.7032	3.3502	5.9133
25.2000	25.3800	2.3805	3.3497	6.0404
25.2000	25.4100	2.4966	3.3494	5.9928
25.2000	25.4600	2.5810	3.3488	5.9596
25.2000	25.5000	2.5417	3.3484	5.9749
25.2000	25.5500	2.6388	3.3478	5.9374
25.2000	25.6000	2.6335	3.3473	5.9394
25.2000	25.6500	2.6641	3.3467	5.9279
25.2000	25.7100	2.4895	3.3460	5.9957
25.2000	25.7800	2.5007	3.3453	5.9912
25.2000	25.8400	2.4799	3.3446	5.9996
25.2000	25.9100	2.5035	3.3438	5.9901
25.2000	25.9800	2.5960	3.3430	5.9538

(f4) $\omega_b = 0.42$ and $\phi_{B+C} = 0.2501$

$\dfrac{T_0}{°C}$	$\dfrac{T}{°C}$	$\dfrac{\tau}{10^{-6} \cdot s}$	$\dfrac{T^{-1}}{10^{-3} \cdot K^{-1}}$	$\ln \tau^{-1}$
25.7700	25.8300	552.76	3.3447	7.5006
25.7700	25.8600	492.26	3.3444	7.6165
25.7700	25.8800	508.00	3.3441	7.5850
25.7700	25.9100	523.38	3.3438	7.5552
25.7700	25.9500	620.99	3.3434	7.3842
25.7700	25.9800	540.94	3.3430	7.5222
25.7700	26.0300	533.70	3.3425	7.5357
25.7700	26.0700	515.00	3.3420	7.5713
25.7700	26.1200	577.44	3.3415	7.4569
25.7700	26.1700	566.73	3.3409	7.4756
25.7700	26.2200	565.21	3.3403	7.4783
25.7700	26.2800	595.40	3.3397	7.4263
25.7700	26.3500	610.70	3.3389	7.4009
25.7700	26.4100	634.25	3.3382	7.3631
25.7700	26.4800	662.39	3.3374	7.3197

Table 9.5: Surfactant / (oil + surfactant) volume fraction ω_b dependence of the activation energies E_a in [kJ / mol] and the standard error ΔE_a in [kJ / mol].

ω_b	$\dfrac{E_a}{\text{kJ} \cdot \text{mol}^{-1}}$	$\dfrac{\Delta E_a}{\text{kJ} \cdot \text{mol}^{-1}}$
0.81	72.6667	12.7410
0.69	297.0000	48.6621
0.58	491.6667	2.5166
0.47	297.3333	169.2375
0.42	-125.5000	177.8511
0.37	-580.0000	121.2436

9.2.2 Isothermal shear experiments

Table 9.6: Surfactant / (oil + surfactant) volume fractions ω_b, bilayer volume fractions ϕ_{B+C}, compositions ($m_{H_2O/NaCl}$, $m_{n-octane}$, and $m_{C_{10}E_4}$) in [g] of the L_3 phase samples for isothermal shear experiments and the phase boundary temperatures $T_{L_3+L_\alpha \to L_3}$ and $T_{L_3 \to L_1'+L_3}$ of the respective L_3 phase coexistence regions in [°C].

ω_b	ϕ_{B+C}	$\dfrac{m_{H_2O/NaCl}}{g}$	$\dfrac{m_{n-octane}}{g}$	$\dfrac{m_{C_{10}E_4}}{g}$	$\dfrac{T_{L_3+L_\alpha \to L_3}}{°C}$	$\dfrac{T_{L_3 \to L_1'+L_3}}{°C}$
0.6874	0.0300	9.6861	0.0660	0.1978	30.3500	30.8800
0.6874	0.0400	12.6944	0.1165	0.3494	30.4500	31.0500
0.6875	0.0500	9.4848	0.1100	0.3301	30.6800	31.1400
0.6874	0.0600	9.3815	0.1319	0.3957	30.7000	31.4500
0.6874	0.0700	9.2841	0.1538	0.4616	30.8300	31.6800
0.6874	0.0801	9.1891	0.1763	0.5288	31.0400	31.9400
0.5765	0.0300	9.6850	0.0894	0.1659	25.4500	26.0000
0.5765	0.0400	9.5826	0.1191	0.2211	25.5900	26.2600
0.5765	0.0500	9.4847	0.1489	0.2766	25.8000	26.5200
0.5765	0.0600	9.3871	0.1787	0.3319	25.9600	26.8000

Table 9.7: Bilayer volume fraction ϕ_{B+C} dependence of the relaxation times τ in [s] and relaxation time constants τ^{-1} in [s⁻¹] for isothermal shear experiments for two surfactant / (oil + surfactant) volume fractions ω_b.

ω_b	ϕ_{B+C}	$\dfrac{\tau}{s}$	$\dfrac{\tau^{-1}}{s^{-1}}$
0.6874	0.0300	306.0725	3.2672e-3
0.6874	0.0400	183.7425	5.4424e-3
0.6875	0.0500	121.4506	8.2338e-3
0.6874	0.0600	54.9551	0.0182
0.6874	0.0700	28.0899	0.0356
0.5765	0.0300	174.1341	5.7427e-3
0.5765	0.0400	106.6246	9.3787e-3
0.5765	0.0500	50.5050	0.0198
0.5765	0.0600	26.8817	0.0372

9.2.3 SANS experiments

Table 9.8: Surfactant / (oil + surfactant) volume fractions ω_b, surfactant volume fractions ϕ_C, compositions $m_{H_2O/NaCl}$, $m_{n-octane}$, and $m_{C_{10}E_4}$ in [g] of the L₃ phase samples for SANS experiments in film contrast and the phase boundary temperatures $T_{L_3+L_\alpha \to L_3}$ and $T_{L_3 \to L_1'+L_3}$ of the respective L₃ phase coexistence region in [°C].

ω_b	ϕ_C	$\dfrac{m_{D_2O}}{g}$	$\dfrac{m_{d-octane}}{g}$	$\dfrac{m_{C_{10}E_4}}{g}$	$\dfrac{T_{L_3+L_\alpha \to L_3}}{°C}$	$\dfrac{T_{L_3 \to L_1'+L_3}}{°C}$
0.6876	0.0802	1.9595	0.0596	0.1544	31.11	32.17
0.6875	0.0997	1.8958	0.0741	0.1919	31.32	32.39
0.6874	0.1250	1.8139	0.0929	0.2405	32.46	33.47
0.6873	0.1562	1.7135	0.1162	0.3007	33.60	34.58
0.6874	0.1954	1.5865	0.1452	0.3759	35.22	36.46
0.6874	0.2444	1.4279	0.1815	0.4699	36.85	38.47
0.6875	0.3057	1.2300	0.2268	0.5875	38.68	41.25
0.6875	0.0247	2.1390	0.0183	0.0475	28.95	>30.50
0.3749	0.0997	1.6268	0.2716	0.1918	24.73	24.78
0.4726	0.0997	1.7491	0.1818	0.1918	25.52	26.06
0.5765	0.0997	1.8338	0.1197	0.1918	27.45	28.06
0.6875	0.0997	1.8960	0.0741	0.1919	31.32	32.38
0.8061	0.0997	1.9434	0.0392	0.1918	40.27	41.40
0.9001	0.0997	1.9721	0.0181	0.1919	47.89	49.26
1.0000	0.0996	1.9969	0.0000	0.1918	51.53	53.62

Table 9.9: Surfactant / (oil + surfactant) volume fractions ω_b, surfactant volume fractions ϕ_C, compositions $m_{H_2O/NaCl}$, $m_{n-octane}$, and $m_{C_{10}E_4}$ in [g] of the L_3 phase samples for SANS experiments in bulk contrast and the phase boundary temperatures $T_{L_3+L_\alpha \to L_3}$ and $T_{L_3 \to L_1'+L_3}$ of the respective L_3 phase coexistence regions in [°C].

ω_b	ϕ_C	$\dfrac{m_{D_2O}}{g}$	$\dfrac{m_{n-octane}}{g}$	$\dfrac{m_{C_{10}E_4}}{g}$	$\dfrac{T_{L_3+L_\alpha \to L_3}}{°C}$	$\dfrac{T_{L_3 \to L_1'+L_3}}{°C}$
0.6873	0.0800	1.9598	0.0513	0.1540	30.86	31.69
0.6874	0.0997	1.8961	0.0638	0.1918	31.60	32.40
0.6874	0.1563	1.7126	0.1000	0.3007	33.29	34.38
0.6874	0.3055	1.2308	0.1955	0.5874	38.74	40.94
0.4726	0.0997	1.7494	0.1567	0.1918	25.17	25.69
0.6874	0.0997	1.8961	0.0638	0.1918	31.60	32.40
1.0000	0.0997	1.9972	0.0000	0.1919	51.46	53.57

Table 9.10: Surfactant volume fractions ϕ_C, scattering length q_d in [Å] for the midplane distance d in film and bulk contrast, and the associated midplane distances d in [Å] in film and bulk contrast.

ϕ_C	$\dfrac{q_d - film}{Å^{-1}}$	$\dfrac{q_d - bulk}{Å^{-1}}$	$\dfrac{d - film}{Å}$	$\dfrac{d - bulk}{Å}$
0.0802	0.0125	0.0125	502.656	502.656
0.0997	0.0167	0.0155	376.240	405.368
0.1250	0.0197	-	318.944	-
0.1562	0.0268	0.0268	234.448	234.448
0.1954	0.0310	-	202.684	-
0.2444	0.0435	-	144.441	-
0.3057	0.0549	0.0549	114.448	114.448

Table 9.11: Surfactant / (oil + surfactant) volume fractions ω_b, fudge factor f, variance t [Å] of the diffuseness of the monolayer, the incoherent background I_{incoh} [cm^{-1}], the polydispersity σ [Å] of the bilayer, distance between the bilayer midplane and one of the monolayers ε in [Å] and the associated bilayer thickness 2ε in [Å] in film contrast for $\phi_C = 0.1$.

ω_b	f	$\dfrac{t}{Å}$	$\dfrac{I_{Incoh}}{cm^{-1}}$	$\dfrac{\sigma}{Å}$	$\dfrac{\varepsilon}{Å}$	$\dfrac{2\varepsilon}{Å}$
0.4726	0.850	5.20	0.132	6.15	20.70	41.40
0.5765	0.875	5.30	0.142	3.95	15.75	31.50
0.6875	0.890	5.25	0.134	2.58	11.70	23.40
0.8061	0.930	5.30	0.130	1.90	8.80	17.60
0.9001	0.930	5.30	0.127	1.85	7.30	14.60

Table 9.12: Surfactant volume fractions ϕ_C, fudge factor *f*, variance *t* [Å] of the diffuseness of the monolayer, the incoherent background I_{incoh} [cm^{-1}], the polydispersity σ [Å] of the bilayer, distance between the bilayer midplane and one of the monolayers ε in [Å] and the associated bilayer thickness 2ε in [Å] in film contrast for ω_b, = 0.69.

ϕ_C	*f*	$\dfrac{t}{\text{Å}}$	$\dfrac{I_{Incoh}}{\text{cm}^{-1}}$	$\dfrac{\sigma}{\text{Å}}$	$\dfrac{\varepsilon}{\text{Å}}$	$\dfrac{2\varepsilon}{\text{Å}}$
0.0802	0.950	5.50	0.120	2.55	11.70	23.40
0.0997	0.890	5.25	0.134	2.58	11.70	23.40
0.1250	0.900	5.30	0.165	2.60	11.70	23.40
0.1562	0.900	5.25	0.185	2.63	11.60	23.20
0.1954	0.620	5.15	0.260	2.60	11.80	23.60
0.2444	0.880	5.25	0.280	2.65	11.45	22.90
0.3057	0.850	5.50	0.348	2.65	11.45	22.90

Table 9.13: Surfactant volume fraction ϕ_C, lower L$_3$ phase boundary temperature $T_l^{L_3}$ [°C], the spontaneous curvature of the monolayers c_0 [Å^{-1}], interbilayer distance *d* [Å], saddle-splay modulus $\overline{\kappa}_{bil}$ [k$_B$T], and the topological persistence length $\xi_{\overline{\kappa}}$ [Å]. Values are calculated with κ_{bil} = 1.96 k$_B$T, $\overline{\kappa}_{mono}$ = -0.37 k$_B$T and *a* = 2ε,

at ω_b = 0.69 $\Rightarrow$ 2ε = 23.4 Å

ϕ_C	$T_l^{L_3}$ / °C	c_0 / Å^{-1}	*d* / Å	$\overline{\kappa}_{bil}$ / k$_B$T	$\xi_{\overline{\kappa}}$ / Å
0.0802	31.1100	-8.9180e-3	502.656	-0.3310	81.4924
0.0997	31.3200	-9.2120e-3	376.240	-0.3175	77.4534
0.1250	32.4600	-0.0108	318.944	-0.2443	58.7755
0.1562	33.6000	-0.0124	234.448	-0.1711	44.6018
0.1954	35.2200	-0.0147	202.684	-0.0671	30.1334
0.2444	36.8500	-0.0170	144.441	0.0376	20.3091
0.3057	38.6800	-0.0195	114.448	0.1551	13.0410

at ω_b = 0.58 $\Rightarrow$ 2ε = 31.5 Å

ϕ_C	$T_l^{L_3}$ / °C	c_0 / Å^{-1}	*d* / Å	$\overline{\kappa}_{bil}$ / k$_B$T	$\xi_{\overline{\kappa}}$ / Å
0.0588	26.6400	-2.6600e-3	663.639	-0.5758	276.0492
0.0881	27.5000	-3.8640e-3	444.764	-0.5014	208.5846
0.1173	28.6800	-5.5160e-3	334.047	-0.3994	142.0015
0.1465	29.1800	-6.2160e-3	267.466	-0.3562	120.6521
0.1755	29.9700	-7.3220e-3	223.269	-0.2879	93.2689

at $\omega_b = 0.47 \Rightarrow 2\varepsilon = 41.4$ Å

ϕ_C	$T_l^{L_3}$ / °C	c_0 / Å^{-1}	d / Å	$\overline{\kappa}_{bil}$ / k$_B$T	$\xi_{\overline{\kappa}}$ / Å
0.0354	23.9900	1.0500e-4	1106.8854	-0.8252	929.0780
0.0494	24.5000	3.3600e-4	793.1932	-0.7673	746.7853
0.0732	25.1800	-6.1600e-4	535.2970	-0.6900	558.1109
0.0966	25.8300	-1.5260e-3	405.6288	-0.6162	422.4984
0.1184	26.5000	-2.4640e-3	330.9438	-0.5401	317.1099
0.1406	27.1000	-3.3040e-3	278.6895	-0.4719	245.2528

at $\omega_b = 0.37 \Rightarrow 2\varepsilon = 48.0$ Å

ϕ_C	$T_l^{L_3}$ / °C	c_0 / Å^{-1}	d / Å	$\overline{\kappa}_{bil}$ / k$_B$T	$\xi_{\overline{\kappa}}$ / Å
0.0281	22.9500	2.5060e-4	1394.4392	-0.9759	1901.7041
0.0375	23.3300	1.9740e-4	1044.8998	-0.9258	1574.5775
0.0586	24.0300	9.9400e-4	668.6646	-0.8336	1112.1166
0.0750	24.5100	3.2200e-4	522.4499	-0.7703	876.1895
0.0937	24.9900	-3.5000e-4	418.1830	-0.7071	690.3125
0.1124	25.4400	-9.8000e-4	348.6098	-0.6478	552.0336

9.2.4 *T*-jump experiments on the oil-rich L$_3$ phase

Table 9.14: Surfactant / (water + surfactant) volume fractions ω_a, bilayer volume fractions ϕ_{A+C}, compositions ($m_{H_2O/NaCl}$, $m_{n-octane}$, and $m_{C_{10}E_4}$) in [g] of the L$_3$ phase samples for experiments on the oil-rich side and the phase boundary temperatures $T_{L_3+L_2 \to L_3}$ and $T_{L_3 \to L_\alpha + L_3}$ of the respective L$_3$ phase coexistence regions in [°C].

ω_a	ϕ_{A+C}	$\dfrac{m_{H_2O/NaCl}}{g}$	$\dfrac{m_{n-octane}}{g}$	$\dfrac{m_{C_{10}E_4}}{g}$	$\dfrac{T_{L_3+L_2 \to L_3}}{°C}$	$\dfrac{T_{L_3 \to L_\alpha + L_3}}{°C}$
0.4723	0.1501	1.0286	7.7728	0.8845	21.9100	22.5000
0.4726	0.2004	1.3713	7.3104	1.1810	20.6300	21.3600
0.4723	0.2501	1.7120	6.8534	1.4722	19.4200	20.3100
0.4731	0.3007	2.0780	6.4602	1.7931	18.1400	19.2700
0.4726	0.3502	2.3982	5.9440	2.0649	16.9800	18.3100
0.4230	0.1502	1.1234	7.7607	0.7915	23.0800	23.2900
0.4224	0.1993	1.5612	7.6510	1.0972	22.0400	22.4500
0.4227	0.2502	1.9236	7.0330	1.3532	21.3000	21.8600
0.4225	0.3005	2.2351	6.3463	1.5710	20.1500	20.8400
0.4228	0.3499	2.6216	5.9442	1.8456	19.1800	20.0300

Table 9.15: Bilayer volume fraction ϕ_{A+C} dependence of the relaxation times τ in [s] and relaxation time constants τ^{-1} in [s^{-1}] for T-jump experiments on the oil-rich L$_3$ phase for two surfactant / (water + surfactant) volume fractions ω_a.

ω_a	ϕ_{A+C}	$\dfrac{\tau}{\text{s}}$	$\dfrac{\tau^{-1}}{\text{s}^{-1}}$
0.4726	0.2004	0.1268	7.8864
0.4723	0.2501	0.0433	23.0946
0.4731	0.3007	0.0137	72.9927
0.4224	0.1993	0.0105	94.9367
0.4227	0.2502	0.0045	221.5453
0.4225	0.3005	0.0017	574.5035
0.4228	0.3499	0.0011	931.5323

10 Literature

[1]   D. Anderson, H. Wennerström, U. Olsson, *J. Phys. Chem.*, **93**, 4243 (1989)

[2]   D. Roux, C. Coulon, M.E. Cates, *J. Phys. Chem.*, **96**, 4174 (1992)

[3]   D. Roux, *Physica A*, **213**, 168 (1995)

[4]   E. Freyssingeas, F. Nallet, D. Roux, *Langmuir*, **12**, 6028 (1996)

[5]   P. Ekwall, *Advances in Liquid Crystals*, Ed. G.H. Brown, Academic Press, New York, **1**, 1 (1975)

[6]   F. Harusawa, S. Nakamura, T. Mitsui, *Colloid Polym. Sci.*, **252**, 613 (1979)

[7]   J.C. Lang, R.D. Morgan, *J. Chem. Phys.*, **73**, 5849 (1980)

[8]   R. Strey, W. Jahn, M. Skouri, J. Marignan, G. Porte, U. Olsson, in: *Structure and Dynamics of strongly interacting Colloids and Supramolecular Aggregates in Solution*, Kluwer Academic Publishers, Netherlands, 351 (1992)

[9]   G. Porte, *J. Phys. Cond. Matter*, **4**, 8649 (1992)

[10]   R. Strey, *Colloid Polym. Sci.*, **272**, 1005 (1994)

[11]   U. Olsson, H. Wennerström, *Adv. Colloid Interface Sci.*, **49**, 113 (1994)

[12]   S.A. Safran, D. Roux, M.E. Cates, D. Andelmann, *Phys. Rev. Letters*, **57**, 491 (1986)

[13]   W. Jahn, R. Strey, *J. Phys. Chem.*, **92**, 2294 (1988)

[14]   R. Strey, W. Jahn, G. Porte, P. Bassereau, *Langmuir*, **6**, 1635 (1990)

[15]   G. Porte, J. Appell, P. Bassereau, M. Marignan, M. Skouri, I. Billard, M. Delsanti, S.J. Candau, R. Strey, W. Jahn, P. Snabre, *Prog. Colloid Polym. Sci.*, **84**, 264 (1991)

[16]   R. Strey, J. Winkler, L. Magid, *J. Phys. Chem.*, **95**, 7502 (1991)

[17]   E.A.G. Aniansson, S.N. Wall, *J. Chem. Phys.*, **78**, 1024 (1974)

[18]   M. Kahlweit, *J. Colloid Interface Sci.*, **90**, 92 (1982)

[19]   S. Friberg, S. Campbell, L. Fei, H. Yang, R. Patel, P.A. Aikens, *Colloids and Surfaces A*, **129-130**, 167 (1997)

[20]   S. Campbell, H. Yang, R. Patel, S. Friberg, P.A. Aikens, *Colloid Polym. Sci.*, **275**, 303 (1997)

[21]   C.A. Miller, M. Gradzielski, H. Hoffmann, U. Krämer, C. Thunig, *Prog.Colloid Polym. Sci.*, **84**, 243 (1997)

[22]   G. Porte, J. Marignan, P. Bassereau, R. May, *J. Physique*, **49**, 511 (1988)

[23]   G. Porte, M. Delsanti, I. Billard, M. Skouri, J. Appell, J. Marignan, F. Debeauvais, *J. Phys. II (France)* **1**, 1101 (1991)

[24]   G. Waton, G. Porte, *J. Phys. II*, **4**, 515 (1993)

[25] T.D. Le, U. Olsson, H. Wennerström, P. Schurtenberger, *Phys. Rev. E*, **60**, 4300 (1999)

[26] T.D. Le, PhD thesis, Lund (2000)

[27] P. Uhrmeister, Diploma thesis, Cologne (1998)

[28] B. Schwarz, G. Mönch, G. Ilgenfritz, R. Strey, *Langmuir*, **16**, 8643 (2000)

[29] R.M. Hill, *Curr. Opin. Colloid Interface Sci.*, **3**, 247 (1998)

[30] R. Wagner, R. Strey, *Langmuir*, **15**, 902 (1999)

[31] T. Stoebe, Z. Lin, R.M. Hill, M.D. Ward, H.T. Davis, *Langmuir*, **13**, 7282 (1997)

[32] A. Kabalnov, *Langmuir*, **16**, 2595 (2000)

[33] K. Shinoda, H. Arai, *J. Colloid Interface Sci.*, **25**, 429 (1967)

[34] M. Kahlweit, R. Strey, P. Firman, *J. Phys. Chem.*, **90**, 671 (1986)

[35] F. Lichterfeld, T. Schmeling, R. Strey, *J. Phys. Chem.*, **90**, 5762 (1986)

[36] K. Shinoda, H. Kunieda, T. Arai, H. Saijo, *J. Phys. Chem.*, **88**, 5126 (1984)

[37] M. Kahlweit, R. Strey, *Angew. Chem.*, **97**, 655 (1985)

[38] M. Kahlweit, E. Lessner, R. Strey, *J. Phys. Chem.*, **87**, 5032 (1983)

[39] M. Kahlweit, R. Strey, G. Busse, *J. Phys. Chem.*, **94**, 3881 (1990)

[40] M.S. Leaver, U. Olsson, H. Wennerström, R. Strey, U. Würz, *J. Chem. Soc. Faraday Trans.*, **91**, 4269 (1995)

[41] M. Kahlweit, R. Strey, D. Haase, H. Kunieda, T. Schmeling, B. Faulhaber, M. Borkovec, H.-F. Eicke, G. Busse, F. Eggers, Th. Funck, H. Richmann, L. Magid, O. Söderman, P. Stilbs, J. Winkler, A. Dittrich, W. Jahn, *J. Colloid Interface Sci.*, **118**, 436 (1987)

[42] K. Shinoda, in: *Principles of Solution and Solubility*, Marcel Dekker, Basel, 86 (1978)

[43] H. Wennerström, J. Daicic, U. Olsson, G. Jerke, P. Schurtenberger, *J. Mol. Liquids*, **72**, 15 (1997)

[44] R. Strey, *Ber. Bunsenges. Phys. Chem*, **100**, 182 (1996)

[45] R. Strey, R. Schomäcker, D. Roux, F. Nallet, U. Olsson, *J. Chem. Soc. Faraday Trans.*, **86**, 2253 (1990)

[46] B. Schwarz, Diploma thesis, Cologne (1998)

[47] G. Porte, private communications (2000)

[48] S. Burauer, PhD thesis, to be published

[49] W. Helfrich, *Z. Naturforsch.*, **28C**, 693 (1973)

[50] D. Nelson, T. Piran, S. Weinberg (Eds.), *Statistical Mechanics of Membranes and Surfaces*, World Scientific, Singapore (1989)

[51]   G. Gompper, M. Schick, Self-Assembling Amphiphilic Systems, Phase Transitions and Critical Phenomena Vol. 16, Academic Press, London (1994)

[52]   L. Peliti, Amphiphilic Membranes, in Fluctuating Geometries in Statistical Mechanics and Field Theory, eds. F. David, P. Ginsparg, Z. Zinn-Justin, Elsevier, 195 (1996)

[53]   D.C. Morse, *Curr. Opin. Colloid Interface Sci.*, **2**, 365 (1997)

[54]   T. Sottmann, R. Strey, *J. Phys.*: *Condens. Matter*, **8**, A39 (1996)

[55]   T. Sottmann, R. Strey, S.H. Chen, *J. Chem. Phys.*, **106**, 6483 (1997)

[56]   T. Sottmann, R. Strey, *J. Chem. Phys.*, **106**, 8606 (1997)

[57]   T. Sottmann, R. Strey, *Ber. Bunsenges. Phys. Chem*, **100**, 237 (1996)

[58]   H. Leitao, A.M. Somoza, M.M. Telo da Gama, T. Sottmann, R. Strey, *J. Chem. Phys.*, **105**, 2875 (1996)

[59]   L. Golubovic, T.C. Lubensky, *Phys. Rev. A*, **41**, 4343 (1990)

[60]   D. Andelman, M.E. Cates, D. Roux, S.A. Safran, *J. Phys. Chem.*, **87**, 7229 (1987)

[61]   L. Peliti, S. Leibler, *Phys. Rev. Lett.*, **54**, 1690 (1985)

[62]   P.G. De Gennes, C. Taupin, *J. Phys. Chem.*, **86**, 2294 (1982)

[63]   D.C. Morse, *Phys. Rev. E.*, **50**, R2423 (1994)

[64]   L. Golubovic, *Phys. Rev. E*, **50**, 2419 (1994)

[65]   G. Gompper, D.M. Kroll, *Phys. Rev. Lett*, **81**, 2284 (1998)

[66]   G. Porte, J. Appell, P. Bassereau, J. Marignan, *J. Physique*, **50**, 1335 (1989)

[67]   J.F. Sadoc, J. Charvolin, *J. Phys.*, **47**, 683 (1986)

[68]   G. Gompper, D.M. Kroll, *J. Phys.*: *Condens. Matter*, **12**, A29 (2000)

[69]   W. Helfrich, *Z. Naturforsch.*, **33A**, 305 (1978)

[70]   G. Gompper, private communication (2001)

[71]   G. Porte, *Curr. Opin. Colloid Interface Sci.*, **1**, 345 (1996)

[72]   H. Leitao, private communication (2000)

[73]   P. Sens, S.A. Safran, *Europhys. Lett.*, **43**, 95 (1998)

[74]   W.M. Gelbart, A. Ben-Shaul, *J. Phys. Chem.*, **100**, 13169 (1996)

[75]   F. Nallet, D. Roux, J. Prost, *Phys. Rev. Lett.*, **62**, 276 (1989)

[76]   J. Brunner-Popela, R. Mittelbach, R. Strey, K.-V. Schubert, E.W. Kaler, O. Glatter, *J. Chem. Phys.*, **110**, 10623 (1999)

[77]   H. Bagger-Jörgensen, U. Olsson, K. Mortensen, *Langmuir*, **13**, 1413 (1997)

[78]   M. Gradzielski, H. Hoffmann, D. Langevin, *J. Phys. Chem.*, **99**, 12612 (1995)

[79]   N. Lei, C.R. Safinya, D. Roux, K.S. Liang, *Phys. Rev. E*, **56**, 608 (1997)

[80]   A. Maldonado, W. Urbach, R. Ober, D. Langevin, *Phys. Rev. E*, **54**, 1774 (1996)

[81]   B. Lindman, N. Kamenka, T.-M. Kathopoulis, B. Brun, P.-G. Nilsson, *J. Phys. Chem.*, **84**, 2485 (1980)

[82]   O. Söderman, P. Stilbs, *Progr. NMR Spectrosc.*, **26**, 445 (1994)

[83]   B. Lindman, U. Olsson, *Ber. Bunsenges. Phys. Chem*, **100**, 344 (1996)

[84]   P. Stilbs, *Progr. NMR Spectrosc.*, **19**, 1 (1987)

[85]   A. Bernheim-Groswasser, T. Tlusty, S.A. Safran, Y. Talmon, *Langmuir*, **15**, 5448 (1999)

[86]   Y. Talmon, *Ber. Bunsenges. Phys. Chem*, **100**, 364 (1996)

[87]   M. Eigen, L. de Maeyer, *Techniques of Organic Chemistry*, **7**, 896, (1963)

[88]   R. Rigler, C.R. Rabl, I.M. Jovin, *Rev. Sci. Instr.*, **45**, 580 (1974)

[89]   H. Strehlow, W. Knoche, *Fundamentals in Chemical Relaxation*, VCH Weinheim (1987)

[90]   L.M.M. Nazario, J.P.S.G. Crespo, J.F. Holzwarth, T.A. Hatton, *Langmuir*, **16**, 5892 (2000)

[91]   W. Knoche, G. Wiese, *Chem Instr.*, **5**, 91 (1973)

[92]   Z.A. Schelly, *Curr. Opin. Colloid Interface Sci.*, **2**, 37 (1997)

[93]   R.E. Verrall, *Chem. Soc. Rev.*, **24**, 135 (1995)

[94]   K. Baumgardt, G. Klar, R. Strey, *Ber. Bunsenges. Phys. Chem.*, **83**, 1222 (1979)

[95]   A. Pakusch, R. Strey, *Ber. Bunsenges. Phys. Chem.*, **84**, 1163 (1980)

[96]   M. Kahlweit, *Pure & Appl. Chem.*, **53**, 2069 (1981)

[97]   Y. Rharbi, M.A. Winnik, *Langmuir*, **15**, 4697 (1999)

[98]   S.U. Egelhaaf, P. Schurtenberger, *Phys. Rev. Lett.*, **82**, 2804 (1999)

[99]   M.T. Yatcilla, K.L. Herrington, L.L. Brasher, E.W. Kaler, S. Chiruvolu, J.A. Zasadzinkski, *J. Phys. Chem.*, **100**, 5874 (1996)

[100]   R. Zana, in: K.L. Mittal, P. Bothorel (Eds.), Surfactants and Solutions, Vol. 4, Plenum Press, New York, 115 (1986)

[101]   W. Mayer, D. Woermann, *J. Chem. Phys.*, **92**, 2036 (1988)

[102]   S.W. Provencher, *Comput. Phys. Commun.*, **27**, 213 (1982)

[103]   A. Pakusch, PhD thesis, Göttingen (1987)

[104]   R. Strey, A. Pakusch, in: K.L. Mittal, P. Bothorel (Eds.), Surfactants and Solutions, Vol. 4, Plenum Publishing Corporation, 465 (1987)

[105]   J. Yamamoto, H. Tanaka, *Phys. Rev. Lett.*, **77**, 4390 (1996)

[106]   M.E. Cates, S.T. Milner, *Phys. Rev. Lett.*, **62**, 1856 (1989)

[107]   R. Wilke, Diploma thesis, Cologne (2000)

[108] M. Skouri, J. Marignan, J. Appell, G. Porte, *J. Phys. II (France)* **1**, 1121 (1991)

[109] G. Porod, in: *Small Angle X-ray Scattering*, eds. O. Glatter, O. Kratky, Academic Press, New York (1982)

[110] R. Strey, private communication (2001)

[111] Y. Talmon, S. Prager, *J. Chem. Phys.*, **69**, 2984 (1978)

[112] T. Sottmann, PhD thesis, Göttingen (1997)

[113] S.T. Milner, M.E. Cates, D. Roux, *J. Physique*, **51**, 2629 (1990)

[114] R. Strey, *Ber. Bunsenges. Phys. Chem*, **97**, 742 (1993)

[115] I. Szleifer, D. Kramer, A. Ben-Shaul, D. Roux, W. Gelbart, *Phys. Rev. Lett.*, **60**, 1966 (1988)

[116] C.R. Safinya, E.B. Sirota, D. Roux, G.S. Smith, *Phys. Rev. Lett.*, **62**, 1143 (1989)

[117] A. Kabalnov, H. Wennerström, *Langmuir*, **12**, 276 (1996)

[118] A. Kabalnov, J. Weers, *Langmuir*, **12**, 1931 (1996)

[119] K.-V. Schubert, R. Strey, M. Kahlweit, *J. Colloid Interface Sci.*, **141**, 21 (1991)

[120] K.V. Schubert, R. Strey, M. Kahlweit, *Prog. Colloid Polym. Sci.*, **84**, 103 (1991)

[121] V. Beckmann, PhD thesis, Cologne (1995)

[122] K. Kluge, PhD thesis, Cologne (2000)

Ich versichere, daß ich die von mir vorgelegte Dissertation selbständig angefertigt, die benutzten Quellen und Hilfsmittel vollständig angegeben und die Stellen der Arbeit - einschließlich Tabellen, Karten und Abbildungen -, die anderen Werken im Wortlaut oder dem Sinn nach entnommen sind, in jedem Einzelfall als Entlehnung kenntlich gemacht habe; daß die Dissertation noch keiner anderen Fakultät oder Universität zur Prüfung vorgelegen hat; daß sie - abgesehen von den unten angegebenen Teilpublikationen - noch nicht veröffentlich worden ist sowie, daß ich eine solche Veröffentlichung vor Abschluß des Promotionsverfahrens nicht vornehmen werde. Die Bestimmungen der Promotionsordnung sind mir bekannt. Die von mir vorgelegte Dissertation ist von Prof. Dr. R. Strey betreut worden.

Köln, den 11.05.2001

Lebenslauf

Persönliche Daten

Geburtsdatum/-ort:	26.03.1969 in Goslar
Familienstand:	ledig
Staatsangehörigkeit:	deutsch

Studium

Okt. 1998 – Juni 2001	Promotion " Dynamics of L_3 phases" unter Anleitung von Prof. Dr. R. Strey
Sept. 1996 – Sept. 1998	Forschungsaufenthalt am University College Dublin, Irland zum Thema "Rheologie und Struktur biologischer Makromoleküle in kolloidalen Systemen
August 1995 - März 1996	Diplomarbeit im Bereich "Technische Chemie", Technische Universität Braunschweig. Titel der Arbeit "Das Phasenverhalten von Mikroemulsionen mit kommerziellen Tensiden"
April 1989 - Mai 1996	Studium der Chemie an der Technischen Universität Braunschweig Schwerpunkte: Anorganische, Organische, Physikalische und Technische Chemie Abschluß: Diplom-Chemikerin (Note: sehr gut)
Okt. 1993 - Juni 1994	Einjähriges Auslandsstudium am Trinity College Dublin, Irland, im Rahmen des Erasmus Austauschprogrammes. Darin viermonatiges Forschungsprojekt mit dem Titel: "Measurement of Work Functions of Mg-Al Alloys by Means of Surface Spectroscopy".

Schule

1981 - 1988	Ratsgymnasium Goslar Abschluß: Allgemeine Hochschulreife
1979 - 1981	Orientierungsstufe Langelsheim
1975 - 1979	Grundschule Langelsheim